

Copyright

by

Sunghwan Jung

2005

The Dissertation Committee for Sunghwan Jung
Certifies that this is the approved version of the following Dissertation:

Statistics of Turbulence in a Rapidly Rotating System

Committee:

Harry L. Swinney, Co-supervisor

Philip J. Morrison, Co-supervisor

Jack B. Swift

Allan H. Macdonald

David G. Bogard

Statistics of Turbulence in a Rapidly Rotating System

by

Sunghwan Jung, B.S., M.S.

Dissertation

Presented to the Faculty of the Graduate School of

The University of Texas at Austin

in Partial Fulfillment

of the Requirements

for the Degree of

Doctor of Philosophy

The University of Texas at Austin

May 2005

I have learned 1 % of physics,
but realized 99 % left to be understood.

Acknowledgments

Harry Swinney was my daily mentor throughout my Ph.D years. He treat me as a son and a friend. His care for students as well as his academic achievement are worthy of respect. He also gave me many opportunities to communicate scientists inside and outside UT.

Also, I greatly admire Philip Morrison. At the first meeting, I was impressed by his kindness. He handed me paper and a pen and gave me a private 2-hour lecture on his non-canonical bracket. I have learned a lot from him in various theoretically fields.

I would like to acknowledge the previous scientists who built the rotating annulus: Joel Sommeria, Steve Meyers, Tom Solomon, Eric Weeks, Charles Baroud and Julien Aubert. Especially, Charles Baroud, Eric Weeks and Tom Solomon encouraged me whenever I met them. I was so lucky because many good students helped me to finish my Ph.D work. HongKi Min, Hoshik Lee, and Jason JenBarge worked on collecting hot film data for their 380N course. Also, JuHyong Kim volunteered to help me on hot film measurements. Wise Abe Raybrough had worked hard with me for a year. Jori Ruppert-Felsot taught me various things whenever I had problems. Dr. Hepeng helped me to get velocity data and provide many ideas.

Beside a rotating annulus, I was enjoying the bouncing jet project. There are a number of people to help the project. Prof. McCormick helped me to continue the experiment as well as providing me advise. ChihPiao Chuu and Yvon Pang had worked hard to develop the system and measurements. I would like to thank Matt Thrasher to give me a chance to work on the bouncing jet together.

Also, I would like to thank Prof. Udagawa for giving me many opportunities to meet other people in various fields. He always praises and encourages me. I am indebted to Dr. Andrew Reynolds and Christian Beck for discussing the statistics of turbulence, Dr. ChangYong Lee for discussing complex networks and Dr. Brian Storey for working with me on geophysical flows. The Harrington fellowship generously supported me for one year. I am so pleased to organize the Harrington Symposium on *Abrupt Climate Changes* with Prof. Harry L. Swinney, Prof. Jay L. Banner, Dr. Charles Jackson, Dr. John Dollard, Dr. MaryLynn Musgrove, Christine Marcin and Julie Ewald. During my graduate years, I have had a lot of fun time with my friends Chihsung Chuu, JungJung Su, Tien-Ming and other Korean friends. Finally, I am indebted to everyone in CNLD and in physics department.

Most of all, I thank all of my family for supporting and raising me for 30 years. My wife, EunYoung Song, is always so supportive for my work and hanging on with the hot Texas weather. My parents, JinSu Jung and ShinJa Kim, always taught me to respect books when I was the kid. That lesson made me want to study for Ph.D. My sister (EunYoung Jung), her husband and their two children always give me love and my brother (SeungHo Jung) and his wife support me devotedly. My parents-in-law (HongKi Song, SukRye Park) and brother-in-law (JongMin Song) support and encourage me in various ways. I

would like to dedicate my dissertation in the memory of my late grandmother,
SamRye Lee.

SUNGHWAN JUNG

The University of Texas at Austin

May 2005

Statistics of Turbulence in a Rapidly Rotating System

Publication No. _____

Sunghwan Jung, Ph.D.

The University of Texas at Austin, 2005

Supervisors: Harry L. Swinney and P. J. Morrison

Turbulence raises many issues such as fundamental questions in mathematics, continuum mechanics in physics and various industrial problems. Turbulence is characterized as a state of fluid flow that is influenced strongly by nonlinear processes compared to dissipation. Turbulence of fluids with strong rotation is of interest in turbo-machinery and geophysical flows that occur in the earth's atmosphere and oceans. Strong rotation can bring a turbulent system into a quasi two-dimensional (2D) turbulence.

Rotation causes anisotropic turbulent motions on large scales. However, on small scales the turbulence is believed to be homogeneous and isotropic and that fluid motions are independent of rotation and large-scale topography. Despite this general belief, in our experiments we find that the energy spectrum in a rotating turbulent flow strongly depends on large-scale topography and a

rotation.

A 2D fluid system with forcing and dissipation neglected has a Hamiltonian structure with conserved quantities. These conserved quantities constrain the dynamics of 2D fluid. For a long time, it has been quite mysterious why only quadratic conserved quantities (energy and the square of vorticity) should be important in a statistical mechanical description of turbulence, especially, in 2D turbulence, where there are an infinite number of conserved quantities (the so-called Casimir invariants). Previous models of statistical mechanics of 2D turbulence have not explicitly taken into account statistical independence of macroscopic subparts, and consequently all or most of the conserved quantities have been used. However, experimental results support the use of only quadratic conserved quantities. Because of statistical independence, we show that only quadratic conserved quantities are crucial in statistical mechanics. In addition, we propose a statistical mechanical theory based on new coordinates that define statistically independent subsystems, and we compare the theory with experiments.

Hamiltonian and action principles elucidate the physics in various fields, from quantum to plasma physics. Such a formulation has been used in plasma physics for the Vlasov-Poisson system to obtain fluctuation spectra. For a fluid, a similar process is possible. In this thesis, we use Hamiltonian principles to formulate the analogous fluctuation spectrum in the fluid case and compare it with experiments.

Contents

Acknowledgments	v
Abstract	viii
List of Tables	xv
List of Figures	xvi
Chapter 1 Introduction	1
Chapter 2 Review of Theory and Literature	5
2.1 Various Approximations	6
2.1.1 Navier-Stokes Equation	6
2.1.2 Inviscid Model	8
2.1.3 Geostrophic Equation	10
2.1.4 Dimensional Analysis	11
2.1.5 Quasi-geostrophic Equation	13
2.2 Turbulence	17
2.2.1 Energy Spectrum	19
2.2.2 Probability Distribution Function (PDF)	27

2.3	Hamiltonian and Action Formulations	30
2.3.1	Canonical Hamiltonian Structure	31
2.3.2	Noncanonical Hamiltonian Structure	32
2.4	Statistical Mechanics	35
2.4.1	Statistics and Entropy	36
2.4.2	Equilibrium Distribution	38
2.4.3	Nonextensive Entropy	39
2.5	Summary and My Work	41
Chapter 3	Experimental Apparatus and Methods	43
3.1	Rotating Tank	43
3.1.1	Flat Bottom	46
3.1.2	Dynamics with Slopping vs. Flat Bottom	46
3.2	Hot Film Anemometry	47
3.2.1	Probe	48
3.2.2	Data Acquisition	50
3.2.3	Probe Calibration	51
3.3	Particle Image Velocimetry (PIV)	54
3.4	Flow Control	54
Chapter 4	Potential Vorticity Mixing	57
4.1	Introduction	57
4.2	Model	60
4.3	Results	61
4.4	Discussion	68

Chapter 5	Statistical Mechanics	71
5.1	Introduction	72
5.1.1	Overview	72
5.1.2	Background	75
5.1.3	Notation Organization	78
5.2	Experiment	81
5.3	Dynamics	82
5.4	Statistical Mechanics and Fluid Mechanics	84
5.4.1	State Variables	84
5.4.2	Phase Space Volume and Liouville's Theorem	86
5.4.3	Canonical Equilibrium Distribution	92
5.5	Mean Field Approximation and Statistical Independence	94
5.5.1	Counting States	95
5.5.2	Mean Field Canonical Distribution	98
5.5.3	Ruggedness and Additivity	100
5.5.4	Statistically Independent Subsystems	103
5.5.5	Prediction for PDFs	109
5.6	Conclusions	116
Chapter 6	Nonextensive Statistical Mechanics	119
6.1	Introduction	119
6.2	Nonextensive Entropy	122
6.3	Energy-entropy Models	123
6.3.1	Extensive Model	124
6.3.2	Nonextensive Model	126
6.4	Results	128

6.4.1	Qualitative Flow Features	129
6.4.2	Stream Function Solution and the Vorticity Profile . .	129
6.4.3	Vorticity PDF	131
6.5	Discussion	132
Chapter 7	Fluctuations	134
7.1	Introduction	134
7.2	Statistical Mechanics	135
7.2.1	Partition Function	136
7.3	Hamiltonian System and Fluctuations	138
7.3.1	Canonization and Diagonalization	140
7.3.2	Solving for ψ_k	144
7.3.3	Fluctuation Spectra	145
7.4	Results	152
7.5	Conclusion	156
Chapter 8	Velocity Difference Statistics	157
8.1	Theory	158
8.1.1	Method of Castaing et al.	158
8.1.2	Superstatistics of Beck and Cohen	159
8.1.3	Unified View of PDFs	160
8.2	Experiment	163
8.3	Results	164
8.3.1	Probability Density Function of Inverse Temperature .	164
8.3.2	Conditional Probability and the Proper Subsystem Size	166
8.3.3	Probability Distribution of δv_r	169
8.3.4	Castaing and Beck-Cohen Methods	171

8.4	Conclusions	173
Chapter 9	Energy spectrum	175
9.1	Introduction	175
9.2	Previous Work	176
9.2.1	Different Scales in a Rotating Fluid	176
9.2.2	Energy Spectrum in 2D Turbulence	177
9.3	Model	179
9.3.1	Ageostrophic Model	179
9.3.2	Two-layers Model	183
9.3.3	Energy Transfer Between BC and BT Modes	185
9.4	Experimental Observations	187
9.4.1	Energy Spectrum over Sloped vs. Flat Bottom	189
9.4.2	Burstings	194
9.5	Conclusion and Future Work	196
Chapter 10	Conclusion	197
10.1	Contributions	198
10.2	Future Work	199
Bibliography		201
Vita		228

List of Tables

2.1	Rossby numbers and Reynolds numbers in various atmospheric motions.	12
2.2	Table of statistics	36
5.1	Comparison of fluctuations for square cells with our streamfunction based cells	109

List of Figures

2.1	Energy transfer in a 2D fluid	21
3.1	Schematic diagrams of the experimental apparatus	44
3.2	Calibration data for a hot-film probe	52
3.3	Calibration data for a hot-film probe induced by contaminations	53
3.4	Flow rate from the flow meter	55
4.1	Potential vorticity fields	59
4.2	Time-averaged potential vorticity field	62
4.3	Well-mixed profiles of potential vorticity	65
4.4	Rms value U_θ of zonal flow	67
5.1	Radial profiles of velocity, vorticity and streamfunction	80
5.2	time-averaged potential vorticity	96
5.3	Contours of the correlation function	105
5.4	Energy and enstrophy fluctuations	107
5.5	Probability distribution of potential vorticity	114
5.6	Plot of ensemble-averaged potential vorticity and time-averaged streamfunction	115

6.1	Experimental and theoretical radial profile of vorticity	128
6.2	Experimental and theoretical PDFs of vorticity	130
7.1	Contour lines of $\psi_k(y, y')$	153
7.2	Contour of correlation of vorticity fluctuation.	154
7.3	Comparison of correlation of vorticity fluctuation.	155
8.1	Couette-Taylor velocity difference time-series	162
8.2	Comparison of χ^2 and log-normal distributions to the experi- mental distribution	165
8.3	Parameters for log-normal distributions	167
8.4	Choice of subsystems	168
8.5	Probability density function of velocity differences	170
8.6	Correlation between β_d and ε_r	172
8.7	Probability density function of $\ln \beta_d$	174
9.1	Variation of streamfunction	180
9.2	Velocity top and bottom	188
9.3	Energy spectra with a flat bottom	190
9.4	Energy spectra with a sloped bottom	191
9.5	Beta effect on energy spectra	193
9.6	Energy spectra near the top and bottom	195

Chapter 1

Introduction

Turbulence is an interesting subject, both because of its importance for applications and because of the fundamental physics involved. It is usually characterized by the Reynolds number, which represents the relative size of the nonlinear term to the dissipative term. Two systems with the same Reynolds number and experimental geometry are thus argued to be the same by rescaling properly. Flows with high Reynolds number are interpreted as a dissipative dynamical system with a large number of degrees of freedom. So, the flow is complex and chaotic in both space and time. Most symmetries (such as time-reversal, spatial symmetries, and so on) are broken at high Reynolds number. However, the statistics of a flow become steady. Even though large scale statistics depend on the geometry of the particular experiment, small scale fluctuations can be statistically isotropic and homogeneous, and thus symmetries can be statistically restored. In the statistical theory of homogeneous and isotropic turbulence, statistical universal features have been proposed and observed.

The experiment discussed in this thesis is designed to represent a plane-

tary flow. Rotation and a sloped bottom mimic the revolution of a planet and the variation of the Coriolis force with latitude, respectively. Due to rapid rotation, the Taylor-Proudman theorem indicates that a flow becomes quasi-two dimensional (quasi-2D). To characterize and investigate turbulence, we use two sets of experimental measurements. One is the measurement of velocity at one point with high temporal resolution. The other is the measurement of velocity fields in a whole domain with low temporal resolution.

An inviscid two-dimensional (2D) flow has Hamiltonian structure and satisfies Liouville's theorem of constant volume in time. This suggests the application of statistical mechanics to 2D flows. Equilibrium statistical mechanics describes equilibrium states of a system with a large number of elements and is used to obtain how a system depends on temperature and other parameters. Our system can be interpreted as a macroscopic manifestation of microscopic vortices. When a system is in a steady state, it will choose one of the possible equilibrium states characterized by temperature and other parameters. Selecting conserved quantities is the crucial step in statistical mechanics.

In classical statistical mechanics, usually only quadratic quantities exist and are used. However, in 2D turbulence there are an infinite number of conserved quantities, the so-called Casimir invariants $\int |\omega|^n d\mathbf{x}$, where ω is the vorticity [186]. We show that only quadratic invariants are additive and statistically independent among macro-cells, while other invariants are not. Previous applications of statistical mechanics to 2D flows do not take into account statistical independence among macro-cells. In Chap. 5, we propose a statistical mechanics based on new coordinates that satisfies statistical independence. Also, we explore the use of nonextensive entropy, instead of

extensive entropy in Chap. 6.

The fluctuation of a physical quantity can be described by the Hamiltonian structure of 2D flow together with statistical mechanics. We describe calculation of general phase space fluctuations in continuous media such as fluid systems, plasma systems, and so on. Following a novel way to calculate the phase space fluctuation in a plasma system with a linearized Hamiltonian, we expand this method in order to describe a fluid system. For a fluid system, the phase space fluctuations are the fluctuations of vorticity. Details of this are given in Chap. 7. These fluctuations might lead to self-similar statistics in turbulence.

To characterize turbulence, the statistics of physical variables or energy spectra are often used. First, most scales contain the self-similar statistics of measured quantities such as velocity, temperature, and so on. Those self-similar turbulent statistics can be described by many different methods. In the study of the statistics of velocity differences, two methods are of interest; one was proposed by Kolmogorov and Castaing [106, 47] and the other was by Beck and Cohen [26]. The two methods are considered to be different since they are based on the different theories. In Chap. 8, we discuss how these two methods are related.

The energy spectrum is important for representations of the dynamical features of turbulence. A turbulent flow has eddies with a spectrum of sizes and with a certain scaling law. This scaling law persists until a system has a constant energy transfer rate across a certain scale size. Rather than the well-known Kraichnan's energy spectrum ($E(k) \sim k^{-5/3}$ if k is less than the forcing wavenumber and $E(k) \sim k^{-3}$ if k is larger than the forcing wavenumber), an anomalous spectrum is observed in our experiments. The full range of

the energy spectrum is discussed in Chap. 9, where experimental results are presented.

Chapter 2

Review of Theory and Literature

Theoretically, one can establish the equation of motion for fluid motions based on Newton's laws. However, the completed equation of motion is hard to solve due to the closure problem. Therefore, various approximated equations are used in many applications. Each approximated equation is used for different applications (See the section 2.1). Experimentally, there are two general ways to analyze the flow. One is to study the statistics. Usually, the velocity statistics is feasible to be obtained in turbulent flows. The other is energy spectrum which contains the spatial information. Details are discussed in the section 2.2. Hamiltonian formulation enables us to understand the structure in equations and to find the similarity between the fluid and other continuum systems (such as plasma). The basic property of the Hamiltonian structure in the fluid is discussed in the section 2.3. Once the Hamiltonian structure is known and a system consists of many fluid elements, the statistical mechanics

emerges naturally. Historically, there are many attempts to use statistical mechanics to describe the turbulence motion. Short descriptions and its failure and success are given in the section 2.4.

2.1 Various Approximations

We can study hydrodynamics in the various levels of the approximated equation. The full description of hydrodynamics is difficult to handle. So, many scientists use physically relevant assumptions to simplify the equation of motion and analyze the fluid motion explicitly. From now, we denote the vector field as the bold font such as $\mathbf{v} := (v_x, v_y, v_z)$ at a point $\mathbf{x} := (x, y, z)$.

2.1.1 Navier-Stokes Equation

For a Newtonian fluid, when density does not change, Navier-Stokes equation[154] from Newton's second law to a fluid element for an incompressible fluid is

$$\frac{\partial \mathbf{v}}{\partial t} + (\mathbf{v} \cdot \nabla) \mathbf{v} = -\frac{1}{\rho} \nabla P' + \nu \nabla^2 \mathbf{v} + \mathbf{F}_v \quad (2.1)$$

$$\nabla \cdot \mathbf{v} = 0 \quad (2.2)$$

where \mathbf{F}_v is the external acceleration, P' is the pressure, ρ is the density and ν is the kinematic viscosity. The kinematic viscosity depends on the molecular property of the fluid. At 20 °C, for water, ν is 0.01 cm²/cm⁻¹ and 0.15 cm²/cm⁻¹ for air. In the case of rotating system and constant density,

the governing equation in the rotating frame will be

$$\begin{aligned}\frac{\partial \mathbf{v}}{\partial t} + (\mathbf{v} \cdot \nabla) \mathbf{v} &= -\frac{1}{\rho} \nabla (P' + \frac{\rho \Omega^2 r^2}{2} - \rho g z) + \nu \nabla^2 \mathbf{v} - 2\mathbf{\Omega} \times \mathbf{v} + \mathbf{f}_v \\ &= -\frac{1}{\rho} \nabla P + \nu \nabla^2 \mathbf{v} - 2\mathbf{\Omega} \times \mathbf{v} + \mathbf{f}_v\end{aligned}\quad (2.3)$$

$$\nabla \cdot \mathbf{v} = 0 \quad (2.4)$$

where \mathbf{f}_v is an acceleration by external forcing, $-2\mathbf{\Omega} \times \mathbf{v}$ is Coriolis acceleration, $\nabla(\rho g z)$ is the gradient of the gravitational potential, $\nabla(\frac{\rho \Omega^2 r^2}{2})$ is the centrifugal acceleration and the redefined pressure is $P = P' + \frac{\rho \Omega^2 r^2}{2} - \rho g z$. Equation (2.3) and (2.4) together with initial boundary conditions are complete to solve since there are four unknown functions (v_x, v_y, v_z, P) and four equations (3 in Eq. (2.3) and 1 in Eq. (2.4)). However, the uniqueness and existence of solution in Eq. (2.3) and (2.4) are an open question. Also, the above equations have a closure problem in statistical sense. For example, if one tries to write down an equation for correlation of second order as $\int v_i(\mathbf{x}) v_j(\mathbf{x}') d\mathbf{x} d\mathbf{x}'$, then the third-order correlation is needed, and so on. This iteration never ends. In the kinetic theory, it is analogue to BBGKY hierarchy [221].

The curl of the velocity field is known as the vorticity $\boldsymbol{\omega}$. Taking the curl of Eq. 2.1 and using the incompressibility condition as in Eq. (2.2) leads to

$$\frac{\partial \boldsymbol{\omega}}{\partial t} + (\mathbf{v} \cdot \nabla) \boldsymbol{\omega} + (\boldsymbol{\omega} \cdot \nabla) \mathbf{v} = \nu \nabla^2 \boldsymbol{\omega} + F_\omega, \quad (2.5)$$

where F_ω is the vorticity forcing. In the rotating turbulence, the Coriolis force term disappears when we take the curl in the Navier-Stokes equation. The second term represents the advection of the vorticity by the velocity. The third term shows the vortex stretching, which is the crucial process to transfer the energy in turbulence. However, this third term is absent in two dimensional flow.

2.1.2 Inviscid Model

To study some statistical properties, we may not need a full understanding of Navier-Stokes equation. First approximation model is the “*inviscid model*”. Small viscous effect and forcing make this model efficient. The inviscid model is written as

$$\frac{\partial \mathbf{v}}{\partial t} + (\mathbf{v} \cdot \nabla) \mathbf{v} = -\frac{1}{\rho} \nabla P - 2\boldsymbol{\Omega} \times \mathbf{v}. \quad (2.6)$$

Eq. (2.6) still contains a nonlinear term $((\mathbf{v} \cdot \nabla) \mathbf{v})$. We might expect to learn some nonlinear behaviors of flow from this model. Taking the curl to Eq. (2.6), we obtain the vorticity equation,

$$\frac{\partial \boldsymbol{\omega}}{\partial t} + (\mathbf{v} \cdot \nabla) \boldsymbol{\omega} = \boldsymbol{\omega} \cdot \nabla \mathbf{v}. \quad (2.7)$$

For the two dimensional flow, we introduce a scalar function which can be related with two-dimensional velocity ($\mathbf{v}_\perp := (v_x, v_y)$) and one-dimensional vorticity ($\omega = \boldsymbol{\omega} \cdot \hat{e}_z$) in a easier way. The vanishing of the divergence of velocity ($\nabla_\perp \cdot \mathbf{v}_\perp$) in the two-dimensional plane enables us to define a *streamfunction* $\psi(\mathbf{x}_\perp)$ (where \mathbf{x}_\perp is the position on a two dimensional plane) such that

$$\mathbf{v}_\perp = \hat{e}_z \times \nabla_\perp \psi = \left(\frac{\partial \psi}{\partial y}, -\frac{\partial \psi}{\partial x} \right). \quad (2.8)$$

Here, \hat{z} is the perpendicular direction to the two-dimensional plane. Hence, the vorticity equation in two-dimensional space is given as

$$\frac{\partial \omega}{\partial t} + (\mathbf{v}_\perp \cdot \nabla_\perp) \omega = 0. \quad (2.9)$$

It leads to the conservation of vorticity. Along the trajectories of fluid particles, the vorticity is constant without any forcing and dissipation. Sometimes, this

property of vorticity equation is explained as *relocation of vorticity* in a sense that fluid particles are moving with a fixed vorticity.

Now, let's consider the two-dimensional flow in a thin spherical shell (e.g. the atmosphere on the planets). The relevant angular velocity due to the rotation is the component of Ω normal to the surface, $2\Omega \sin \theta$. Kelvin's theorem shows that the circulation, the integral of vorticity over the area is conserved. With the local vorticity of the fluid, the circulation over the small area A is constant such as

$$A(\omega + 2\Omega \sin \theta) = \text{const.} \quad (2.10)$$

Columns of fluid of the area A and the depth h in the two-dimensional incompressible flow have the property as [63, 165]

$$\frac{\omega + 2\Omega \sin \theta}{h} = \text{const.} \quad (2.11)$$

It implies that the vorticity changes with θ and h to satisfy Eq. (2.11). In a narrow range of θ , the potential vorticity is defined as

$$q = \omega + 2\Omega \sin \theta_0 + \beta_{Ro} y, \quad (2.12)$$

where $y = (\theta - \theta_0)/R$, R is the radius of sphere and $\beta_{Ro} := (2\Omega \cos \theta_0)/R$ shows the variation of Coriolis force with θ direction.

In a laboratory experiment with a sloping bottom, the height of fluid is given as $h(r) = h_0 - \eta r$ where r is the radius and η is the slope of bottom. In this case, the potential vorticity is defined as

$$q = \omega + 2\Omega + \beta_{Ro} r, \quad (2.13)$$

where $\beta_{Ro} := (2\Omega \eta)/h_0$ is negative if h increases radially. Therefore, the equation of motion for an inviscid incompressible fluid with a sloping bottom

is

$$\frac{\partial q}{\partial t} + (\mathbf{v}_\perp \cdot \nabla_\perp)q = 0. \quad (2.14)$$

This conservation of potential vorticity is similar to the conservation of angular momentum for a classical body. For example, a figure skater is spinning up with her arms close to her body and she spins slowly down with her arms stretched out. Similarly, when a fluid column is squeezed horizontally, its vorticity increases to conserve the potential vorticity. In later chapters, this equation is useful to describe flows in a system with a sloping bottom.

Later, we will show that the inviscid model has Hamiltonian structure in the two-dimensional flow. Without the Coriolis force term, it is often called *Euler equation*. The Euler equation can be derived from the kinetic theory in the hydrodynamic limit [49]. The inviscid model is the basic equation in approaches of the statistical mechanics.

2.1.3 Geostrophic Equation

More approximated model for a flow is the “*geostrophic model*”. For slow, steady ($\frac{D\mathbf{v}}{Dt} := \frac{\partial \mathbf{v}}{\partial t} + \mathbf{v} \cdot \nabla \mathbf{v} \sim 0$), inviscid ($\nu \nabla^2 \mathbf{v} \sim 0$) flow, Eq. (2.3) simplifies to

$$\frac{1}{\rho} \nabla_\perp P = -2\boldsymbol{\Omega} \times \mathbf{v}_\perp \quad (2.15)$$

It expresses a balance between the Coriolis force and the pressure gradient force perpendicular to the rotation axis. A velocity of this model can be written as

$$\mathbf{v} = \frac{1}{2\Omega\rho} \hat{z} \times \nabla_\perp P := \hat{z} \times \nabla_\perp \psi. \quad (2.16)$$

If the density and Ω do not change in space, the stream function can be written as

$$\psi = \frac{P}{2\Omega\rho}. \quad (2.17)$$

It shows that lines of constant pressure are contours of stream function of geostrophic flow.

Mathematicians and meteorologists are interested in a model between the geostrophic model and inviscid one. It is called *semi-geostrophic model*. By substituting the velocity in Eq. (2.6) by the expression in terms of the pressure as in Eq. (2.16), we get

$$\nabla_{\perp} \frac{\partial P}{\partial t} + (\nabla_{\perp} P \cdot \nabla_{\perp}) \nabla_{\perp} P = -\frac{1}{\rho} \nabla_{\perp} P - 2\Omega \times \mathbf{v}. \quad (2.18)$$

Time evolution of pressure field gives a way to predict changes of the weather.

2.1.4 Dimensional Analysis

We introduce a velocity scale U and as typical length scale L the characteristic length scale of a system. We then rewrite equation Eq. (2.3) with the Coriolis effect by using non-dimensional variables :

$$\frac{U^2}{L} \frac{\partial \mathbf{v}^*}{\partial t^*} + \frac{U^2}{L} (\mathbf{v}^* \cdot \nabla^*) \mathbf{v}^* = -\frac{U^2}{L} \nabla^* P^* + \frac{\nu U}{L^2} \nabla^{*2} \mathbf{v}^* - 2U\Omega \hat{e}_z \times \mathbf{v}^*. \quad (2.19)$$

Here, variables with superscript $*$ are non-dimensional quantities. Details are given in [165].

The Rossby number ($Ro := \frac{U}{2\Omega L}$) is useful to measure the importance of rotation effects on a flow and what scales a given flow feel the effect of rotation. The ratio of two time scales is the way to measure the Rossby number: The first scale is the time scale associated with the rotation ($1/\Omega$,

Type	Feature	L_H	U
Earth $\Omega = 7.3 \times 10^{-5} s^{-1}$	Gulf stream	100 km	1 m/s
	Weather system	1000 km	20 m/s
	Core	3000 km	0.1 cm/s
Jupiter $\Omega = 1.7 \times 10^{-4} s^{-1}$	Bands	10^4 km	50 m/s

Type	Feature	Ro	Re
Earth $\Omega = 7.3 \times 10^{-5} s^{-1}$	Gulf stream	0.07	10^7
	Weather system	0.14	2×10^9
	Core	2×10^{-7}	3×10^7
Jupiter $\Omega = 1.7 \times 10^{-4} s^{-1}$	Bands	0.015	5×10^{10}

Table 2.1: Rossby numbers in various atmospheric motions [80]. Small Ro means that the effects of rotation are important and large Reynolds number makes a system under a strong nonlinear effect.

where Ω is the rotation rate in rad/s). The second time scale is the fluid advection time scale, e.g. the ratio of a typical horizontal length to a typical horizontal velocity (L/U). A small Rossby number shows that a flow motion is dominated by a Coriolis effect. Rotation plays an important role in shaping the pattern of flows on large scales.

The ratio of the viscous force to the Coriolis force is called the Ekman number (Ek). It is defined as the ratio of the frictional force to the Coriolis force, or the ratio of the viscous diffusion time scale (L^2/ν) to the rotation time scale (Ω^{-1}) where L is the typical length scale in a system. We may define two Ekman numbers; One is the vertical Ekman number (Ek_V) which is related to the direction parallel to the rotation axis. Hence, it is defined as $\frac{\nu}{2\Omega L_V^2}$ where

L_V is the length scale in the vertical direction along the rotation axis. The other is the horizontal Ekman number $Ek_H := \frac{\nu}{2\Omega L_H^2}$. L_H is the length scale on the plane perpendicular to the rotation axis. In most experiments and large scale geophysical motions, Ekman numbers are very small. It means that the viscous forces are negligible except near boundaries.

The other important parameter is the Reynolds number, which compares the inertial forces to the viscous forces in the flows. Viscous effect is important at low Re ; flows are called *laminar*. Interestingly, the transition to turbulence occurs at very high Re . Typically fluids become weakly turbulent for $Re \sim 10^3 - 10^4$. For planetary flows, typically $Re \sim 10^7$. The large size of the geophysical flows implies that the Reynolds numbers are usually very large. Therefore the dependence of the flow characteristics on the Reynolds number is weak, since we are always in the high-turbulence regime.

Using all non-dimensional numbers, Eq. (2.19) becomes

$$Ro \left(\frac{\partial \mathbf{v}^*}{\partial t^*} + (\mathbf{v}^* \cdot \nabla^*) \mathbf{v}^* \right) = -Ro \nabla^* P^* + Ek_H \nabla^{*2} \mathbf{v}^* - \hat{e}_z \times \mathbf{v}^*. \quad (2.20)$$

2.1.5 Quasi-geostrophic Equation

At the limit of $Ek \rightarrow 0$ and $Ro \rightarrow 0$, the flow is geostrophic as in Eq. (2.20). In order to describe the flow in the bulk more accurately, one may introduce the small perturbation to the geostrophic equation. The parameter measure of departure from geostrophic flow is assumed to be Ro [165]. For the bulk velocity, we expand the velocity as

$$\mathbf{v} = \mathbf{v}_0 + \mathbf{v}_1 + \mathbf{v}_2 + \cdots \quad (2.21)$$

$$p = p_0 + p_1 + p_2 + \cdots, \quad (2.22)$$

where \mathbf{v}_1 and p_1 are the order of Ro and \mathbf{v}_2 and p_2 are the order of Ro^2 . It means that we expand \mathbf{v} by the geostrophic part \mathbf{v}_0 and small corrections \mathbf{v}_1 in the order of Ro in rapidly rotating systems.

The Reynolds number, Re is the ratio of Ro to Ek_H . More precisely, substituting Eq. (2.21) and (2.22) into Eq. (2.3) with the Coriolis effect, the first order equations become

$$\frac{\partial v_{x0}}{\partial t} + v_{x0} \frac{\partial v_{x0}}{\partial x} + v_{y0} \frac{\partial v_{x0}}{\partial y} - 2\Omega v_{y1} = -\frac{\partial p_1}{\partial x} + \nu \nabla_{\perp}^2 v_{x0} \quad (2.23)$$

$$\frac{\partial v_{y0}}{\partial t} + v_{x0} \frac{\partial v_{y0}}{\partial x} + v_{y0} \frac{\partial v_{y0}}{\partial y} + 2\Omega v_{x1} = -\frac{\partial p_1}{\partial y} + \nu \nabla_{\perp}^2 v_{y0} \quad (2.24)$$

$$\frac{\partial v_{x1}}{\partial x} + \frac{\partial v_{y1}}{\partial y} + \frac{\partial v_{z1}}{\partial z} = 0, \quad (2.25)$$

where $\mathbf{v}_0 = (v_{x0}, v_{y0}, v_{z0})$ and $\mathbf{v}_1 = (v_{x1}, v_{y1}, v_{z1})$. These equations are called *Quasi-geostrophic equation*. Note that there is no term of v_{z0} since a geostrophic equation results in zero v_{z0} as well as v_{x0} and v_{y0} are independent of z . That also implies that a geostrophic equation is the two-dimensional flow.

Taking $\frac{\partial}{\partial y}$ on Eq. (2.23) and $\frac{\partial}{\partial x}$ on Eq. (2.24) and subtracting one by the other, the pressure dependence disappears. In other words, we take the curl of equation of motion with the additional constraint that v_{x0} and v_{y0} are independent of z (so that we can permute x -derivation and y -averaging). The z -component of the vorticity $\boldsymbol{\omega}$ is denoted by ω and is also z -invariant. After expanding the vorticity as $\omega = \omega_0 + \omega_1 + \dots$, we get

$$\begin{aligned} \frac{\partial \omega_0}{\partial t} + \left(v_{x0} \frac{\partial \omega_0}{\partial x} + v_{y0} \frac{\partial \omega_0}{\partial y} \right) &= -2\Omega \left(\frac{\partial v_{x1}}{\partial x} + \frac{\partial v_{y1}}{\partial y} \right) + \nu \nabla_{\perp}^2 \omega_0 \\ &= 2\Omega \frac{\partial v_{z1}}{\partial z} + \nu \nabla_{\perp}^2 \omega_0, \end{aligned} \quad (2.26)$$

where $\omega_0 = \frac{\partial v_{y0}}{\partial x} - \frac{\partial v_{x0}}{\partial y}$. Taking the z average from the bottom ($z = 0$) to the

top ($z = h$) leads to

$$\frac{\partial \langle \omega_0 \rangle_z}{\partial t} + \left\langle \left(v_{x0} \frac{\partial \omega_0}{\partial x} + v_{y0} \frac{\partial \omega_0}{\partial y} \right) \right\rangle_z = 2\Omega \frac{(v_{z1}(x, y, h) - v_{z1}(x, y, 0))}{h} + \nu \nabla_{\perp}^2 \langle \omega_0 \rangle_z \quad (2.27)$$

where we define the z -averaging $\langle \cdot \rangle_z$ by

$$\langle \mathbf{v} \rangle_z = \frac{1}{h} \int_0^h \mathbf{v}(x, y, z) dz. \quad (2.28)$$

The boundary-layer theory gives the no-slip condition on the tangential velocity on boundaries for a geostrophic flow. Their thickness is supposed to be small ($Ek_H \ll 1$), and we will use the asymptotic expression given by [86] and [165]. The simplified expression is

$$\mathbf{v} \cdot \mathbf{n}|_0 = \frac{Ek_H^{1/2}}{2} \omega_0 \quad (2.29)$$

$$\mathbf{v} \cdot \mathbf{n}|_h = \frac{Ek_H^{1/2}}{2} (\omega_T - \omega_0), \quad (2.30)$$

where ω_T is the vorticity of the upper boundary. If $\omega_T > \omega_0$, there is the radially outward flow in the upper Ekman layer and the vertically upward flow. The physical mechanism of Ekman pumping is that a small vertical velocity, v_{z0} is pumped out of the small layers near boundaries (Ekman layers) and into the bulk. A cyclonic vorticity is sitting over the converging flow in the Ekman layer. Similarly, an anticyclonic vorticity pushes fluid out radially in the Ekman layer. So, the first order vertical velocity without any topography is

$$\begin{aligned} v_{z1}(x, y, 0) &= \frac{Ek_H^{1/2}}{2} \omega_0 \\ v_{z1}(x, y, h) &= \frac{Ek_H^{1/2}}{2} (\omega_T - \omega_0). \end{aligned} \quad (2.31)$$

An important point is that expression 2.30 is valid for time-dependent flows with time scales larger than a few rotation periods. Greenspan used that expression to study the spin-up process in a sphere, which is a time-dependent flow with time scale of order $Ek_H^{-1/2}$.

In the case of a system with topography which has a radially changing bottom, one needs to consider the geometry on boundaries. Therefore, assuming ω_T is zero, we get

$$v_z(x, y, h) - v_z(x, y, 0) = -Ek_V^{1/2}\omega_0 + \frac{\partial h}{\partial r}v_r. \quad (2.32)$$

Without the beta-plane, the second term in the right hand side disappears.

The vorticity equation becomes

$$\frac{\partial \omega_0}{\partial t} + \left(v_x \frac{\partial \omega_0}{\partial x} + v_y \frac{\partial \omega_0}{\partial y} \right) = -2\Omega \frac{Ek_V^{1/2}}{h} \omega_0 - \beta_{Ro} v_r + \nu \nabla_{\perp}^2 \omega_0 \quad (2.33)$$

$$= -\frac{1}{\tau_E} \omega_0 - \beta_{Ro} v_r + \nu \nabla_{\perp}^2 \omega_0, \quad (2.34)$$

where $\tau_E := h_0/(2\sqrt{\nu\Omega})$ is called Ekman friction time. We note that the Ekman friction is a dissipative term whereas the β_{Ro} -term is not, it is thus expected to play an important role for the non-linear dynamics of quasi-geostrophic flows. Using the definition of potential vorticity as Eq. (2.13), Eq. (2.34) becomes

$$\frac{\partial q_0}{\partial t} + \left(v_r \frac{\partial q_0}{\partial r} + \frac{v_{\theta}}{r} \frac{\partial q_0}{\partial \theta} \right) = -\frac{1}{\tau_E} \omega_0 + \nu \nabla_{\perp}^2 q_0. \quad (2.35)$$

It is often called *potential vorticity equation*.

2.2 Turbulence

At low Reynolds number, an incompressible flow behaves very regular and stable (*Laminar*). However, at high Reynolds number, a highly irregular and chaotic behavior is observed with a wide range of length and time scales in a fluid (*Turbulence*). Obviously, there exists a transition from laminar to turbulent flows. Those turbulent flows are very common and important in industrial applications in a sense of heat and momentum transfer. In the limit of very high Reynolds number, the chaotic behavior involves fluctuations from large to small scales of space and time. This stage is often called *fully developed turbulence*.

Energy in 3D fully developed turbulence cascades in the range of scales between the large scales where energy enters and the small ones where it is dissipated. The qualitative ideas of Richardson [174] have been further developed and formulated in a more precise language by Kolmogorov [105, 106]. The cascade of energy among the eddies is expected at small scales compared to the external length scale (L). The range which has the constant energy flux across scales is called *inertial range*. Turbulence has statistically restored symmetries or statistical universal features [76]. Here, we list two main ways to investigate the properties of turbulence.

One is to investigate the spatial information of turbulent field such as energy spectrum. Due to homogeneity and small fluctuations compared to mean flow in turbulence, temporal information (recorded with velocity probes fixed in space) is converted into spatial information and vice versa. This condition is often called *Taylor frozen hypothesis* [205]. If the velocity of the stream which carries eddies is very large compared to the turbulent velocity (or

the velocity of eddies), the sequence of changes in the velocity at the fixed point results from the passage of an unchanging pattern of turbulent motion over the point. For example, the energy spectrum ($E(w)$) in the frequency (w) is the same as the energy spectrum ($E(k)$) in the wavenumber (k). Kolmogorov [104] proposed the universality of the energy spectrum based on the conservation of energy flux through scales and the locality in the wavevector. Dimensional analysis leads to $-5/3$ exponent for energy spectrum of turbulent velocity in the inertial range. Onsager [160] and Heisenberg [88] should be credited for the similar discovery. This idea is supported by many experiments [182, 189] and numerical simulations [224].

The other approach is to analyze the statistics of measured quantities in turbulence. Traditionally, the statistics in turbulence is investigated in terms of longitudinal velocity differences ($\delta v_r(\mathbf{x}) = \hat{e}_r \cdot [\mathbf{v}(\mathbf{x} + \mathbf{r}) - \mathbf{v}(\mathbf{x})]$) where \mathbf{x} is an arbitrary point in space, \mathbf{r} is the separation vector and \hat{e}_r is the unit vector of \mathbf{r} . The primitive method to study statistics is to look at *Probability distribution function* (PDF). Intermittency in turbulent flows has been observed in many experiments [76] and predicted by various models [76, 141]. PDF of velocity difference at the small separation r , which lies in the inertial range has an exponential-like wings shape whereas it has Gaussian at large separation r . The tails of PDF have the higher probability than Gaussian, and rare events become significant in turbulent flows. Intermittency in the inertial range is characterized by preserving a shape of PDF by rescaling $\delta v_r(\mathbf{x})$ [47].

2.2.1 Energy Spectrum

Energy spectrum is a measure of the spatial information of the velocity field. To obtain the energy spectrum, the velocity field is Fourier-transformed using periodic boundary conditions. So, the velocity field can be expressed as

$$\mathbf{v}(\mathbf{x}, t) = \sum \hat{\mathbf{v}}_{\mathbf{k}}(t) \exp(i\mathbf{k} \cdot \mathbf{x}), \quad (2.36)$$

where $\hat{\mathbf{v}}_{\mathbf{k}} = ((\hat{v}_{\mathbf{k}})_x, (\hat{v}_{\mathbf{k}})_y, (\hat{v}_{\mathbf{k}})_z)$ and $\mathbf{k} = (k_x, k_y, k_z)$. The Fourier transformed Navier-Stokes equation is

$$\frac{\partial}{\partial t}(\hat{v}_{\mathbf{k}})_i + ik_j P_{im} Q_{jm} = -\nu k^2 (\hat{v}_{\mathbf{k}})_i + F_{\mathbf{k}}, \quad (2.37)$$

where δ_{im} is the Dirac delta function, $P_{im} = \delta_{im} - \frac{k_i k_m}{k^2}$ and $Q_{jm} = \sum_{\mathbf{p}+\mathbf{q}=\mathbf{k}} (\hat{v}_{\mathbf{p}})_j (\hat{v}_{\mathbf{q}})_m$. The incompressibility condition becomes $\mathbf{k} \cdot \mathbf{v} = 0$. One remark is that the pressure is dropped out by the Fourier transformation and incompressibility.

By multiplying $(\hat{v}_{-\mathbf{k}})_i$ to Eq. 2.37, one gets

$$\frac{\partial}{\partial t} E(k) + T(k) = -2\nu k^2 E(k) + F(k), \quad (2.38)$$

where $T(k)$ is a cubic term in $\hat{\mathbf{v}}_{\mathbf{k}}$ from nonlinear terms (which shows the interactions between different wave vectors) and $F(k)$ is the Fourier transformed forcing term. Energy transfers between different wave numbers are described by a term $T(k)$. For a rotating turbulence, there is no dependence on Ω in the energy equation as Eq. (2.38). Since a Coriolis force does not do any work, a rotation effect does not appear in the energy equation explicitly. However, people believe that energy transfer term $T(k)$ depends on a rotation rate [234].

Kolmogorov Spectrum in the three dimensional turbulence

Kolmogorov [105] claimed that turbulence should exhibit universal and isotropic properties in the small scales. Those scales (often called as the *inertial*

range) are smaller than the *integral scale* or the system scale (L) and larger than the dissipation scale (η) where the viscous dissipation plays an essential role. Associated wavenumbers are denoted as $k_0 := 1/L$ and $k_\eta := 1/\eta$.

Let's assume that $E(k)$ depends only on the wavenumber k and on the averaged energy dissipation rate $\varepsilon = \frac{d[2 \int \nu k^2 E(k) dk]}{dt}$. Units of $E(k)$ are $\frac{L^3}{T^2}$, ε has $\frac{L^2}{T^3}$ and k is the unit of $\frac{1}{L}$. Dimensional analysis of energy spectrum $E(k)$ is

$$[E(k)] = \frac{L^3}{T^2} = C \left(\frac{L^2}{T^3} \right)^\alpha \left(\frac{1}{L} \right)^\beta = C[\varepsilon]^\alpha [k]^\beta \quad (2.39)$$

where C is a constant and bracket $[\cdot]$ means a unit of quantities inside. The above equation gives $-3\alpha = -2$, $2\alpha - \beta = 3$. Then, the solution is $\alpha = 2/3$ and $\beta = -5/3$. Therefore, the energy spectrum in the cascade range is

$$E(k) = C\varepsilon^{2/3} k^{-5/3}. \quad (2.40)$$

where C is expected to be a universal constant. (Universality is quite questionable [75].) The Kolmogorov energy spectrum describes a wide variety of data in the turbulence [182].

Kraichnan's dual cascade in the two dimensional turbulence

Kraichnan [107] proposed a dual cascade in the two dimensional turbulence. Two dimensional turbulence exhibits a forward cascade of enstrophy to large wavenumbers and an inverse cascade of energy to small wavenumbers. Here, enstrophy is defined as $\int |\boldsymbol{\omega}|^2 d\mathbf{x}$ whereas energy is defined as $\int |\mathbf{v}|^2 d\mathbf{x}$. Those two quantities are known as conserved quantities in the Euler equation. For a forward cascade of enstrophy, transferred enstrophy to large wavenumbers until it is dissipated due to viscosity. Similarly, the inverse cascaded energy is dissipated in the small wavenumbers (such as Ekman drag).

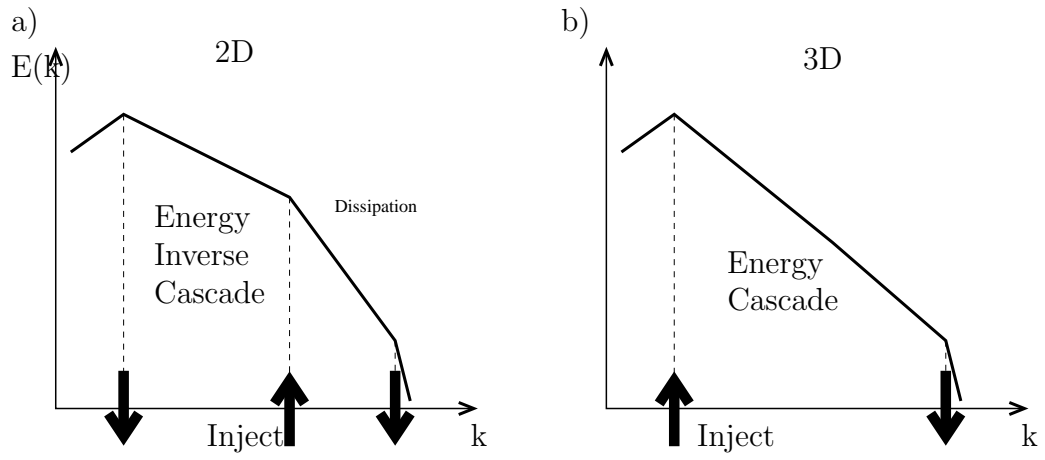


Figure 2.1: (a) The classical picture of mechanisms in 2 dimensional turbulence is that the enstrophy is transferred into small scales (high k) and the energy is transferred into large scales (low k) due to nonlinear interactions. (b) In 3 dimensional turbulence, the energy is cascaded into small scales. Enstrophy is not important in 3 dimensional turbulence. [107]

For the inverse cascade, the same dimensional analysis leads to energy spectrum in 2D as in 3D Eq. (2.40). Therefore, the energy spectrum in 2D is also

$$E(k) = C_1 \varepsilon^{2/3} k^{-5/3}, \quad (2.41)$$

where C_1 would be different from the C for 3D. In small scales, an enstrophy cascade is expected. Here, we assume that $E(k)$ depends only on the wavevector k and on the enstrophy dissipation rate $\varepsilon_\Omega = \frac{\partial \int 2\nu \nabla_\perp^2 \omega^2 d\mathbf{x}}{\partial t}$. Units of $E(k)$ are $\frac{L^3}{T^2}$, ε_Ω has $\frac{1}{T^3}$ and k is the unit of $\frac{1}{L}$. Dimensional analysis of energy spectrum $E(k)$ is

$$[E(k)] = \frac{L^3}{T^2} = C_2 \left(\frac{1}{T^3}\right)^\alpha \left(\frac{1}{L}\right)^\beta = C_2 [\varepsilon_\Omega]^\alpha [k]^\beta \quad (2.42)$$

where C_2 is a constant. It is trivial to get the solution for α and β . So, the energy spectrum where the enstrophy cascades is

$$E(k) = C_2 \varepsilon_\Omega^{2/3} k^{-3}. \quad (2.43)$$

Here, the direction of the energy flux is not known by dimensional analysis. Equilibrium statistical mechanics can determine the directions of these energy fluxes. Only two experiments, both recent, have shown the Kraichnan energy spectrum in two dimensional systems [29, 163, 164].

Problem of Kraichnan's dual cascade

The classical Kraichnan spectrum, $k^{-5/3} - k^{-3}$ is put in question by rigorous analysis. Constantin et. al [61] and Tran et. al [213] show that a single mode at any wave number driving a 2-D flow cannot lead to the Kraichnan spectrum [213, 211, 61].

Consider Eq. (2.1) with the forcing which has the property such as $-\nabla_{\perp}^2 \mathbf{F}_v = k_f^2 \mathbf{F}_v$. Here, k_f^2 is one of the eigenvalues of a Laplacian $-\nabla_{\perp}^2$. The energy spectrum has two parts. The first is the inertial range from k_0 to k_f and the second range is the decaying dissipation range from k_f to k_{η} .

The scalar product and the total quantities in periodic boundaries (the norm in L^2 periodic space) are given by

$$\langle \mathbf{u}, \mathbf{v} \rangle_{\alpha} = \int \mathbf{u} \cdot (-\nabla_{\perp}^2)^{\alpha} \mathbf{v} dx dy \quad (2.44)$$

$$\|\mathbf{v}\|_{\alpha}^2 = \langle \mathbf{v}, \mathbf{v} \rangle_{\alpha} \quad (2.45)$$

The norm with $\alpha = 0$ (or $\alpha = 1$) is known as the total energy (or enstrophy).

Taking the operator as in Eq. (2.44) into the nonlinear convective term in the Navier-Stokes equation, we get

$$\langle \mathbf{v}, \mathbf{v} \cdot \nabla_{\perp} \mathbf{v} \rangle_{0 \text{ or } 1} = 0. \quad (2.46)$$

Therefore, the energy and enstrophy equation lead to

$$\frac{\partial \|\mathbf{v}\|_0^2}{\partial t} = 2\nu \|\mathbf{v}\|_1^2 + \varepsilon, \quad (2.47)$$

$$\frac{\partial \|\mathbf{v}\|_1^2}{\partial t} = 2\nu \|\mathbf{v}\|_2^2 + \varsigma, \quad (2.48)$$

where we define that $\varepsilon := \int \mathbf{v} \cdot \mathbf{F}_v(x, y) dx dy$ is the energy injection rate and $\varsigma := \int -\mathbf{v} \cdot \nabla_{\perp}^2 \mathbf{F}_v(x, y) dx dy$ is the enstrophy injection rate. If the forcing f is concentrated into the monoscale k_f , then $\varsigma = k_f^2 \varepsilon$. Multiplying Eq. (2.47) by k_f^2 and subtracting it by Eq. (2.48), we get

$$k_f^2 \frac{\partial \|\mathbf{v}\|_0^2}{\partial t} - \frac{\partial \|\mathbf{v}\|_1^2}{\partial t} = 2\nu (\|\mathbf{v}\|_2^2 - k_f^2 \|\mathbf{v}\|_1^2). \quad (2.49)$$

Taking the time mean of Eq. (2.49) gives to

$$\begin{aligned}\int 2\nu (\|\mathbf{v}\|_2^2 - k_f^2 \|\mathbf{v}\|_1^2) dt &= 0, \\ \int 2\nu \|\mathbf{v}\|_1^2 \left(\frac{\|\mathbf{v}\|_2^2}{\|\mathbf{v}\|_1^2} - k_f^2 \right) dt &= 0.\end{aligned}\tag{2.50}$$

The wavenumbers, where viscosity strongly operates in the dissipation of energy and enstrophy, are estimated as

$$\begin{aligned}K_E &= \left(\frac{\|\mathbf{v}\|_1^2}{\|\mathbf{v}\|_0^2} \right)^{1/2}, \\ K_\Omega &= \left(\frac{\|\mathbf{v}\|_2^2}{\|\mathbf{v}\|_1^2} \right)^{1/2}.\end{aligned}\tag{2.51}$$

The larger value of K_Ω than the forcing wave number k_f means the forward cascade of enstrophy. However, if K_Ω is close to k_f , then enstrophy does not cascade in any direction. Since $2\nu \|\mathbf{v}\|_1^2 > 0$ at any given t , the requirement to satisfy Eq. (2.50) is

$$K_\Omega = k_f.\tag{2.52}$$

It implies that the enstrophy is dissipated around the forcing scale since the enstrophy-dissipated wavenumber K_Ω is equal to the forcing scale k_f .

Suppose the energy spectrum in steady states is given as $E(k) \sim k^{-\delta}$ over a range $k_f < k < k_\nu$ where k_ν is the wavenumber associated with the Kolmogorov scale. The dissipation of enstrophy over this range is

$$\int_{k_f}^{k_\nu} k^4 E(k) dk = \frac{1}{5-\delta} (k_\nu^{5-\delta} - k_f^{5-\delta}).\tag{2.53}$$

According to Eq. (2.52), the dissipation of enstrophy over dissipated range should be dominated around the forcing scale. As a result, δ should be larger than 5 for the noncascading case.

When we consider the Ekman friction ($-\frac{1}{\tau_E}\mathbf{v}$), the analysis above should be modified. Eq. (2.49) becomes

$$k_f^2 \frac{\partial \|\mathbf{v}\|_0^2}{\partial t} - \frac{\partial \|\mathbf{v}\|_1^2}{\partial t} = 2\nu (\|\mathbf{v}\|_2^2 - k_f^2 \|\mathbf{v}\|_1^2) + \frac{1}{\tau_E} (\|\mathbf{v}\|_1^2 - k_f^2 \|\mathbf{v}\|_0^2). \quad (2.54)$$

Taking the time mean, one gets the balance equation between two dissipations such as

$$\begin{aligned} 2\nu (\|\mathbf{v}\|_2^2 - k_f^2 \|\mathbf{v}\|_1^2) + \frac{1}{\tau_E} (\|\mathbf{v}\|_1^2 - k_f^2 \|\mathbf{v}\|_0^2) &= 0 \\ \|\mathbf{v}\|_1^2 \left[2\nu (K_\Omega^2 - k_f^2) + \frac{1}{\tau_E} \left(1 - \frac{k_f^2}{K_E^2} \right) \right] &= 0. \end{aligned} \quad (2.55)$$

The dynamical constraint gives that the energy dissipation is confined to scales larger than the forcing scale [206, 61]. It implies

$$K_E = \left(\frac{\|\mathbf{v}\|_1^2}{\|\mathbf{v}\|_0^2} \right)^{1/2} \leq k_f. \quad (2.56)$$

Using Eq. (2.56) and Eq. (2.55), one gets an inequality such as

$$2\nu K_\Omega^2 + \frac{1}{\tau_E} = 2\nu k_f^2 + \frac{1}{\tau_E} \frac{k_f^2}{K_E^2} \geq 2\nu k_f^2 + \frac{1}{\tau_E} \quad (2.57)$$

$$\Rightarrow K_\Omega^2 \geq k_f^2. \quad (2.58)$$

The above equation represents that enstrophy dissipation occurs at the scales smaller than the forcing scale k_f . Physical explanation of this process is that the dissipation mechanism in energy spectrum is shifted to small scales due to Ekman drag [211]. Contrast to the above case only with molecular viscosity, a system with molecular viscosity and Ekman drag dissipate the enstrophy at smaller scale than the forcing scale.

For a system with Ekman dissipation and molecular viscosity, the energy dissipation ($E(k) \sim k^{-\gamma}$) over a range $k_0 < k < k_f$ is given as

$$\int_{k_0}^{k_f} \left(\nu k^2 E(k) + \frac{1}{\tau_E} E(k) \right) dk = \frac{\nu}{3-\gamma} (k_f^{3-\gamma} - k_0^{3-\gamma}) + \frac{1}{\tau_E(1-\gamma)} (k_f^{1-\gamma} - k_0^{1-\gamma}). \quad (2.59)$$

If we assume that $\frac{1}{\tau_E} \gg \nu k_f^2$ so that Ekman drag dominates on the large scale, then the energy dissipation mostly occurs on the large scales if $\gamma > 1$. The negligible dissipation of enstrophy on the large scales requires $\gamma < 3$. Energy spectrum ($E(k) \sim k^{-5/3}$) of Kraichnan picture is in this range.

For a system with Ekman dissipation and molecular viscosity, the enstrophy dissipation ($E(k) \sim k^{-\delta}$) over a range $k_f < k < k_\nu$ is given as

$$\int_{k_f}^{k_\nu} \left(\nu k^4 E(k) + \frac{1}{\tau_E} k^2 E(k) \right) dk = \frac{\nu}{5-\delta} (k_\nu^{5-\delta} - k_f^{5-\delta}) + \frac{1}{\tau_E(3-\delta)} (k_\nu^{3-\delta} - k_f^{3-\delta}). \quad (2.60)$$

The Ekman dissipation dominates on the large scale. $3 < \delta < 5$ gives the negligible energy dissipation and the strong dissipation of enstrophy on the small scales.

Energy spectrum in a rotating turbulence

A rapidly rotating turbulence is close to two dimensional turbulence, but different from the general turbulence in two points [44, 43]. First, the energy cascade from large to small scales is slowed down due to a rotation effect. It results in the slow decay of the rate of energy without the forcing [94]. The next one is that there exists a process of two dimensionalization from three dimensional initial conditions. It is often credited to a Taylor-Proudman theorem [91]. However, this process toward two dimensional state is still an open question [193].

The effects of rotation are taken into account to calculate the proper energy spectrum by Zhou [234, 125, 156]. He assumes that the energy dissipation has a linear relation with the angular velocity, Ω^{-1} , since the time scale for the decay of the triple correlations is proportional to the energy dissipa-

tion. Then, the energy spectrum in the inverse cascade range is expected to be $E(k) \sim k^{-2}$. Similar result is derived in a rotating turbulence with the dissipation and the Ekman forcing. Constantin [60] considers the bounded energy spectrum ($E(k) \leq Ck^{-2}$) of the inverse cascade range in a rotating turbulent flow.

2.2.2 Probability Distribution Function (PDF)

In Kolmogorov's 1941 theory (K41), the energy in fully developed three-dimensional turbulence cascades from large scales to small scales where it is dissipated [104]. Turbulence in the cascade (the inertial range) is characterized by the probability distribution function (PDF) $P(\delta v_r)$ for longitudinal velocity differences over a distance r , $\delta v_r(\mathbf{x})$ [76]. For r approaching the integral scale where energy is injected, the PDF is Gaussian, while in the inertial range extending down to the dissipation scale η , intermittent large fluctuations lead to a non-Gaussian PDF with approximately exponential tails [222].

Structure function ($S^p(r) \equiv \langle (\delta v_r)^p \rangle$) is used as a statistical tool to measure this departure from Gaussian PDFs [105, 141]. Here, δv_r is the longitudinal velocity differences over different distance r and $\langle \cdot \rangle$ is the ensemble average (spatial average). In the inertial range, the power-law behavior of structure functions with respect to the distance (r) is proposed in [105] ($S^p(r) \propto r^{\zeta_p}$). However scaling exponent ζ_p is observed to be nonlinear rather than linear function ($\zeta_p = p/3$) as given by Kolmogorov's similarity prediction [2, 76, 4].

Log-normal Model

Kolmogorov assumed a constant energy dissipation rate per unit volume, ε [104]. In 1944 Landau [122] suggested that fluctuations of ε averaged at scale r , $\varepsilon_r(\mathbf{x}, t) \left(= \int_{\mathbf{x}}^{\mathbf{x}+\mathbf{r}} \varepsilon(\mathbf{x}', t) d\mathbf{x}' \right)$ play a key role in turbulence. Such fluctuations were subsequently observed in experiments [21, 84, 85]. In 1962 Kolmogorov [106] and Obukhov [158] proposed a log-normal model of ε_r in the inertial range. The log-normal distribution was obtained in subsequent experiments [166] and numerical simulations ε_r [152]. The non-Gaussian PDF of δv_r and the log-normal PDF of ε_r characterize turbulent flows. It is known as the *refined similarity hypothesis*.

In the log-normal model, the PDF of dissipation energy (ε_r) is assumed to be

$$P(\varepsilon_r) = \frac{1}{\sqrt{2\pi}\lambda_r\varepsilon_r} \exp\left(-\frac{(\ln \varepsilon_r - m_r)^2}{\lambda_r^2}\right), \quad (2.61)$$

where m_r and λ_r are the mean and standard deviation of $\ln \varepsilon_r$. Its moment will be $\langle \varepsilon_r^q \rangle \sim \exp\left(qm_r + \frac{\lambda_r^2}{2}q^2\right)$ when the possible value for $\ln \varepsilon_r$ is $(-\infty, \infty)$. The condition that the mean value of dissipation energy is constant gives $m_r = -\lambda_r^2/2$. So, the exponent of moments is $\tau_q = m_r q(1 - q)$. Experiments show m_r is about -0.36 [12, 11]. Assuming that δv_r and $(r\varepsilon_r)^{1/3}$ are statistically independent, the structure function is

$$\langle (\delta v_r)^p \rangle = r^{\zeta_p} \propto (r\varepsilon_r)^{p/3} = r^{p/3 + \tau_{p/3}}. \quad (2.62)$$

Therefore, assuming that $m_r \propto 1/(2 \log(L/r))$, we get

$$\zeta_p = p/3 + \tau_{p/3} = \frac{p}{3} + m_r \frac{p}{9}(3 - p). \quad (2.63)$$

Log-normal distribution in ε_r is plausible. However, the structure function significantly deviates from Eq. (2.63) that Kolmogorov predicted, especially

for high p [2, 4, 12]. Afterward, the most models require without plausible physical arguments a set of parameters to determine two exponent (ζ_p and τ_p) in structure functions of velocity differences and energy dissipation rate.

Log-Poisson Model (She-Leveque model)

She and Leveque [190] proposed a hierarchical structure for the moments of the local energy dissipation rate and an associated hierarchical structure for velocity differences. It is a phenomenological theory associated with a hierarchical structure of energy dissipation rate. They got the relation as

$$\zeta_p = p/9 + 2 - 2(2/3)^{p/3}. \quad (2.64)$$

This model is supported by the velocity measurements taken in turbulent jets and wake [18, 42, 55]. This moment hierarchy leads to log-Poisson distribution for the local energy dissipation rate [67, 191] in contrast to the log-normal PDF given by Eq. (2.61).

2.3 Hamiltonian and Action Formulations

Foundation of statistical mechanics minimize the appropriate thermo potential (or maximize the entropy) in thermodynamic equilibrium. Similarly, most physical systems are found to behave in the way to minimize some quantities. Conversely, those extremal principles constrain the motion of physical objects. For example, it is found by setting a derivative of some quantity, the action or the free energy, to zero. Especially, the action principles motivate many physical systems. We may say that action principles provide a framework for 20th century physics: the most successful models of physics, Maxwells equations, Einsteins equations for general relativity, Schrödingers equation, Yang-Mills and other theories of particle physics, etc. Here we consider infinite-dimensional systems such as a two-dimensional fluid system [146].

We briefly describe some action principles for the two-dimensional fluid system in Lagrangian and Eulerian variables.

- Lagrangian Variable Actions: The basic Lagrangian fluid variable is the position of fluid element $\mathbf{x}(\mathbf{a}, t)$, where \mathbf{a} is the position of a fluid element at $t = 0$ and t is the time. Since a system has conservation laws along the fluid trajectories, Lagrangian variable actions are useful. Descriptions of these action principles can be found in [146] for classical fluids.
- Eulerian Variable Actions: Eulerian variable is the velocity of fluid element $\mathbf{v}(\mathbf{x}, t)$. Most experiments generates data in the Eulerian variables. However, Eulerian variables are not canonical variables. We may need some techniques to use action principle with Eulerian variables [147].

2.3.1 Canonical Hamiltonian Structure

Consider the motion of objects in space. First, we find the function of configuration, $Q^i(t)$ where $i = 1, 2, \dots, N$ and N is the number of particles of the system. Given the Lagrangian $L := T - V$ where T is the kinetic energy and V is the potential energy, the action functional is written as

$$S[Q] = \int_{t_0}^{t_1} L(Q, \dot{Q}, t) dt, \quad (2.65)$$

where $Q = \{Q^i\}$. Hamilton's principle says that a trajectory with fixed end and beginning points is given by minimizing the action functional. Mathematically, extremal is that the functional derivative of the action is zero such as

$$\frac{\delta S[Q]}{\delta Q^i} = 0. \quad (2.66)$$

More details of the functional derivative are in [146]. Eq. (2.66) results in Euler-Lagrange's equation as

$$\frac{\partial L}{\partial Q^i} - \frac{d}{dt} \frac{\partial L}{\partial \dot{Q}^i} = 0. \quad (2.67)$$

Due to Legendre transformation as $P_i := \partial L / \partial \dot{Q}^i$, the Hamiltonian is given as $H(Q, P) = P_i \dot{Q}^i - L$. It gives

$$\dot{P}_i = -\frac{\partial H}{\partial Q^i}, \quad \dot{Q}_i = \frac{\partial H}{\partial P^i}. \quad (2.68)$$

However, there does not always exist this transformation from Lagrangian to Hamiltonian. By introducing the phase space coordinates such as $z = (Q, P)$, the Hamilton's equation is simplified as

$$\dot{z}^i = J_c^{ij} \frac{\partial H}{\partial z^j} = [z^i, H], \quad \text{where } J_c^{ij} = \begin{pmatrix} 0_N & I_N \\ -I_N & 0_N \end{pmatrix}, \quad (2.69)$$

where I_N is $N \times N$ diagonal of 1's and the index i goes up to two times the number of degrees of freedom, $2N$. Here, $[,]$ is the Poisson bracket which is defined as $[f, g] := \frac{\partial f}{\partial z^i} J_c^{ij} \frac{\partial g}{\partial z^j}$. The Hamiltonian satisfies two properties of the Poisson bracket that are transformation invariant

1. antisymmetry: $[f, g] = -[g, f]$
2. Jacobi identity: $[f, [g, h]] + [g, [h, f]] + [h, [f, g]] = 0$

which are to be satisfied for all functions f, g , and h of phase space [146].

2.3.2 Noncanonical Hamiltonian Structure

Not all systems have an equation of motion with canonical variables. For example, ideal fluid equations, the Vlasov equation, the Liouville equation, the BBGKY hierarchy, gyrokinetic theories, MHD, tokamak reduced fluid models and so on contain noncanonical variables [148]. The common property of those equations is that they are composed with Eulerian variables. The non-canonical variables result from the transformation from Lagrangian variables to Eulerian variables. However, those have Hamiltonian structure inside since the transformation preserves the form of Hamiltonian equations.

Consider a general system with noncanonical J (which is defined with noncanonical variables) and the Poisson brackets such as

$$\dot{z}^i = J^{ij} \frac{\partial H}{\partial z^j} = [z^i, H], \quad [f, g] := \frac{\partial f}{\partial z^i} J^{ij}(z) \frac{\partial g}{\partial z^j}. \quad (2.70)$$

Given the above two properties of the Poisson bracket and the requirement that $\det J \neq 0$, a 19th century theorem due to G. Darboux says that there exists a transformation that takes $J \rightarrow J_c$ [8]. Thus we can get back to canonical coordinates and the usual form of Hamiltons equations.

For the case where $\det J = 0$, the essential theorem was proven by S. Lie [69]. This theorem states that one can transform to a set of coordinates, part of which are canonical and part of which are in a sense redundant. The canonical coordinates describe a space of dimension equal to the rank of J and the remaining coordinates are described by a set of functions that have become known as Casimir invariants, because they are invariant under the dynamics.

The equation of motion in terms of Eulerian variables generally has $\det J = 0$. In addition, J is linear in the phase space coordinates. For example, finite dimensional system has a form as $J_{ij}(z^k) = c_k^{ij} z^k$ where c_k^{ij} are structure constants of a Lie algebra. Brackets with this form are called as Lie-Poisson brackets [8].

In infinite dimensions we represent a general field by $\varphi(\mathbf{x}, t)$ labeled by \mathbf{x} , where e.g., for two-dimensional fluid system $\mathbf{x} = (x, y)$ and for Vlasov-type plasma system $\mathbf{x} = (x, v)$. In those cases, the noncanonical Poisson brackets of interest have the form

$$\{F, G\} = \int \frac{\delta F}{\delta \varphi} \mathcal{J}(\psi) \frac{\delta G}{\delta \varphi} d\mathbf{x}, \quad (2.71)$$

where we now have a operator \mathcal{J} . Moreover, the Lie-Poisson form of continuous media is given by

$$\{F, G\} = \int \varphi \left[\frac{\delta F}{\delta \varphi}, \frac{\delta G}{\delta \varphi} \right] d\mathbf{x}, \quad (2.72)$$

where $[,]$ is a Lie-Poisson bracket. In the two-dimensional fluid case, φ is analogous to the vorticity ω and \mathbf{x} to (x, y) .

The noncanonical Poisson bracket for two-dimensional fluid system is given by

$$\{F, G\} = \int \omega \left[\frac{\delta F}{\delta \omega}, \frac{\delta G}{\delta \omega} \right] dx dy, \quad (2.73)$$

where

$$[A, B] = \left(\frac{\partial A}{\partial x} \frac{\partial B}{\partial y} - \frac{\partial A}{\partial y} \frac{\partial B}{\partial x} \right), \quad (2.74)$$

where $\omega(x, y)$ is the vorticity. With those definitions, the equation of motion for two-dimensional fluid as in the two dimensional case of Eq. (2.7) is

$$\frac{\partial \omega}{\partial t} = \{\omega, H\} = [\omega, \psi] \quad (2.75)$$

with the Hamiltonian

$$\begin{aligned} H[\omega] &= -\frac{1}{2} \int \psi \omega dx dy = \frac{1}{2} \int \psi \nabla^2 \psi dx dy \\ &= \frac{1}{2} \int |\nabla \psi|^2 dx dy = \frac{1}{2} \int |\mathbf{v}|^2 dx dy. \end{aligned} \quad (2.76)$$

Here, $[\omega, \psi] := \psi_y \omega_x - \psi_x \omega_y$ and the stream function and vorticity are related by $-\nabla^2 \psi = \omega$ or in the case of quasigeostrophy another integral relation such as $\psi = -\Delta^{-1}(\omega - \beta_{Ro} r)$ in our annulus geometry. This Hamiltonian formulation is useful to understand chapters on statistical mechanics and fluctuations.

2.4 Statistical Mechanics

Statistical mechanics provides a feasible way to calculate the macroscopic properties of matter from the behavior of microscopic constituents. Instead of considering all motions of the individual constituents, one describes observable quantities averaged over constituent Hamiltonian trajectories and the average is evaluated using the probability distribution of possible microstates. Likewise, fluid systems with a local balance between dissipation and forcing have been described by statistical mechanics with the inclusion of constraints based on invariants of the dynamics. In general, such statistical theories for fluids are based on the idea that the macroscopic behavior of the fluid turbulence can be described without knowing detailed information about small scale vortices [35, 161, 124].

Statistical mechanics seems not to be the proper method to describe the turbulence motion. There are two main reasons; One is that the turbulence is not a conservative system. To maintain a stationary turbulent state, the energy is continuously supplied and is dissipated in consequence of the viscous force at the same time. The second is that what in the turbulence can be used as *microscopic objects* and macroscopic quantities. In a classical statistical mechanics, microscopic objects are particles and physical quantities such as energy are observed in macroscopic scales.

The first problem is not fully justified yet. However, if we consider the only fluctuating part, the amount of energy dissipated in the short time is very small compared to the amount of energy present in the motion. So, we may treat the fluctuating motion as if it was the motion of an ideal fluid and constituted a conservative system.

	Indistinguishable objects	Distinguishable objects
No exclusion	Bose-Einstein	Maxwell-Boltzmann
Exclusion	Fermi-Dirac	Lynden-Bell

Table 2.2: Four possible statistics in physics.

The basic step to overcome the second difficulty is the consideration of two-dimensional case. Hamiltonian and basic properties of flow are functionals of vorticity. The stream function ψ is used as a basis for the description of the motion. From the stream function, we may calculate the velocity and the vorticity. In this case, the vortices can be regarded as the basic elements for statistical mechanics and the stream function as constraints or fields for the vortices.

Ultimately, such justifications are very difficult and would rely on delicate mathematical limits. However, its success amounts to the idea that the fluid system can in some sense be described by weakly interacting subsystems, where the behavior of a single subsystem can be described by weak coupling to a heat bath that embodies all of the other subsystems and all of the omitted effects. In the end ‘the proof of the pudding is in the eating’ and our justification is based on experimental observations in the latter chapter. With those justifications, the application of statistical mechanics is promising to describe the motion in turbulence.

2.4.1 Statistics and Entropy

All statistics start from the counting argument for micro-cells inside a macro-cell. First, consider the number of ways to distribute n_i phase elements

into m micro-cells with no cohabitation. The number of ways of assigning micro-cells to all elements is

$$\frac{m!}{(m - n_i)!}. \quad (2.77)$$

Beside, the statistics with the allowed cohabitation (No exclusion) is

$$m^{n_i}, \quad (2.78)$$

and the indistinguishable elements have a factor $1/(n_i!)$ in the statistics.

In physics, statistics of interest can be classified into four categories follows;

1. Bose-Einstein statistics is

$$W = \prod_i \frac{(n_i + m - 1)!}{n_i!(m - 1)!}. \quad (2.79)$$

2. Maxwell-Boltzmann statistics is

$$W = \frac{N!}{\prod_i n_i!} \times \prod_i m^{n_i}. \quad (2.80)$$

3. Fermi-Dirac statistics is

$$W = \prod_i \frac{m!}{n_i!(m - n_i)!}. \quad (2.81)$$

4. Lynden-Bell statistics is

$$W = \frac{N!}{\prod_i n_i!} \times \frac{m!}{(m - n_i)!}. \quad (2.82)$$

The two-dimensional Euler equation, like the Vlasov and other transport equations, can be viewed as mean field theory. Such equations are known to generate fine structure in the course of evolution. This led Lynden-Bell [124] to

consider a coarse graining procedure coupled with the idea of preserving all of the infinity of invariants such theories possess. He applied his ideas in the context of stellar dynamics, but the ideas are akin to those used in treatments of the classical electron gas by generalizations of Debye-Hückle theory [e.g. [101]].

2.4.2 Equilibrium Distribution

There have been many previous attempts to describe fluid flows by means of equilibrium statistical mechanics ideas. [See e.g. [72] for a recent review.] Following early work by Burgers [35], Onsager [161] began with a representation of the vorticity field in terms of a set of point vortices, zero-area vortices, of equal strength. Because this results in a finite-dimensional particle-like Hamiltonian system, Onsager could proceed to apply techniques of classical statistical mechanics. He gave arguments for the existence of negative temperatures and the occurrence of coherent structures in a confined region, which are often observed in nature. Also, he [161] studied the statistical mechanics of point vortices within a mean field approximation, and argued that in the negative temperature regime, large like-signed vortices are the most probable state. Related ideas have been further pursued by many researchers [e.g. [96, 131, 71, 233, 72]].

T.D. Lee [117] introduced a different approach when he projected three-dimensional fluid equations onto a Fourier basis and truncated to obtain a finite-dimensional system. He demonstrated that his truncated system satisfies a version of Liouville's theorem and was thus amenable to techniques of statistical mechanics. The evolution of density ρ in the phase space is given

as

$$\frac{\partial \rho}{\partial t} = \frac{\partial \dot{\omega}_{\mathbf{k}}}{\partial \omega_{\mathbf{k}}} = 0 \quad (2.83)$$

where $\omega_{\mathbf{k}} = \int \omega(x, y) e^{i\mathbf{k} \cdot \mathbf{x}} d\mathbf{x}$. It implies that the variation of the density of vorticity in course of time is zero.

Later, Kraichnan considered two-dimensional fluids [107, 108, 111] and noted that out of the infinite number of invariants, two quadratic invariants, the so-called rugged invariants, remained invariants after truncation. They argued that these rugged invariants are the important ones, and obtained an equilibrium state, which is related to that obtained by minimum enstrophy arguments put forth by selective decay hypotheses [118, 132, 32]. Also, using Kolmogorov-like arguments and the rugged invariants, Kraichnan argued for the existence of forward and inverse cascades for two-dimensional turbulence [107].

More recently, the necessity of incorporating the infinite number of invariants in statistical mechanics theories has been brought into question, and theories based on finite-dimensional models with a fewer constraints have been developed. Majda and Holen [126] have argued that including an infinite number of invariants provides no additional statistical information, and Turkington [220] has argued that previous theories have not properly handled the neglected small scale phenomena, and has proposed a theory that uses inequality constraints associated with only the convex invariants.

2.4.3 Nonextensive Entropy

The analysis based on Boltzmann-Gibbs statistics with extensive entropy only describes weak interactions and does not capture long-range inter-

actions [115]. Our observations of large coherent vortices in experiments on flow in a rotating annulus [18, 19, 10] lead us to consider a generalization of statistical mechanics that is applicable to systems with long range interactions: the nonextensive formalism proposed by Tsallis [215, 216].

A system composed of sub-systems A and B has entropy [215]

$$S_q(A + B) = S_q(A) + S_q(B) + (1 - q)S_q(A)S_q(B), \quad (2.84)$$

where $S_q(A)$ is the entropy of system A and q is the nonextensive parameter. When $q = 1$, the entropy is extensive. Tsallis proposed a form of the entropy that satisfies the above equation [217],

$$S_q = \frac{k}{q-1} \left(1 - \sum_i^W p_i^q \right), \quad (2.85)$$

where W is the total number of possible microstates of the system, p_i is the probability of i^{th} state and k is the Boltzmann constant.

However, additional fitting parameters in nonextensive statistics play a role in making the better curve for experimental data [27, 20, 30]. Tsallis statistics is still debated. I can not judge this theory. However, Beck and Cohen proposed a new interpretation on Tsallis statistics and other statistics. It is called *Superstatistics* [26, 25, 58]. It is similar to the old idea of local equilibrium in driven-dissipative systems. Superstatistics shows that various statistics can be obtained when the intensive parameter (such as temperature) in subsystems is fluctuating. Tsallis statistics corresponds to statistics with the χ^2 -distributed intensive parameter.

2.5 Summary and My Work

In this chapter, we have reviewed most classical theories on turbulence such as Kolmogorov energy spectrum, self-similar PDFs, Lynden-bell's statistical mechanics and so on. We try to test the classical theories and propose alternative theories in the later chapters.

In our rotating tank, potential vorticity is conserved and well-mixed. This implies the existence of nonzero axisymmetric vorticity. The strength of zonal flow has an upper bound imposed by complete depletion of the beta-plane potential vorticity reservoir. The detail study of potential vorticity mixing and the boundness of zonal flows is presented in the chapter 4.

Previous theories applying statistical mechanics ideas to fluids have regarded macro-cells without considering their statistical independence. Crucial requirements for equilibrium in classical statistical mechanics are statistical independence of small parts of a system (macro-cells) and additivity of invariants in macro-cells. In chapter 5, we propose a novel way to apply statistical mechanics to a two-dimensional fluid system with regarding statistical independence among macro-cells. More generally, we also prove why only the quadratic quantities are crucial in statistical mechanics. We also test the statistical mechanics with the non-extensive entropy in the chapter 6.

Statistical mechanics requires a proper set of canonical coordinates (such as action-angle variables) to evaluate the ensemble-averaged measure. The ensemble-averaged measure leads for statistical mechanics to directly connect to a real experiment in a classical system. For a long time, this measure has been performed treating non-canonical variables as canonical variables [111]. For the Vlasov case, Morrison [149] proposed a novel new method to

estimate an ensemble-averaged measure with canonical coordinates. However, the similar work for the fluid has not been reported because of the complication of calculations. In the chapter 7, we formulate an ensemble-averaged measure with a set of canonical coordinates and compare the result with experiment.

In the chapter 8, we unify two approaches that have been taken to explain the non-Gaussian probability distribution functions (PDFs) obtained in measurements of longitudinal velocity differences in turbulence, and we apply our approach to Couette-Taylor turbulence data. We show that the two methods are related, even though two methods are based on different concepts. One is an idea on the division of systems regarding energy dissipation rates [47], and the other considers a turbulent system to consist of subsystems regarding the fluctuating intensive parameters (such as temperature) [26]. The application of our approach to Couette-Taylor turbulence (Reynolds number 540 000) yields a good agreement with the observed non-Gaussian velocity difference PDFs.

The classical picture of two-dimensional turbulence is the inverse cascade with $E(k) \sim k^{-5/3}$ and the forward cascade with $E(k) \sim k^{-3}$. However, our rotating turbulence is not the case of classical picture. Baroud shows that the inverse cascade ($E(k) \sim k^{-2}$) in a rotating system is steeper than the classical guess by Kraichnan [18]. The chapter 9 gives a full description of energy spectrum in a rotating turbulence by investigating ranges of the inverse and forward cascades. Interestingly, we find that $E(k) \sim k^{-5}$ energy spectrum in the high k regime and the consistent break point of two energy spectrum scalings at the time frequency 2Ω . Also, by measuring velocity at the top and bottom, we present the difference of two energy spectra. This separation of energy spectrum represents the three-dimensional effect.

Chapter 3

Experimental Apparatus and Methods

In our laboratory, a rotating annulus has been operated to study the geophysical flow [196, 197, 228, 210], the instability of flows [195], the anomalous diffusion of passive tracers in mixing [229, 226, 227] and quasi-two dimensional turbulence [18, 19, 20]. Over a decade, researchers modified bottom topography and forcing configurations [136, 229, 17]. Most recent development was done by C. N. Baroud [17].

3.1 Rotating Tank

The apparatus consists of a rotating tank with an outer radius of 86.4 cm and an inner radius of 21.6 cm. Two bottoms are used to study the beta-effect and the flat bottom case. The sloping bottom has the depth of tank at the inner radius 17.1 cm and linearly increasing to 20.3 cm at the outer radius whereas the flat bottom has a fixed depth of tank 15.6 cm. There are three

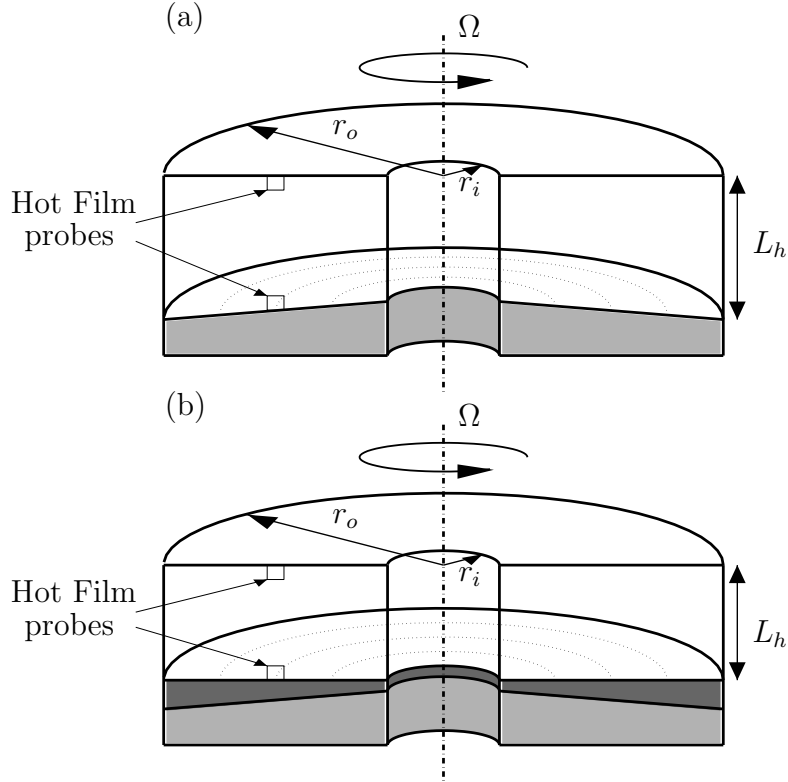


Figure 3.1: Schematic diagrams of the experimental apparatus. Fig. (a) is for a sloped bottom and the depth of tank, L_h varies from 17.1 cm for the inner boundary to 20.3 cm for the outer boundary. Fig. (b) is for a flat bottom and the depth of tank is fixed at 15.6 cm. The tank rotates from 1 Hz to 2 Hz. Flow is produced by pumping water through a inner ring as inlets and a outer ring as outlets in the bottom of the tank. The Coriolis force acts on the radially pumped fluid to produce a counter-rotating jet. By using two different rings as inlets and outlets, the radial length scale of forcing is varied. We measure velocity by using PIV as described in Chap. 3.3 or by using Hot film probes which are located on the top and bottom in the middle of two forcing rings as in figures.

concentric rings at the bottom with radii $r = 18.9$ cm, 27 cm, 35.1 cm. The water is circulated through three rings on the bottom. At each of three rings, 120 holes are distributed uniformly in azimuthal direction with 3 separation to initiate the forcing for a system. The amount of fluid into and out of annulus is same. So, there is no net change of water in the tank. The material is aluminum for the bottom and inner wall of the tank and Plexiglass for the upper lid and outer wall.

The tank is mounted on a steel rotating shaft 6.35 cm in diameter and 41.0 cm long. Two super-precision bearings were mounted at 9.9 cm and 24.5 cm from the bottom of the shaft. Near the bottom of the shaft, there is a 30.1 cm diameter gear belt pulley connected to a 7.3 cm gear belt pulley mounted on an I-620 AC servo-motor by Compumotor. It is rotated up to 3 Hz (rev/s) by a computer-controlled alternating current stepping servomotor with a gear-belt. The motor is placed 0.6 m from the tank shaft.

In this thesis, two different forcing configurations are used. The first one is that source and sink are generated through a ring of 120 circular holes located at the bottom of the tank at $r = 27.0$ cm, halfway between the annulus boundaries. Holes in a semi-circle (see Figure 4.1) are sources, and holes in the opposite semi-circle are sinks. Above each source (sink) the vertical flow creates a local divergence (convergence) which, in less than one tank turn, is converted by the Coriolis force into an anticyclone (cyclone). This forcing creates three zones for azimuthal flow: a prograde zonal circulation in the middle and two retrograde zonal circulations near the boundaries. Details of this three-zone flow structure are discussed in Chap. 4. The second configuration is that we pump flow in at the inner radius ($r = 18.9$ cm) and out at the outer radius ($r = 35.1$ cm). This forcing generates a strong azimuthal

counter-rotating flow due to the Coriolis force.

3.1.1 Flat Bottom

A 35" \times 35" \times 2" Delrin slab (purchased from Boedeker Plastics) is used for a flat bottom. We designed the flat bottom to fit on the top of the sloped bottom. The height of tank is 15.6 cm with the flat bottom attached on the top of the sloped bottom. Forcing holes in the flat bottom are located at the same place where the forcing holes are in the sloped bottom with radii $r = 18.9$ cm, 27 cm, and 35.1 cm. Fig. 3.1 shows the design of the flat bottom. Due to the flexibility of a Delrin slab, the flat bottom is warped after the installation. To adjust the flatness of the flat bottom, we tighten and loose each screw on the bottom. We can make the surface flat with 0.5 millimeters variations over the entire bottom.

3.1.2 Dynamics with Slopping vs. Flat Bottom

The effect of beta plane is to stretch the vortex columns due to changing of fluid height over a topography. Similarly, the figure skater spins up with her arms folded. For the annulus, as the vortex column moves away from the center, its vorticity increases to preserve the potential vorticity. In consequence, the potential vorticity is an important variable to describe the flow on the sloping bottom instead of the vorticity. It has been shown that when a vortex column evolves on the beta plane, it rapidly loses its coherence and is dispersed into Rossby waves if its potential vorticity anomaly gradient is less than β_{Ro} [134]. Each Rossby wave propagates against its zonal velocity and its ambient velocity field reinforces the wave to propagate [63, 165]. However,

the flat bottom does not play these roles in the dynamics of flows.

Rayleigh-Kuo condition of marginal stability can explain a symmetry-breaking of co-rotating and counter-rotating jets over a sloped bottom [113, 13]. The jet broadens until an averaged potential vorticity has an inflection point with zero slope radially. Co-rotating jets (Eastward jets) are bounded on either side by a region of uniform potential vorticity whereas counter-rotating jets (Westward jets) have only a central region of uniform potential vorticity. Therefore, the counter-rotating jet broadens further than the co-rotating jet. Co-rotating jets tend to be laminar and narrow, whereas counter-rotating jets are broad and often turbulent because of the interaction with boundaries. The symmetry-breaking of co-rotating and counter-rotating results from the β_{Ro} term in the equation of motion. Without the β_{Ro} term, there is no symmetry-breaking of co-rotating and counter-rotating jets.

3.2 Hot Film Anemometry

Even though there are many good techniques to measure velocities such as Particle Image Velocimetry, Hot Film Anemometry (HF) is used to measure the smallest and the fastest velocity fluctuations in turbulent flows. A HF measurement consists of a probe, calibration, data acquisition and processing systems. A probe consists of one miniature metallic element, whose electrical resistance is a function of temperature. The main process is constant resistance compensating electronic circuitry with a feedback loop, which keeps the temperature of the sensor constant under changing heat transfer conditions due to the turbulent fluctuating velocity. The voltage output is interpreted as the velocity via a calibration process.

3.2.1 Probe

The time series were obtained using constant-temperature hot-film anemometers (TSI model 1750) with the corresponding probes (TSI model 1210-60W and 1260A-10W). The probe sensing element is either 3 mm long and 152 μm in thickness for 1210-60W probes or 1.27 mm long and 25 μm in thickness for 1260A-10W probes. The sensor is held with two prongs, which penetrate a distance of 0.9 cm for 1210-60W or 0.6 cm for 1260-10W into the flow from the bottom and the top of the annulus.

A driving circuit maintains the constant temperature through a probe as the fluid advects heat away from the wire. The operating temperature of the probes is set by a control resistor for each probe separately. We keep an overheat temperature as approximately 42°C to minimize the effect of small temperature drifts from the ambient. The temperature of the water was also measured before and after the experiments, and we verified that the change in temperature was usually smaller than 1°C over the two-hour runs with two probes. This was achieved by ventilating the annulus room with an air-conditioning hose. The probes were calibrated before and after each of the experiments, so it was not crucial to know the exact overheat ratio.

The penetration depth 0.9 cm from the boundaries ensures that the measured velocity is away from the Ekman boundary layer. Quantitatively, we can estimate the length scale of the vertical Ekman layer balancing the viscous force and the Coriolis force. This balance is described by the Ekman number, defined in Chapter 2 as $Ek_V = \nu/(2\Omega L_V^2)$ where L_V is an appropriate length scale. The thickness δ_V of the boundary layer (the Ekman layer) is determined by taking $Ek_V \simeq 1$. In our experiment, $\nu = 0.01 \text{ cm}^2/\text{s}$ and

$6.3 < \Omega < 12.6$ rad/s. This gives values of δ_V in the range 0.02–0.03 cm. To investigate the instability in the Ekman layer, the Reynolds number can be defined as

$$Re_{Ek} = \frac{\delta_V \overline{U}}{\nu}. \quad (3.1)$$

The Ekman layer becomes unstable if Reynolds number based on the Ekman layer is above the critical value 85 ± 10 [170, 140]. In our experiment, Re_{Ek} is about 40 with $\overline{U} \sim 10 - 20$ cm/s. Therefore, we assume that these boundary layers are quite thin and laminar and that the probes are measuring the velocity outside Ekman layer.

To obtain the reliable hot-film data, several difficulties should be overcome. The first one is the contaminants in the water. Sources of contaminants can be algae and dirt from the boundaries (a tank and tubes) and fragments and particles from PIV measurement that adhered to the tubing walls and other surfaces. To reduce those contaminants, we are filtering and circulating the water and brushing the surface of tank and tubes for 1 or 2 hours every two days. The next difficulty is the bubble-forming near probes. Sometimes, the high overheat temperature can initiate bubbles near the probe. It is avoided by changing the control resistance to set the overheat temperature as approximately 42°C. Finally, the water was always allowed to sit still at least 10 hours after refilling or an hour after filtering water in the tank; this process is suggested in order to de-gas the water to avoid the formation of bubbles at the hot-films [17].

3.2.2 Data Acquisition

The signal from the probes is then carried with coaxial cables to the anemometers, then through the slip rings to the acquisition computer. In the typical experiments reported here, the probe signal is sampled at 150 Hz for periods of 30 minutes to 2 hours, thus yielding data files that had $2 \times 10^5 - 10^6$ velocities per probe for 30 minutes to 2 hours. The individual probes and the repeated runs were essential in confirming the measurements and in improving the statistical significance of the results.

The process of measuring the velocity is following; We assume that the wire is initially at the temperature T_f as the fluid and has electrical resistance R_f . Then if we heat up the wire to some temperature T_w , the resulting resistance R_w will be

$$R_w = R_f \{1 + \sigma(T_w - T_f)\} \quad (3.2)$$

where σ is the temperature coefficient of resistance. If a current I flows in the wire, then heat is generated at a rate ($= I^2 R_w$). This heat is transferred from the wire to the fluid at a rate ($= hS(T_w - T_f)$), where h is the heat transfer coefficient and S is the surface area of a HF. For thermal equilibrium,

$$\begin{aligned} I^2 R_w &= hS(T_w - T_f) \\ &= hS \frac{R_w - R_f}{\sigma} \end{aligned} \quad (3.3)$$

The fluid velocity U_n perpendicular to a probe cools the HF and affects the heat transfer coefficient h .

$$\frac{I^2 R_w}{R_w - R_f} = A + B\sqrt{U_n} \quad (3.4)$$

where A and B are assumed to be independent of the fluid velocity.

Let's consider a single HF in a turbulent flow with mean velocity \bar{U}_1 . The fluid will flow in three directions and fluctuating velocity has three components. We align the HF with the radial direction. So, the radial component of velocity v_3 does not contribute much to the cooling of HF.

$$\begin{aligned}
U_n &= \{(\bar{U}_1 + v_1)^2 + v_2^2\}^{1/2} \\
&= \bar{U}_1 \left(1 + \frac{2v_1}{\bar{U}_1} + \frac{v_1^2 + v_2^2}{\bar{U}_1^2}\right)^{1/2} \\
&= \bar{U}_1 + v_1 + \bar{U}_1 \mathcal{O}\left(\frac{v_1^2}{\bar{U}_1^2}\right) + \bar{U}_1 \mathcal{O}\left(\frac{v_2^2}{\bar{U}_1^2}\right), \tag{3.5}
\end{aligned}$$

where v_1 is the horizontal velocity (for annulus, the azimuthal velocity) and v_2 is the vertical velocity (for annulus, the velocity along the axis of rotation). If the vertical velocity v_2 is relatively small compared to the horizontal mean velocity \bar{U}_1 , we can approximate our measured velocity as the azimuthal component of the velocity. Furthermore, the small turbulent intensities (v_1/\bar{U}_1) leads that our measured velocity is simply expressed as a linear combination of the horizontal mean velocity, \bar{U}_1 and the fluctuation velocity, v_1 . [218]

3.2.3 Probe Calibration

The probes were calibrated before and after each run by first setting the tank at a constant rotation rate with no pumping, until the fluid reached solid-body rotation. The solid-body rotation is achieved usually after 5 – 10 minutes rotation. By suddenly stopping the tank, a velocity jump corresponding to the tank's previous speed is measured: $v = \Omega r_{\text{probes}}$, where v is the velocity of the flow when we stop the tank and r_{probes} is the radial position of a probe. This process was repeated at several rotation rates and a quadratic curve was fit

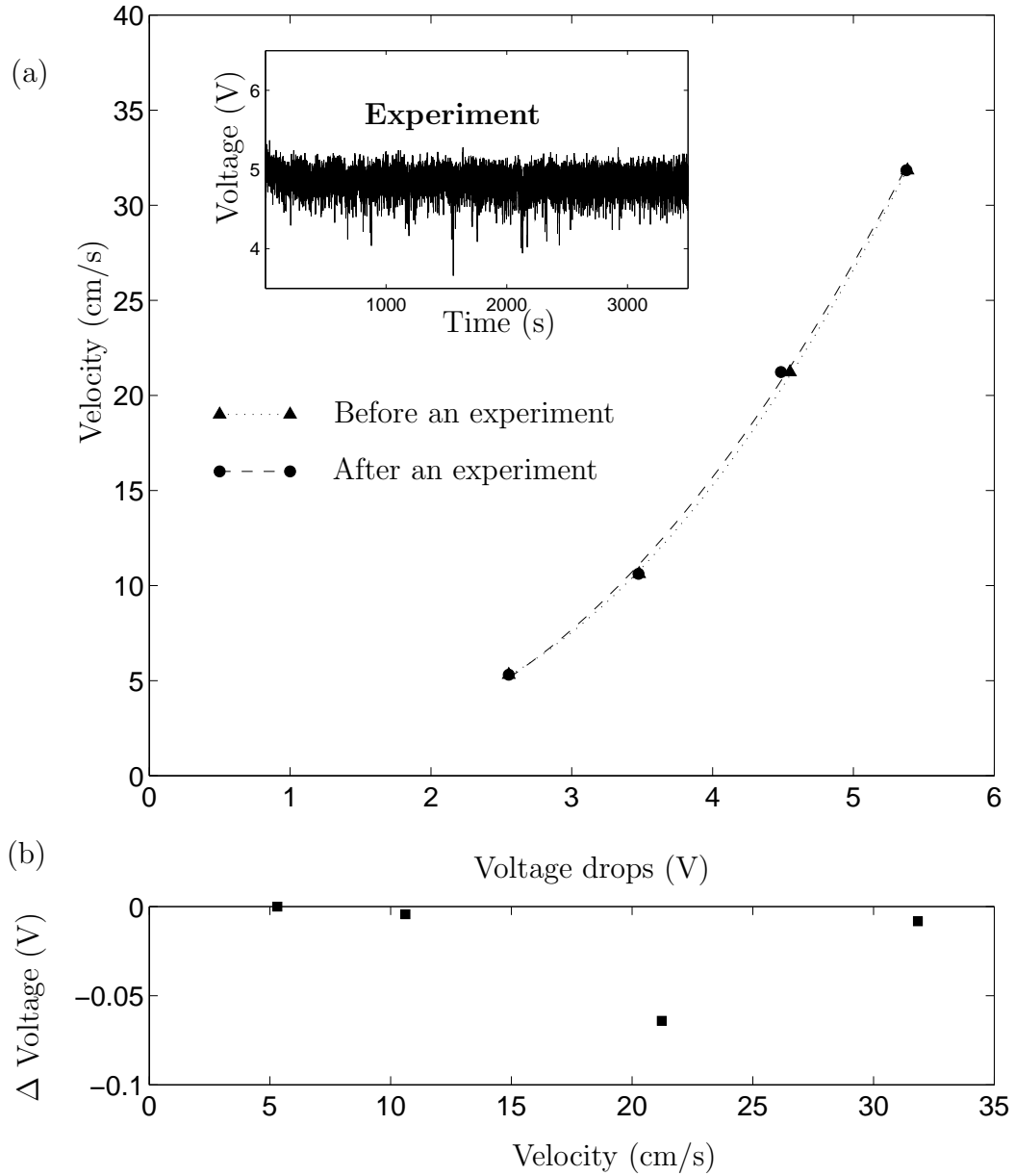


Figure 3.2: Calibration data for a hot-film probe. We calibrate probes before and after each experiment. In Fig. (a), triangles (circles) are measured voltage drops after (before) an experiment and the dotted (dashed) line is a least-square fitting curve of four data points. As shown here, the voltage drops do not change much before and after the experiment. Inset shows the voltage output from the experiment. During the experiment, there is no significant voltage drops. Fig. (b) shows how much the voltage drops changes during the experiment.

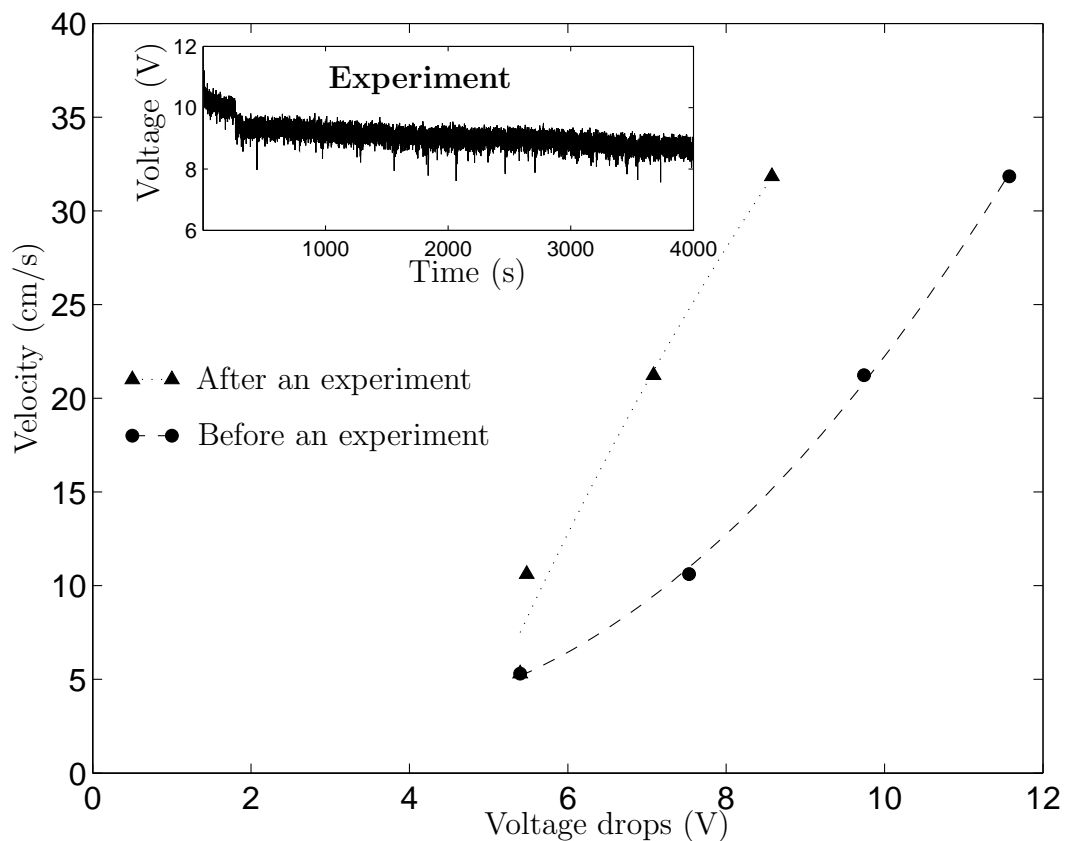


Figure 3.3: Calibration data for a hot-film probe induced by contaminations. We calibrate probes before and after an experiment. Triangles (circles) are measured voltage drops after (before) an experiment and the dotted (dashed) line is a least-square fitting curve of four data points. As shown here, the voltage drops significantly changes before and after the experiment. Inset shows the voltage output from the experiment. During the experiment, the voltage from a probe suddenly changes at 250 seconds and gradually decreases afterwards.

through the points to obtain a relation between velocity and voltage drops. A sample calibration curve along with the voltage range is shown in Fig. 3.2. However, we can see the shifted voltage drop before and after experiments when the water is contaminated or has a gas inside as in Fig. 3.3. Based on the calibration, we obtain the velocity time series from the voltage time series.

3.3 Particle Image Velocimetry (PIV)

Quantitative measurements of velocity fields were obtained by particle image velocimetry (PIV), using 100-micron particles with density 1.003 g/cm^3 to seed the flow. The PIV system was developed by Baroud [17]. These particles were illuminated by a ring of 360 red LEDs(AND model 190CRP) of a few centimeter thickness. Images of the particles were captured using a high-resolution KODAK ES1.0 Megapixels (1008×1018 pixels) camera, and transferred in real time to a rotating PC. The image acquisition was controlled by an external timing circuitry that was triggered when LEDs illuminated the particles. Although the image rate could be on average 30 Hz, but a rotating camera and PC can not follow up this rate. We could arrange for pairs of images, for determining the velocity, to have a time separation of 8 ms. Pairs of images were analyzed using cross-correlation of sub-images as described in [17].

3.4 Flow Control

We measure the flow rate by using the volumetric flow EG+G Flow Tech (FT-10AEYW-LEG-1). The flow meter has a freely rotating rotor positioned

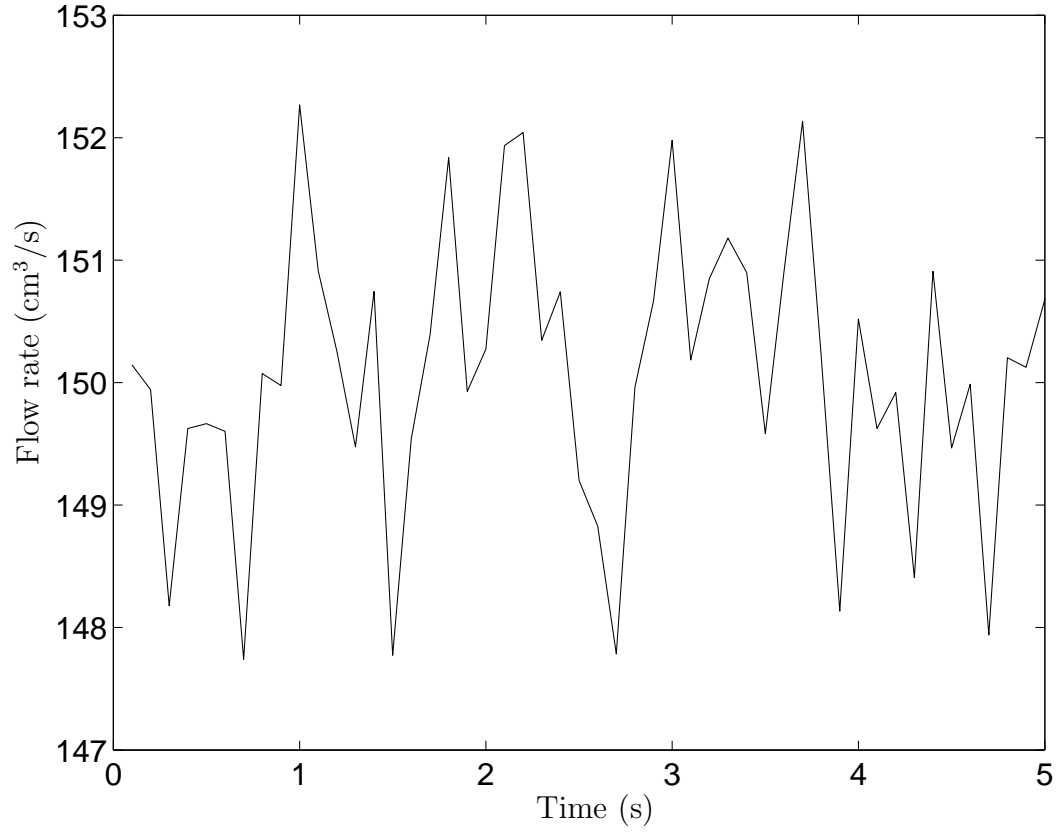


Figure 3.4: Flow rate from the flow meter. This is example by setting the flow rate as $150 \text{ cm}^3/\text{s}$. The root mean square (rms) value of fluctuation of flow rate is $0.95 \text{ cm}^3/\text{s}$. This feedback controller results in a long-term stability within 2 %.

axially in the flow stream with the flowing fluid pushing against the blades. The rotational speed of the rotor is proportional to the velocity of the fluid. Each rotation of the turbine rotor generates electrical pulses in the pickoff which is attached to the flowmeter. Each one of these pulses represent a discrete volume of fluid. The frequency or pulse repetition rate represents the flow rate.

Feedback system makes more accurate flow rate in a system. By monitoring flow rate through the flow meter, the pumping rate is controlled. The flow rate of pumping varies from 80 to 750 cm³/s which is limited by the capacity of flow meter. Measured flow rate is shown in Fig. 3.4. Variations of flow rate in time lie within 2 % and its rms value is 0.95 cm³/s.

Chapter 4

Potential Vorticity Mixing

4.1 Introduction

Fluid dynamics in many planetary systems is strongly influenced by the dominance of the Coriolis force over all other forces present in the system. A common feature of these systems is the generation of a zonal flow, i.e., a mean flow in the azimuthal direction with respect to the rotation vector. Zones of alternating azimuthal velocity have been observed on Saturn and Jupiter by Voyager spacecraft [93]. The general circulation in the earth's atmosphere and oceans also displays azimuthal streams. Experiments [9] on convection in a rotating sphere of liquid metal modeling the earth's liquid core and numerical simulations [57] show evidence of surface zonal flow generation from apparently chaotic, small scale deep convection plumes. A common feature of these systems is that mechanical or thermal forcing occurs at a scale which is small compared to the size of the system, and that zonal motion is therefore not directly forced.

In quasi-geostrophic dynamics (see, e.g., [165]), the beta-plane, a variation of the Coriolis force with latitude in the case of constant depth systems, or a variation of depth with radius in constant Coriolis force systems, plays an important role in the nonlinear mechanism of energy transfer to the zonal scale [179, 89]. The beta-plane can be seen as a reservoir of planetary vorticity. Potential vorticity (PV) can be defined as the sum of the planetary vorticity and the vorticity component parallel to the rotation vector in the rotating frame. In an inviscid fluid, PV is materially conserved and is therefore well-mixed in strongly forced environments. This leads to the development of zones of constant PV [173], and the resultant mean zonal shear leads to zonal flow.

Laboratory experiments [197] and numerical simulations [128] demonstrated that regions of constant PV existed within prograde and retrograde jets generated by forcing directly at the zonal scale. In those experiments, PV mixing, which is the process of geophysical interest, was not implied as a driving mechanism but as a consequence. Using the same rotating annulus system as Sommeria et al. [198] used in a different forcing configuration, we have conducted experiments and complementary numerical simulations where forcing occurs only at a small scale, and the strength and length scales of zonal flow are left unspecified and are selected by the dynamics.

Earlier experiments by Colin [59] and McEwan [133] on topographical and source-sink forced rotating flows demonstrated the role of Reynolds stresses in the generation of zonal circulation. Our study shows that the magnitude of zonal flow has an upper bound determined by the quantity of PV available in the planetary reservoir. The evolution of the flow towards its perfect mixing limit is studied as a function of the two control parameters of the experiment, rotation rate and pumping rate.

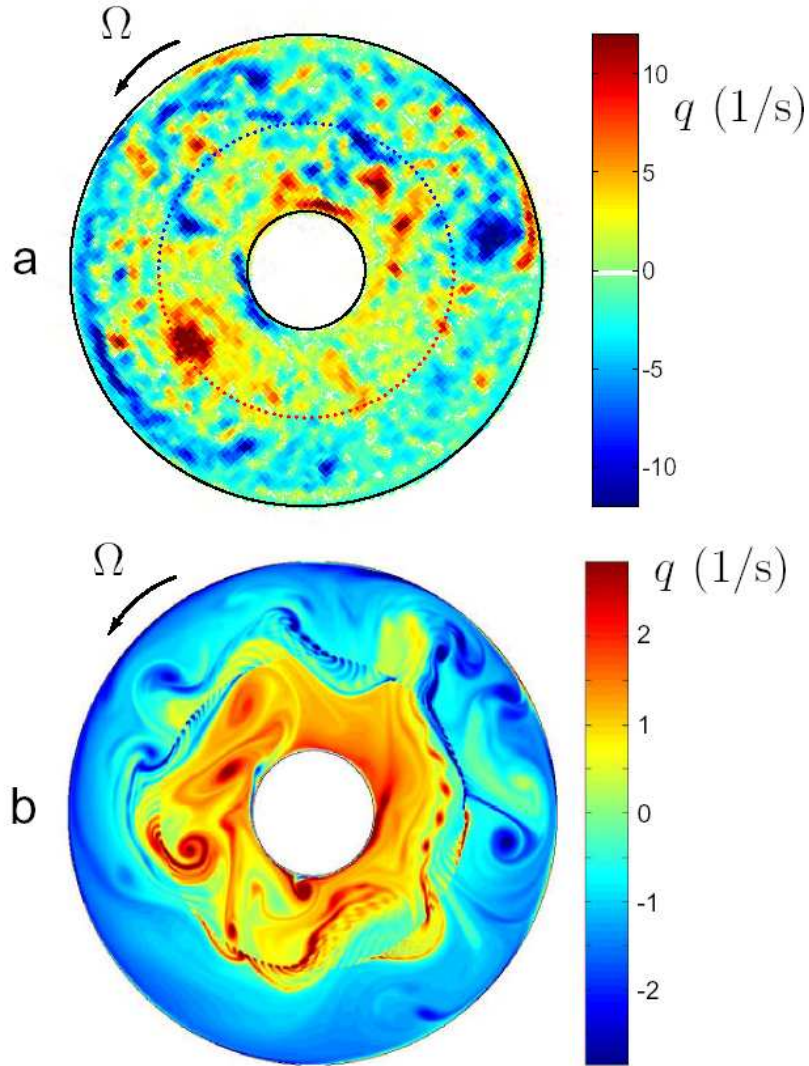


Figure 4.1: The potential vorticity fields obtained from (a) experiment, and (b) numerical simulation contain strong cyclones (red) and anticyclones (blue). Image (a) shows the location of the forcing holes, arranged in semi-circles of 60 sources (blue) and 60 sinks (red); the same forcing was used in the simulations. This forcing produces vortex filaments of the same width as holes (see striations in b); the filaments merge and mix potential vorticity in the inner and outer regions of the annulus, and a retrograde drifting Rossby wave (visible particularly in b) prevents mixing between the two regions. In (a), rotation rate $\Omega/2\pi = 2.5$ Hz and pumping rate $F = 550\text{cm}^3/\text{s}$ (Reynolds number, 20000); in (b), $\Omega/2\pi = 1.5$ Hz and $F = 75\text{cm}^3/\text{s}$. Numerical simulations with stronger forcing than in b exhibit behavior similar to a, with more small scale vortices than b.

4.2 Model

The experimental set-up is a water-filled annular tank of inner radius $r_i = 10.8$ cm and outer radius $r_o = 43.2$ cm. The tank is covered by a solid transparent lid. It can be spun up to rotation frequencies $\Omega/2\pi$ of 3 Hz. The bottom depth varies from 17.1 cm at the inner radius to 20.3 cm at the outer radius, with a mean height $h_0 = 18.7$ cm and a slope $\eta = -0.1$. Water is continuously pumped in closed circuit in and out of the tank, through a ring of 120 circular holes located at the bottom of the tank at $r_f = 27.0$ cm, halfway between the annulus boundaries. Each hole has a diameter of 0.25 cm, and the total pumping rate F is in the range 50-550 cm³/s. Holes in a semi-circle (see Figure 4.1) are sources, and holes in the opposite semi-circle are sinks. Above each source (sink) the vertical flow creates a local divergence (convergence) which, in less than one tank turn, is converted by the Coriolis force into an anticyclone (cyclone). Small scale forcing of the flow is achieved in this way. Since the net vorticity produced is zero, zonal flow is not directly forced. This system is therefore a convenient approximation of the examples described in the introduction.

The Rossby number $Ro = (\tau_\omega \Omega)^{-1}$ is defined using the nonzonal vortex turnover time

$$\tau_\omega = \left(\frac{1}{\pi(r_o^2 - r_i^2)} \int_{r_i}^{r_o} \int_0^{2\pi} \overline{r(\omega - \overline{\omega_\theta})_t^2} dr d\theta \right)^{-1/2} \quad (4.1)$$

where ω is the vorticity component parallel to the rotation axis, $\overline{\omega_t}$ its time-average and $\overline{\omega_\theta}$ its azimuthal average. Ro is kept under 0.2 to maintain quasi-geostrophy and a flow reasonably two-dimensional by the Taylor-Proudman theorem.

In the experiment, Particle Image Velocimetry was used to determine

the complete velocity field in a plane perpendicular to the axis of rotation [18]. A horizontal light sheet was produced using a ring of light emitting diodes at mid-depth of the tank. Water in the tank was seeded with neutrally buoyant plastic particles of size ~ 0.1 mm. For each pair of values for the control parameters Ω and F , 100 instantaneous velocity fields were acquired at intervals of about 1, 2, 4 or 8 seconds for forcings of 550, 350, 150 and 50 cm^3/s , respectively.

Direct two-dimensional numerical simulations have been performed in addition to the experiments. We resolved the advection-diffusion of PV including viscous dissipation (viscosity ν), realistic forcing, and drag characterized by the Ekman spin-up time τ_E :

$$\frac{\partial q}{\partial t} + (\mathbf{v}_\perp \cdot \nabla_\perp)q = -\frac{\omega}{\tau_E} + \nu \nabla^2 \omega + \frac{2\Omega}{h_0} v_f, \quad (4.2)$$

$$\tau_E = \frac{h_0}{2}(\nu\Omega)^{-1/2}, \quad (4.3)$$

where the vertical velocity at each forcing hole is described by v_f , which was chosen to be constant over each hole and zero elsewhere. Equation (4.2) was solved on an annulus of the same aspect ratio as the experiment, with rigid boundary conditions at the inner and outer radii. The numerical technique was finite-differencing in the radial direction and spectral decomposition in the lateral direction. Each forcing hole typically spanned ten mesh points.

4.3 Results

The potential vorticity is given by $q = \omega + \beta_{Ro}(r - r_f)$, where r is the radial coordinate, and the beta-plane parameter is $\beta_{Ro} = 2\eta\Omega/h_0$. A snapshot of the measured q is shown in Figure 4.1 a. We observe that one

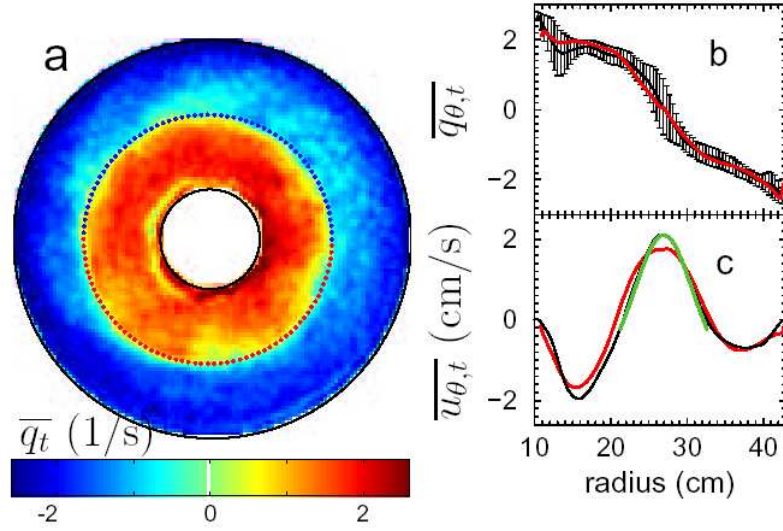


Figure 4.2: The experimental time-averaged potential vorticity field $\overline{q_t}$ (a) and azimuthally-averaged profile $\overline{q_{\theta,t}}$ (b, black line) have a positive (negative) fairly uniform value in the inner (outer) region of the annulus. Numerical simulations (b-c, red lines) yield a similar profile. (c) The average azimuthal velocity profile $\overline{v_{\theta,t}}$ is consistent with profile (b) and Stokes theorem (see text) and reveals three zonal flows, retrograde in the regions of well-mixed potential vorticity and prograde in the gradient region. The vicinity of the peak of zonal flow is described by $\text{sech}^2(r)$ (green line in c). Conditions for experiment and simulation were $\Omega/2\pi = 2.5$ Hz and $F = 150\text{cm}^3/\text{s}$.

large anticyclone (cyclone) appears intermittently in the source (sink) half of the annulus. Both drift in the retrograde direction with respect to the annulus. The strongly forced flow is dominated by vortices so no zonal pattern is apparent in snapshots; however, time averaging clearly reveals a zonal flow pattern, as Figure 4.2 illustrates. A PV gradient exists above the forcing ring, while PV is well mixed (fairly uniform) in the inner region ($r_i < r < r_f$) and in the outer region ($r_f < r < r_o$). Graphs of the azimuthally averaged PV (Figure 4.2 b) and the azimuthal velocity (Figure 4.2 c) as a function of r show that the forcing has created three zones for azimuthal flow: the PV gradient region corresponds to a prograde zonal circulation, while the regions of constant PV correspond to retrograde zonal circulations. The prograde flow has a profile consistent with $\text{sech}^2(r)$ (Figure 4.2 c). The retrograde flow is weaker in the outer region. This three-zone flow structure was observed for all parameter values F and Ω studied.

The numerical simulation shows that small scale PV filaments are released above each hole in the forcing ring (Figure 4.1 b), and positive (negative) filaments merge into cyclonic (anticyclonic) structures. The beta plane acts as a vorticity selector: cyclonic (anticyclonic) structures cannot move outwards (inwards) because their motion outwards (inwards) triggers a Rossby wave which restores them to their original position. In contrast, nothing prevents a cyclone from moving to the inside. In this way, positive (negative) PV is carried by cyclones (anticyclones) to the inner (outer) region of the annulus. A gradient therefore sets up above the forcing ring, separating the two regions where vortical structures efficiently mix PV into two homogenized, constant levels. A retrograde-drifting Rossby wave, similar to that observed by Sommeria et al. [198], rides on the PV gradient, preventing the inner and

outer regions from exchanging fluid most of the time, although there are a few leaks across the PV gradient, as can be seen in Figure 4.1 b.

The net vorticity injected by the forcing system is zero (cyclonic and anticyclonic vorticity are injected in balance); hence material conservation of PV implies that the only PV to be homogenized is the planetary background $\beta_{Ro}(r - r_f)$. In the limit of perfect mixing, the PV has two levels, q_i in the inner region and q_o in the outer region, and these levels are given by the mean values of the planetary background in each region,

$$q_{i,o} = \frac{2\pi}{\pi(r_f^2 - r_{i,o}^2)} \int_{r_{i,o}}^{r_f} r \beta_{Ro}(r - r_f) dr = \frac{\beta}{3} \left(-r_f + \frac{2r_{i,o}^2}{r_f + r_{i,o}} \right) \quad (4.4)$$

which are independent of the forcing strength. This perfect mixing model has infinite gradients above the forcing ring and near the boundaries. However, such sharp gradients are prevented by the Rayleigh-Kuo instability criterion [113]: a PV gradient greater than $2\beta_{Ro}$ is unstable because $d^2 \overline{u\theta}/dr^2 - \beta_{Ro}$ changes sign. In our flow, the PV gradients observed above the forcing ring and near the boundaries are in good accord with the Rayleigh-Kuo criterion, as Figure 4.3 illustrates.

In the limit of strong mixing, both the maximum PV gradient and the homogenized PV levels scale linearly with β_{Ro} . Therefore, the shape of the well-mixed radial PV profiles, when normalized by β_{Ro} , is independent of forcing rate and rotation rate (Figure 4.3). The width l of the gradient zone is also independent of the two control parameters, and is given by $l \approx (r_o - r_i)/4$. For a jet with a sech^2 profile, the modenumber m of the Rossby wave riding on the steep PV gradient is predicted by linear theory to be $m = 2^{1/2} l^{-1} r_f$, which is also independent of control parameters. The value $m = 5$ observed in our numerical simulations at low forcing level (Figure 4.1 b) agrees with the

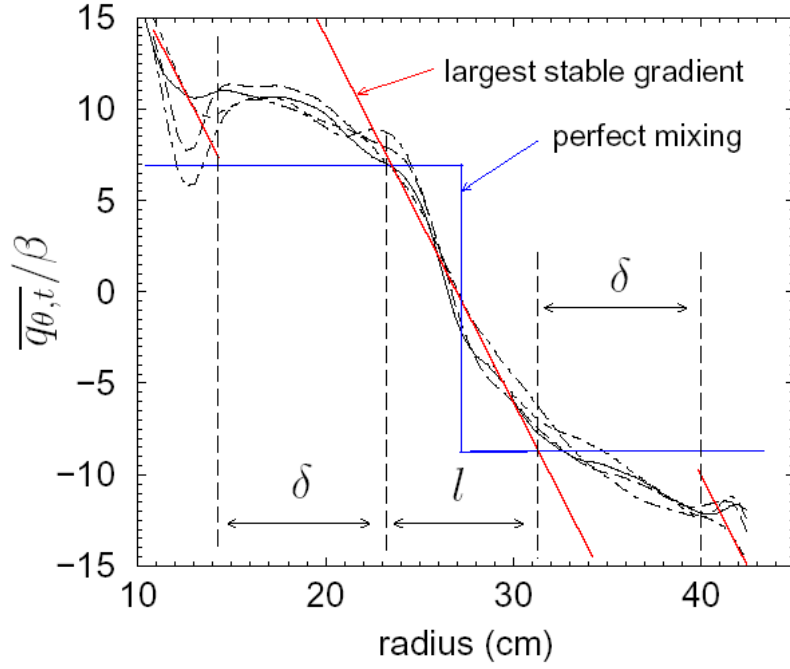


Figure 4.3: The observed well-mixed profiles of potential vorticity are similar when normalized by the beta plane coefficient β_{Ro} . Lengths δ and l of the mixing and gradient regions are then determined solely by the geometry. The values of $\Omega/2\pi$ (Hz) and F (cm^3/s) were 1.25, 150 (-); 2.5, 150 (- -); 2.5, 350 (- -); 2.5, 550 (- - -). replacements

prediction of linear theory.

The mean zonal flow $\overline{u_\theta}$ is related to azimuthally averaged vorticity $\overline{\omega_\theta}$ through Stokes theorem

$$\overline{v_\theta}(r) = \frac{1}{r} \int_{r_i}^r r \overline{\omega_\theta} dr = \frac{1}{r} \int_{r_i}^r r (\overline{q_\theta} - \beta_{Ro}(r - r_f)) dr . \quad (4.5)$$

Equation (4.5) shows that zonal shear, and therefore zonal motion, exists as a consequence of PV mixing by smaller scale eddies. A perfectly mixed zonal flow will have the same properties as perfectly mixed PV, i.e., it will be proportional to β_{Ro} and independent of forcing. It will also have a cusp at $r = r_f$ (due to the discontinuity in the PV profile), and will be always retrograde and of equal strength in the inner and outer regions. The cusp is not observed in our flow because the PV discontinuity is broadened by instability. A prograde region exists because flow near boundaries does not conserve PV and injects some into the fluid (see Figure 4.1 b). Zonal flow is asymmetric with respect to r_f because the inner region is smaller and therefore better mixed than the outer region (see distribution of vortices in Figure 4.1 b).

Any dependence of the observed zonal flow on the forcing strength is due to incomplete PV mixing. The mixing is nearly complete, as illustrated by Figure 4.4, where the rms value U_θ of the measured time-averaged zonal motion is normalized with respect to its perfect mixing value, obtained from equations (4.4) and (4.5):

$$U_\infty = \beta_{Ro} \delta^2 \sqrt{\frac{2}{15}} \approx \frac{\beta_{Ro} \delta^2}{3} \quad (4.6)$$

where the curvature of the annulus has been neglected, and $\delta = (ro - r_f)/4$ is a length representative of the width of constant PV zones. U_θ/U_∞ is plotted in Figure 4.3 as a function of the ratio of time scales τ_E/τ_ω , which measures the

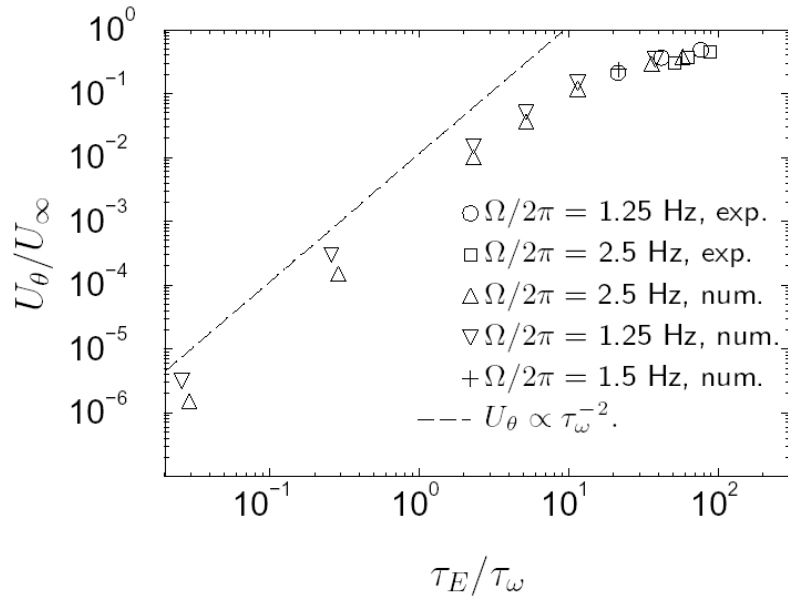


Figure 4.4: The forcing configuration has zero net potential vorticity injection, and the planetary reservoir has a limited capacity: The rms value U_θ of zonal flow approaches an upper bound U_∞ when mixing, measured by the ratio of Ekman spin-up time τ_E to vortex turnover time τ_ω , becomes large.

importance of nonzonal motion, which favors mixing, relative to the friction (in the top and bottom Ekman layers), which inhibits mixing. The experiments, conducted mainly in the well-mixed regime ($\tau_E/\tau_\omega \gg 1$), and the numerical simulations are in reasonable agreement in the region of overlap. In the viscous regime ($\tau_E/\tau_\omega \gg 1$), the rms value of zonal motion grows with the square of non-axisymmetric motion, reflecting the action of the axisymmetric part of the Reynolds stresses that feed the zonal flow [133]. In the well-mixed regime, the zonal motion clearly saturates and never exceeds the perfect mixing value. In this limit, the planetary reservoir is depleted and there is no way the system can put more energy into zonal flow. In the experiments, perfect mixing will never be reached due to the Rossby wave instability and non-conservation of PV near boundaries of the annulus.

4.4 Discussion

These experiments illustrate how non-axisymmetric motion mixes PV and produces a zonal circulation. As the PV mixing grows, a state is reached where the reservoir of planetary vorticity is fully used, and the zonal motion saturates at an rms value given by Equation (4.6), as Figure 4.4 illustrates. Saturation of zonal flow has been observed in the three-dimensional numerical simulations of Christensen [57], and has been attributed to a loss of geostrophy in the system as the Rossby number grows. Here we show that a two-dimensional model also produces saturation.

The criterion for saturation may be written in terms of non-dimensional numbers, namely the Rossby number $Ro = U/\Omega D$ and the Ekman number $Ek = (\tau_E \Omega)^{-2} = \nu/\Omega D^2$ where D is a typical length scale for the system and

U a typical nonzonal velocity:

$$RoEk^{-1/2} \gg 1. \quad (4.7)$$

With this condition satisfied, relation (4.6) may be expected to hold quite generally, since it only expresses that $\overline{\omega}$ is bounded. Approximating the atmosphere of Jupiter with a well-mixed, piece-wise constant PV, such as done by Marcus [127], one can thus relate the typical zonal velocity to the size of the zones. We obtain the correct order of magnitude for the zonal velocity, $U_\infty = 50$ m/s, using the following values: $\delta = 2000$ km for the width of a zone $\beta_{Ro} = 2\Omega \cos \theta / r$ where θ is the latitude; $\Omega = 1.75 \times 10^{-4}$ rad/s; $\theta = \pi/4$; and $r = 71400$ km.

In the case of the earth's liquid core, the usual values for the Ekman and Rossby numbers are $Ek \sim 10^{-14}$ and $Ro \sim 10^{-6}$ (e.g., see Aubert et al. [9]). A nonmagnetic flow in this liquid shell would therefore be quasi-geostrophic, and condition (7) would be satisfied. The configuration here is a thick spherical shell, but it can be described with beta-plane equations. In this case, the β_{Ro} parameter is constrained by the slope of the boundaries, and outside a cylinder tangent to the inner core it becomes $\beta_{Ro} = 2r\Omega/(r_e^2 - r^2)$, where r_e is the external radius of the core and r is the cylindrical radius. Taking $r_e = 3400$ km, $r = 1500$ km, and a zonal velocity $U_\infty = 10^{-4}$ m/s, as estimated by Jault et al. [95], relation (4.6) yields a typical size as low as $\delta = 10$ km for one zone, a value very small compared to the 2200 km of the liquid shell. Such a zonal flow would therefore contain many layers, which would act as strong barriers to the convective transport of heat, in the same way as they act as barriers to the transport of PV. This would therefore not be very efficient in maintaining the earth's magnetic field, which is thought to get its energy

from convective motion through the geodynamo process. This underlines the necessary influence of magnetic Lorentz forces, which change the balance from geostrophic to magnetostrophic.

In the flow in an annulus that we have studied, even though the characteristics of zonal flow are not specified by the forcing, the system evolves towards a state with fixed number of zones whose strength and length scale are prescribed by the geometry. The question of how many zones a random small-scale mechanical or thermal forcing would produce remains open and will be examined in forthcoming experimental studies. There is an energetic cost each time the fluid creates a gradient of PV separating two zones. This problem could therefore be examined through free energy minimization.

Chapter 5

Statistical Mechanics

A statistical mechanical description is proposed for two-dimensional inviscid fluid turbulence. Using this description, we make predictions for turbulent flow in a rapidly rotating laboratory annulus. Measurements on this system reveal coherent vortices in a mean zonal flow. The flow is anisotropic and inhomogeneous but has low dissipation and forcing. In statistical mechanics two crucial requirements for equilibrium are statistical independence of macro-cells (subsystems) and additivity of invariants of the macro-cells. One of these invariants is energy, an extensive quantity, which should be additive; i.e. the interaction energy between a macro-cell and the rest of the system (reservoir) should be small. We use additivity to select the appropriate Casimir invariants from the infinite set available in vortex dynamics. Exchange of micro-cells within a macro-cell should not alter an invariant of a macro-cell. Statistical analyses of turbulence for several decades have considered macro-cells without explicitly considering their statistical independence. A novel feature of the present study is our choice of the macro-cells, which are continuous phase space surfaces based on mean values of the streamfunction; the surfaces can

be used to define a canonical distribution. We show that this approach can describe anisotropic and inhomogeneous properties of a flow. Quantities such as energy and enstrophy can be defined on each surface. Our approach leads to the prediction that on a surface there should be a linear relation between the ensemble-averaged potential vorticity and the time-averaged streamfunction; our laboratory data are in good accord with this prediction. Further, the approach predicts that although the probability distribution function for potential vorticity in the entire system is non-Gaussian, the distribution function of micro-states should be Gaussian on the macro-cells, i.e., for surfaces defined by mean values of the streamfunction. This prediction is also supported by the turbulence data. While our statistical mechanics approach was motivated by and applied to experiments on turbulence in a rotating annulus, the approach is quite general and is applicable to a large class of Hamiltonian systems, including drift-wave plasma models, Vlasov-Poisson dynamics, and kinetic theories of stellar dynamics.

5.1 Introduction

5.1.1 Overview

Statistical mechanics provides a way to calculate the macroscopic properties of matter from the behavior of microscopic constituents. Instead of considering all motions of the individual constituents, one describes observable quantities averaged over constituent Hamiltonian trajectories, and averages are evaluated using the probability distribution of possible microstates. Likewise, fluid systems with a local balance between dissipation and forcing have

been described by statistical mechanics with the inclusion of constraints based on invariants of the dynamics. In general, such statistical theories for fluids are based on the idea that the macroscopic behavior of the fluid turbulence can be described without knowing detailed information about small scale vortices.

The justification of statistical mechanics based on ideal two-dimensional fluid equations is open to question, given the existence of forcing, dissipation, three-dimensional effects, temperature gradients, etc. that certainly occur in real fluid flows. Moreover, one must square the idea of cascading with the approach to statistical equilibrium. Ultimately, such a justification is very difficult and would rely on delicate mathematical limits. However, its success amounts to the idea that the fluid system can in some sense be described by weakly interacting subsystems, where the behavior of a single subsystem can be described by weak coupling to a heat bath that embodies all of the other subsystems and all of the omitted effects. In the end ‘the proof of the pudding is in the eating’, and our justification is based on experimental observations.

Intimately related to the existence of subsystems is the question of which invariants to incorporate into a statistical mechanics treatment of fluids. One aim of the present chapter is to investigate this question. We investigate this question both theoretically and experimentally and come to the conclusion that quadratic invariants (energy and enstrophy) are most important. Our conclusion follows from the observation that these invariants possess the property of additivity.

The microscopic dynamics of conventional statistical mechanics is finite dimensional, but to describe macroscopic phenomena one takes the thermodynamic limit in which the number of degrees of freedom tends to infinity. However, the dynamics of a two-dimensional fluid is already infinite dimensional

and possesses an infinite number of invariants; so, in order to make progress with a statistical mechanics approach one must extract a finite-dimensional model, and such a model cannot conserve all of the invariants of the original fluid system. In calculations one may also take limits of this finite-dimensional model, but the results of these limits may depend upon which of the invariants are maintained. Additivity of macroscopic invariants and statistical independence of subsystems are crucial properties in conventional statistical mechanics [see e.g. [114]]. Because not all invariants of a system are additive, this property can be used to select invariants for statistical mechanics from the infinite number possessed by two-dimensional fluid systems.

Related to the choice of additive invariants is the choice of subsystems. This choice requires the identification of two scales, a macroscopic scale and a microscopic scale, which we call Δ and δ , respectively, and phase space cells of these characteristic sizes are considered. In classical statistical mechanics, the micro-cells usually refer to individual particles, while the macro-cells, the subsystems, are selected to be large enough to contain many particles yet small enough to have uniform invariants. We address in detail the choice of these cells for the fluid in §5.5, but it is clear that a macro-cell should contain many micro-cells, yet be small enough so that the vorticity and streamfunction are constant. This condition is sufficient for statistical independence, but the converse is not always true. In any event we seek to define macro-cells that are nearly statistically independent and consider only invariants that are additive over these cells.

A second aim of the present work is to propose the idea that temporal mean values of the streamfunction provide a natural coordinate system for describing inhomogeneous turbulence, a coordinate system that can be used

to define statistically independent subsystems. We suggest this idea because contours of the streamfunction for two-dimensional inviscid fluid flow tend to be smooth and because there tends to be a strong statistical dependence of vorticity or potential vorticity along those contours. Streamfunction contours are much smoother than vorticity contours because of the smoothing property of the inverse Laplacian. Therefore, there is a natural separation of length scales: the large scale associated with variation of the streamfunction contours and the fine scale that is needed to resolve the vorticity or potential vorticity. We take these to be our scales Δ and δ , respectively. We test this idea experimentally by measuring the independence of subsystems so defined. We then construct a theory based on this definition of subsystem together with the additivity of quadratic invariants, and compare its predictions with the measured vorticity probability density function.

5.1.2 Background

In a remarkable series of papers [35, 36, 37, 38, 39, 40, 41] [reprinted in [157]] Burgers appears to be the first researcher to apply statistical mechanics ideas to the description of fluid turbulence. Many basic ideas used by later researchers were introduced first by Burgers in these rarely cited papers. Burgers introduced both lattice and Fourier models and showed that such models satisfy Liouville's theorem when viscosity is neglected. He used a counting argument to derive an entropy expression and obtained a corresponding entropy maximization principle. He proposed a microscopic scale for describing turbulent motion during short intervals of time and defined macroscopic quantities by counting possible streamfunction realizations for sequences of time inter-

vals. His analysis is based on the Reynolds stress equation, and he obtained a probability distribution that can be used to calculate the mean value of the Reynolds stress.

Motivated by the work of Burgers, Onsager [161] took up the subject and considered a representation of the vorticity field in terms of a set of point vortices, zero-area vortices, of equal strength. Because this results in a finite-dimensional particle-like Hamiltonian system, Onsager could proceed to apply techniques of classical statistical mechanics. He gave arguments for the existence of negative temperatures and the occurrence of coherent structures in a confined region, which are often observed in nature. Related ideas have been further pursued by many researchers [e.g. [96, 131, 71, 233]] [see [72] for a recent review]. For example, Joyce et. al [96] studied the statistical mechanics of point vortices within a mean field approximation, and argued that in the negative temperature regime, large like-signed vortices are the most probable state.

T.D. Lee [117] projected three-dimensional fluid equations (including MHD) onto a Fourier basis and truncated to obtain a finite-dimensional system. Evidently unaware of the early work of Burgers [41], he again demonstrated that his truncated system satisfies a version of Liouville's theorem and was thus amenable to techniques of statistical mechanics. Later, Kraichnan considered two-dimensional fluids [107, 108, 111] and noted that out of the infinite number of invariants, two quadratic invariants, the so-called rugged invariants, remained invariants after truncation. They argued that these rugged invariants are the important ones, and obtained an equilibrium state, which is related to that obtained by minimum enstrophy arguments put forth by selective decay hypotheses [118, 132, 32]. Also, using Kolmogorov-like dimensional

arguments and the rugged invariants, Kraichnan argued for the existence of direct and inverse cascades for two-dimensional turbulence [107].

The two-dimensional Euler equation, like the Vlasov and other transport equations, can be viewed as mean field theory. Such equations are known to generate fine structure in the course of evolution. This led Lynden-Bell [124] to consider a coarse graining procedure coupled with the idea of preserving all of the infinity of invariants such theories possess. He applied his ideas in the context of stellar dynamics, but the ideas are akin to those used in treatments of the classical electron gas by generalizations of Debye-Hückle theory [e.g. [101]]. Later, such ideas were used in the fluid context by Robert and Miller [175, 176, 177, 138, 139], and again in the stellar dynamics context by Chavanis et. al [54]. In these theories a microscopic probability distribution represents a local description of the small-scale fluctuations of microscopic vortices. The streamfunction is assumed to be uniform on the microscopic scale, and an equilibrium state is obtained by maximizing the Boltzmann entropy of microstates, an entropy that is obtained by a counting argument first given by Lynden-Bell. This produces a most probable state.

More recently, the necessity of incorporating the infinite number of invariants in statistical mechanics theories has been brought into question, and theories based on finite-dimensional models with a fewer constraints have been developed. Majda et. al [126] have argued that including an infinite number of invariants provides no additional statistical information, and Turkington [220] has argued that previous theories have not properly handled the neglected small scale phenomena, and he has proposed a theory that uses inequality constraints associated with only the convex invariants. Our approach is perhaps most closely aligned to these works, but is distinguished by the fact

that the invariants chosen are explicitly based on the additivity argument, the choice of subsystems, and detailed experimental observation.

Natural phenomena in atmospheres and oceans have served as a motivation for the application of statistical mechanics to two-dimensional fluid flow [e.g. [187]]. Examples include zonal flows in planets, such as the jet stream and the polar night jet, and organized coherent vortices, such as the Great Red Spot of Jupiter [132, 198, 196, 127, 32]. Attempts have been made to explain such naturally occurring phenomena in terms of the coherent structures found to emerge in quasi-geostrophic and two-dimensional turbulence after long time evolution. With external small-scale forcing a few long-lived and large structures resulting from nonlinear merging processes are seen to be stable self-organized states that persist in a strongly turbulent environment [135, 31]. These structures have been studied over many years, often because of their relevance to large-scale geophysical and astrophysical flows [127]. In statistical mechanics, such steady states with large structures are envisioned to be the most probable state arising from some extremization principle. Various extremization principles [e.g. [118]] have been proposed with selected global invariants of the system used as constraints. Observations of turbulent flow with large coherent structures in a rotating annulus [196, 18, 19, 10, 98] have led us to reconsider statistical mechanics in the context of rapidly rotating systems.

5.1.3 Notation Organization

By necessity this chapter contains much notation. To aid the reader we give a brief summary here. As noted above, statistical mechanics deals

with two scales: the microscopic scale δ , characteristic of microscopic m -cells, and the macroscopic scale Δ , characteristic of macroscopic M -cells. Several averages are considered. The symbol $\langle \cdot \rangle_S$ denotes an average with probability density P_S , where choices for the subscript S will be used to delineate between different cases. The appropriate volume measure will be clear from context but is also revealed by the argument of P_S . Averages with uniform density are denoted by $\prec \cdot \succ_S$, where the subscript denotes the integration variable. An exception is the time average, which we denote by an overbar. Thus, the time average of a function is denoted by \bar{f} , and $\bar{f} = \int_0^T f dt / T = \prec f \succ_t$. The limits of integration for this kind of average will either be stated or will be clear from context. We denote the potential vorticity field by $q(x, y, t)$, by which we always mean a function. For the potential vorticity distribution on a M -cell (subsystem) we use ζ , an independent variable. Another source of possible confusion is that the symbol β is used for the energy Lagrange multiplier, as is conventional in statistical mechanics, while the beta-effect of geophysical fluid dynamics is embodied here in the symbol h .

The chapter is organized as follows. The experiment is described in §5.2 and equations that govern the dominant physics are reviewed in §5.3. In §5.4 we describe some basic ideas about statistical mechanics, as needed for the application to the fluid system of interest. In §5.5 we describe statistical mechanics in the mean field approximation and compare predictions with experiments. Here we show that predictions of the theory are in accordance with experiments. Finally, in §5.6 we conclude.

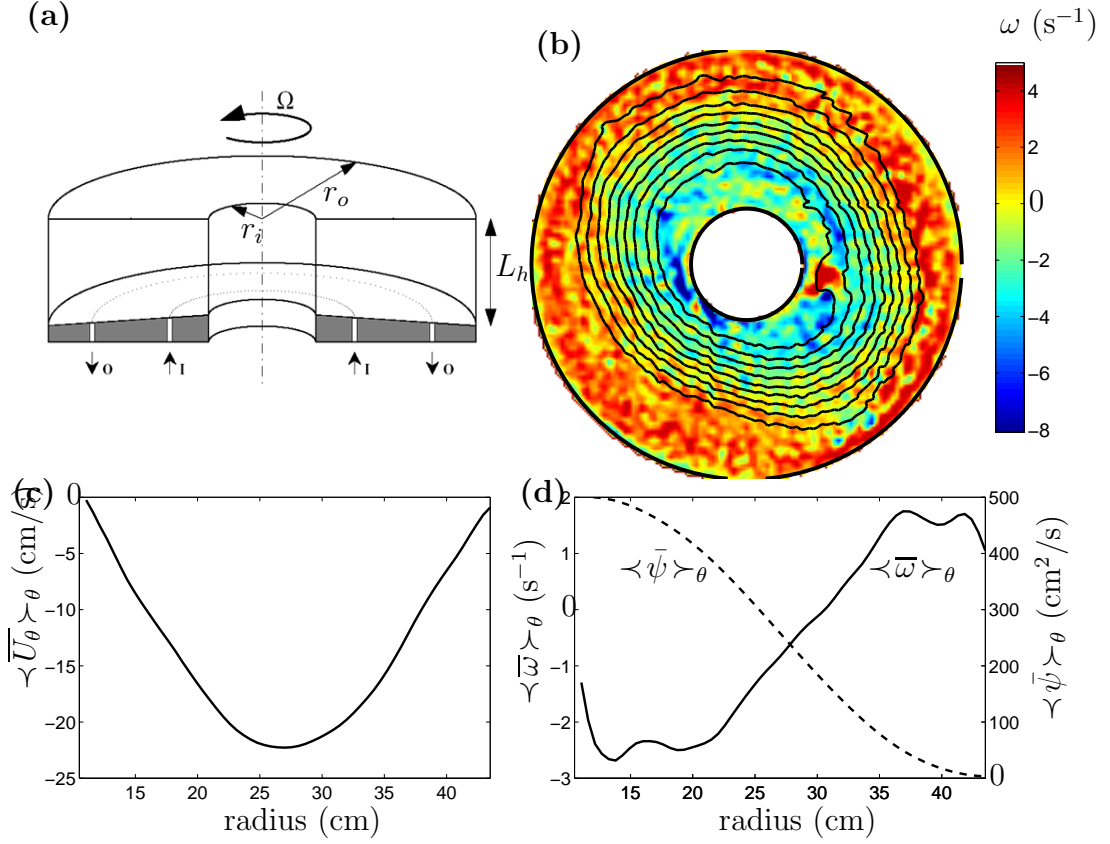


Figure 5.1: (a) Schematic diagram of the experimental apparatus. The tank rotates at 1.75 Hz. Flow is produced by pumping water through a ring of inlets (I) and outlets (O) in the bottom of the tank. The Coriolis force acts on the radially pumped fluid to produce a counter-rotating jet. (b) The vorticity field and contours of streamfunction at mid-height of the tank, determined from Particle Image Velocimetry measurements. The streamfunction contours are equally spaced in streamfunction value. (c) The azimuthal velocity averaged over both time and azimuthal angle, as a function of radial position. (d) The vorticity (solid line) and streamfunction (dashed line) averaged over time and azimuthal angle, as a function of radial position.

5.2 Experiment

The experiments are conducted in a rotating annulus (Fig. 5.1). The annulus has an inner radius $r_i = 10.8$ cm, outer radius $r_o = 43.2$ cm, a sloping bottom, and a flat transparent lid. The bottom depth varies from 17.1 cm at the inner radius to 20.3 cm at the outer radius, giving a bottom slope of $\eta = -0.1$. For the data analyzed in this chapter, the rotation frequency of the annulus is $\Omega/2\pi = 1.75$ Hz. An azimuthal jet is generated in the annulus by pumping water in a closed circuit through two concentric rings of holes at the bottom. Fluid is pumped into the annulus through an inner ring at $r = 18.9$ cm and extracted through an outer ring at $r = 35.1$ cm; both rings have 120 circular holes. Each hole has a diameter of 2.5 mm, and the total pumping rate is $150 \text{ cm}^3/\text{s}$. The action of the Coriolis force on the outward flux generates a counter-rotating azimuthal jet. A counter-rotating flow is generally more unstable than a co-rotating flow [198].

The water is seeded with neutrally buoyant particles (polystyrene spheres, diameter $150\text{--}200 \text{ }\mu\text{m}$). Light emitting diodes produce a 3 cm thick horizontal sheet of light that illuminates the annulus at mid-depth. The particles suspended in the water are imaged with a camera located 2 m above the annulus, and the camera rotates with the tank. Particle Image Velocimetry (PIV) is used to obtain the full two-dimensional velocity field [19].

The flow can be characterized by the Reynolds, Rossby, and Ekman numbers. The maximum velocity $U_{\text{max}} \approx 22 \text{ cm/s}$, the length $L = 16.2 \text{ cm}$ (taken to be the distance between the two forcing rings) and the kinematic viscosity $\nu = 0.01 \text{ cm}^2/\text{s}$ yield a Reynolds number $UL/\nu = 3.5 \times 10^4$, indicating that the flow is turbulent. The Rossby number (ratio of inertial to Coriolis

force) is $\omega_{rms}/2\Omega = 0.11$ (where ω_{rms} is the rms vorticity), which indicates that the Coriolis force is dominant, as is the case for planetary flows on large length scales. Finally, the small Ekman number, $\nu/2L^2\Omega = 3 \times 10^{-4}$, indicates that dissipation in the bulk is small. Use the other notation for the height. The Ekman time, $\tau_E = L_h/2(\nu\Omega)^{1/2}$ (where L_h is the mean fluid height) for dissipation in the boundary layers is 30 sec, a time much longer than the typical vortex turnover time, 2 sec. The dimensionless numbers indicate that the flow is quasi-geostrophic; previous studies of turbulence in the annulus have indeed confirmed the strong two-dimensionality of the flow [19].

5.3 Dynamics

The barotropic assumption is widely used to describe the flow inside the tank. The equation of motion for a barotropic fluid with topography is given by

$$\frac{\partial q}{\partial t} + \mathbf{v}_\perp \cdot \nabla_\perp q = D + F, \quad (5.1)$$

where $q = (-\nabla_\perp^2 \psi + 2\Omega)/L_h$ is the potential vorticity, L_h is the tank depth, ψ is the streamfunction, $\mathbf{v}_\perp = (\partial\psi/\partial y, -\partial\psi/\partial x)$, and D denotes dissipation, such as that due to molecular viscosity, $\nu\nabla_\perp^2 \omega$, or Ekman drag, $-\omega/\tau_E$, and F denotes a vorticity source due to the pumping. When $L_h = \langle L_h \rangle(1 - \eta r)$ where η is the bottom slope, the potential vorticity is approximated by

$$q = -\nabla_\perp^2 \psi + h, \quad (5.2)$$

where h accounts for the beta-effect and is here a linear function of radius, $h = 2\Omega\eta r/\langle L_h \rangle$. Over the years strong evidence has accumulated that (5.1) describes the dominant features of the experiment [198, 66, 137, 195].

For inviscid flow with zero Rossby number, there is no vertical variation in the velocity [178], and there is evidence that to leading order the drag and forcing terms cancel. We are primarily interested in the statistics of motions that occur on the vortex turnover time, and these are governed by the inviscid equation,

$$\frac{\partial q}{\partial t} + \mathbf{v}_\perp \cdot \nabla_\perp q = 0, \quad (5.3)$$

which is a Hamiltonian theory.

A manifestation of the Hamiltonian nature of two-dimensional Euler-like flows such as (5.3) is the finite-dimensional Hamiltonian description of point vortices provided by Kirchhoff [102], which played an essential motivating role in Onsager's theory [e.g. [72]]. For a distributed vorticity variable such as q the Hamiltonian form is infinite-dimensional and is given in terms of a noncanonical Poisson bracket as follows:

$$\frac{\partial q}{\partial t} = \{q, H\} = [\psi, q], \quad (5.4)$$

where the Hamiltonian $H[q] = \int \psi(q-h) dx dy / 2$, and the noncanonical Poisson bracket is given by

$$\{F, G\} = \int q \left[\frac{\delta F}{\delta q}, \frac{\delta G}{\delta q} \right] dx dy, \quad (5.5)$$

with F and G being functionals, $\delta F / \delta q$ the functional derivative, and $[f, g] = f_x g_y - f_y g_x$. Observe that $\mathbf{v}_\perp \cdot \nabla_\perp q = -[\psi, q]$. This Hamiltonian formulation of the two-dimensional Euler equation appeared in [144, 145], based on the identical structure for the Vlasov-Poisson system [143], and in [159]. A review of this and other formulations can be found in [146]. The infinite family of Casimir invariants $C[q] = \int \mathcal{C}(q) dx dy$, where \mathcal{C} is arbitrary, satisfies $\{F, C\} = 0$ for all functionals F , and is thus conserved by (5.3). The presence of these

invariants is one way that the statistical mechanics of fluids differs from that of particle systems.

5.4 Statistical Mechanics and Fluid Mechanics

As noted in §5.1 many attempts have been made to apply statistical mechanics to fluids and other infinite-dimensional systems. In this section we introduce our notations and discuss some basic ideas.

5.4.1 State Variables

In classical statistical mechanics the microscopic dynamics is governed by Hamilton's equations and the phase space is the $2N$ dimensional manifold with canonical coordinates (Q_α, P_α) , $\alpha = 1, 2, \dots, N$, where (Q_1, \dots, Q_N) is the configuration coordinate and (P_1, \dots, P_N) is the corresponding canonical momentum. Typically N , the number of degrees of freedom, is a very large number $\sim 10^{23}$. We call this $2N$ dimensional phase space Γ , a standard notation introduced by P. and T. Ehrenfest [68]. Our fluid is assumed to be governed by (5.3), an infinite-dimensional Hamiltonian theory, and thus the instantaneous state of our system is determined by the vorticity-like variable $q(x, y)$, which we suppose is contained in some space of functions \mathcal{G} . The index α for coordinates of Γ is analogous to the Eulerian position (x, y) , a point in the physical domain occupied by the fluid, which is viewed as an index for \mathcal{G} .

In conventional statistical mechanics, the microscopic dynamics is finite dimensional, and one attempts to explain phenomena on the macroscopic level

by considering the thermodynamic limit in which $N \rightarrow \infty$. However, for a fluid, the dynamics is already infinite dimensional, and thus as noted in §5.1, to apply statistical mechanics researchers have introduced various finite-dimensional discretizations. Onsager's description of the continuum vortex dynamics in terms of a collection of point vortices amounts to the specification of the coordinates of the manifold analogous to Γ as the spatial positions of the point vortices, $(x_1, \dots, x_N, y_1, \dots, y_N)$ [161]. Alternatively, Lee's representation of a three-dimensional fluid in terms of a truncated Fourier series has the Fourier amplitudes being coordinates of a space analogous to Γ [117]. This procedure was carried over to two dimensions by Kraichnan and Montgomery [111]. For our potential vorticity variable the Fourier amplitudes are given by $q_{\mathbf{k}} = \int \exp i(k_x x + k_y y) q(x, y) dx dy$, where $\mathbf{k} = (k_x, k_y)$. Another alternative is to replace the continuum vorticity by a lattice model [e.g. [35, 175, 176, 177, 138, 139, 126, 220]], i.e., an expansion in terms of tent functions or finite elements of scale size δ . In the present context the vorticity is replaced by its values on the lattice, $q_i = \int K_i(x, y; x_i, y_i) q(x, y) dx dy$, where the kernel K_i is typically chosen to represent a square lattice with a finite number N of sites located at (x_i, y_i) . In general $N = N_x N_y$, where N_x and N_y are the number of lattice points in the x and y directions, respectively. We will refer to this discretization as a division into m -cells.

Given a finite-dimensional system one can make various assumptions, e.g., the probabilistic assumptions of 'molecular chaos', but this requires a notion of phase space volume conservation.

5.4.2 Phase Space Volume and Liouville's Theorem

In classical statistical mechanics one calculates averages over the manifold Γ , and the natural volume element is given by $\prod_{\alpha=1}^N dQ_\alpha dP_\alpha$. However, for \mathcal{G} the situation is not so straightforward, and so we explore candidates for the analogous volume element.

Volume Element

The calculation of averages in a statistical theory requires a phase space measure, $\mathcal{D}q$, which is a sort of volume element for \mathcal{G} . The volume element can be interpreted as a probability measure defined on functions that take values between q and $q + dq$. Averages calculated using the probability measure are functional integrals akin to those used in Feynman's path integral formulation of quantum mechanics and in field theory [e.g. [188, 202]]. The various discretizations introduced above have been employed to give meaning to functional integrals, but the Fourier and lattice models are most common.

For the Fourier discretization, Kraichnan and Montgomery used the volume element $\mathcal{D}q = \prod_{\mathbf{k}} dq_{\mathbf{k}}$, where the product is truncated at some maximum wave number. Alternatively, the volume element for lattice models is written as $\mathcal{D}q = \prod_i^N dq_i$, where dq_i is a volume element associated with the potential vorticity varying from q to $q + dq$ in a lattice partition (x_i, y_i) , and $N = N_x N_y$ is as above the number of lattice sites, which have a scale δ . Here, a total volume element $\mathcal{D}q$ is a product of volume elements of each lattice site dq_i . In the case of a finite small lattice, dq_i becomes an one-dimensional volume, i.e., $dq_i = q(x_i, y_i) + dq(x_i, y_i) - q(x_i, y_i)$ at the lattice point (x_i, y_i) of the physical two-dimensional space. In order for a notion of measure based on

phase space volume to be useful, the volume must be preserved in the course of time.

Liouville's Theorem

Preservation of phase space volume is assured by Liouville's theorem, an important theorem of mechanics. As noted above, Burgers and Lee showed that a version of Liouville's theorem applies to the system governing the Fourier amplitudes for the inviscid fluid. For vorticity dynamics the amplitudes satisfy

$$\dot{q}_{\mathbf{k}} = \sum_{\mathbf{l}, \mathbf{m}} \frac{\epsilon_{\mathbf{k}\mathbf{l}\mathbf{m}}}{|\mathbf{l}|^2} (q_{\mathbf{l}} - h_{\mathbf{l}}) q_{\mathbf{m}}, \quad (5.6)$$

where $h_{\mathbf{l}}$ is the fourier transformation of the beta effect and $\epsilon_{\mathbf{k}\mathbf{l}\mathbf{m}} = \hat{\mathbf{z}} \cdot (\mathbf{l} \times \mathbf{m}) \delta(\mathbf{k} + \mathbf{l} + \mathbf{m})$ is completely antisymmetric, i.e., $\epsilon_{\mathbf{k}\mathbf{l}\mathbf{m}} = -\epsilon_{\mathbf{l}\mathbf{k}\mathbf{m}} = -\epsilon_{\mathbf{m}\mathbf{l}\mathbf{k}}$ and $\epsilon_{\mathbf{k}\mathbf{k}\mathbf{m}} = \epsilon_{\mathbf{k}\mathbf{l}\mathbf{k}} = 0$. Therefore, antisymmetry directly implies Liouville's theorem, $\sum_{\mathbf{k}} \partial \dot{q}_{\mathbf{k}} / \partial q_{\mathbf{k}} \equiv 0$.

Similarly, we have shown directly that the lattice model possesses a version of Liouville's theorem, which we recently discovered was anticipated in [36]. This result was also inferred in [220]. We assume periodic boundary conditions. The lattice model discretization can be viewed as an expansion of the vorticity in terms of a tent function basis [e.g. [74]].

The technique for the lattice model discretization is widely used in Finite Element Methods(FEM). FEM assumes that the solution of a partial differential equation can be expressed by approximating functions. In this case, the original function q is approximated by discrete values on periodic lattice sites. The potential vorticity function is written as

$$q(\mathbf{x}) = \sum_i K(\mathbf{x}, \mathbf{x}_i) q(\mathbf{x}_i) \quad (5.7)$$

where $K(\mathbf{x}, \mathbf{x}_i)$ is a symmetric function at the center of \mathbf{x}_i (In other words, $K(\mathbf{x}, \mathbf{x}_i) = K(|\mathbf{x} - \mathbf{x}_i|)$). For example, the *Tent function* is often used in a finite element method. We denote that a potential vorticity at lattice sites $q(x_i) =: q_i$ and a function $K(\mathbf{x} - \mathbf{x}_i) =: K_i$. We assume that lattice sites are separated by equal distance Δx .

The discrete stream function on the lattice sites $\psi_i = M_{ij}(q_j - h_j)$ where M is a discrete matrix of Laplacian, with imposed periodic boundary conditions that have a symmetric property $M = M^T$. The derivative of a function q with respect to space x can be approximated as

$$\partial_x q(x) = \sum_i K_i N_{ij}^{(x)} q_j. \quad (5.8)$$

where $N_{ij}^{(x)}$ is defined as the differential operator along the x -direction in a finite-dimensional function which has an antisymmetric property as $N^{(x)} = -(N^{(x)})^T$.

Plugging Eq. (5.8) and (5.7) into Eq. (5.4), one gets

$$\sum_i K_i \dot{q}_i + \sum_{\mu\nu} \sum_{jk} K_j K_k [N_{j\mu}^{(x)} N_{k\nu}^{(y)} - N_{j\mu}^{(y)} N_{k\nu}^{(x)}] \psi_\mu q_\nu = 0. \quad (5.9)$$

If we multiply the above equation by K_s and integrate it over \mathbf{x} , one gets

$$\begin{aligned} \sum_i \mathcal{Z}_{si} \dot{q}_i &= - \sum_{\mu\nu} \sum_{jk} \mathcal{G}_{sjk} [N_{j\mu}^{(x)} N_{k\nu}^{(y)} - N_{j\mu}^{(y)} N_{k\nu}^{(x)}] \psi_\mu q_\nu \\ \Rightarrow \dot{q}_i &= - \sum_{\mu\nu} \sum_s \sum_{jk} \mathcal{Z}_{is}^{-1} \mathcal{G}_{sjk} [N_{j\mu}^{(x)} N_{k\nu}^{(y)} - N_{j\mu}^{(y)} N_{k\nu}^{(x)}] \psi_\mu q_\nu \\ \dot{q}_i &= \sum_{\mu\nu} B_{i\mu\nu} \psi_\mu q_\nu \end{aligned} \quad (5.10)$$

where a symmetric \mathcal{Z}_{ij} is defined as $\int K(\mathbf{x} - \mathbf{x}_i) K(\mathbf{x} - \mathbf{x}_j) d\mathbf{x}$ and a symmetric \mathcal{G}_{ijk} , the third order correlation, is defined as $\int K(\mathbf{x} - \mathbf{x}_i) K(\mathbf{x} - \mathbf{x}_j) K(\mathbf{x} - \mathbf{x}_k) d\mathbf{x}$.

The matrix which represents the nonlinear interaction in Eq. (5.10) can be expressed as

$$B_{i\mu\nu} := S_{ijk} A_{j\mu} A_{k\nu} , \quad (5.11)$$

composed of one symmetric tensor S_{ijk} (originated from $\mathcal{Z}_{is}^{-1} \mathcal{G}_{sjk}$) and two antisymmetric tensors $A_{j\mu}$ and $A_{k\nu}$ (originated from $N_{j\mu}^{(x)} N_{k\nu}^{(y)} - N_{j\mu}^{(y)} N_{k\nu}^{(x)}$). One remark is that each matrix is defined in periodic lattice sites. For readers who are not familiar with matrices, we will start some definitions and properties of matrices with periodic boundaries.

A *symmetric matrix* is a square matrix that satisfies

$$A^T = A \quad (5.12)$$

where A^T denotes the transpose of matrix, so $a_{ij} = a_{ji}$. Similarly, an *anti-symmetric matrix* (is also often called as *skew symmetric matrix*) is a square matrix that satisfies the identity

$$A^T = -A . \quad (5.13)$$

With imposing the periodic boundary conditions, a symmetric square matrix ($N \times N$) with the same diagonals is defined as

$$S_{ij} = f(|i - j|) , \quad (5.14)$$

and an antisymmetric square matrix is

$$A_{ij} = \text{sgn}(i - j) g(|i - j|) . \quad (5.15)$$

From the above definitions, other properties can be obtained as

$$\begin{aligned} S_{i,i+n} &= S_{i-n,i} = S_{k-n,k} \\ A_{i,i+n} &= -A_{i+n,i} = A_{i-n,i} = A_{k-n,k} \end{aligned} \quad (5.16)$$

By using above properties, the multiplication of symmetric and antisymmetric matrices is

$$\begin{aligned}
(S \cdot A)_{i,k} &= \sum_{n=0}^{N-1} S_{i,i+n} A_{k+(i+n-k),k} \\
&= \sum_{n=0}^{N-1} A_{i,i-(i+n-k)} S_{k-n,k} = (A \cdot S)_{i,k}.
\end{aligned} \tag{5.17}$$

It implies that any symmetric and antisymmetric matrices with properties Eq. (5.16) commute. Therefore, the multiplication of symmetric and antisymmetric matrices with periodic boundary conditions is antisymmetric. Next, we will give a simple example to show the above properties.

For example, the differential operator (5×5) with periodic boundary conditions is written as

$$\begin{bmatrix} 0 & -1 & 0 & 0 & 1 \\ 1 & 0 & -1 & 0 & 0 \\ 0 & 1 & 0 & -1 & 0 \\ 0 & 0 & 1 & 0 & -1 \\ -1 & 0 & 0 & 1 & 0 \end{bmatrix}. \tag{5.18}$$

Those symmetric and anitsymmetric matrices with the periodic boundary conditions have special properties. For example, the multiplication of symmetric (S) and antisymmetric (A) matrices commute.

$$S \cdot A = \begin{bmatrix} 2 & 1 & 0 & 0 & 1 \\ 1 & 2 & 1 & 0 & 0 \\ 0 & 1 & 2 & 1 & 0 \\ 0 & 0 & 1 & 2 & 1 \\ 1 & 0 & 0 & 1 & 2 \end{bmatrix} \cdot \begin{bmatrix} 0 & -1 & 0 & 0 & 1 \\ 1 & 0 & -1 & 0 & 0 \\ 0 & 1 & 0 & -1 & 0 \\ 0 & 0 & 1 & 0 & -1 \\ -1 & 0 & 0 & 1 & 0 \end{bmatrix} \tag{5.19}$$

$$\begin{aligned}
&= \begin{bmatrix} 0 & -2 & -1 & 1 & 2 \\ 2 & 0 & -2 & -1 & 1 \\ 1 & 2 & 0 & -2 & -1 \\ -1 & 1 & 2 & 0 & -2 \\ -2 & -1 & 1 & 2 & 0 \end{bmatrix} \\
&= \begin{bmatrix} 0 & -1 & 0 & 0 & 1 \\ 1 & 0 & -1 & 0 & 0 \\ 0 & 1 & 0 & -1 & 0 \\ 0 & 0 & 1 & 0 & -1 \\ -1 & 0 & 0 & 1 & 0 \end{bmatrix} \cdot \begin{bmatrix} 2 & 1 & 0 & 0 & 1 \\ 1 & 2 & 1 & 0 & 0 \\ 0 & 1 & 2 & 1 & 0 \\ 0 & 0 & 1 & 2 & 1 \\ 1 & 0 & 0 & 1 & 2 \end{bmatrix} = A \cdot S. \quad (5.20)
\end{aligned}$$

Furthermore, the multiplication of symmetric and antisymmetric matrices with periodic boundary conditions is also antisymmetric.

$$(S \cdot A)^T = A^T \cdot S^T = -(A \cdot S) = -(S \cdot A). \quad (5.21)$$

Let's go back to Eq. (5.11). A product of symmetric S_{ijk} and antisymmetric matrices $A_{j\mu}$ is also antisymmetric for the first two indices (i, μ) since Eq. (5.21) is true. So, this tensor has antisymmetric property as $B_{(i\mu)\nu} := \frac{1}{2}(B_{i\mu\nu} + B_{\mu i\nu}) = 0$. Also, $B_{i\mu\nu} = B_{i\nu\mu}$ since $B_{i\mu\nu} := S_{ijk}A_{j\mu}A_{k\nu} = S_{ikj}A_{k\nu}A_{j\mu}$ is symmetric under an exchange of μ and ν . Therefore, it has a symmetric property as $B_{i[\mu\nu]} := \frac{1}{2}(B_{i\mu\nu} - B_{i\nu\mu}) = 0$. In short, the first two indices and the first and third indices are antisymmetric and the latter two indices are symmetric. $B_{\nu\mu\nu} = B_{\mu\mu\nu} = 0$ since $S_{i\mu\nu}A_{\mu\nu} = 0$ where S and A are respectively symmetric and antisymmetric tensors.

Finally, the quantity B_{ijk} is easily seen to be completely antisymmetric, i.e., $B_{ijk} = -B_{jik} = -B_{kji}$ and $B_{iji} = B_{iik} = 0$, just as was the case for $\epsilon_{\mathbf{k}\mathbf{l}\mathbf{m}}$.

Therefore, Liouville's theorem follows,

$$\sum_i \frac{\partial \dot{q}_i}{\partial q_i} = \sum_{i,j,k} B_{ijk} (M_{ji} q_k + \delta_{ki} \psi_j) = \sum_{i,j} (B'_{ii} q_j + B_{iji} \psi_j) = 0, \quad (5.22)$$

where each term of the last sum vanishes. Here the matrix M represents the inverse Laplacian and B' is another matrix that has the same antisymmetry property as B .

Invariants

In a finite-dimensional lattice model, we can show that rugged invariants are globally conserved and higher-order invariants are not. By multiplying q_i into Eq. (5.10) and using properties of $B_{i\mu\nu}$, one gets

$$\frac{1}{2} \frac{dq_i^2}{dt} = \sum_i q_i \dot{q}_i = \sum_{i\mu\nu} B_{i\mu\nu} q_i \psi_\mu q_\nu = 0 \quad (5.23)$$

The last equality holds from an antisymmetric property of the first two indices $B_{i\mu\nu}$. Therefore, the quadratic term such as $\sum_i q_i^2$ is constant. However, the higher order terms such as $\sum_i q_i^3$ are not globally conserved since $\frac{1}{3} d(\sum q_i^3 + \sum q_\mu^3)/dt = \sum B_{i\mu\nu} q_i^2 q_\mu q_\nu + \sum B_{\mu i\nu} q_i q_\mu^2 q_\nu = \sum B_{i\mu\nu} q_i q_\mu q_\nu (q_i - q_\mu) \neq 0$. That is why the quadratic term is so special in a discretized function space. It shows that the circulation ($\sum_i q_i$) and enstrophy ($\sum_i q_i^2$) are conserved in a discretized function space and higher-order invariants are not. Later, statistical independence argument confirms the importance of quadratic invariants out of infinitely many invariants.

5.4.3 Canonical Equilibrium Distribution

Having defined phase space and verified Liouville's theorem, we are poised to write a partition function and to define phase space averages. The

natural expression for the partition function associated with the canonical (Gibbs) ensemble is

$$\mathcal{Z}_c = \int_{\mathcal{G}} e^{-\beta H[q] - C[q]} \mathcal{D}q, \quad (5.24)$$

where H is the Hamiltonian of §5.3 and C denotes the infinite family of Casimir invariants. Averages corresponding to (5.24) are given by

$$\langle F \rangle_c = \int_{\mathcal{G}} F[q] P_c[q; \beta, \mathcal{C}] \mathcal{D}q, \quad (5.25)$$

where F is a functional of q and the phase space probability density is given by

$$P_c[q; \beta, \mathcal{C}] = \mathcal{Z}_c^{-1} e^{-\beta H[q] - C[q]}. \quad (5.26)$$

Expressions (5.24) and (5.25) are functional integrals [188, 202], and the intent is to give them meaning by discretizing as in §§5.4.1 and then taking the limit $N \rightarrow \infty$ and $\delta \rightarrow 0$. Finding unique well-defined results with this procedure for such integrals, with other than quadratic functionals in the exponent, is usually a difficult task. Consequently, a mean field approach has been taken, which we turn to in §5.5.

An alternative to the direct evaluation of (5.25) is to appeal to the fact that the dynamics of (5.3) is an area preserving *rearrangement* [e.g. [121]]. This means for an initial condition q_0 , the solution at time t is given formally by $q(x, y, t) = q_0(x_0(x, y, t), y_0(x, y, t))$, where $(x_0(x, y, t), y_0(x, y, t))$ are the initial conditions of the characteristics, which satisfy $\partial(x_0, y_0)/\partial(x, y) = 1$. The Casimir invariants are associated with relabelling symmetry [e.g. [185, 162]] and possess the same value when evaluated on functions that are related by rearrangement. Thus if one restricts the domain of integration \mathcal{G} to be rearrangements of a given function, denoted by $\mathcal{G}_{\mathcal{R}}$, then we should obtain the same answer because $\langle F[q] \rangle_{\mathcal{R}} = F[q]$ for functionals with integrands that

depend only on q , such as Casimirs and $\exp(C[q])$. Here $\langle \rangle_{\mathcal{R}}$ is defined with $P_{\mathcal{R}}[q; \beta] = \mathcal{Z}_{\mathcal{R}}^{-1} \exp(-\beta H[q])$ and $\mathcal{Z}_{\mathcal{R}} = \int_{\mathcal{G}_{\mathcal{R}}} \exp(-\beta H[q]) \mathcal{D}q$.

5.5 Mean Field Approximation and Statistical Independence

It is well-known that vorticity equations like (5.3), the Vlasov equation, and other transport equations develop fine structure in the course of time. Because of this Lynden-Bell [124] proposed a coarse graining procedure to obtain a most probable state. He divided phase space up into hyper-fine cells that are assumed to be capable of resolving the fine structure. These are the m -cells referred to in §§5.4.1, which have a scale size δ . Experimentally δ is determined by the resolution, but in ideal theory the fine structure can become arbitrarily fine and so a limiting procedure is required. In addition Lynden-Bell [124] proposed larger cells, which we have called M -cells, that characterize a macroscopic scale Δ . The M -cells contain many m -cells that can be freely exchanged within an M -cell without changing any macroscopic quantity. Thus one is able to count states and obtain an expression for a coarse grained or mean field entropy that can be maximized subject to constraints. Later, Miller [138] and Robert [176] reconstructed and improved this formulation. Miller defined m -cells and M -cells based on scales with the property that the energy averaged over M -cells approximates the energy averaged over m -cells. However, we argue that the most important condition for separating the M -cell and m -cell scale lengths is *statistical independence*, which assures near independence of the probability densities of M -cells, which are viewed as

subsystems, and is associated with near additivity of the constraints. These are crucial properties.

Experimentally the two scales can be demonstrated as in Fig. 5.2. Observe in the upper plot of this figure the fine scale structure in the potential vorticity, while in the lower plot the streamfunction, due to the integration over the Green's function, is considerably smoother. We take the upper scale to be δ and the lower scale to be Δ .

5.5.1 Counting States

According to Lynden-Bell's statistics, the number of ways to distribute m -cells into M -cells is

$$W = \prod_r \frac{N_r!}{\prod_I N_r^{(I)}!} \prod_I \frac{N^{(I)}!}{\left(N^{(I)} - \sum_r N_r^{(I)}\right)!} \quad (5.27)$$

where N_r is the total number of m -cells with the r th value of potential vorticity in the whole space, and $N_r^{(I)}$ is the total number of m -cells with the r th value of potential vorticity in the I th M -cell. Also, $N^{(I)}$ is the total number of m -cells in the I th M -cell. The first product in Eq. (5.27) represents the number of ways to distribute N_r m -cells into groups of $\{N_r^{(I)}\}$, where I counts all M -cells and the second product is the number of ways to distribute inside an M -cell. Also, $N^{(I)} - \sum_r N_r^{(I)}$ can be understood as the number of empty m -cells. Lynden-Bell proposed this manner of counting for stellar dynamics [124, 54], where m -cells represent stars, which are considered to be distinguishable, and there may be empty m -cells. However, the statistics for the two-dimensional continuum Euler model is a special case of Lynden-Bell's general counting procedure.

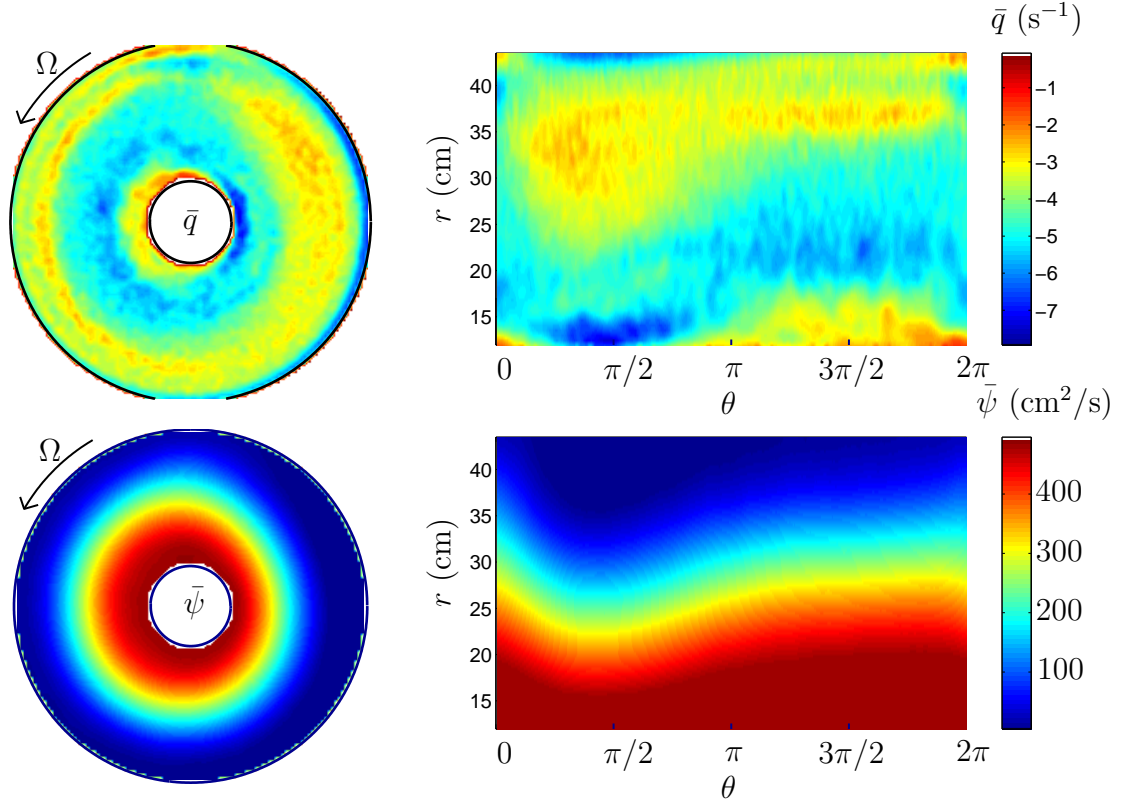


Figure 5.2: The time-averaged potential vorticity (top two figures) and the streamfunction (bottom two figures) in the Rossby wave frame. The figures on the left show the fields in the rotating tank; the figures on the right show the same fields unwrapped. The streamfunction field is smoother than the potential vorticity field since the vorticity is given by a second derivative (the Laplacian) of the streamfunction. Hence the characteristic length scale in the azimuthal direction is larger for the streamfunction than for the potential vorticity.

In Miller's application to the two-dimensional continuum Euler model, he assumes that all m -cells are occupied by a vortex and these vortices are indistinguishable if they have the same value of vorticity. Because there are no empty m -cells, $N^{(I)} = \sum_r N_r^{(I)}$ and because the m -cells are indistinguishable a factor of $\prod_r 1/(N_r!)$ is added. This counting produces

$$W = \prod_I \frac{N^{(I)}!}{\prod_r N_r^{(I)}!}. \quad (5.28)$$

The above equation already involves statistical independence among different M -cells.

Boltzmann articulated the entropy as a measure of the number of possible configurations of the system. Therefore, the entropy S is defined to be the logarithm of the total number of configurations, $\ln W$. If $N_r^{(I)}$ is large, Stirling's formula gives

$$S = \ln W \cong - \sum_{r,I} (N_r^{(I)}) \ln \left(\frac{N_r^{(I)}}{N^{(I)}} \right). \quad (5.29)$$

In the continuum limit of potential vorticity levels, $N_r^{(I)}/N^{(I)}$ is replaced by $P_M(\zeta; x, y)$, and $\sum_{r,I}$ by $\int d\zeta dx dy$. In short, the index I represents the coordinates for the discretized M -cells and the index r represents the ordered level sets of potential vorticity inside the M -cells. Thus, it is replaced by the continuum vorticity variable ζ , the vorticity on an M -cell. With these observations, the resulting total mean field entropy is seen to be

$$S_M[P_M] = - \int P_M(\zeta; x, y) \ln P_M(\zeta; x, y) d\zeta dx dy = - \int \langle \ln P_M \rangle_M dx dy \quad (5.30)$$

where $P_M(\zeta; x, y)$ is the probability density in the mean field approximation. The density of $P_M(\zeta; x, y)$ is centered at the point (x, y) and satisfies the

normalization $\int P_M d\zeta = 1$. The integration over $dx dy$ can be viewed as a sum over the M -cells that cover the domain of the fluid. The second equality of (5.30) follows from the definition $\langle A \rangle_M = \int A P_M d\zeta$, and thus $S_M[P_M]$ can be naturally termed the (mean field) Boltzmann-Gibbs entropy.

In closing this subsection, we reiterate that the potential vorticity variable q is a field variable, a function of coordinates. However, when we introduced the probability density P_M on M -cells, we used ζ , an independent variable, to represent the values of the potential vorticity on an M -cell.

5.5.2 Mean Field Canonical Distribution

Given the mean field entropy S_M we can proceed to obtain the mean field density $P_M(\zeta; x, y)$ as the most probable state by extremization subject to particular mean field constraints. These constraints and their corresponding Langrange multipliers are given as follows:

1. The *Hamiltonian constraint* is obtained by replacing the vorticity variable q in $H[q]$ with its mean field average, to obtain a mean field energy,

$$\begin{aligned} H_M[P_M] &= \frac{1}{2} \int (\zeta P_M(\zeta; x, y) - h) \zeta' P_M(\zeta'; x', y') G(x, y; x', y') d\zeta dx dy d\zeta' dx' dy' \\ &= \frac{1}{2} \int \langle \psi \rangle_M (\langle \zeta \rangle_M - h) dx dy \end{aligned} \quad (5.31)$$

where $\langle \zeta \rangle_M = \int \zeta P_M d\zeta$ and $\langle \psi \rangle_M$ is defined by

$$\langle \zeta \rangle_M = -\nabla^2 \langle \psi \rangle_M + h. \quad (5.32)$$

The Lagrange multiplier associated with this constraint is taken to be the constant value, $-\beta$, where the minus sign is by convention.

2. The *normalization constraint* is $\int P_M d\zeta = 1$. This is a normalization on each M -cell; thus, although P_M depends on position, the integration does not. Because this is a constraint for each point (x, y) , the Lagrange multiplier in this case depends on position. We call it $\gamma(x, y)$, and the quantity that appears in the variational principle is

$$N_M[P_M] = \int \gamma(x, y) P_M(\zeta; x, y) d\zeta dx dy. \quad (5.33)$$

3. The *mean field Casimir constraint*, roughly speaking, contains the information that on average, the area between any two contours of vorticity remains constant in time. More precisely, the quantity $g(\zeta) = \int P_M dx dy$ is taken to be constant. Because this is true for all ζ , the Lagrange multiplier μ is likewise a function of ζ and the constraint can be written as

$$C_M[P_M] = -\beta \int \mu(\zeta) g(\zeta) d\zeta = -\beta \int \mu(\zeta) P_M(\zeta; x, y) d\zeta dx dy, \quad (5.34)$$

where the prefactor of $-\beta$ is again by convention. This constraint is the mean field version of the family of Casimir invariants $C[q]$.

Now we are in position to obtain the most probable state by extremizing the quantity $F_M = S_M - \beta H_M + N_M + C_M$, i.e. upon functional differentiation with respect to P_M , $\delta F_M / \delta P_M = 0$ implies

$$P_M(\zeta; x, y; \beta, \mu) = \mathcal{Z}_M^{-1} e^{-\beta[\zeta \langle \psi \rangle_M - \mu(\zeta)]}, \quad (5.35)$$

where $\mathcal{Z}_M = \int e^{-\beta[\zeta \langle \psi \rangle_M - \mu(\zeta)]} d\zeta$ and evidently P_M is normalized. Equation (5.35) is the mean field counterpart to (5.26) and could aptly be termed the canonical (Gibbs) mean field distribution. The above variational principle and extremal distribution (5.35) appeared in essence in an appendix of [124].

Given (5.35) we are in a position to calculate $\langle \zeta \rangle_M$ and then substitute the result into (5.32). This gives the mean field Poisson equation,

$$\nabla^2 \langle \psi \rangle_M = \mathcal{Z}_M^{-1} \int \zeta e^{-\beta[\zeta \langle \psi \rangle_M - \mu(\zeta)]} d\zeta + h. \quad (5.36)$$

Versions of this equation have been solved in various references [e.g. [176, 138, 126]], but we will not do this here.

We conclude this subsection by giving a heuristic connection between $\langle \rangle_M$, a prescription for averaging functions, and $\langle \rangle_c$, a prescription for averaging functionals. Consider the functional $q(x', y')$, by which we mean the evaluation of the function q at the point (x', y') , and evaluate

$$\langle q(x', y') \rangle_c = \int_{\mathcal{G}} q(x', y') P_c[q; \beta, \mathcal{C}] \mathcal{D}q. \quad (5.37)$$

If we rewrite (5.37) as an integral on M -cells, where $q(x', y')$ is $q_{I'}$, write $\mathcal{D}q = \prod_J dq_J$, and then assume statistical independence of M -cells, $P_c = \prod_I P_I$, we obtain

$$\langle q(x', y') \rangle_c = \int q_{I'} \prod_I P_I \prod_J dq_J = \int q_{I'} P_{I'} dq_{I'} = \int \zeta P_M d\zeta = \langle \zeta \rangle_M. \quad (5.38)$$

This derivation emphasizes the need for near statistical independence of M -cell subsystems.

5.5.3 Ruggedness and Additivity

Classical statistical mechanical treatments of the canonical ensemble allow for subsystems to interact and exchange energy, but their interaction is assumed to be weak and the details of the interaction are usually ignored in calculations. Neglect of the interaction energy results in the energy being

equal to the sum of the energies of the individual subsystems, i.e., the energy is an additive quantity. In conventional treatments only additive invariants are used in calculating the most probable distributions, and in some treatments [e.g. [114]] this requirement is explicitly stated. The reason for this is that additive invariants give rise to statistical independence of subsystems. In our treatment of fluids, subsystems are M -cells and so we consider invariants that are additive over these regions. There is a close connection between ruggedness of invariants and the property of additivity. We show that only the rugged invariants are additive, and thus they characterize the statistical properties of M -cells. In §§5.5.4 and §§5.5.5 we will see that experimental results support this reasoning.

Kraichnan [111] Fourier transformed and truncated to obtain a finite-dimensional system. They argued that the truncated remnants of the total vorticity, enstrophy, and energy are the only invariants to be used in a statistical mechanics treatment because these invariants are rugged, i.e. they remain invariants of the truncated system. They also appear to be aware that these invariants possess the property of additivity, but they do not emphasize this point. Although Turkington [220] has argued that this kind of truncation does not properly handle small scale behavior, we find that this theory does a fairly good job at predicting the energy spectrum, but we will report on this elsewhere. We argue in general that such invariants are important because they are the only additive invariants. Below we consider a somewhat more general setting.

Because of Parseval's identity, the quadratic invariants are additive and higher order invariants are not. To see this, suppose we define M -cells to be composed of amplitudes of some subsets of Fourier modes, which we denote

by κ_I . Then a sum over modes can be done in groupings, i.e. $\sum_{\mathbf{k}} = \sum_I \sum_{\kappa_I}$. (This is the idea behind spectral reduction [33], a computational method where groupings of Fourier modes (bins) are described by a single representative.) For the quadratic Casimir invariant, the enstrophy, we have

$$C_2 = \int q^2 dxdy = (2\pi)^2 \sum_{\mathbf{k}} |q_{\mathbf{k}}|^2, \quad (5.39)$$

and defining an M -cell enstrophy by $C_2^{(I)} = (2\pi)^2 \sum_{\kappa_I} |q_{\mathbf{k}}|^2$, we obtain $C_2 = \sum_I C_2^{(I)}$. Similarly, the energy can be written as a sum over M -cell energies, $E = \sum_I E^{(I)}$. The linear Casimir invariant $C_1 = \int q dxdy$ merely reduces to the zeroth Fourier coefficient, and is thus in a trivial sense additive. Higher order invariants, $C_n = \int q^n dxdy$ for $n > 2$, have Fourier representations that are not reducible to expressions in terms of a single sum over M -cells.

The discretized lattice model has properties similar to those described above. The quadratic Casimir invariant and energy reduce to sums over a finite number of m -cell lattice variables, q_i , h_i and ψ_i , which are potential vorticity, height and streamfunction represented in terms of the kernel function K_i of §§5.4 as follows:

$$\begin{aligned} C_2 &= \int q^2 dxdy = \sum_{i,j} \int K_i K_j q_i q_j dxdy = \sum_{i,j} q_i Z_{ij} q_j, \\ H &= \frac{1}{2} \int q \psi dxdy = \frac{1}{2} \sum_{i,k} \int K_i K_k (q_i - h_i) \psi_k dxdy \\ &= \frac{1}{2} \sum_{i,k} (q_i - h_i) Z_{ik} \psi_k = \sum_{i,j} (q_i - h_i) \hat{Z}_{ij} (q_j - h_j) \end{aligned} \quad (5.40)$$

where $Z_{ij} = \int K_i K_j dxdy$ and $\hat{Z}_{ij} = \sum_k Z_{ik} M_{kj}$ are symmetric commuting matrices. These invariants are rugged, i.e, they are conserved by the finite dynamical system obtained by projection onto the lattice. In addition, because

Z and \hat{Z} commute, one can always find an orthogonal matrix \mathcal{O} that satisfies $Z = \mathcal{O}^T D \mathcal{O}$ and $\hat{Z} = \mathcal{O}^T \hat{D} \mathcal{O}$, where $D_{ij} = d_i \delta_{ij}$ and $\hat{D}_{ij} = \hat{d}_i \delta_{ij}$ are diagonal matrices. Defining $q' = q\mathcal{O}$, $h' = h\mathcal{O}$ and $\psi' = \psi\mathcal{O}$, the enstrophy and energy become

$$\begin{aligned} C_2 &= \sum_{i,j} q'_i D_{ij} q'_j = \sum_i d_i (q'_i)^2 = \sum_I \sum_{\kappa_I} d_i (q'_i)^2 \\ H &= \sum_i \hat{d}_i (q'_i - h'_i)^2 = \sum_I \sum_{\kappa_I} \hat{d}_i (q'_i - h'_i)^2, \end{aligned} \quad (5.41)$$

where I is the index for the I th M -cell and κ_I denotes the set of m -cells in the I th M -cell.

This coordinate transformation simultaneously diagonalizes the quadratic Casimir invariant and the energy. However, higher-order Casimir invariants are in general not rugged and are in general not simultaneously diagonalizable. Thus, higher order invariants are not additive, which means M -cells share contributions from these invariants. In this sense, invariants of order higher than quadratic are not useful for describing the statistics of M -cells, which by assumption are independent.

5.5.4 Statistically Independent Subsystems

Now we turn to the question of how to find subsystems, i.e, how to find a good definition of the M -cells. First we note that flows inside the rotating tank with the sloped bottom have azimuthal undulations in most physical quantities (streamfunction, potential vorticity, etc.), and these undulations have been identified as Rossby waves [66, 195]. In a co-rotating frame, these waves propagate in the rotation direction at constant velocity. Thus, by shifting to a frame moving at the phase velocity of the Rossby wave, we

obtain a pattern that is statistically stationary on large scales. For example, the wavy patterns corresponding to the time-averaged streamfunction and potential vorticity are shown in Fig. 5.2. As noted before, the streamfunction is fairly smooth, characteristic of the scale Δ , is monotonically decreasing in the radial direction, and describes a strong zonal flow. However, the time-averaged potential vorticity is scattered with fine structure in space, the δ scale, but still has a wavy mean pattern similar to that of the time-averaged streamfunction. Because the streamfunction involves the integral over the Green's function, one expects it to be smoother than the time-averaged potential vorticity. So, this suggests that the first step toward defining M -cells is to consider a frame moving at the phase velocity of the Rossby wave.

Having determined the frame, we seek M -cells that are statistically independent. Because strong correlation in a preferential direction might affect the geometry of M -cells and associated additive invariants, we have measured the correlation function,

$$C_{\text{cor}}(\Delta r, r\Delta\theta) = \frac{1}{T} \int_0^T \frac{\int q(r, r\theta; t) q(r + \Delta r, r\theta + r\Delta\theta; t) r dr d\theta}{\int q(r, r\theta; t)^2 r dr d\theta} dt, \quad (5.42)$$

where (θ, r) are the usual polar coordinates. From a large data set of PIV measurements we obtain the time average of the velocity field, whence we calculate the potential vorticity at different positions. Then the integrals of (5.42) are performed with the spatial limits being the bulk of the area occupied by the fluid with a resolution of $\delta \approx 0.8$ cm and the time limit taken to be 80 revolutions with 47 measurements. The result of this procedure is presented in Fig. 5.3, which shows contours of C_{cor} plotted on a $\Delta\theta - \Delta r$ plane. The highly anisotropic nature of the contours suggests there is significantly less correlation in the radial direction than in the azimuthal direction. Thus to

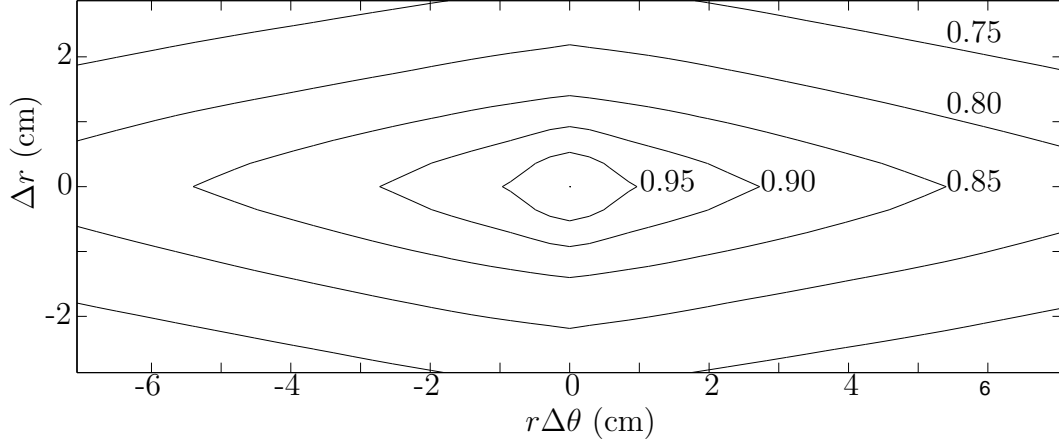


Figure 5.3: Contours of the correlation function $C_{\text{cor}}(\Delta r, r\Delta\theta)$ illustrating the anisotropic nature of the potential vorticity field, which has longer range correlation in the azimuthal direction than in the radial direction (cf. Fig. 5.2).

achieve consistent independence the shape of an M -cell should be elongated.

In the course of tracking blobs of fluid we generally observe that to good approximation such blobs follow contours of the time-averaged streamfunction. This, together with the the C_{cor} plot suggest that a good coordinate for dividing the system into subsystems is the time-averaged streamfunction,

$$\bar{\psi}(r, \theta) = \frac{1}{T} \int_0^T \psi(\theta, r; t) dt. \quad (5.43)$$

Contours of $\bar{\psi}$ tend to be smooth and, we argue, are part of a natural coordinate system for describing turbulence with a mean flow that has slow spatial dependence. (We have also considered \bar{q} but found it to be not as good because of its greater variability.) To complete the coordinate system, we introduce a coordinate χ , which is conjugate to $\bar{\psi}$ and therefore satisfies

$$\frac{1}{r} \frac{\partial \bar{\psi}}{\partial \theta} \frac{\partial \chi}{\partial r} - \frac{1}{r} \frac{\partial \bar{\psi}}{\partial r} \frac{\partial \chi}{\partial \theta} = 1. \quad (5.44)$$

Thus the coordinate transformation $(\theta, r) \longleftrightarrow (\chi, \bar{\psi})$ satisfies $rdrd\theta = d\chi d\bar{\psi}$.

We propose that contours of $\bar{\psi}$ define M -cells, which we take to be of small (infinitesimal) width in this coordinate, and we propose that the χ coordinate at fixed $\bar{\psi}$ represents a continuum of m -cells. We imagine an M -cell to be a region (nearly a curve) at fixed $\bar{\psi}$. Hence with this definition, the probability density P_{Mexp} , depends only on the potential vorticity variable ζ and on the coordinate $\bar{\psi}$; i.e., $P_{Mexp}(\zeta; \bar{\psi})$ is the probability of finding a potential vorticity value ζ in the $\bar{\psi}$ M -cell. Thus the ensemble average of an arbitrary function f is written as

$$\langle f \rangle_{Mexp}(\bar{\psi}) = \int f(\zeta, \bar{\psi}) P_{Mexp}(\zeta; \bar{\psi}) d\zeta, \quad (5.45)$$

where P_{Mexp} is normalized as $\int P_{Mexp} d\zeta = 1$. In practice we can determine the probability P_{Mexp} from data by the relative frequency definition (cf. §§5.5.5), and then proceed to calculate (5.45). However, this is equivalent to averaging over χ and t ; e.g. $\langle \zeta \rangle_{Mexp} = \overline{\prec q \succ_\chi}$, where $\prec q \succ_\chi = \int q d\chi / \int d\chi$. Given $\langle \zeta \rangle_{Mexp}$ and using (5.32) to define $\langle \psi \rangle_{Mexp}$ we similarly have the equivalence $\langle \psi \rangle_{Mexp}(\bar{\psi}) = \overline{\prec \psi(\bar{\psi}, \chi; t) \succ_\chi} = \bar{\psi}$, where the second equality follows by definition. The undular streamfunction of Fig. 5.2 mainly represents Rossby waves. These wavy patterns are quite robust and often behave as barriers to mixing. In the Rossby wave frame, our data indicate that the instantaneous streamfunction is close to the time-averaged streamfunction, i.e. $\prec \psi(\bar{\psi}, \chi; t) \succ_\chi$ deviates from $\bar{\psi}$ by less than 10 percent. The above comments can be viewed as an experimental verification of ergodicity.

In terms of the above notation the energy and enstrophy densities on

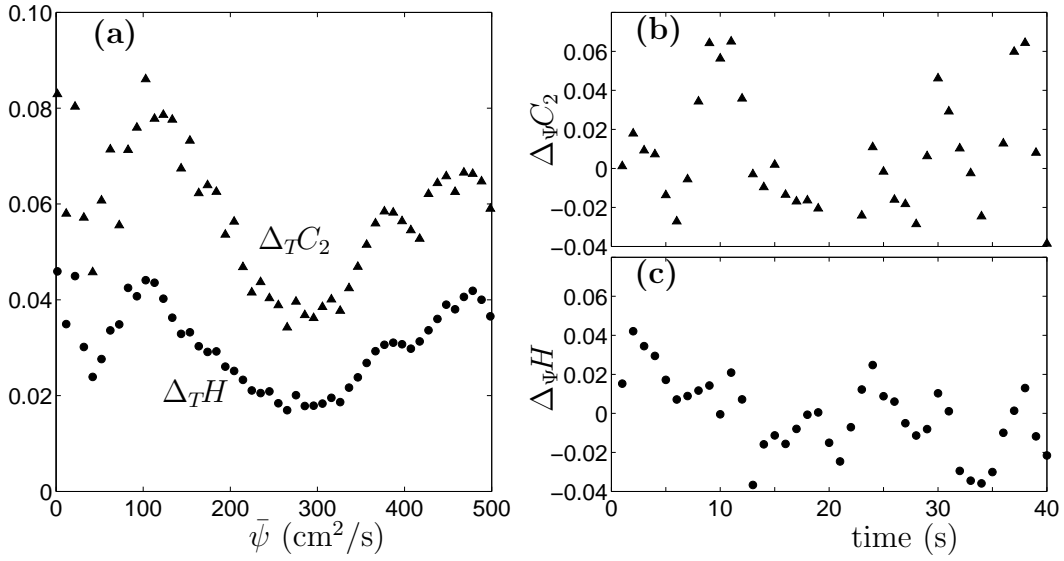


Figure 5.4: (a) Enstrophy fluctuations $\Delta_T C_2(\bar{\psi})$ [Eq. (5.47)] and energy fluctuations $\Delta_T H(\bar{\psi})$ as a function of $\bar{\psi}$. The fluctuations are small, indicating that energy and enstrophy are nearly conserved for our choice of subsystem. (b) Total enstrophy variations $\Delta_\Psi C_2(t)$ [Eq. (5.48)] and (c) total energy variations $\Delta_\Psi H(t)$ with time; the variation is small, indicating that the quantities for our choice of subsystem are almost conserved in time.

M -cells can be written as

$$\begin{aligned}
\langle H \rangle_{M_{exp}}(\bar{\psi}) &= \frac{1}{2} \left[\int \zeta \bar{\psi} P_{M_{exp}}(\zeta; \bar{\psi}) d\zeta - \prec \bar{\psi} h(\chi, \bar{\psi}) \succ_{\chi} \right] \\
&= \frac{1}{2} \overline{\prec \bar{\psi} [q(\chi, \bar{\psi}, t) - h(\chi, \bar{\psi})] \succ_{\chi}}, \\
\langle C_2 \rangle_{M_{exp}}(\bar{\psi}) &= \frac{1}{2} \int \zeta^2 P_{M_{exp}}(\zeta; \bar{\psi}) d\zeta = \frac{1}{2} \overline{\prec q^2(\chi, \bar{\psi}, t) \succ_{\chi}}, \quad (5.46)
\end{aligned}$$

and two quantities that measure spatial and temporal fluctuations of these invariants can be compactly written as follows:

$$\Delta_T C_2(\bar{\psi}) = \frac{\left[\overline{\left(\prec q^2 \succ_{\chi} - \overline{\prec q^2 \succ_{\chi}} \right)^2} \right]^{1/2}}{\overline{\prec q^2 \succ_{\chi}}}, \quad (5.47)$$

$$\Delta_{\Psi} C_2(t) = \frac{\left[\overline{\prec \left(\prec q^2 \succ_{\chi} - \overline{\prec q^2 \succ_{\chi \bar{\psi}}} \right)^2 \succ_{\bar{\psi}}} \right]^{1/2}}{\overline{\prec q^2 \succ_{\chi \bar{\psi}}}}, \quad (5.48)$$

with similar expressions for $\Delta_T H(\bar{\psi})$ and $\Delta_{\Psi} H(t)$. Figure 5.4 depicts these quantities. Panel (a) shows temporal fluctuations as a function of the spatial coordinate $\bar{\psi}$. The middle regions of the experiment, where strong zonal flows exist, is describable by statistical mechanics. However, near the walls, corresponding to high and low $\bar{\psi}$ values, statistical mechanics fails because of large fluctuations. Similarly, in panel (b) the spatial fluctuations are plotted versus time, and it is observed that these fluctuations are quite small. We have measured similar quantities for the cubic and quartic Casimir invariants and the fluctuations are two or three times greater.

An integrated measure of the goodness of our streamfunction based M -cells is displayed in Table 5.1. Here we have integrated $\prec \Delta_T H \succ_{\bar{\psi}}$ and $\prec \Delta_T C_2 \succ_{\bar{\psi}}$ over central values of $\bar{\psi}$ and compared them with counterparts derived using square cells. By this measure streamfunction based cells are nearly ten times better than square cells.

Fluctuation Measure	$\prec \Delta_T H \succ_{\bar{\psi}}$	$\prec \Delta_T C_2 \succ_{\bar{\psi}}$
square cells	0.2233	0.6425
streamfunction cells	0.0343	0.0627

Table 5.1: Comparison of fluctuations for square cells with our streamfunction based cells. Both the energy fluctuation measure $\prec \Delta_T H \succ_{\bar{\psi}}$ and enstrophy fluctuation measure $\prec \Delta_T C_2 \succ_{\bar{\psi}}$ are considerably smaller with the streamfunction based cells. These small fluctuations allow the division of the system into M -cells, consistent with the statistical independence and additivity assumptions of statistical mechanics.

Thus, in summary, we have strong evidence supporting the use of streamfunction based M -cells. The evidence of Fig. 5.4 and Table 5.1 imply both statistical independence and the additive nature of the quadratic invariants of these macro-cells.

5.5.5 Prediction for PDFs

Based on the arguments in the previous section, we consider only two invariants out of the infinitely many invariants conserved by the ideal dynamics. With these given invariants, there are various ways to calculate the probability in a M -cell, $P_{Mexp}(\zeta; \bar{\psi})$. All different methods give the same answer after all. Here, we list only two different ways.

1. Probabilistic relations

Consider an isolated system composed of a M -cell and a large reservoir. They are in contact with interchanging energy (H) and Casimir invariants (C). According to Gibbs statistical mechanics, a reservoir (denoted as R) is assumed to be infinitely larger than a M -cell and to nearly in-

teract with a M -cell. This interaction may produce a correction for the extensivity of entropy [98]. For the fixed volume, allowing energy and Casimir exchanges, the probability of a M -cell is given as

$$P(H_M, C_M | H, C, V_M, V_R) = \frac{Z(H_M, C_M, V_M) Z(H - H_M, C - C_M, V_R)}{Z(H, C, V_M, V_R)}, \quad (5.49)$$

where Z is the partition function and H , H_M and H_R are the energy of a total system, a M -cell and a reservoir, respectively. Its associated entropies for a M -cell and a reservoir are defined as

$$\begin{aligned} S(H_M, C_M, V_M) &= \ln Z(H_M, C_M, V_M) \\ S(H - H_M, C - C_M, V_R) &= \ln Z(H - H_M, C - C_M, V_R) \\ &\simeq S(H, C, V) - \frac{\partial S(H, C, V)}{\partial H} H_M - \frac{\partial S(H, C, V)}{\partial C} C_M \\ &= \text{const.} - \beta H_M - \gamma C_M \end{aligned} \quad (5.50)$$

where $\frac{\partial S}{\partial H} =: \beta$, $\frac{\partial S}{\partial C} =: \gamma$ and $S(H, C, V)$ is constant since the total system is assumed to keep the same invariants as initial conditions.

$$P(H_M, C_M | \gamma, \beta, V) = \frac{\exp(S(H_M, C_M, V) - \beta H_M - \gamma C_M)}{Z(\gamma, \beta, V)}. \quad (5.51)$$

By using the simple conditional probability relation and Eq. (5.51), the probability of potential vorticity is given as

$$\begin{aligned} P(\zeta | \gamma, \beta, V) &= \int dH_M dC_M P(\zeta | H_M, C_M) P(H_M, C_M | \gamma, \beta, V) \\ &= \int dH_M dC_M \frac{\delta(H(\zeta) - H_M) \delta(C(\zeta) - C_M)}{Z(H_M, C_M, V)} \\ &\quad \times \frac{\exp(S(H_M, C_M, V) - \beta H_M - \gamma C_M)}{Z(\gamma, \beta, V)} \\ &= \frac{\exp(-\beta H(\zeta) - \gamma C(\zeta))}{Z(\gamma, \beta, V)}. \end{aligned} \quad (5.52)$$

Assuming M_{exp} -cells are chosen to be contours of time-averaged stream-function $\bar{\psi}$, a resulting probability distribution that maximizes the entropy is

$$\begin{aligned} P_{M_{exp}}(\zeta; \bar{\psi}) &= \frac{1}{Z'(\bar{\psi})} \exp \left(-\frac{\beta}{2} \bar{\psi} \zeta - \frac{\gamma}{2} \zeta^2 \right) \\ &= \frac{1}{Z(\bar{\psi})} \exp \left(-\frac{\gamma}{2} \left(\zeta + \frac{\beta}{2\gamma} \bar{\psi} \right)^2 \right) \end{aligned} \quad (5.53)$$

where Z and Z' are normalization factors, γ and β are Lagrange multipliers. Gaussian probability distribution in Eq. (5.53) is obtained as in a canonical ensemble of a system. Mainly, Gaussian probability distribution is from a quadratic form of enstrophy.

2. Landau's Way

Classical statistical mechanics describes the behavior and properties of macroscopic systems without knowing the motion of the finite individual particles in a phase space. A rising question on 2D inviscid fluid is whether the similar argument is true in the infinite dimensional function space.

First, a system should be divided into M -cells which are spatially disjoint subsets. The division into M -cells can be done in various ways and M -cells interact with each other. The proper choice of the division, which satisfies the relatively weak interaction among M -cells, leads to establishment of statistical mechanics.

Consider two noninteracting parts of a system. In 2D inviscid fluid, there exist two independent additive integrals of motion, energy and enstrophy. The total Hamiltonian functional might be separable into

many non-interacting parts such that

$$\langle H \rangle = \sum_i \langle H \rangle_{M_{exp}}(\bar{\psi}_i), \quad (5.54)$$

where $\langle H \rangle_{M_{exp}}(\bar{\psi}_i) := \int \frac{1}{2} \bar{\psi}(\zeta - h) P_{M_{exp}}(\zeta; \bar{\psi}_i) d\zeta$ is the Hamiltonian functional which is integrated over the subset $(D^{(i)})$ of a configuration space. Also, the total enstrophy is separable as

$$\langle C \rangle = \sum_i \langle C \rangle_{M_{exp}}(\bar{\psi}_i). \quad (5.55)$$

Similarly, $\langle C \rangle_{M_{exp}}(\bar{\psi}_i) := \int \frac{1}{2} \zeta^2 P_{M_{exp}}(\zeta; \bar{\psi}_i) d\zeta$.

Weakly interacting M -cells are characterized by the statistical independence of probabilities of M -cells. For example, we suppose that a system is composed of many M -cells ($i = 1, 2, \dots, N$). The total probability can be written as the product of probabilities of M -cells.

$$P(\zeta) = \prod_i P(\zeta; \bar{\psi}_i) \quad (5.56)$$

Hence, one easily concludes that another additive quantity as

$$\ln P(\zeta) = \sum_i \ln P(\zeta; \bar{\psi}_i). \quad (5.57)$$

Associated entropy is given as

$$\langle S \rangle_{M_{exp}}(\bar{\psi}_i) := \int P_{M_{exp}}(\zeta; \bar{\psi}_i) \ln P_{M_{exp}}(\zeta; \bar{\psi}_i) d\zeta. \quad (5.58)$$

From Eq. (5.54), (5.55) and (5.57), a linear combination of these quantities for the i th M -cell can be written as

$$\begin{aligned} & \langle S \rangle_{M_{exp}}(\bar{\psi}_i) + \alpha^{(i)} + \beta^{(i)} \langle H \rangle_{M_{exp}} + \gamma^{(i)} \langle C \rangle_{M_{exp}} \\ & \int P(\zeta; \bar{\psi}_i) \left[\ln P(\zeta; \bar{\psi}_i) + \alpha^{(i)} + \beta^{(i)} \frac{1}{2} \bar{\psi}(\zeta - h) + \gamma^{(i)} \frac{1}{2} \zeta^2 \right] d\zeta = 0 \end{aligned}$$

where $\alpha^{(i)}, \beta^{(i)}$ and $\gamma^{(i)}$ are Lagrange multipliers. From the above equality and nonzero probability, one gets the same equation as Eq. (5.53).

The above derivation starts from the assumption of *local equilibrium*. We might pose the question how we can assume the equilibrium in a local subsystem (M -cell). A system with a short relaxation time scale attains an equilibrium state shortly. The relaxation time scale for equilibrium state increases with the size of system. Subsystems (small parts of a system) can reach *local equilibrium* over short time and behave approximately as closed systems. Therefore, $\alpha^{(i)}, \beta^{(i)}$ and $\gamma^{(i)}$ of i th M -cell are different values from that of other M -cells. If a system gradually approaches to an equilibrium state, the variation of parameters such as $\alpha^{(i)}, \beta^{(i)}$ and $\gamma^{(i)}$ for each M -cell converges to zero.

Consequently, we obtain the following equilibrium distribution:

$$P_{Mexp}(\zeta; \bar{\psi}) = \mathcal{Z}_{Mexp}^{-1} e^{-\beta \bar{\psi} \zeta - \gamma \zeta^2}, \quad (5.59)$$

where $\mathcal{Z}_{Mexp} = \int e^{-\beta \bar{\psi} \zeta - \gamma \zeta^2} d\zeta$ depends only on $\bar{\psi}$. Note, the function h has cancelled out in the normalization. This probability density function (PDF) has the form of Gaussian that is shifted by $\beta \bar{\psi} / 2\gamma$.

In Fig. 5.5 we compare (5.59) with experimental results. Figures 5.5(a) and 5.5(b) show that experimental data on a typical M -cell closely agree with the Gaussian distribution of (5.59). Each distribution is shifted by its mean value of potential vorticity $\langle \zeta \rangle_{Mexp}$. Figures 5.5(c) and 5.5(d) show the total probability $P^{tot}(\zeta)$, which is the sum of the probabilities over all the M -cells, i.e., $P^{tot}(\zeta) = \prec P_{Mexp}(\zeta; \bar{\psi}) \succ_{\bar{\psi}}$. These plots are decidedly non-Gaussian.

The next question is, what is the most probable value of potential vorticity in each M -cell? The probability distribution of Eq. (5.59) gives a relation

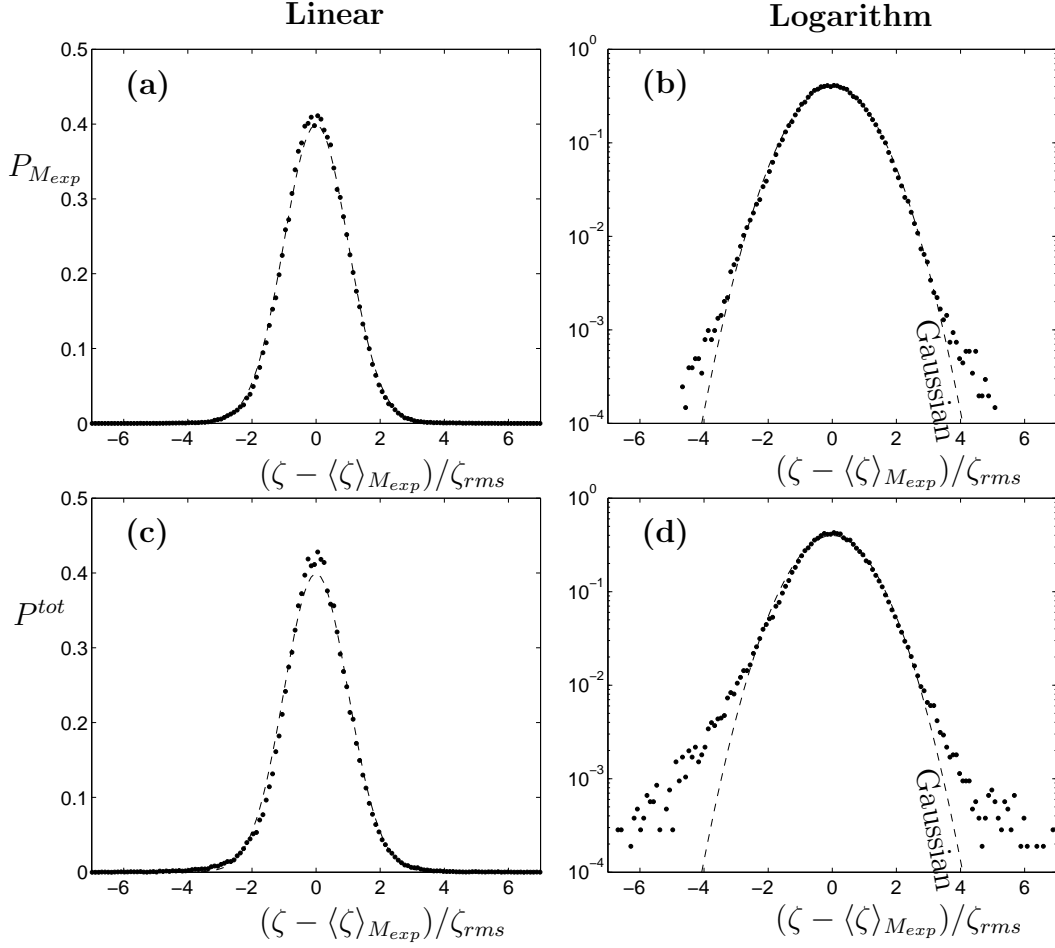


Figure 5.5: The measured probability distribution of potential vorticity (data points) on a typical M -cell is nearly Gaussian (dashed line), in accord with (5.59), as illustrated by these plots on (a) linear and (b) logarithmic scales. In contrast, the potential vorticity of the whole system, shown in (c) and (d) respectively, departs significantly from a Gaussian.

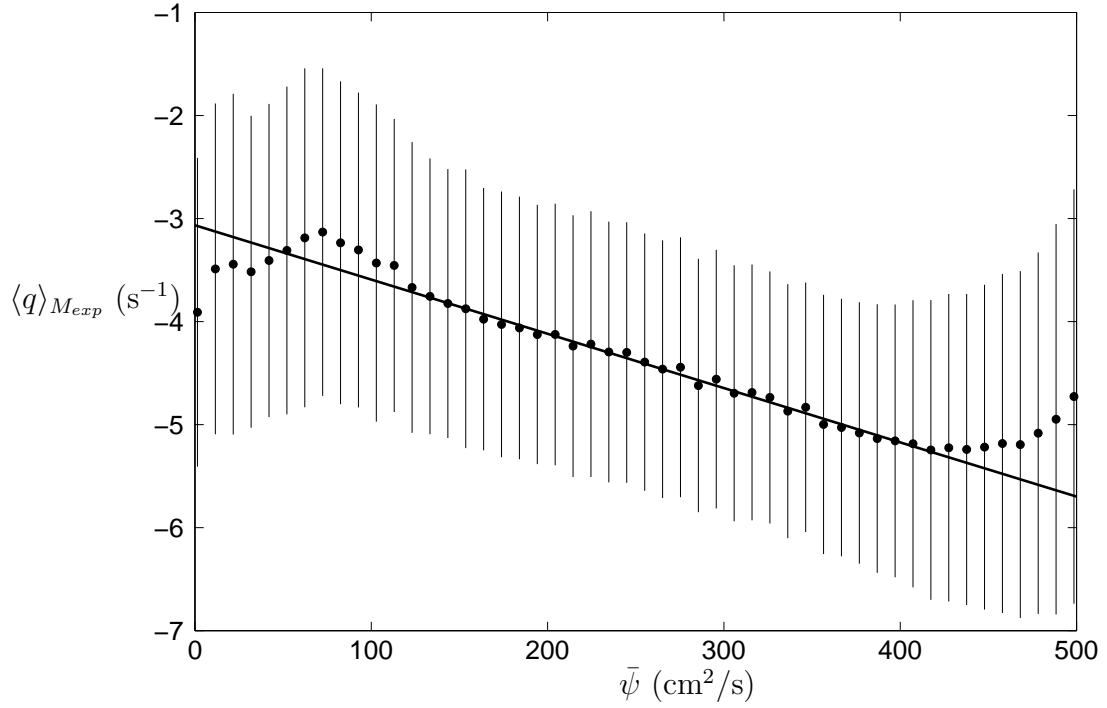


Figure 5.6: The ensemble-averaged potential vorticity $\langle q \rangle_{Mexp}$ exhibits a dependence on the time-averaged streamfunction $\bar{\psi}$ that is linear except near the walls (at the ends of the range of $\bar{\psi}$). The dots are mean values of $\langle q \rangle_{Mexp}$, and the vertical lines correspond to standard deviations of $\langle q \rangle_{Mexp}$ at a fixed $\bar{\psi}$. The data fit well the straight line (a least-squares fit), in accord with the prediction of Eq. (5.60), where the slope is the ratio of two Lagrange multipliers.

between the averaged vorticity and the streamfunction,

$$\langle \zeta \rangle_{M_{exp}} = \int \zeta P_{M_{exp}}(\zeta; \bar{\psi}) d\zeta = -\epsilon \bar{\psi}, \quad (5.60)$$

which follows by elementary integration. Here $\epsilon = \beta/(2\gamma)$ is the ratio of two Lagrange multipliers. Figure 5.6 shows a linear relation between the ensemble-averaged potential vorticity $\langle \zeta \rangle_{M_{exp}}$ and the time-averaged streamfunction $\bar{\psi}$, as predicted by Eq. (5.60).

Therefore, our theoretical predictions based on a mean field approximation are in good accord with PDFs on M -cells and the averaged values of potential vorticity and streamfunction from experiments. Our theory also indicates that equilibrium can be locally achieved in M -cells, even though the system as a whole is turbulent and non-Gaussian.

5.6 Conclusions

In this chapter we have emphasized the the relationship between additive invariants and statistical independence: probability densities that result from entropy maximization principles, such as that of §§5.5.2, will decompose into a product over subsystems if the entropy is logarithmic (extensive) and the invariants included as constraints in the principle are additive over subsystems (M -cells). We have also emphasized that additivity and, consequently, independence depend on the definition of subsystem. This idea appears, at least implicitly, in conventional statistical mechanics. For example, in the classical calculation of the specific heat of a solid, where one considers a solid to be a collection of lattice sites with spring-like nearest neighbor interactions, the Hamiltonian achieves the form of a sum over simple harmonic oscillators.

However, such a diagonal form requires the use of normal coordinates, and only then is the partition function equal to a product over those of the individual oscillators. Thus the notions of subsystem, here a single oscillator, additivity, and statistical independence are intimately related.

In our application of statistical mechanics to inhomogeneous damped and driven turbulence, we have discovered experimentally that a good definition of subsystem is provided by the temporal mean of the streamfunction. With this definition, the quadratic invariants (energy and enstrophy) are additive, and the concomitant probability density of (5.59) agrees quite well with experimental results for both the distribution of vorticity, as depicted in Fig. 5.5 (a) and (b), and the mean state, as depicted in Fig. 5.6.

An alternative interpretation of our results can be obtained by the counting argument of §5.5.1. Our definition of subsystem amounts to the idea that potential vortices on the same contour of time-averaged streamfunction can exchange their positions with little change in the energy and enstrophy. However, the relocation of two potential vortices that are on different contours of the streamfunction should result in a large change of the invariants. In this sense, the number of possible configurations in phase space can be counted, and the maximization of the entropy so obtained gives our result.

Although in this chapter we have focused on a geostrophic fluid, our procedure is of general utility and is applicable to physical systems governed by a variety of transport equations. The unifying formalism is the noncanonical Hamiltonian description of §5.3, which plays the unifying role played by finite-dimensional canonical Hamiltonian systems in conventional statistical mechanics. Thus we expect our approach to apply to Vlasov-Poisson dynamics, kinetic theories of stellar dynamics, and drift-wave plasma models, and

other single-field models that possess the noncanonical Poisson bracket of (5.5). Generalization to multi-field models such as reduced magnetohydrodynamics, stratified fluids, and a variety of physics models governed by generalization of the Poisson bracket [207] of (5.5) provides an avenue for further research.

Chapter 6

Nonextensive Statistical Mechanics

6.1 Introduction

Equilibrium statistical mechanics has long been used to describe turbulence [203]. Early work by Onsager predicted coherent structure formation through consideration of the interactions of point vortices [161]. Later Kraichnan constructed a statistical theory based on energy and enstrophy conservation [107] and showed that the Euler equation (for inviscid flow) with truncation below a certain small length scale could describe turbulent flows [109, 110]. More recently, Miller showed that large scale coherent structures could be described by equilibrium statistical mechanics of the Euler equation through a continuous distribution of microscopic vorticity [138]. These analyses assumed that the asymptotic behavior depends upon the values of the conserved quantities rather than on the details of initial structures. Further,

the analyses were based on Boltzmann-Gibbs statistics, which only describes weak interactions and does not capture long-range interactions [115]. Our observations of large coherent vortices in experiments on flow in a rotating annulus [18, 19, 10] lead us to consider a generalization of statistical mechanics that is applicable to systems with long range interactions: the nonextensive formalism proposed by Tsallis [215, 214].

Probability distribution functions (PDFs) for the velocity increment, $\delta v(r) = \langle v(x+r) - v(x) \rangle_x$, have been derived from nonextensive theory assuming conservation of an *effective energy* proportional to $(\delta v)^2$, and these PDFs have been found to describe several turbulent flows [27, 23, 18, 22]; however, $(\delta v)^2$ is not a conserved quantity for the rotating flows of interest here. Experiments on a plasma of electrons in a strong magnetic field have been interpreted using both extensive entropy [92] and nonextensive entropy [30] with conservation of energy. These analyses did not consider Miller’s distinction between the macroscopic and microscopic quantities.

For our laboratory flow, we exploit an additional conservation property that holds for geostrophic flows. A geostrophic flow is one that is dissipationless and rotates sufficiently fast so that it is two-dimensional, varying only in the plane perpendicular to the rotation axis [165]. The additional conserved quantity is the *potential enstrophy*, which is defined as [165, 90]

$$\Pi = \int \left(\frac{\omega(\mathbf{x}) + 2\Omega}{h(\mathbf{x})} \right)^2 d\mathbf{x} \quad (6.1)$$

where $\omega(\mathbf{x})$ is the local vorticity and in our system, Ω is the rotation rate of the annulus, and h is the height of fluid, which increases in the r -direction. A sloping bottom in our rotating annulus models the variation of the Coriolis force with latitude in a real geophysical flow. Flow in our

laboratory system is only approximately geostrophic because the rotation rate is finite rather than infinite and the dissipation is nonzero. However, the rotation rate is large enough and dissipation effects are small enough so that the flow is strongly two-dimensional (*quasi-geostrophic*) [19] and the potential enstrophy should be nearly conserved. The potential enstrophy is only one of an infinite number of conserved quantities in a geostrophic flow, $\int d\mathbf{x} Q^n$ (with n an integer), where $Q \equiv \frac{\omega+2\Omega}{h}$ is the potential vorticity; the potential enstrophy corresponds to $n = 2$. The higher order conserved terms are more dependent on viscous effects than energy and potential enstrophy terms [119], so we limit our analysis to the two latter conserved quantities, which are often called *Rugged Invariants* [111, 64, 130, 34].

In this chapter we use the Euler equation, which neglects viscous dissipation, to obtain predictions of statistical properties of turbulence that we then compare with our experimental observations. The Euler equation has been found to describe phenomena in large scale oceanic and atmospheric flows [138, 176, 139], and should provide a useful description to flow in our rotating annulus, where dissipation is small, i.e., the spin down time ($= \sqrt{\frac{h^2}{\nu\Omega}} \approx 47$ sec) is much longer than the typical vortex turnover time (≈ 2 sec).

The chapter is organized as follows: In Section 2 we briefly describe the nonextensive formalism. In Section 3 we introduce our nonextensive model for two-dimensional flows with energy and enstrophy conservation. We derive expressions for the radial dependence of the azimuthally averaged vorticity and for the probability distribution function of the vorticity. In Section 6.4 we compare the predictions of our model with the experimental data. Finally, in Section 6.5 we compare the nonextensive parameter q deduced from our work with values obtained in other work.

6.2 Nonextensive Entropy

A system composed of sub-systems A and B has entropy [215]

$$S_q(A + B) = S_q(A) + S_q(B) + (1 - q)S_q(A)S_q(B), \quad (6.2)$$

where $S_q(A)$ is the entropy of system A and q is the nonextensive parameter. When $q = 1$, the entropy is extensive. Tsallis proposed a form of the entropy that satisfies the above equation [214],

$$S_q = \frac{k}{q-1} \left(1 - \sum_i^W p_i^q \right), \quad (6.3)$$

where W is the total number of possible microstates of the system, p_i is the probability of i^{th} state and k is the Boltzmann constant. There are two constraints on the system, the normalization

$$\sum_{i=1}^W p_i = 1 \text{ and,} \quad (6.4)$$

and the conservation of total energy

$$\frac{\sum_{i=1}^W p_i^q E_i}{\sum_{i=1}^W p_i^q} = \hat{U}_q, \quad (6.5)$$

where E_i is the energy of i^{th} state and \hat{U}_q is a normalized q -expectation total energy. The normalized q -expectation of any observable, O , can be expressed as

$$\hat{O}_q = \frac{\sum_{i=1}^W p_i^q O_i}{\sum_{i=1}^W p_i^q}. \quad (6.6)$$

Other definitions of observable quantities are inconsistent with the first principle of thermodynamics [216].

When a system is in contact with a thermal reservoir, the entropy under appropriate constraints is maximized. The probability p_i of microstate i can be obtained by introducing Lagrange parameters α' and β' and finding the maximum with respect to p_i of

$$\phi_q[p_i] = \frac{S_q}{k} + \alpha' \sum_{i=1}^W p_i - \beta' \frac{\sum_{i=1}^W p_i^q (E_i - \hat{U})}{\sum_{i=1}^W p_i^q}. \quad (6.7)$$

Solving for p_i yields

$$p_i = \frac{1}{Z} [1 - (1 - q)\beta E_i]^{1/(1-q)}, \quad (6.8)$$

where $\beta = \frac{\beta'}{\sum_j p_j^q + (1-q)\beta' \hat{U}}$ and Z is the normalization factor. In the limit $q \rightarrow 1$, Boltzmann-Gibbs statistics is recovered, $p_i = \frac{1}{Z} e^{-\beta E_i}$.

6.3 Energy-entropy Models

We now compute the azimuthally averaged vorticity as a function of radius for the extensive and nonextensive cases and derive expressions for the vorticity probability distribution function (PDF). We assume in each case three constraints: normalization, conserved energy, and conserved enstrophy. We follow Miller [138, 124] in considering the “microscopic vorticity” field σ , which he used to develop a statistical mechanics formalism for two-dimensional flows. The macroscopic variables are then defined by averaging the microscopic vorticity, which obeys the conservation laws [124]. The microscopic vorticity is replaced by the probability density function $p(\sigma, \mathbf{x})$, which is a conserved quantity as a consequence of the incompressibility of the flow [139]. The macroscopic vorticity ω and macroscopic enstrophy ω^2 are defined in terms of

the microscopic vorticity σ as

$$\begin{aligned}\omega(\mathbf{x}) &= \int d\sigma \sigma p(\sigma, \mathbf{x}) \\ \omega^2(\mathbf{x}) &= \int d\sigma \sigma^2 p(\sigma, \mathbf{x}).\end{aligned}\tag{6.9}$$

In the following subsections, we show that the extensive and nonextensive models predict the same radial profile for the vorticity, but predict different vorticity PDFs.

6.3.1 Extensive Model

The conserved energy and potential enstrophy expressed in terms of the microscopic vorticity $p(\sigma, \mathbf{x})$ are

$$\begin{aligned}\hat{U} &= \int d\mathbf{x} \int d\sigma \sigma p(\sigma, \mathbf{x}) \psi(\mathbf{x}) \\ \hat{\Pi} &\approx \int d\mathbf{x} |\omega(\mathbf{x}) + \beta_{Ro} r|^2\end{aligned}\tag{6.10}$$

$$= \int d\mathbf{x} \left(\int d\sigma (\sigma^2 + 2\beta_{Ro} r \sigma) p(\sigma, \mathbf{x}) + \beta_{Ro}^2 r^2 \right),\tag{6.11}$$

where $\beta_{Ro} \equiv \frac{2\eta\Omega}{h_0}$ is the beta-plane coefficient, Ω is the rotation rate of the laboratory annulus system, η is the slope of the annulus bottom (the beta plane), and h_0 is the mean depth of the annulus. Eq. (6.11) follows from Eq. (6.1) by rescaling for quasi-geostrophic flow [90]. We analyze this rescaled form for the enstrophy.

When the extensive entropy ($S \equiv -k p_i \ln p_i$) is maximized with energy and potential enstrophy constraints using the corresponding Lagrange multipliers β and γ , the probability of the equilibrium state becomes

$$p(\sigma, \mathbf{x}) = \frac{1}{Z} e^{-\gamma(\sigma + \beta_{Ro}r + \frac{\beta}{\gamma}\psi(\mathbf{x}))^2}, \quad (6.12)$$

where γ is the Lagrange multiplier of the potential enstrophy.

The radial dependence of the vorticity is obtained from the equation for the stream function.

$$\nabla^2\psi - \left(\beta_{Ro}r + \frac{\beta}{\gamma}\psi \right) = 0. \quad (6.13)$$

Solving this equation with appropriate boundary conditions allows us to determine the parameter $\frac{\beta}{\gamma}$ by comparing the predicted radial profile of vorticity with our measurements. The results are presented in Section 5.3. The linear relation between our stream function and its Laplacian is similar to a result that was obtained from a minimum enstrophy principle, $\nabla^2\psi + \mu + \lambda\psi = 0$ [118, 87].

The PDF of the microscopic vorticity σ can be expressed as

$$g(\sigma) = \int p(\sigma, \mathbf{x}) d\mathbf{x} = \frac{1}{Z} \int d\mathbf{x} e^{-\gamma(\sigma + \beta_{Rossby}r + \frac{\beta}{\gamma}\psi(\mathbf{x}))^2}. \quad (6.14)$$

Since the microscopic vorticity σ cannot be measured, this PDF cannot be verified. Miller uses $g(\sigma)$ to compute the PDF of the measurable (“dressed”) vorticity in a finite volume [139]. We conduct a similar analysis obtain the following prediction for the measurable vorticity:

$$g_d(\omega) \propto \int d\mathbf{x} \frac{1}{(\omega + \beta_{Ro}r + \frac{\beta}{\gamma}\psi(\mathbf{x}))} e^{-\gamma(\omega + \beta_{Ro}r + \frac{\beta}{\gamma}\psi(\mathbf{x}))^2} \sinh \left(2\gamma\omega_m \left(\omega + \beta_{Ro}r + \frac{\beta}{\gamma}\psi(\mathbf{x}) \right) \right) \quad (6.15)$$

where ω_m is the fluctuation limit of the microscopic vorticity and γ is the Lagrange multiplier of the potential enstrophy.

6.3.2 Nonextensive Model

Non-additivity can be achieved by defining any observable as in Eq. (6.6). The vorticity and vorticity squared can be redefined within the nonextensive formalism as

$$\omega_q(\mathbf{x}) = \frac{\int d\sigma \sigma p^q(\sigma, \mathbf{x})}{\int d\sigma p^q} \quad (6.16)$$

$$\omega_q^2(\mathbf{x}) = \frac{\int d\sigma \sigma^2 p^q(\sigma, \mathbf{x})}{\int d\sigma p^q}. \quad (6.17)$$

In the nonextensive formalism, the two conserved quantities, energy and potential enstrophy, become

$$\hat{U} = \frac{\int d\mathbf{x} \int d\sigma \sigma p^q(\sigma, \mathbf{x}) \psi(\mathbf{x})}{\int d\mathbf{x} \int d\sigma p^q(\sigma, \mathbf{x})} \quad (6.18)$$

$$\begin{aligned} \hat{\Pi} &\approx \frac{\int d\mathbf{x} (\omega + \beta_{Ro} r)^2}{\int d\mathbf{x} \int d\sigma p^q(\sigma, \mathbf{x})} \\ &= \frac{\int d\mathbf{x} \{ \int d\sigma (\sigma^2 + 2\beta_{Ro} r \sigma) p^q(\sigma, \mathbf{x}) + \beta_{Ro}^2 r^2 \}}{\int d\mathbf{x} \int d\sigma p^q(\sigma, \mathbf{x})}. \end{aligned} \quad (6.19)$$

The PDF for the microscopic entropy, subject to the three constraints (normalization, conserved energy, and conserved enstrophy), becomes

$$p(\sigma, \mathbf{x}) = \frac{1}{Z} \left[1 - \frac{(1-q)\gamma}{f(\omega)} \left(\sigma + \frac{\beta\psi(\mathbf{x})}{\gamma} + \beta_{Ro} r \right)^2 \right]^{\frac{1}{1-q}}, \quad (6.20)$$

where $f(\omega) \equiv 1 + (1 - q)\gamma\omega^2$. The expression for the stream function remains identical to the extensive case, Eq. (6.13). We derive the following PDF of the microscopic vorticity for $q > 1$,

$$\begin{aligned}
g(\sigma) &= \int d\mathbf{x} \frac{p^q}{\int p^q d\sigma} \\
&= \Xi \int d\mathbf{x} \left[1 - \frac{(1-q)\gamma}{f(\beta_{Ro}r + \frac{\beta}{\gamma}\psi)} \left(\sigma + \beta_{Ro}r + \frac{\beta}{\gamma}\psi \right)^2 \right]^{\frac{q}{1-q}} \\
&\quad f\left(\beta_{Ro}r + \frac{\beta}{\gamma}\psi\right)^{-1/2}
\end{aligned} \tag{6.21}$$

where Ξ is the normalization constant. The equation for the dressed (measurable) vorticity is

$$\begin{aligned}
g_d(\omega) &\propto \int d\mathbf{x} \frac{f(\omega)}{(\omega + \beta_{Ro}r + \frac{\beta}{\gamma}\psi(\mathbf{x}))} \\
&\quad \left[1 - \frac{(1-q)\gamma}{f(\omega)} \left(\omega + \beta_{Ro}r + \frac{\beta}{\gamma}\psi(\mathbf{x}) \right)^2 \right]^{\frac{q}{1-q}} \\
&\quad \left(\left[1 + 2 \frac{(1-q)\gamma\omega_m}{f(\omega) - (1-q)\gamma(\omega + \beta_{Ro}r + \frac{\beta}{\gamma}\psi(\mathbf{x}))^2} \right. \right. \\
&\quad \left. \left. \left(\omega + \beta_{Ro}r + \frac{\beta}{\gamma}\psi(\mathbf{x}) \right) \right]^{\frac{1}{1-q}} \right. \\
&\quad \left. - \left[1 - 2 \frac{(1-q)\gamma\omega_m}{f(\omega) - (1-q)\gamma(\omega + \beta_{Ro}r + \frac{\beta}{\gamma}\psi(\mathbf{x}))^2} \right. \right. \\
&\quad \left. \left. \left(\omega + \beta_{Ro}r + \frac{\beta}{\gamma}\psi(\mathbf{x}) \right) \right]^{\frac{1}{1-q}} \right)
\end{aligned} \tag{6.22}$$

Thus if we first solve Eq. (6.13) for the stream function, then we can use ψ in Eq. (6.22) to compute the PDF of the dressed vorticity. In Section 5

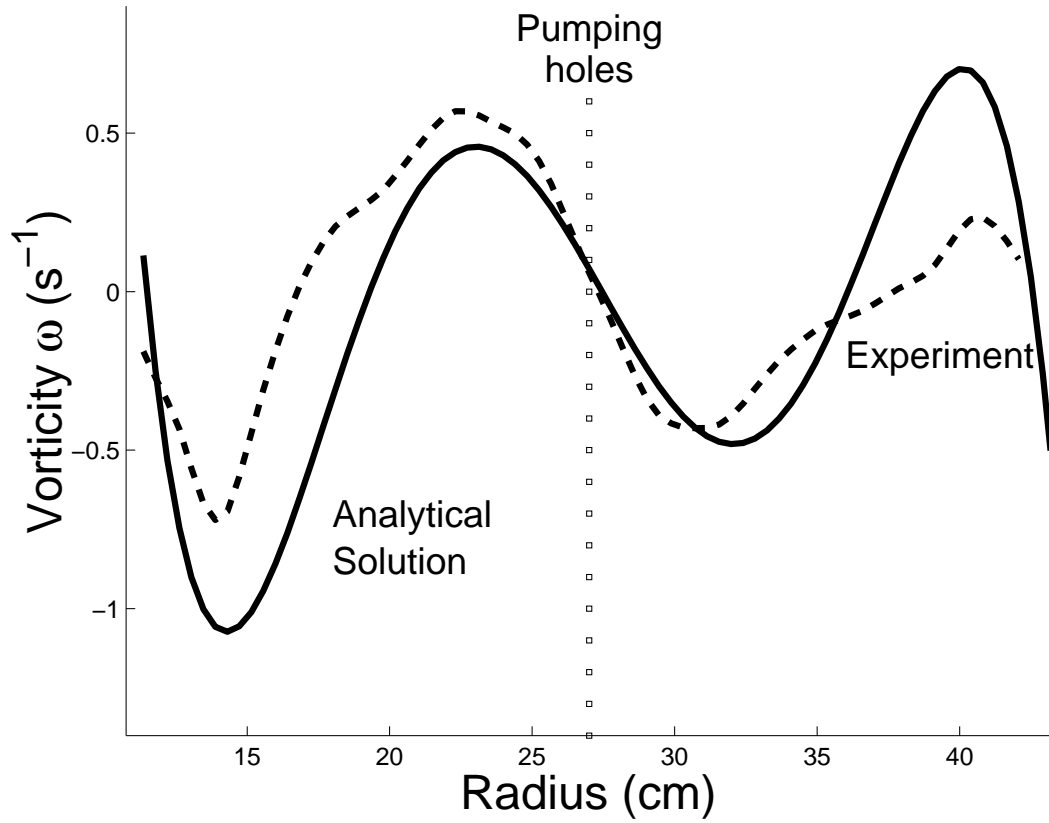


Figure 6.1: A comparison of the measured and the predicted radial profile for the vorticity. The theoretical curve is given by a least square fit to the solution of Eq. (6.13), which yields a value for the only adjustable parameter, $\frac{\beta}{\gamma} = -0.169$.

we compare the vorticity PDFs predicted for the extensive and nonextensive cases with the experimental observations.

6.4 Results

In this section we compare the solution for the stream function in Eq. (6.13) with the measurements of the azimuthally averaged vorticity. Using

that stream function we compare the PDF of the measured vorticity with the expressions derived using the extensive and nonextensive formalisms, Eqs. (6.15) and (6.22), respectively.

6.4.1 Qualitative Flow Features

In previous work, we demonstrated that our forcing configuration with no net vorticity injection yields a quasi-geostrophic flow with three jets alternating in their azimuthal direction [10]. Although the net vorticity injected is zero, the beta plane (sloping bottom) acts as vorticity selector: cyclonic (anticyclonic) structures cannot move outward (inward) because their motion outward (inward) would trigger a Rossby wave, thus restoring them to their original position. Positive (negative) potential vorticity is carried to the inner (outer) region of the annulus. Within the inner and outer regions the potential vorticity is well-mixed. Further, we found the potential vorticity profile was independent of forcing and rotation rate [10].

We observe the intermittent appearance of large anticyclones and cyclones. These structures drift in the direction opposite to the annulus rotation. The coherent vortices are created and decay in the region where the inlet-outlet semi-circles meet. A large coherent vortex is typically dissipated after traveling 180° in the azimuthal direction.

6.4.2 Stream Function Solution and the Vorticity Profile

Equation (6.13) involves two parameters: the beta plane coefficient, $\beta_{Ro} \equiv \frac{2\eta\Omega}{h_0} = 0.196 \text{ rad/s} \cdot \text{cm}$ (see Section 4), and the unknown parameter

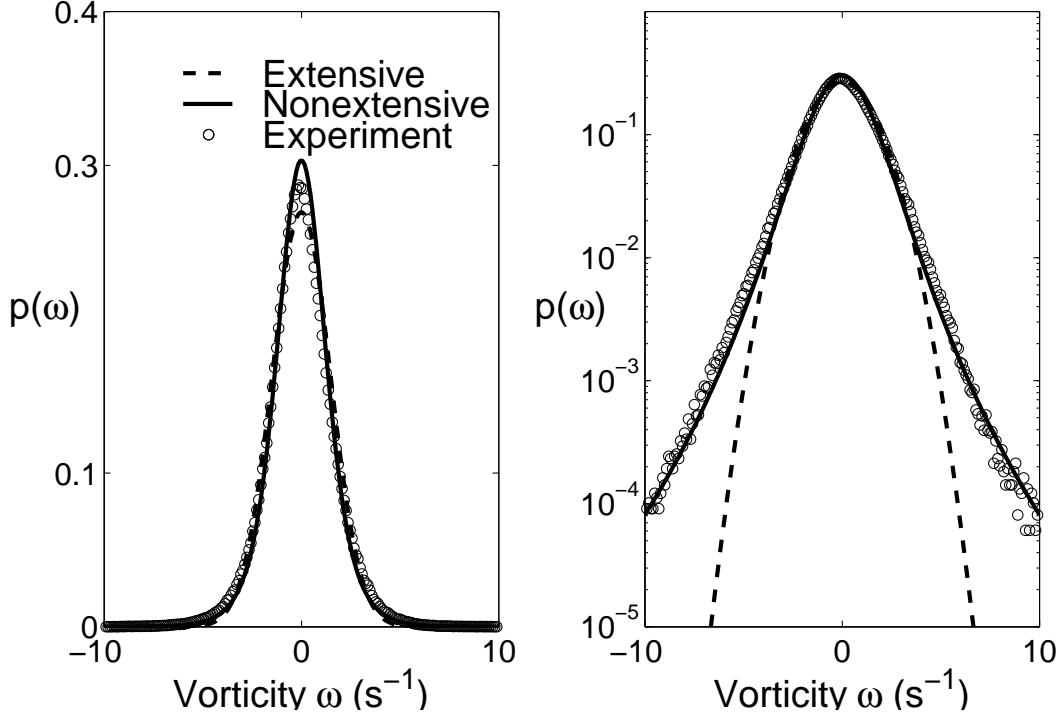


Figure 6.2: Comparison of the measured vorticity probability distribution function with the predictions of the extensive and nonextensive energy-entropy models, Equations (6.15) and (6.22), respectively. The linear plot on the left facilitates a comparison of the peaks of the PDF, and the log plot on the right facilitates a comparison of the tails of the distribution. The theoretical curves are least square fits that minimize $\left| \frac{p_{\text{experiment}}(\omega) - p_{\text{model}}(\omega)}{p_{\text{model}}(\omega)} \right|^2$ over 96 velocity fields. Using $\frac{\beta}{\gamma} = -0.169$ from the fit to the vorticity radial profile (Fig. 1) leaves two fit parameters, ω_m (0.7 ± 0.2) and γ (0.25 ± 0.03) for the extensive model, and three parameters for the nonextensive model, ω_m (0.7 ± 0.2), γ (0.15 ± 0.01) and the nonextensive parameter, q (1.9 ± 0.2). The uncertainties are the standard deviations of the fits to 96 different velocity fields.

$\frac{\beta}{\gamma}$, which is determined by fitting the predicted vorticity profile to the experimental data. One of boundary conditions needed to solve Eq. (6.13) is given by the condition that the azimuthally averaged vorticity is zero at $r = r_f$ because one-half of the forcing ring contains sources and the other half sinks; thus $\int \omega|_{r=r_f} d\theta = 0$. The other boundary condition is that the total circulation should be conserved, $\oint \mathbf{v} \cdot d\mathbf{l} = 0 = \int \omega r dr d\theta$ is compared with the best fit profile in Fig. 6.1. The predicted vorticity profile exhibits the qualitative features of the measured vorticity, and the locations of the predicted maxima and minima are in reasonable quantitative agreement with experiment. Note that value of the fit parameter is $\frac{\beta}{\gamma} = -0.169$. One reason for the difference between the model and the measurements is that the real fluid is viscous while the model assumes an inviscid fluid. The viscosity is dominant near the walls and is responsible for the generation of vorticity that is injected into the mean flow, an effect not captured by the theory.

6.4.3 Vorticity PDF

The extensive and nonextensive formalisms yield the same equation for the stream function, but the two approaches predict different PDFs for the vorticity, Eqs. (6.15) and (6.22), respectively. The nonextensive model involves the parameter q , which is absent from the extensive theory; the tails of the vorticity distribution are broad for $q > 1$ and narrow for $q < 1$. The predictions from the two models are compared to the measurements in Fig. 6.2. Using the value of $\frac{\beta}{\gamma} = -0.169$ obtained in the previous subsection, we have a single fit parameter, ω_m , for the extensive model and two fit parameters, ω_m and q , for the nonextensive model (see Fig. 6.2). The nonextensive model

describes the data over the entire range of vorticity, including both the peak and the broad tails of the distribution. In contrast, the extensive model fails to capture the broad tails of the distribution. The broad tails arise from the large coherent cyclones and anticyclones.

6.5 Discussion

Assuming conservation of energy and enstrophy, we have constructed models of two-dimensional inviscid flows using both extensive and nonextensive entropy. The two models yield the same prediction for the radial dependence of the azimuthally averaged vorticity. The model involves a single fit parameter and provides good agreement with the observations (Fig. 6.1). The extensive and nonextensive models yield different predictions for the vorticity PDF. The nonextensive model accurately describes the entire PDF, including the broad tails of the distribution (Fig. 6.2), which are not described by the extensive model. The value obtained for the nonextensive parameter is $q = 1.9 \pm 0.2$. Previous experiments with our system configured with an inner ring of sources and an outer ring of sinks produced a strong turbulent anti-cyclonic circulation. An analysis of structure function data from that experiment yielded $q = 1.32 \pm 0.03$ [18]. Experiments in our laboratory on turbulent Couette-Taylor flow were analyzed by Beck et al. [27], who found that the velocity increment structure function data yielded $q = 1.17$ for nearby spatial points. As expected, q decreased to unity for large separations between the points. Measurements by Porta et al. [1] of the acceleration of passive scalar particles in a strong turbulent shear flow have been analyzed by Beck [25], who obtained $q = 1.49$. The meaning of the different values of q is unclear and

remains a challenge for future work.

Chapter 7

Fluctuations

7.1 Introduction

In classical mechanics, the transformation to action-angle form makes a problem easier. An analogous transformation in shear flow was developed by Balmforth and Morrison [14, 15]. Later, Vanneste studied nonlinear interactions of modes by using this technique for flows on the β plane [223]. This technique started in studies of the Vlasov-Poisson system of plasma physics [150, 149]. Morrison [148] generalized the technique for a variety of fluid and plasma systems. Morrison and Shadwick [151] used the technique to obtain density fluctuations of plasma in action-angle variables. In this chapter, we obtain an expression for fluctuations of vorticity (or potential vorticity in the quasi-geostrophic case) in action-angle variables.

The partition function ($\int dpdq e^{-\beta E(p,q)}$) is defined in terms of the integration over canonical variables. Statistical mechanics for fluids uses a similar technique to determine the partition function over noncanonical variables

for a field theory [111]. Here we have a more sophisticated way to calculate fluctuations of vorticity by using the transformation which diagonalizes the Hamiltonian. First, we will find the normal form for the linear Hamiltonian of shear flow. Then, we present the calculation of ensemble-averaged vorticity fluctuations using the normal form of the linear Hamiltonian.

7.2 Statistical Mechanics

Our goal is to calculate the spectrum of vorticity fluctuations about shear flow. This is done by ensemble-averaging with the partition function as in statistical physics and field theory by diagonalization of the Hamiltonian formulation. New results are obtained for vorticity fluctuations. The results are compared to experiments of a rapidly rotating quasi-two dimensional shear flow.

In fluids, statistical mechanics of fluctuations have been treated by Burgers [35, 36, 37, 38, 39, 40, 41], Onsager [161], Lee [117], and others using point vortices, Fourier modes, or amplitudes at lattice sites as degrees of freedom (see e.g. [111, 220]). We differ from all of these approaches in that the ensemble-average measure is performed by using eigenmodes associated with the continuous spectrum (van Kampen modes for the Vlasov system) as degrees of freedom.

Our calculation is motivated by early statistical mechanical treatments of the lattice vibrations of a simple solid. We assume the existence of stable dynamical equilibrium states for 2D fluid systems, which are analogous to the vibrating lattice of the solid. Continuous spectrum of stable eigenmodes exists on the top of equilibrium velocity profile. Here, the equilibrium velocity profile

is determined by Rayleigh-Kuo's marginal stability criterion. In experiments, such dynamical equilibria can be selected by the competition between forcing and damping. The oscillations that occur on top of these equilibria are treated analogously to the solid lattice vibrations: they are assumed to be weakly interacting and the partition function is evaluated. From the partition function the fluctuation spectra are obtained.

7.2.1 Partition Function

Einstein and Debye calculated the specific heat of a solid by treating it as a collection of $3N$ quantized simple harmonic oscillators. They summed the partition function explicitly and then used it to obtain an expression that reproduced the Dulong-Petit relation in the classical limit, $C_v = 3Nk_B$. Thus they obtained the well-known equipartition result for a solid, i.e., that the average energy contains a full $k_B T_b$ per degree of freedom, where T_b is the temperature of the heat bath.

For classical systems the expression for the partition function is given by the following:

$$\mathcal{Z} = \int e^{-\beta E(q,p)} \prod_i^N dq_i dp_i, \quad (7.1)$$

where $E(p, q)$ is a conserved energy and $\prod_i^N dq_i dp_i$ is a phase space volume. In general, $\beta E(p, q)$ can be replaced by the free energy including other conserved quantities such as the number of particles and so on. In those systems, the Hamiltonian defines the energy of a state, and a volume measure (integration measure) arises from Liouville's theorem on the preservation of phase space volume in the course of time.

Partition functions are easily evaluated for stable Hamiltonian systems

that are quadratic forms in the phase space variables, $H = \sum (pMp/2 + qGp + qVq/2)$ where $M, G,$ and V are any symmetric matrices, by using canonical transformations to diagonalize the Hamiltonian. However, cubic and higher order terms are generally not diagonalizable. This indicates why quadratic conserved quantities are important in the statistical mechanics (Details are in [97]). For stable systems, canonical transformations result in any of the following normal forms:

$$H = \sum_i^N W_i(Q_i^2 + P_i^2)/2 = \sum_i^N i\hat{W}_i\hat{Q}_i\hat{P}_i, \quad (7.2)$$

where Q and P are functions of p and q . The frequency of the i th mode is written as W_i and \hat{W}_i in the normal forms. Therefore, the ensemble-averaged energy of the system interacting with a heat bath is calculated by performing a simple Gaussian integral. The results indicate energy equipartition with a $k_B T_b/2$ contribution for each degree of freedom.

For the 2D Euler fluid, we find an analog of the calculation above. However, the partition function should be evaluated in the context of a field theory. The partition function is written as a functional integral of the form

$$\mathcal{Z} = \int e^{-\beta H[q,p]} \mathcal{D}q \mathcal{D}p, \quad (7.3)$$

where $q(x, y)$ and $p(x, y)$ are functions of coordinates x and y . Functional integrals were introduced by Wiener [230] and used in Feynman's path integral formulation of quantum mechanics. When the Hamiltonian is a quadratic function one can consistently do calculations by discretizing into lattice sites or Fourier modes and reducing the calculation to a sequence of ordinary integrals. Transformation of infinite-degree-of-freedom Hamiltonian systems into action-angle form is done in [149, 151].

7.3 Hamiltonian System and Fluctuations

The 2D Euler equation that describes an incompressible and inviscid fluid is

$$\frac{\partial \omega}{\partial t} + [\psi, \omega] = 0, \quad (7.4)$$

where $[\psi, \omega] := \psi_x \omega_y - \psi_y \omega_x$ and the streamfunction and vorticity are related by $\psi = -\Delta^{-1} \omega$, or in the case of quasigeostrophy another integral relation such as $\psi = -\Delta^{-1}(q - \beta_{Ro} r)$ is used in our annulus geometry, where q is the potential vorticity. Thus, small modifications are required for quasigeostrophic systems. Eq. (7.4) can be written in the form

$$\frac{\partial \omega}{\partial t} = \{\omega, H\} = [\omega, \psi], \quad (7.5)$$

where the noncanonical Poisson bracket is given by

$$\{A, B\} = \int_{\mathbf{D}} \omega \left[\frac{\delta A}{\delta \omega}, \frac{\delta B}{\delta \omega} \right] dx dy, \quad (7.6)$$

and the Hamiltonian is given by

$$H = -\frac{1}{2} \int_{\mathbf{D}} \omega \psi dx dy. \quad (7.7)$$

We note that \mathbf{D} is the domain occupied by the fluid and ψ is constant on the boundary. The equations of motion of the 1D Vlasov equation and the 2D fluid system have the isomorphic form of Eq. (7.5) including the noncanonical Poisson bracket. This isomorphic equation of motion is an infinite dimensional Hamiltonian system or field system with a similar noncanonical Poisson bracket. Our method in this chapter can be generalized for magnetohydrodynamics (MHD) and other continuum systems.

We consider linear fluctuations about the following class of stable equilibria. For the Vlasov system, ω and ψ are replaced by an electron phase

space density f and a particle energy $\frac{m}{2}v^2 + e\phi$ and the phase space variables x and y are replaced by the position x and the velocity v . We suppose the phase space density is given by a Maxwellian, $f_0 \sim \exp(-mv^2/2k_B T_e)$, where we note that the temperature is merely a parameter that describes the equilibrium state. We can be assured of stability if this function is a monotonic function of v^2 [79]. Because plasmas can reside for a long time in dynamical equilibrium states away from Maxwellian, we can distinguish between the equilibrium temperature T_e and the bath temperature of the fluctuations T_b .

In the case of shear flow, we suppose the equilibrium is a flow along a finite channel with a cross stream variation: $U_x(y)$. For our annulus system, U_x is the azimuthal velocity and y is the radius when we neglect the curvature of annulus. By Rayleigh's criterion we are assured of stability if $U'_x \neq 0$. Setting $\omega = U'_x(y) + \delta\omega(x, y, t)$ (where the prime means y derivative) and linearizing we obtain the linearized Euler equation for vorticity oscillations. For the Vlasov case, the system was investigated by Landau, van Kampen and others. We follow papers [149, 147] and solve it as one would solve a Hamiltonian system.

By linearizing the vorticity $\omega = U'_x(y) + \delta\omega(y, x)$ and the streamfunction $\psi = \psi_e(y) + \delta\psi(y, x)$, Eq. (7.5) becomes

$$\frac{\partial \delta\omega}{\partial t} + [\delta\omega, \psi_e] + [U'_x, \delta\psi] = 0. \quad (7.8)$$

If we define $U_x(y) := d\psi_e/dy$, then

$$\frac{\partial \delta\omega}{\partial t} + U_x(y) \frac{\partial \delta\omega}{\partial x} - U''_x(y) \frac{\partial \delta\psi}{\partial x} = 0. \quad (7.9)$$

The linear theories of the Euler equation are Hamiltonian with the Poisson bracket

$$\{F, G\}_L := \int U'_x \left[\frac{\delta F}{\delta \delta\omega}, \frac{\delta G}{\delta \delta\omega} \right] dx dy, \quad (7.10)$$

and the linear Euler model has the Hamiltonian

$$H_L = -\frac{1}{2} \int_{\mathbf{D}} \int_{\mathbf{D}} \left(\frac{U_x}{U''_x} (\delta\omega)^2 - \delta\omega \delta\psi \right) dx dy, \quad (7.11)$$

which is the fluid version of the Kruskal and Oberman energy [112]. It is easy to verify that the linear Euler equation can be written as

$$\frac{\partial \delta\omega}{\partial t} = \{\delta\omega, H_L\}_L. \quad (7.12)$$

The fact that $\delta\omega$ depends on both x and y makes the problem difficult. By decomposing it into x and y -dependence separately, Eq. (7.12) is easier to handle when diagonalizing the Hamiltonian.

7.3.1 Canonization and Diagonalization

In order to calculate the functional integral of Eq. (7.3) for the partition function, we transform the bracket of Eq. (7.10) into canonical form and then find a canonical transformation to variables in which H_L is diagonal. To this end, we expand the fluctuating parts of the vorticity and streamfunction as

$$\delta\omega(x, y; t) = \sum_{k=-\infty}^{\infty} \omega_k(y, t) e^{ikx}, \quad \delta\psi(x, y; t) = \sum_{k=-\infty}^{\infty} \psi_k(y, t) e^{ikx}, \quad (7.13)$$

where ω_k and ψ_k depend on y and t , whereas $\delta\omega$ and $\delta\psi$ depend on x, y and t . The equation of motion becomes

$$\frac{\partial \omega_k}{\partial t} + ik U_x \omega_k = ik U''_x \psi_k \quad (7.14)$$

$$(U_x - c) \omega_k = U''_x \psi_k. \quad (7.15)$$

Eq. (7.10) and (7.11) yield the Poisson bracket

$$\{A, B\}_L = \sum_{k=1}^{\infty} ik \int_{\mathbf{D}} U''_x \left(\frac{\delta A}{\delta \omega_k} \frac{\delta B}{\delta \omega_{-k}} - \frac{\delta B}{\delta \omega_k} \frac{\delta A}{\delta \omega_{-k}} \right) dy \quad (7.16)$$

and the Hamiltonian for the linear dynamics

$$\begin{aligned} H_L &= -\frac{1}{2} \sum_{k=1}^{\infty} \int_{\mathbf{D}} \left(\frac{U_x}{U_x''} \omega_k - \psi_k \right) \omega_{-k} dx \\ &= \sum_{k,k'} \int_{\mathbf{D}} \int_{\mathbf{D}} \omega_k(y) \mathcal{A}_{k,k'}(y|y') \omega_{k'}(y') dy dy', \end{aligned} \quad (7.17)$$

where $\mathcal{A}_{k,k'}(y|y') := \frac{U_x}{U_x''} \delta_{k,-k'} \delta(y - y') - \mathcal{K}_k(y, y') \delta_{k,-k'}$. Here, ψ_k is given by the following expression.

$$\psi_k(y, t) = \int_{\mathbf{D}} \mathcal{K}_k(y, y') \omega_k(y', t) dy', \quad (7.18)$$

where the kernel \mathcal{K}_k is given as

$$\mathcal{K}_k(y, y') = \begin{cases} \frac{\sinh(k(1-y)) \sinh(k(1+y'))}{k \sinh(2k)} & \text{for } y > y', \\ \frac{\sinh(k(1-y')) \sinh(k(1+y))}{k \sinh(2k)} & \text{for } y \leq y'. \end{cases} \quad (7.19)$$

For convenience, we normalize the range of y axis as $[-1, 1]$ and set the streamfunction to zero at $y = -1$ and $y = 1$. If you set the streamfunction to zero at $y = -1$ and $y = 1$, the hyperbolic sine function in Eq. (7.19) is replaced by the hyperbolic cosine function. This kernel is also called *Green's function*.¹

¹The Green's function is calculated as follows. The basic equation for Green's function is

$$\left(\frac{\partial^2}{\partial y^2} + k^2 \right) \mathcal{K}_k(y, y') = \delta(y - y'). \quad (7.20)$$

We can find the solutions for

$$\frac{\partial^2 u_1}{\partial y^2} = k^2 u_1 \quad (7.21)$$

$$\frac{\partial^2 u_2}{\partial y^2} = k^2 u_2 \quad (7.22)$$

with boundary conditions as

$$u_1(-1) = 0, \quad u_2(1) = 1. \quad (7.23)$$

Trivial calculation gives

$$u_1(y_{<}) = \sinh(k(y_{<} + 1)), \quad u_2(y_{>}) = \sinh(k(y_{>} - 1)). \quad (7.24)$$

All situations in the Vlasov equation are similar to our shear flow case. Details are given in [149, 147] for Vlasov.

Time-dependence in Eq.(7.15) can be converted as $\omega_k(y, c) = \int \omega_k(y, t) e^{-ikct} dt$ where c is a phase velocity in the x direction. If the flow profile is monotonic, then we can find a unique point y_c where the phase velocity c matches with $U_x(y_c)$. For a convenience, we replace c by y_c . Then, the expression for ω_k is given by

$$\omega_k(y, y_c) = \lambda_k \delta(U_x(y) - U_x(y_c)) + \mathcal{P} \frac{U_x''(y) \psi_k(y, y_c)}{U_x(y) - U_x(y_c)} \quad (7.26)$$

where \mathcal{P} means the Cauchy principal value, $\delta(U_x(y) - U_x(y_c))$ is the Dirac delta distribution and λ_k is yet to be determined. Decomposing ω_k into two parts, we get Eq. (7.26). This expression shows the singular nature of the mode.

The unknown λ_k is obtained by the normalization condition $1 = \int_{\mathbf{D}} \omega_k dy$. Consequently,

$$\frac{\lambda_k}{|U_x'(y)|} = 1 - \mathcal{P} \int_{\mathbf{D}} \frac{U_x''(y) \psi_k(y, y_c)}{U_x(y) - U_x(y_c)} dy. \quad (7.27)$$

Plugging Eq. (7.27) into Eq. (7.26), we get

$$\begin{aligned} \omega_k(y, y_c) &= \left(1 - \mathcal{P} \int_{\mathbf{D}} \frac{U_x''(y') \psi_k(y', y_c)}{U_x(y') - U_x(y_c)} dy' \right) \delta(U_x(y) - U_x(y_c)) \\ &\quad + \mathcal{P} \frac{U_x''(y) \psi_k(y, y_c)}{U_x(y) - U_x(y_c)}. \end{aligned} \quad (7.28)$$

Equation (7.16) is not quite of canonical form. In order to find the canonical variables, we transform from one set of variables another set that

The Wronskian for u_1 and u_2 is $u_1 u_2' - u_2 u_1' = -k \sinh(2k)$. Therefore, the Green's function is given as

$$\mathcal{K}_k(y_>, y_<) = \frac{u_1(y_<) u_2(y_>)}{u_1 u_2' - u_2 u_1'} = \frac{\sinh(k(1 - y_>)) \sinh(k(1 + y_<))}{k \sinh(2k)}. \quad (7.25)$$

is more suitable. In Eq. (7.16), ω_k and ω_{-k} are independent variables. By introducing new variables

$$q_k = \frac{\omega_k}{ikU_x''}, \quad p_k = \omega_{-k}, \quad (7.29)$$

we obtain Hamiltonian equation in terms of canonical variables. Consequently, the canonical Poisson bracket becomes

$$\{A, B\}_L = \sum_{k=1}^{\infty} \int_{\mathbf{D}} \left(\frac{\delta A}{\delta q_k} \frac{\delta B}{\delta p_k} - \frac{\delta B}{\delta q_k} \frac{\delta A}{\delta p_k} \right) dy. \quad (7.30)$$

Because of the term $\psi_k \omega_k$ of H_L , the energy is not a diagonal quadratic form. Diagonalizing the Hamiltonian is done by using a type-2 mixed variable generating functional [82]

$$\mathcal{F}[q, P] = \sum_{k=1}^{\infty} \int_{\mathbf{D}} q_k(y) G_k[P_k](y, y_c) dy \quad (7.31)$$

to effect the canonical coordinate change $(q_k, p_k) \leftrightarrow (Q_k, P_k)$ according to

$$p_k(y, y_c) = \frac{\delta \mathcal{F}[q, P]}{\delta q_k(y, y_c)} = G_k[P_k](y, y_c), \quad Q_k(y', y_c) = \frac{\delta \mathcal{F}[q, P]}{\delta P_k(y', y_c)} = G_k^\dagger[q_k](y', y_c), \quad (7.32)$$

where G_k^\dagger is the adjoint of G_k , which is defined by $\int q_k G_k[P_k](y, y_c) dy = \int G_k^\dagger[q_k] P_k(y', y_c) dy'$. The essential ingredient of Eq. (7.31) is the integral transform G_k . Eq. (7.28) gives a form of G_k as

$$\begin{aligned} \omega_k(y, y_c) &=: G_k[\Lambda_k](y, y_c) := \int_{\mathbf{D}} \mathcal{G}_k(y, y') \Lambda_k(y', y_c) dy' \\ &:= \epsilon_R(y) \Lambda_k(y, y_c) + \mathcal{H} \left[-\frac{\pi \psi_k(y, y') U_x''(y)}{U_x'(y')} \Lambda_k(y', y_c) \right] (y, y_c), \end{aligned} \quad (7.33)$$

where

$$\epsilon_I(y, y') = -\frac{\pi \psi_k(y, y') U_x''(y')}{U_x'(y')}, \quad \epsilon_R(y) = 1 + \mathcal{H} \left[-\frac{\pi \psi_k(y', y) U_x''(y')}{U_x'(y')} \right] (y) \quad (7.34)$$

with $\mathcal{H}[g]$ being the Hilbert transform

$$\mathcal{H}[g(y, y')](y) := \frac{\mathcal{P}}{\pi} \int_{\mathbf{D}} \frac{g(y, y')}{U_x(y') - U_x(y)} dU_x(y'), \quad (7.35)$$

with \mathcal{P} denoting the Cauchy principal value. The inverse and identities of this transform are discussed in [16, 147].

The transformation generated by \mathcal{F} diagonalizes the Hamiltonian. Finally, the linear Hamiltonian becomes

$$H_L = \sum_{k=1}^{\infty} \int_{\mathbf{D}} iW_k(y)Q_k(y)P_k(y)dy, \quad (7.36)$$

where $W_k(y) = kU_x(y)$. Equation (7.36) represents the normal form of Hamiltonian dynamics in infinite dimensions. Now we obtain fluctuation spectra with this diagonalized Hamiltonian and these canonical variables. Details are presented in [16, 148].

7.3.2 Solving for ψ_k

Once a function ψ_k is given, we can calculate the G_k transformation. Plugging Eq. (7.28) into Eq. (7.18) and replacing y_c with y' , we have

$$\begin{aligned} \psi_k(y, y') &= \mathcal{K}_k(y, y') + \int_{\mathbf{D}} \frac{\mathcal{K}_k(y, y'') - \mathcal{K}_k(y, y')}{U_x(y'') - U_x(y')} U_x''(y'') \psi_k(y'', y') dy'' \\ &= \mathcal{K}_k(y, y') + \int_{\mathbf{D}} \mathcal{F}_k(y, y''; y') \psi_k(y'', y') dy''. \end{aligned} \quad (7.37)$$

This equation is classified as a Fredholm equation of the second kind: $u(x) = f(x) + \lambda \int_a^b K(x, t)u(t)dt$ where $u(x)$ is the unknown function, $K(x, t)$ and $f(x)$ are known. For this case, λ plays the role of an eigenvalue and $K(x, t)$ is the kernel of the integral equation.

There are several ways to solve Fredholm equations [62]. We will use Neumann series to solve Eq. (7.37) by iteration. This method is applicable when the integral is small. We begin with the approximation

$$\psi_k(y, y') \approx \mathcal{K}_k(y, y') . \quad (7.38)$$

A second approximation is obtained by substituting the beginning approximation into Eq. (7.37).

$$\psi_k(y, y') \approx \mathcal{K}_k(y, y') + \int_{\mathbf{D}} \mathcal{F}_k(y, y'; t_1) \mathcal{K}_k(t_1, y') dt_1 . \quad (7.39)$$

After repeating this process over and over and we get

$$\begin{aligned} \psi_k(y, y') \approx & \mathcal{K}_k(y, y') + \int_{\mathbf{D}} \mathcal{F}_k(y, y'; t_1) \mathcal{K}_k(t_1, y') dt_1 \\ & + \int_{\mathbf{D}} \int_{\mathbf{D}} \mathcal{F}_k(y, y'; t_1) \mathcal{F}_k(t_1, y'; t_2) \mathcal{K}_k(t_2, y') dt_1 dt_2 + \dots \end{aligned} \quad (7.40)$$

This series can be written as

$$\psi_k(y, y') = \sum_{i=1}^{\infty} \phi_i(y, y') , \quad (7.41)$$

where

$$\begin{aligned} \phi_0(y, y') &= \mathcal{K}_k(y, y') \\ \phi_1(y, y') &= \int_{\mathbf{D}} \mathcal{F}_k(y, y'; t_1) \mathcal{K}_k(t_1, y') dt_1 \\ \phi_2(y, y') &= \int_{\mathbf{D}} \int_{\mathbf{D}} \mathcal{F}_k(y, y'; t_1) \mathcal{F}_k(t_1, y'; t_2) \mathcal{K}_k(t_2, y') dt_1 dt_2 . \end{aligned} \quad (7.42)$$

The series will converge if the integral is bounded and small.

7.3.3 Fluctuation Spectra

The ensemble average of a quantity \mathcal{O} is given in terms of \mathcal{Z} according to

$$\langle \mathcal{O} \rangle = \int \mathcal{D}q \mathcal{D}p \mathcal{O} e^{-\beta H} / \mathcal{Z} . \quad (7.43)$$

where the partition function \mathcal{Z} with canonical coordinates is

$$\mathcal{Z} = \int e^{-\beta H_L[q,p]} \mathcal{D}q \mathcal{D}p = \int e^{-\beta \sum_k \int i W_k P_k Q_k dy} \prod_k \mathcal{D}P_k \mathcal{D}Q_k. \quad (7.44)$$

We note that the two canonical coordinates are defined as $P_k := G_k^{-1}[\omega_{-k}]$ and $Q_k := G_k^{-1}[\omega_k/(ikU''_x)]$. For the Vlasov case, P_k and Q_k are the electric fields of a van Kampen mode. Analogous to the Vlasov system, we suppose that $\Lambda_k(y)$ are independent from other modes and positions $\Lambda_{k'}(y)$ such as

$$\langle \Lambda_k(y, y_c) \Lambda_{k'}^*(y', y_c) \rangle = \mathcal{M}_k(y) \delta_{kk'} \delta(U(y) - U(y')), \quad (7.45)$$

where, $\Lambda_k(y) := G_k^{-1}[\omega_k]$ and $\mathcal{M}_k(y)$ is the coefficient depending on y . In this form of expression, an equipartition of energy is not clear. However, if one transforms from Λ_k , to the correct canonical variables, the variables in which the Hamiltonian is diagonal, then equipartition is obtained for all k -values. For the Vlasov system, f_0 is Maxwellian and the bath and equilibrium temperatures are equal, and Eq. (7.45) agrees with a result first given by Thompson [209, 208]. However, for general equilibria, the form of f_0 differs from Thompson's. Derivations (e.g. [180, 181]) are not performed as asymptotic expansions in a dimensionless number, so it is at present unclear why the results differ.

Analogous to the energy, H_L , we start from the quadratic structure of canonical coordinates

$$\begin{aligned} Q &= \sum_{k=1}^{\infty} \int_{\mathbf{D}} \int_{\mathbf{D}} \langle \Lambda_k(y, y_c) \Lambda_k^*(y', y_c) \rangle f_k(y) f_k(y') dy dy' \\ &= \sum_{k=1}^{\infty} \int_{\mathbf{D}} \int_{\mathbf{D}} \langle \omega_k(y'', y_c) \omega_k^*(y''', y_c) \rangle g_k(y'') g_k(y''') dy'' dy'''. \end{aligned} \quad (7.46)$$

Using with the transformation $f_k(y) = G_k^\dagger[g_k(y'')](y)$,

$$\begin{aligned}
Q &= \sum_{k=1} \int_{\mathbf{D}} \int_{\mathbf{D}} \langle \Lambda_k(y, y_c) \Lambda_k^*(y', y_c) \rangle G_k^\dagger[g_k(y'')](y) G_k^\dagger[g_k(y''')](y') dy dy' \quad (7.47) \\
&= \sum_{k=1} \int_{\mathbf{D}} \int_{\mathbf{D}} \langle G_k[\Lambda_k(y, y_c)](y'') G_k[\Lambda_k^*(y', y_c)](y''') \rangle g_k(y'') g_k(y''') dy'' dy''' \\
&= \sum_{k=1} \int_{\mathbf{D}} \int_{\mathbf{D}} \langle \omega_k(y'', y_c) \omega_k^*(y''', y_c) \rangle g_k(y'') g_k(y''') dy'' dy''' . \quad (7.48)
\end{aligned}$$

Our guess ($f_k(y) = G_k^\dagger[g_k(y'')](y)$) in the beginning leads to Eq. (7.47) to Eq. (7.48).

Plugging Eq. (7.45) into Eq. (7.47), we get

$$\begin{aligned}
Q &= \sum_{k=1}^{\infty} \int_{\mathbf{D}} \int_{\mathbf{D}} \mathcal{M}_k(y) \delta(U_x(y) - U_x(y')) G_k^\dagger[g_k(y'')](y) G_k^\dagger[g_k(y''')](y') dy dy' \\
&= \sum_{k=1}^{\infty} \int_{\mathbf{D}} \int_{\mathbf{D}} G_k \left[\mathcal{M}_k(y) \left(\epsilon_R(y''') \delta(U_x(y) - U_x(y''')) + \mathcal{P} \frac{U_x''(y''') \psi_k(y''', y)}{U_x(y''') - U_x(y)} \right) \right] (y'') \\
&\quad g_k(y'') g_k(y''') dy'' dy''' . \quad (7.49)
\end{aligned}$$

The above equation is split into four terms

$$\begin{aligned}
Q &= \sum_k \int_{\mathbf{D}} \int_{\mathbf{D}} \left(\mathcal{M}_k(y'') \epsilon_R(y'') \epsilon_R(y''') \delta(U_x(y'') - U_x(y''')) \right. \\
&\quad + \epsilon_R(y''') \mathcal{P} \frac{U_x''(y'') \psi_k(y'', y''') \mathcal{M}_k(y''')}{U_x(y'') - U_x(y''')} \\
&\quad + \epsilon_R(y'') \mathcal{P} \frac{U_x''(y''') \psi_k(y''', y'') \mathcal{M}_k(y'')}{U_x(y''') - U_x(y'')} \\
&\quad \left. + \int_{\mathbf{D}} \mathcal{P} \frac{U_x''(y'') \psi_k(y'', y)}{U(y_c) - U(y)} \mathcal{P} \frac{U_x''(y''') \psi_{k'}(y''', y)}{U_x(y''') - U_x(y)} \mathcal{M}_k(y) dy \right) \\
&\quad g_k(y'') g_k(y''') dy'' dy''' . \quad (7.50)
\end{aligned}$$

The last term in Eq. (7.50) is evaluated by using Poincaré-Bertrand transpo-

sition formula.²

Finally, we get

$$\begin{aligned}
Q &= \sum_{k=1}^{\infty} \int_{\mathbf{D}} \int_{\mathbf{D}} \left(\mathcal{M}_k(y'') |\epsilon_k(y'')|^2 \delta(U_x(y'') - U_x(y''')) \right. \\
&\quad + \mathcal{P} \frac{U_x''(y'')}{U_x(y'') - U_x(y''')} G_k [\mathcal{M}_k(y) \psi_k(y'', y)](y''') \\
&\quad \left. + \mathcal{P} \frac{U_x''(y''')}{U_x(y''') - U_x(y'')} G_k [\mathcal{M}_k(y) \psi_k(y''', y)](y'') \right) g_k(y'') g_k(y''') dy'' dy'''.
\end{aligned} \tag{7.53}$$

Comparing Eq. (7.46) and Eq. (7.53), one gets the vorticity fluctuation

²Poincare-Bertrand transposition formula is like

$$\begin{aligned}
\mathcal{P} \frac{1}{y - z_1} \mathcal{P} \frac{1}{y - z_2} &= \lim_{\nu \rightarrow 0} \frac{1}{4} \left[\frac{1}{y - z_1 - i\nu} + \frac{1}{y - z_1 + i\nu} \right] \left[\frac{1}{y - z_2 - i\nu} + \frac{1}{y - z_2 + i\nu} \right] \\
&= \lim_{\nu \rightarrow 0} \frac{1}{4} \left[\frac{1}{y - z_1 - i\nu} - \frac{1}{y - z_2 - i\nu} \right] \frac{1}{z_1 - z_2} \\
&\quad + \frac{1}{4} \left[\frac{1}{y - z_1 + i\nu} - \frac{1}{y - z_2 + i\nu} \right] \frac{1}{z_1 - z_2} \\
&\quad + \frac{1}{4} \left[\frac{1}{y - z_1 - i\nu} - \frac{1}{y - z_2 + i\nu} \right] \frac{1}{z_1 - z_2 + 2i\nu} \\
&\quad + \frac{1}{4} \left[\frac{1}{y - z_1 + i\nu} - \frac{1}{y - z_2 - i\nu} \right] \frac{1}{z_1 - z_2 - 2i\nu} \\
&= \left(\mathcal{P} \frac{1}{y - z_1} - \mathcal{P} \frac{1}{y - z_2} \right) \frac{1}{z_1 - z_2} \\
&\quad + \frac{1}{4} [\{i\pi\delta(y - z_1) - i\pi\delta(y - z_2) - i\pi\delta(y - z_1) + i\pi\delta(y - z_2)\} \cdot \frac{1}{z_1 - z_2} \\
&\quad - 2i\pi\delta(z_2 - z_1) \{i\pi\delta(y - z_1) + i\pi\delta(y - z_2)\} \\
&\quad - 2i\pi\delta(z_2 - z_1) \{i\pi\delta(y - z_1) + i\pi\delta(y - z_2)\}] \\
&= \left(\mathcal{P} \frac{1}{y - z_1} - \mathcal{P} \frac{1}{y - z_2} \right) \frac{1}{z_1 - z_2} + \frac{\pi^2}{2} [\delta(y - z_1) + \delta(y - z_2)] \delta(z_1 - z_2) \\
&= \left(\mathcal{P} \frac{1}{y - z_1} - \mathcal{P} \frac{1}{y - z_2} \right) \frac{1}{z_1 - z_2} + \pi^2 \delta(y - z_1) \delta(z_1 - z_2) \tag{7.51}
\end{aligned}$$

by using

$$\lim_{\nu \rightarrow 0} \frac{1}{x \pm i\nu} = \mathcal{P} \frac{1}{x} \mp i\pi\delta(x). \tag{7.52}$$

such as

$$\begin{aligned}
\langle \omega_k(y) \omega_k^*(y') \rangle &= \mathcal{M}_k(y) |\epsilon_k(y)|^2 \delta(U_x(y) - U_x(y')) \\
&+ \mathcal{P} \frac{U_x''(y)}{U_x(y) - U_x(y')} G_k [\mathcal{M}_k(y'') \psi_k(y, y'')] (y') \\
&+ \mathcal{P} \frac{U_x''(y')}{U_x(y') - U_x(y)} G_k [\mathcal{M}_k(y'') \psi_k(y', y'')] (y) \\
&= \delta_{k,k'} [\mu(y) \delta(y - y') + \nu_k(y, y')] , \tag{7.54}
\end{aligned}$$

where μ and ν_k are determined by the equilibrium shear flow profile and \mathcal{M}_k . One remark is that the results are symmetric under changing y to y' . In short, our process transforms from the variable $\Lambda_k(y_c)$ back to $\omega_k(y)$ and obtains the above result for phase space fluctuations.

Vlasov Case

In the case of the Vlasov-Poisson system, both y and $U(y)$ in our previous formulations are replaced by the velocity v . The variable ϵ is the dielectric function and has two components; an imaginary part ϵ_I and a real part ϵ_R ,

$$\epsilon_I(v') = -\pi \omega_p^2 \frac{f_e'(v')}{k^2}, \quad \epsilon_R(v') = 1 + \mathcal{H}[\epsilon_I(v)](v'), \tag{7.55}$$

where f is the phase space density of electrons, ω_p is the plasma frequency and v represents the momentum part of phase space. For the Vlasov case, the function analogous to $\psi_k(y', y)$ is constant and equal to ω_p^2/k^2 .

The particle energy \mathcal{E}_k is simply ω_p^2/k^2 , which is analogous to ψ_k in the 2D fluid. From the above relations, the imaginary part of dielectric function is expressed as $\epsilon_I(v') = -\pi f_e'(v') \mathcal{E}_k$. The function \mathcal{M}_k of Eq. (7.45), when $Q_k = \delta E_k$, is expressed as

$$\mathcal{M}_k(v) = \frac{16}{V\beta} \frac{\epsilon_I(v)}{v |\epsilon_k(v)|^2}, \tag{7.56}$$

where the Hilbert transform is

$$\mathcal{H}[g(v)](v') = \frac{\mathcal{P}}{\pi} \int_{\mathbb{R}} \frac{g(v)}{v - v'} dv. \quad (7.57)$$

where v is the electron velocity. Since $H_L = \frac{V}{32\pi} \sum_k \int dv v \pi \frac{|\epsilon_k|^2}{\epsilon_I} |\delta E_k|^2$, we can evaluate the ensemble average over this Hamiltonian.

The main transformation in the plasma case is

$$G_k[P_k(u)](v) = \epsilon_R(v) P_k(v) + \epsilon_I \mathcal{P} \int \frac{P_k(u)}{u - v} du. \quad (7.58)$$

With the aid of Eq.(7.53), the fluctuation, for electrons $\langle \delta f_k \delta f_{k'} \rangle$ in a plasma is deduced from the electric field fluctuation $\langle \delta E_k \delta E_{k'} \rangle$.

$$\begin{aligned} & \langle G_k[\delta E_k(v)](v') G_{k'}[\delta E_{k'}^*(v'')](v''') \rangle \\ &= \frac{16}{V\beta} \frac{\epsilon_I(v')}{v'} \delta(v' - v''') - \frac{(\epsilon_I(v') G_k[\mathcal{M}_k(v)](v''') - \epsilon_I(v''') G_k[\mathcal{M}_k(v'')](v'))}{\pi(v' - v''')} \end{aligned} \quad (7.59)$$

Before we go further, one identity is needed to simplify this equation. Kramer-Kronig relation yields the relation between the real and imaginary part of $1/\epsilon_k$ such as [149]

$$\mathcal{H} \left[\frac{\epsilon_I(v)}{|\epsilon_k(v)|^2} \right] (v') = 1 - \frac{\epsilon_R(v')}{|\epsilon_k(v')|^2}. \quad (7.60)$$

Also, use simple factorizing algebra like

$$\frac{1}{v(v - v')} = \frac{1}{v'} \left[\frac{1}{v - v'} - \frac{1}{v} \right]. \quad (7.61)$$

Two identities above are enough to simplify the expression for the electron

fluctuations $\langle ff \rangle$. The last term inside the bracket in Eq. (7.59) is

$$\begin{aligned}
& \frac{16}{V\beta} \left[\frac{\epsilon_I(v')}{v''} \left\{ \frac{\epsilon_R(v'')\epsilon_I(v'')}{|\epsilon_k(v'')|^2} + \epsilon_I(v'') \left(\mathcal{H} \left[\frac{\epsilon_I(v)}{|\epsilon_k(v)|^2} \right] (v'') - \frac{\mathcal{P}}{\pi} \int_{\mathbb{R}} \frac{\epsilon_I(v)}{v|\epsilon_k|^2} dv \right) \right\} \right. \\
& - \left. \frac{\epsilon_I(v'')}{v'} \left\{ \epsilon_R(v') \frac{\epsilon_I(v')}{|\epsilon_k(v')|^2} + \epsilon_I(v') \left(\mathcal{H} \left[\frac{\epsilon_I(v)}{|\epsilon_k(v)|^2} \right] (v') - \frac{\mathcal{P}}{\pi} \int_{\mathbb{R}} \frac{\epsilon_I(v)}{v|\epsilon_k|^2} dv \right) \right\} \right] \\
& = \frac{\epsilon_I(v'')\epsilon_I(v')}{v''} \left(1 - \frac{\mathcal{P}}{\pi} \int_{\mathbb{R}} \frac{\epsilon_I(v)}{v|\epsilon_k|^2} dv \right) - \frac{\epsilon_I(v')\epsilon_I(v'')}{v'} \left(1 - \frac{\mathcal{P}}{\pi} \int_{\mathbb{R}} \frac{\epsilon_I(v)}{v|\epsilon_k|^2} dv \right).
\end{aligned} \tag{7.62}$$

By using the identity (Eq.(7.60)), the two terms in the parentheses cancel out.

Finally, the third terms in each parentheses survive. Here, we have a term like

$$\frac{\mathcal{P}}{\pi} \int_{\mathbb{R}} \frac{\epsilon_I(v)}{|\epsilon_k|^2 v} dv = \frac{\mathcal{P}}{\pi} \int_{\mathbb{R}} \frac{\epsilon_I(v)}{|\epsilon_k|^2 (v-0)} dv = \mathcal{H} \left[\frac{\epsilon_I(v)}{|\epsilon_k(v)|^2} \right] (0) = 1 - \frac{\epsilon_R(0)}{|\epsilon_k(0)|^2}. \tag{7.63}$$

Therefore, we get

$$\langle G_k[\delta E_k(v)](v') G_{k'}[\delta E_{k'}^*(v'')](v''') \rangle = \frac{16}{V\beta} \left[\frac{\epsilon_I(v')}{v'} \delta(v' - v''') - \frac{\epsilon_I(v')\epsilon_I(v''')}{\pi v' v'''} \frac{\epsilon_R(0)}{|\epsilon_k(0)|^2} \right]. \tag{7.64}$$

By substituting the definition of [149]

$$f_k = \frac{ik}{4\pi e} G_k[\delta E_k(v)](v'), \tag{7.65}$$

we obtain

$$\langle f_k(v') f_k^*(v'') \rangle = \delta_{k,k'} \frac{k^2}{\pi^2 e^2 V \beta} \left[\frac{\epsilon_I(v')}{v'} \delta(v' - v'') - \frac{1}{\pi} \frac{\epsilon_I(v')\epsilon_I(v'')}{v' v''} \frac{\epsilon_R(0)}{|\epsilon_k(0)|^2} \right]. \tag{7.66}$$

This expression simply contains two terms: diagonal part and an off-diagonal part with respect to the velocity. This is a more general expression, whereas the same result is obtained when we assume Maxwellian distribution[103].

Consequently, the phase space fluctuation for a Vlasov system is obtained as

$$\langle f_k(v) f_{k'}^*(v') \rangle = \delta_{k,k'} \frac{k^2}{\pi^2 e^2 V \beta} \left[\frac{\epsilon_I(v)}{v} \delta(v - v') - \frac{1}{\pi} \frac{\epsilon_R(0)}{|\epsilon(0)|^2} \frac{\epsilon_I(v') \epsilon_I(v)}{v v'} \right]. \quad (7.67)$$

Details are described in [149, 148].

7.4 Results

Our rotating annulus has a shear flow profile in the radial direction as shown in Fig. 5.1. The azimuthal velocity is maximum in the middle and close to zero near the walls. To use the monotonicity of velocity, either the inner or outer region of annulus should be selected for the analysis.

First, we will check whether our measurements are far away from the boundary layers or not. Since a thin Ekman layer that dissipates energy forms near the rigid boundaries, the inviscid model fails. The vertical boundary layers are called Ekman layers and they scale as

$$\delta_V = \sqrt{\frac{\nu}{2\Omega}} \quad (7.68)$$

whereas horizontal boundary layers (side-wall layers) scale as

$$\delta_H = \sqrt{h_0 \delta_V}, \quad (7.69)$$

where h_0 is the mean height of tank along the rotation axis. This horizontal layer is often called as *Proudman-Stewartson layer*. For our experiment, $\delta_V = 0.02$ cm and $\delta_H = 0.4$ cm. This implies that our measurements are away from the boundary layers.

We have compared the result Eq. (7.54) with particle tracking (PIV) and hot film probe measurements of the pumped rotating tank experiment as

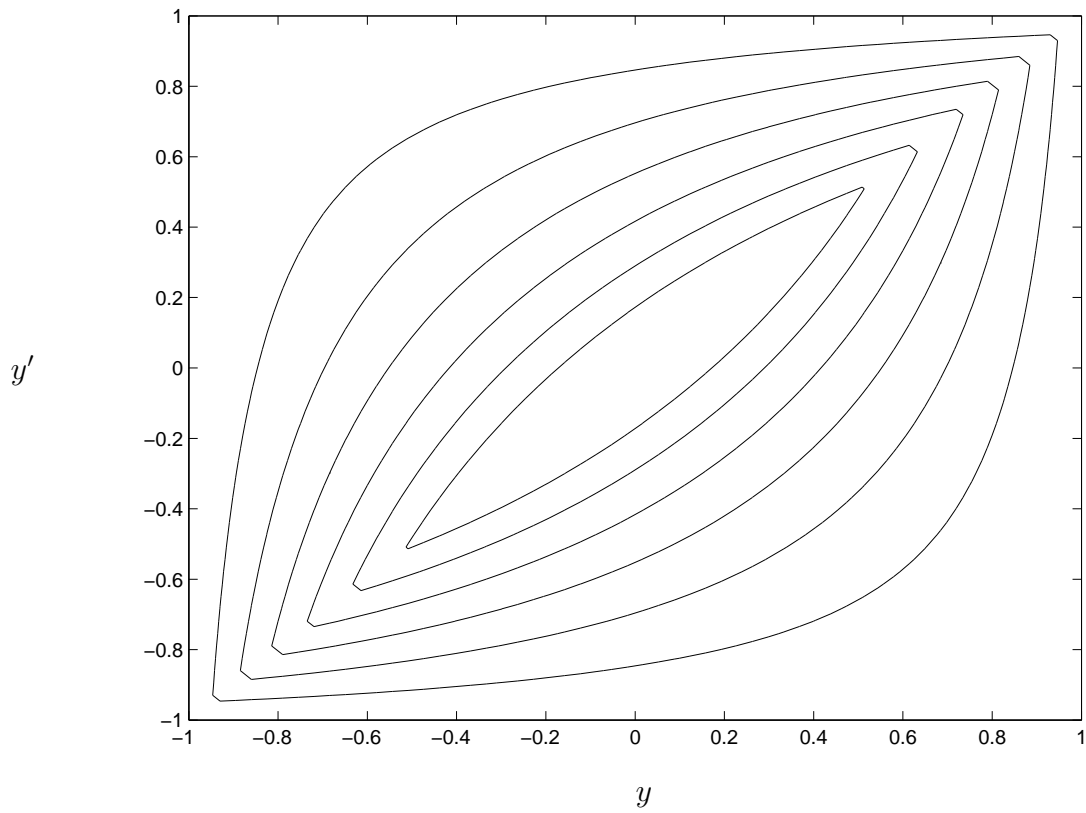


Figure 7.1: Contour lines of $\psi_k(y, y')$ when $k = 1$. We can notice that it is quite symmetric because the symmetric first order in the Neumann series is dominant.

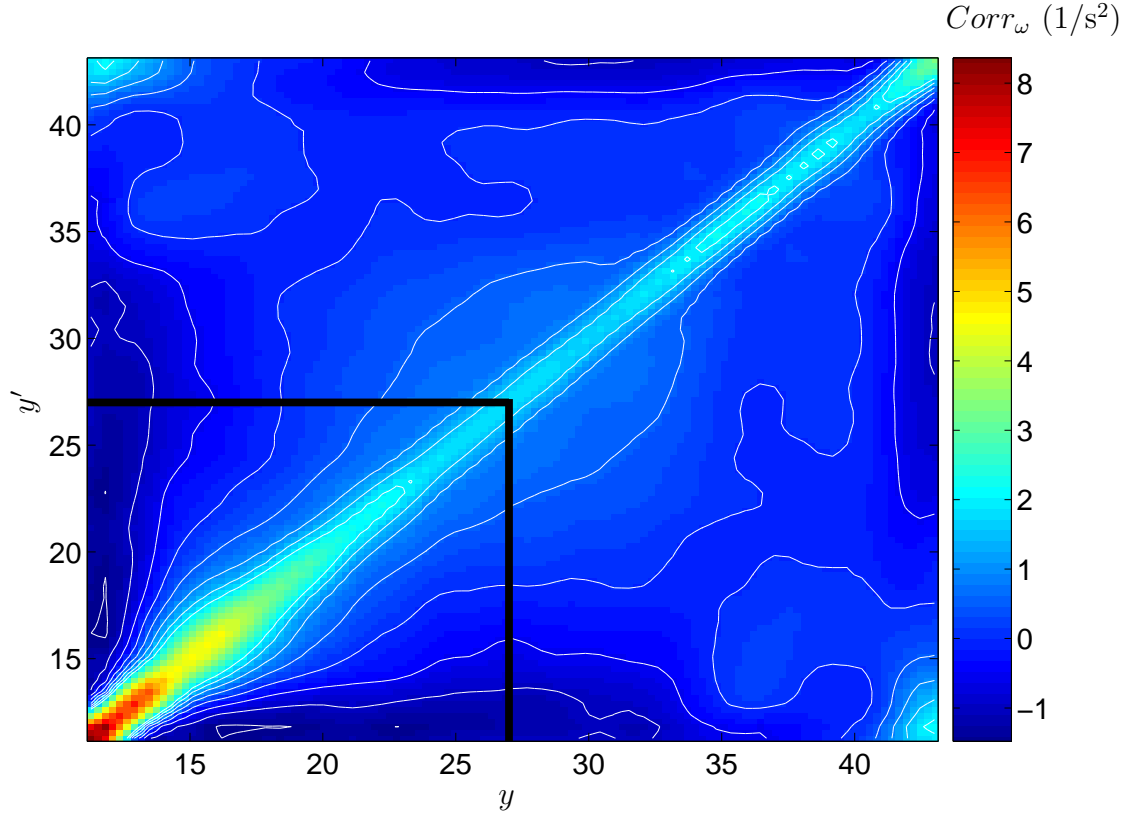


Figure 7.2: Contour plots of vorticity fluctuations $Corr_\omega := \langle \omega_k(y) \omega_k^*(y') \rangle$. Azimuthally and temporally averaged covariance of vorticity fluctuations measured with a counter-rotating jet at 1.75 Hz and $150 \text{ cm}^3/\text{s}$. Here, y and y' indicate different radii ranging from the inner boundary 11 cm to the outer boundary 43 cm. When $U'_x(y)$ equals to zero, the theoretical prediction fails. Therefore, we consider only the inner part where flow has no maximum point in the mean velocity profile. The blue boxed region will be compared with the theory.

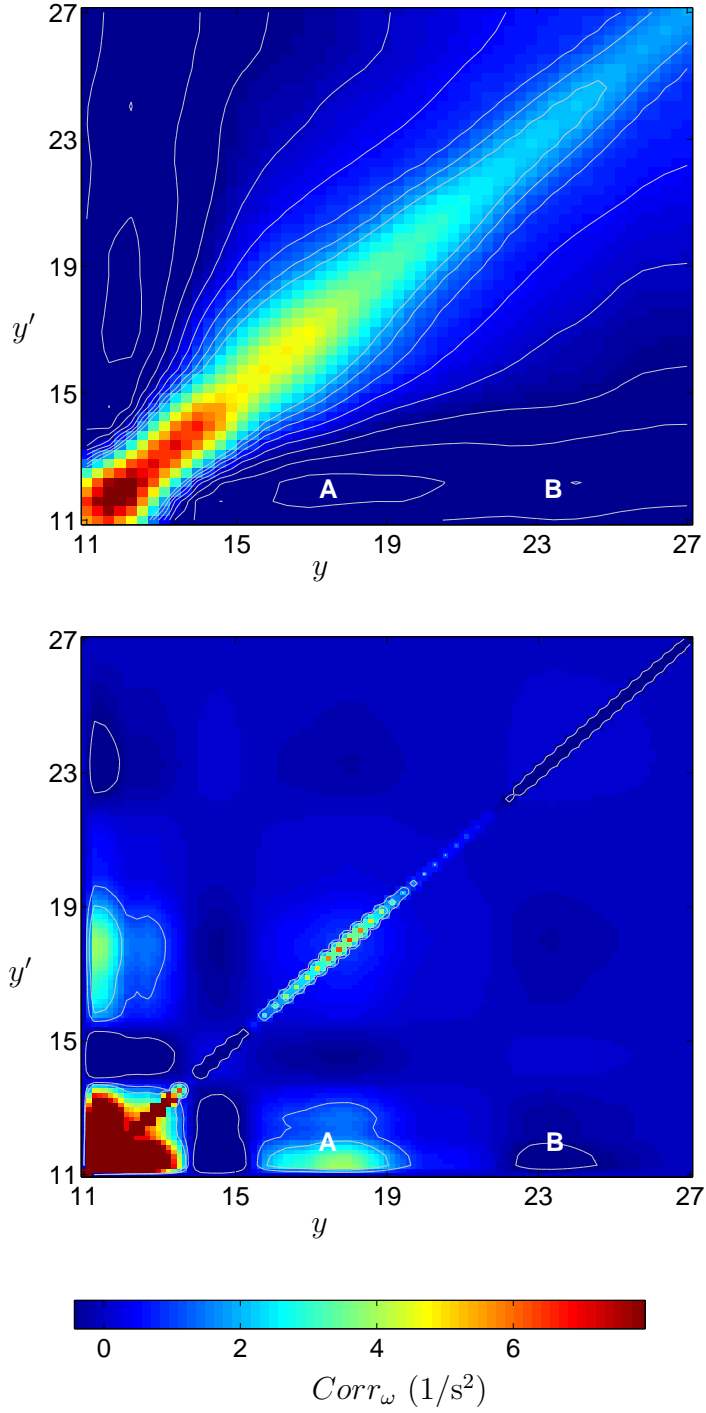


Figure 7.3: Fig (a) is the vorticity fluctuation only in the inner region of the annulus ($11 \text{ cm} < y < 26 \text{ cm}$). Strong correlation appears in diagonal axis and small correlations A and B lie away from diagonal axis. Fig. (b) is the predicted vorticity fluctuation from Eq. 7.54.

shown in Figure 7.2. Near the line $y = y'$ the delta function term dominates and we expect the vorticity spectrum to be independent of k , which implies the velocity spectrum should vary as k^{-2} . Indeed, this is surprisingly close to what is seen in Chap. 9.

7.5 Conclusion

Statistical mechanics requires a proper set of canonical coordinates (such as action-angle variables). Ensemble-averages with canonical coordinates should be used. For a long time, this approach has been performed with noncanonical variables instead of canonical variables. The result with noncanonical variables leads to the diagonal correlation of vorticity fluctuations such as $\langle \omega_k(y) \omega_k^*(y') \rangle = C(y) \delta(y - y')$ where $C(y)$ is a function of y . Following novel work for the Vlasov case [149], our calculation with canonical variables was done for the fluid case. The theoretical prediction gives surprising agreement with experiments.

Chapter 8

Velocity Difference Statistics

We unify two approaches that have been taken to explain the non-Gaussian probability distribution functions (PDFs) obtained in measurements of longitudinal velocity differences in turbulence, and we apply our approach to Couette-Taylor turbulence data. The first approach we consider was developed by Castaing and coworkers, who obtained the non-Gaussian velocity difference PDF from a superposition of Gaussian distributions for subsystems that have a particular energy dissipation rate at a fixed length scale [47]. Another approach was proposed by Beck and Cohen, who showed that the observed PDFs can be obtained from a superposition of Gaussian velocity difference PDFs in subsystems conditioned on the value of an intensive variable (inverse “effective temperature”) in each subsystem [26]. We show that the Castaing and Beck-Cohen methods are related, and we present a way to determine subsystem size in the Beck-Cohen method. The application of our approach to Couette-Taylor turbulence (Reynolds number 540 000) yields a log-normal distribution of the intensive parameter, and the resultant velocity difference PDF agrees well the observed non-Gaussian velocity difference PDFs.

8.1 Theory

8.1.1 Method of Castaing et al.

Castaing et al. [47] started with the observation from their experiments that that velocity difference distributions for a given ε_r are Gaussian, and that ε_r is described by a log-normal distribution [47, 48, 6, 45, 50, 46]. The log-normal distribution for ε_r have also been obtained for ε_r in other experiments on fully developed turbulence [7, 51, 6, 99], and in analyses of images of cloud patterns [5], temperature fields in turbulence [169], and magnetic fields in solar winds [199].

To describe the evolution of $P(\delta v_r)$ from Gaussian at large scales to non-Gaussian at small scales [100, 204, 28], Castaing et al. proposed [47, 48]

$$P(\delta v_r) = \int P(\varepsilon_r) P(\delta v_r | \varepsilon_r) d\varepsilon_r. \quad (8.1)$$

The conditional PDF $P(\delta v_r | \varepsilon_r)$ in Eq. (8.1) is assumed to be a Gaussian distribution, $P(\delta v_r | \varepsilon_r) = e^{-(\delta v_r)^2 / (r \varepsilon_r)^{2/3}}$, in accord with experimental observations [56, 78, 201].

A difficulty in applying the approach of Castaing et al. is that energy dissipation rate at length scale r , ε_r , is not directly measured in experiments. By assuming homogeneous and isotropic conditions, ε_r is defined as $15\nu (\partial v / \partial x)^2$. In practice, ε_r is determined from time series data for only a single variable, so that

$$\varepsilon_r = \frac{15\nu}{(\Delta x)^2} \sum_{i=1}^{N-1} [v(x_{i+1}) - v(x_i)]^2, \quad (8.2)$$

where $\Delta x (\equiv x_2 - x_1)$ is the sampling separation the summation i is over subsystems and $x_N - x_1 = r$ [201, 225, 200]. Even with this assumption,

determination of $\varepsilon_r(x)$ is difficult because of errors in evaluating the derivative from velocity data. Further error arises from the application of the Taylor frozen hypothesis at high frequencies [73, 53, 99, 70, 232, 168, 231, 3, 123, 52].

Kolmogorov [106] and Obukhov [158] assumed a log-normal distribution of ε_r , while Castaing et al. started by assuming a log normal distribution of ε_r ,

$$P(\varepsilon_r) = \frac{1}{\lambda_\varepsilon(2\pi)^{1/2}\varepsilon_r} \exp\left(-\frac{(\ln \varepsilon_r - m_\varepsilon)^2}{2\lambda_\varepsilon^2}\right), \quad (8.3)$$

where m_ε and λ_ε are respectively the mean and the standard deviation of $\ln \varepsilon_r$.

8.1.2 Superstatistics of Beck and Cohen

Beck and Cohen's statistical approach considers a system far from thermodynamic equilibrium to consist of subsystems in local thermodynamic equilibrium [26]. Each subsystem has a well-defined "temperature", but the subsystem temperatures need not be the same since the whole system is not in equilibrium. Beck and Cohen identify $(\delta v_r)^2$ with the kinetic energy of eddies of size r , $E(\delta v_r) = \frac{1}{2}(\delta v_r)^2$, and the variance of δv_r is identified with an inverse temperature β [155]), given for a subsystem of size d by

$$\beta_d = \frac{1}{\langle(\delta v_r)^2\rangle_d - (\langle\delta v_r\rangle_d)^2}, \quad (8.4)$$

where $\langle\cdot\rangle_d$ is an average over the size d . Then we have

$$P(\delta v_r) = \int_0^\infty P(\beta_d)P(\delta v_r|\beta_d)d\beta_d. \quad (8.5)$$

where $P(\beta_d)$ is the distribution of inverse temperature in subsystems of size d .

A particular choice of $P(\beta_d)$, the χ^2 distribution, leads to the distribution associated with the nonextensive statistical mechanics of Tsallis,

$P(E) = (1 + \beta E^2)^{-1/(1+q)}$, where q is a parameter characterizing the nonextensivity ($S(1+2) = S(1) + S(2) + qS(1) \cdot S(2)$, where S is entropy function.) [215, 26]. A phenomenology similar to Beck and Cohen's was used in earlier oceanographic analysis that described the global non-Gaussian distribution of ocean surface velocity as a mixture of local Gaussians with χ^2 -distributed variance [81, 194]. The method of Beck and Cohen has been applied to fully developed turbulence [24, 25] by introducing a fitting parameter to determine the PDF of inverse temperature, rather than by directly measuring the PDF of inverse temperature.

The Beck-Cohen method requires that the size d should be large compared to the distance r separating two points, and d should also be large enough so the subsystems contain enough data points to yield good statistics, but d must also be small enough so that subsystems are each described by a Gaussian distribution. Beck determined the size of d using a fitting parameter involving the kurtosis of $P(\delta v_r)$ [25].

8.1.3 Unified View of PDFs

The Castaing and Beck-Cohen methods are similar except in the way they divide a system into subsystems. Castaing et al. sample velocity differences conditioned by the averaged energy dissipation rate ε_r , while Beck and Cohen use velocity differences conditioned by the inverse temperature β_d . Castaing et al. need one fixed length scale, the separation distance r between two points; δv_r and ε_r are defined at this scale and are related through Bayes' theorem. The Beck-Cohen method involves two length scales, the distance r separating two points and the size d of the subsystems in the statistical

analysis.

The Castaing and Beck-Cohen methods can be connected if the two conditioning variables (ε_r and β_d) are correlated. Using Eq. (8.1) and Bayes' theorem, we convert Castaing's method into Beck-Cohen's method,

$$\begin{aligned}
P(\delta v_r) &= \int_0^\infty P(\delta v_r|\varepsilon_r)P(\varepsilon_r)d\varepsilon_r \\
&= \int_0^\infty \int_0^\infty P(\delta v_r|\beta_d)P(\beta_d|\varepsilon_r)d\beta_dP(\varepsilon_r)d\varepsilon_r \\
&= \int_0^\infty P(\delta v_r|\beta_d)\left[\int_0^\infty P(\beta_d|\varepsilon_r)P(\varepsilon_r)d\varepsilon_r\right]d\beta_d \quad (8.6)
\end{aligned}$$

$$= \int_0^\infty P(\delta v_r|\beta_d)P(\beta_d)d\beta_d. \quad (8.7)$$

Now, let's assume a log-normal distribution of β_d at the fixed ε_r ,

$$P(\beta_d|\varepsilon_r) \propto \frac{1}{\beta_d} \exp \left[-\frac{(\ln \beta_d - a \ln \varepsilon_r)^2}{2\lambda_t^2} \right], \quad (8.8)$$

where λ_t is the standard deviation of $\ln \beta_d$ conditioned to ε_r and a is a parameter. Using Eqs. (8.3), (8.6), and (8.8), we have

$$\begin{aligned}
P(\delta v_r) &\propto \int_0^\infty P(\delta v_r|\beta_d) \int_0^\infty \exp \left(-\frac{(\ln \beta_d - a \ln \varepsilon_r)^2}{2\lambda_t^2} \right) \\
&\quad \times \exp \left(-\frac{(\ln \varepsilon_r - m_\varepsilon)^2}{2\lambda_\varepsilon^2} \right) d(\ln \varepsilon_r)d(\ln \beta_d) \\
&\propto \int_0^\infty P(\delta v_r|\beta_d) \exp \left(-\frac{(\ln \beta_d - m)^2}{\lambda_\varepsilon^2 \lambda_t^2} \right) d(\ln \beta_d). \quad (8.9)
\end{aligned}$$

Thus with the assumption of a log-normal distribution of β_d conditioned on ε_r , we have that Castaing's method is equivalent to Beck-Cohen's method. by assuming log-normal distribution of β_d conditioned on ε_r . In Section 8.3.4, the log-normal PDF of $P(\beta_d|\varepsilon_r)$ is verified in experiments.

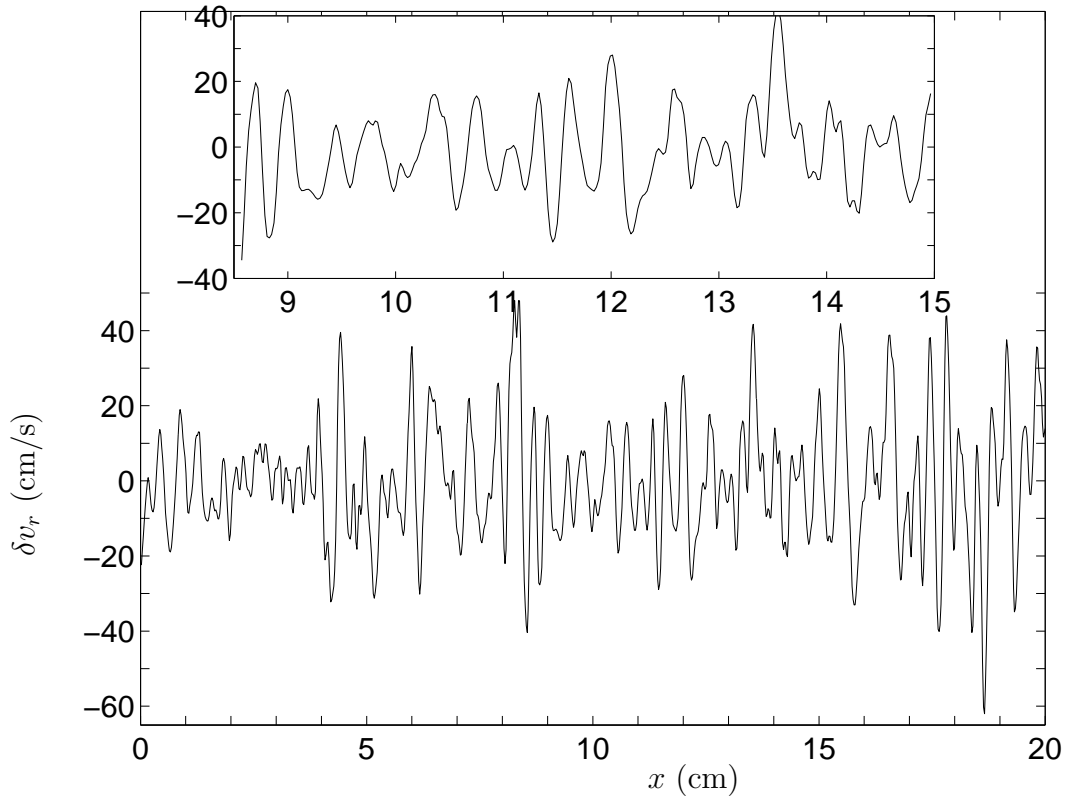


Figure 8.1: An example of the Couette-Taylor velocity difference data, obtained by subtracting velocities at two points with a separation $r = 46\eta = 0.134$ cm, where η is the Kolmogorov length scale. The inset shows the velocity differences on a finer length scale.

8.2 Experiment

We describe here an experiment on turbulent Couette-Taylor flow by Lewis and Swinney [120, 116], and in the next section we will analyze data from this experiment to deduce $P(\beta)$ and a prediction for $P(\delta v_r)$. The fluid was contained in the annular region between two concentric cylinders with an inner radius of $b = 22.085$ cm and an outer radius of $a = 15.999$ cm; thus the ratio of inner to outer radius was 0.724. The height of the annulus was 69.5 cm, which yields a value of 11.4 for the ratio of height to the gap. The inner cylinder angular rotation rate Ω was $8 \times 2\pi$ rad/s; the outer cylinder was at rest. The ends of the annulus rotated at the same rate as the inner cylinder. The fluid was water with a viscosity ν of 0.00968 cm²/s at the working temperature. Defining the Reynolds number as $Re = \Omega a(b - a)/\nu$ yields for the Reynolds number 540 000 [120].

A hot film probe was used to measure the time dependence of the azimuthal component of the velocity in the center of the gap at a distance 4.35 cm above mid-height of the annulus. The Taylor frozen turbulence hypothesis was used to convert the velocity time series data to velocity field data. The turbulent intensity (the ratio of the root mean squared velocity to the mean velocity) was less than 6%.

The uncertainties shown on our graphs correspond to the standard deviation of 20 independent experiments. The velocity measurements were made with a sampling rate 2500 times the inner cylinder rotation frequency; this corresponds to a spatial separation of 0.017 cm between successive velocity values. The longitudinal velocity differences δv_r that we analyze are for points separated by a small distance, $r = 0.134$ cm, where the probability distribu-

tion function has approximately exponential tails [120]. An example of the measurements of $\delta v_r(t)$ is shown in Fig. 8.1. The separation $r = 0.134$ cm corresponds to 46η , where η is Kolmogorov scale [120]. [The Kolmogorov dissipation scale was obtained by calculating the dissipation from energy spectra: $\eta \equiv (\nu/\varepsilon)^{1/4}$, where the dissipation rate is given by $\varepsilon = 15\nu \int k^2 E(k) dk$ [120].] The window size d we use for determining the local inverse temperature β is typically 1.1 cm, 10 times larger than the value of r .

8.3 Results

8.3.1 Probability Density Function of Inverse Temperature

Several distributions for inverse temperature β_d have been discussed by Beck and Cohen [26]. Here we consider the log normal and χ^2 distributions, which are most applicable to turbulent flow. Due to multiplicative processes in turbulence, the log-normal distribution is often observed for positive-definite quantities (such as ε_r) [47, 48, 6, 45, 50, 46]. A log-normally distributed β_d is given by

$$P(\beta_d) = \frac{1}{\beta_d s \sqrt{2\pi}} \exp\left(-\frac{(\log \beta_d - m)^2}{2s^2}\right) \quad (8.10)$$

where $s = \sqrt{\ln(1 + \sigma_{\beta_d}^2 / \bar{\beta}_d^2)}$ and $m = \log(\bar{\beta}_d^2 / \sqrt{\bar{\beta}_d^2 + \sigma_{\beta_d}^2})$ are parameters, and $\bar{\beta}_d$ and σ_{β_d} are respectively the mean and standard deviation of β_d .

The χ^2 distribution of β_d is given by

$$P(\beta_d) = \frac{1}{\beta_d \Gamma(c)} \left(\frac{\beta_d}{b}\right)^c \exp\left(-\frac{\beta_d}{b}\right) \quad (8.11)$$

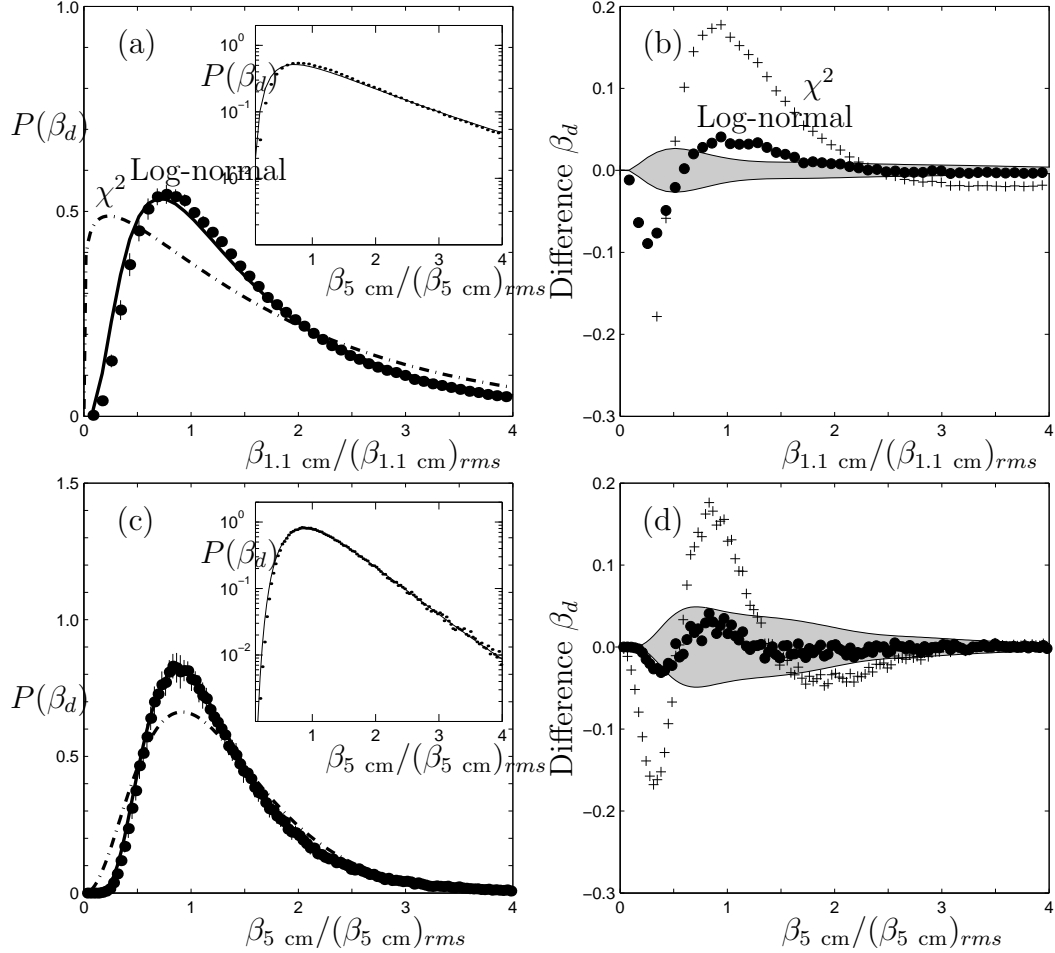


Figure 8.2: Comparison of χ^2 and log-normal distributions to the experimental distribution for inverse temperature in subsystems of size (a) $d=1.1$ cm and (c) $d=3$ cm. The dash-dotted lines represent the χ^2 distribution, and the solid line represents the log-normal distribution; both have the same mean and variance as the 20 independent experiments (error bars correspond to one standard deviation). The panels on the right, (b) and (d), show the difference between the experimental PDF for β_d and the χ^2 (plus signs) and log-normal (bullets) distributions for (a) $d=1.1$ cm and (c) $d=3$ cm. The shaded area represents the experimental uncertainty (standard deviation of 20 experiments). Difference between the experimental PDF for β_d and the χ^2 (plus signs) and log-normal (asterisks) distributions for (a) $d=1.1$ cm and (b) $d=3$ cm. The shaded area represents the experimental uncertainty (standard deviation), which is evaluated for 20 independent experiments.

where $c = \bar{\beta}_d^2 / \sigma_{\beta_d}^2$ and $b = \sigma_{\beta_d}^2 / \bar{\beta}_d$ and Γ is the gamma function. The statistical properties of different distributions are discussed in [26].

The experimental PDF for β_d is compared in Fig. 8.2 with a log-normal distribution and with a χ^2 distribution for two subsystem sizes d , 1.1 cm and 3 cm. The mean $\bar{\beta}_d$ and variance $\sigma_{\beta_d}^2$ of the inverse temperature determine the parameters s, m, b and c . For small d , the log-normal and χ^2 differ significantly, but for large d they become close together [Fig. 8.2(c) and (d)]. The decrease in variance of β_d with increasing d is similar to decrease observed in the variance of ε_r with increasing r [219].

The difference between the PDF of β_d from experiment and the χ^2 and log-normal distributions is shown in Fig. 8.2(b) and (d). For $d=1.1$ cm, the log-normal distribution fits the data within the experimental uncertainty except small β_d regions, while the χ^2 distribution deviates from the observations by an amount that is large compared to the uncertainty. For $d=3$ cm, similar features as in the case of $d=1.1$ cm are observed.

The log normal distribution (8.10) involves two parameters, s and m , which depend on subsystem size, as shown in Fig. 8.3. This figure suggests a relationship between s and m : $m = \frac{s^2}{2}$, which is supported by a calculation in Castaing et al. (see Section 4.3.1 in [47]).

8.3.2 Conditional Probability and the Proper Subsystem Size

In the statistical approach of Beck and Cohen, the subsystem size d should be sufficiently small so that $P(\beta_d)$ is Gaussian, corresponding to local thermodynamic equilibrium in the subsystems. However, in practice the $d \rightarrow$

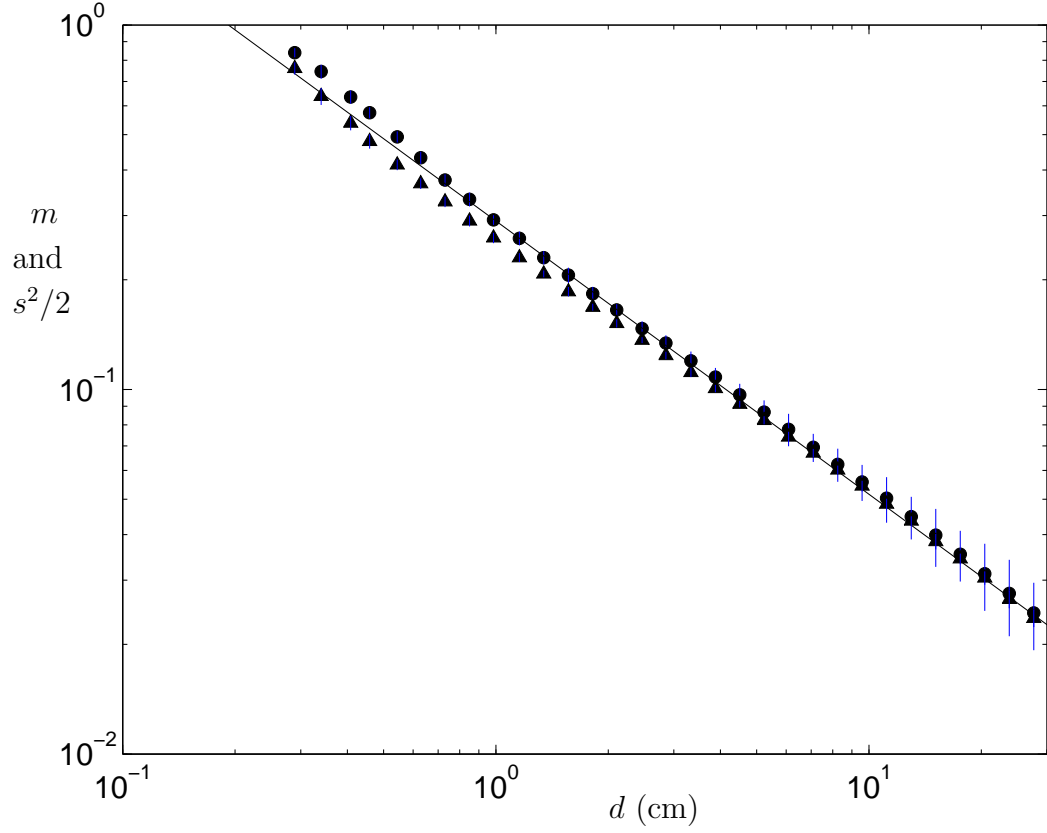


Figure 8.3: The parameters $\frac{s^2}{2}$ (circles) and m (triangles), obtained from fits of the inverse temperature β_d (deduced from Couette-Taylor turbulence data) to a log-normal distribution, as a function of subsystem size d (see Eq. (8.10)). (s and m are the variance and mean of logarithmic inverse temperature.) The parameters $\frac{s^2}{2}$ and m are approximately equal (see text) and are described by a power law, $m \propto d^{-3/4}$ (solid line).

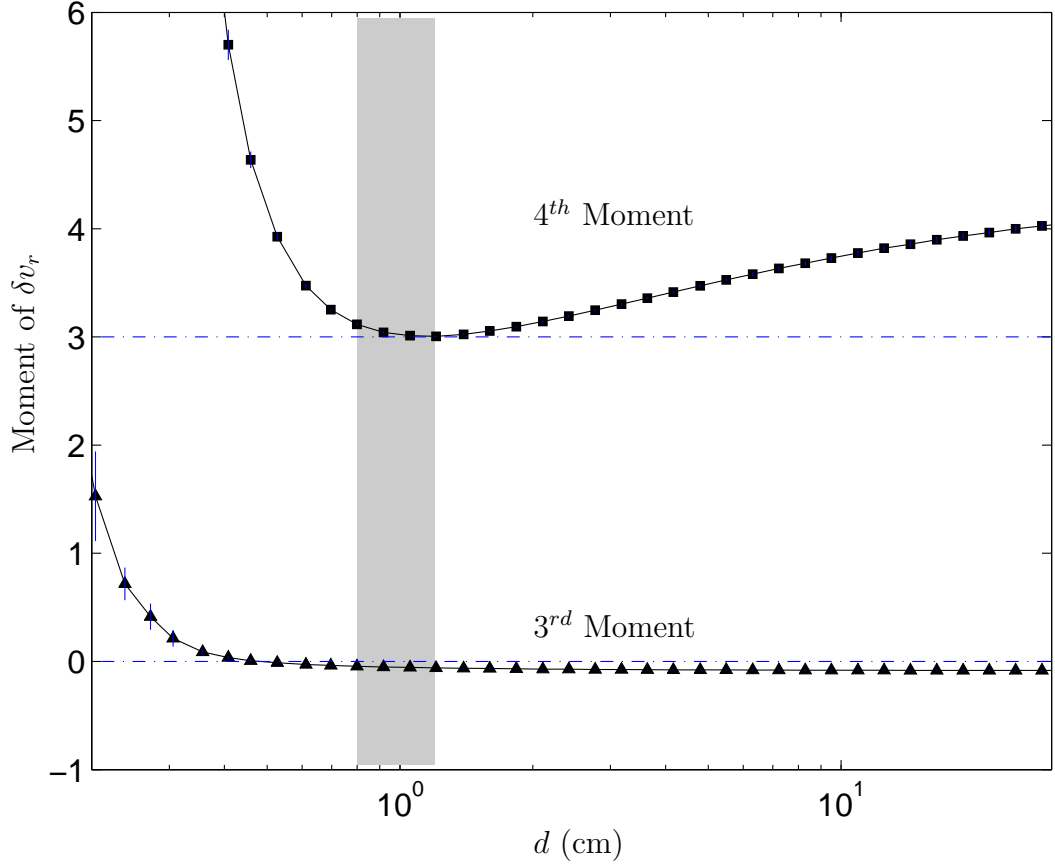


Figure 8.4: The dependence of the third and fourth moments of $P(\delta v_r)$ on the size d of the subsystems. For sufficiently small d , $P(\delta v_r)$ should be Gaussian, which means the values of the third and fourth moments should have the values zero and three, respectively. We find that at $d \approx 1.1$ cm, the conditional distribution Eq. (8.10) is close to Gaussian (see text).

0 limit is inaccessible because as d becomes very small, the number of data points becomes too small to allow accurate determination of the variance of β_d . So what is optimal choice of d ? We address this question by examining the third moment (skewness) and fourth moment (kurtosis) of δv_r , which should be equal respectively to zero and three for a Gaussian distribution. In principle we could also examine fifth and higher moments, but because of the sensitivity of the higher moments to noise, we limit our considerations to the third and fourth moments. Plotting the third and fourth moments as a function of d , as shown in Fig. 8.4, we find that the optimal value of d for our data is 1.0-1.2 cm, which is the only range in which the kurtosis is approximately given by the value for a Gaussian. The skewness is small and negative for $d > 0.5$ cm, but becomes strongly positive for $d < 0.5$ cm, reflecting a cascade of energy to smaller length scales. We conclude that $d=1.1$ cm is the optimal subsystem size for our data.

8.3.3 Probability Distribution of δv_r

We found a log-normal distribution of β_d fits the turbulence data over a wide range in d (Section 8.3.1). With the log normal distribution of β_d for the optimal value of d (1.1 cm, Fig. 8.4) and the conditional Gaussian distribution of δv_r for that β_d , we obtain the probability distribution of δv_r by the method of Beck and Cohen,

$$P(\delta v_r) = \frac{1}{2\pi s} \int_0^\infty d\beta_d \beta_d^{-1/2} \exp\left(-\frac{(\log \beta_d - m)^2}{2s^2}\right) \times \exp\left(-\frac{1}{2}\beta_d(\delta v_r)^2\right), \quad (8.12)$$

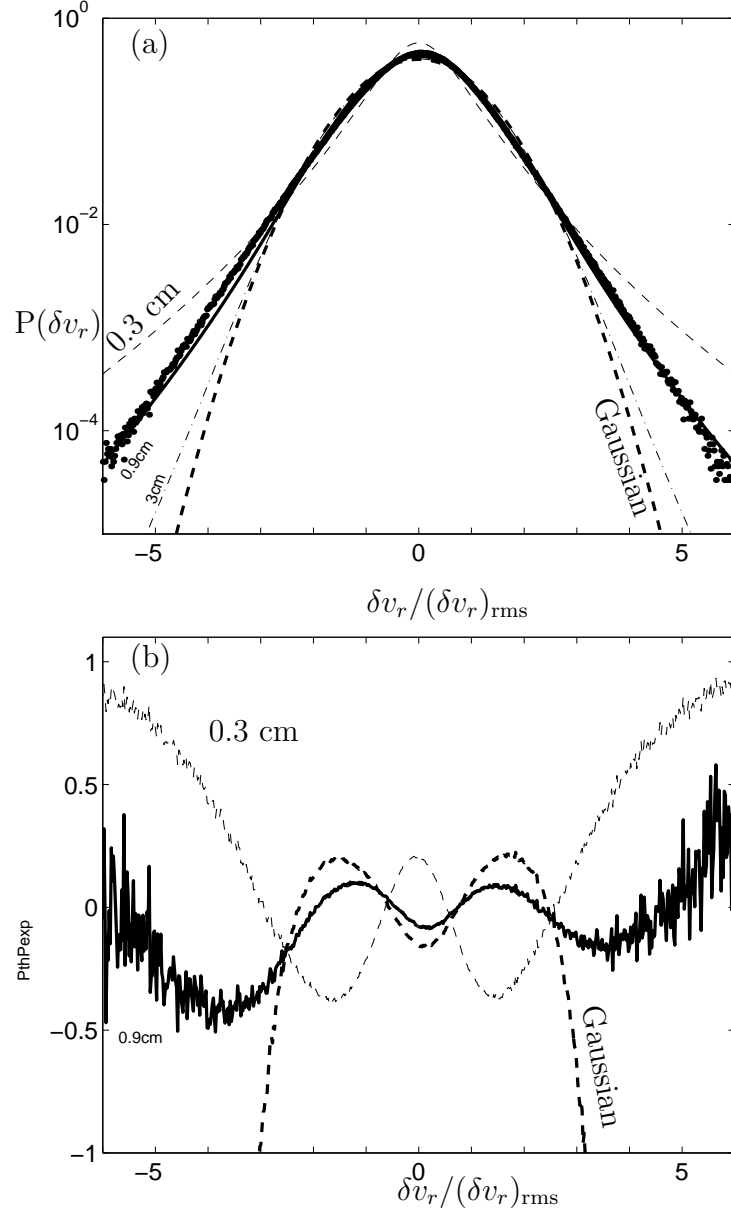


Figure 8.5: Comparison experimental results (dots) for $P(\delta v_r)$ with the prediction of the Beck-Cohen method for a subsystem with the optimal size of 1.1 cm (bold line), on (a) log and (b) linear scales. For comparison, we also show the predictions for subsystems of size 0.3 cm (thin dashed line) and 3 cm (thin dash-dot line) and a Gaussian distribution (dashed line).

where s and m are determined from experiment for the optimal subsystem size d . There is no explicit form for the improper integral in Eq. (8.12) so we evaluate the integral numerically, using the limits $([\min \beta_d, \max \beta_d])$ of β_d measured in experiments instead of the theoretical integral domain, $[0, \infty)$.

The results for $P(\delta v_r)$ obtained by numerical integration of (8.12) are shown in Fig. 8.5. The data are described much better by the predicted probability distribution than by a Gaussian. The observed approximate power law tails are similar to the predicted distribution function. Figure 8.5 shows also the prediction for subsystems of sizes larger and smaller than the optimal size of 1.1 cm.

8.3.4 Castaing and Beck-Cohen Methods

If the two conditioning quantities in the Castaing and Beck-Cohen methods (ε_r and β_d , respectively) are correlated as a power-law, through Bayes' theorem the two methods can be seen to be the same (see Eq. (8.7)). With the surrogate definition of ε_r as in Eq. (8.2) and a proper subsystem size (Section 8.3.2), we find that β_d and ε_r exhibit a power-law relation, as Fig. 8.6 illustrates. In this sense, the Castaing and Beck-Cohen methods describe the same PDF of δv_r through the different conditional values which are correlated. Our experimental observation of a relation $\beta_d \propto (\varepsilon_r)^{-2/3}$ in Fig. 8.6 follows also from a dimensional analysis,

$$\begin{aligned} [\beta_d] = \left[\frac{T^2}{L^2} \right] &= [L]^{-2/3} \times \left[\frac{L^2}{T^3} \right]^{-2/3} \\ \Rightarrow \beta_d &\propto r^{-2/3} \varepsilon_r^{-2/3}, \end{aligned} \quad (8.13)$$

where square brackets $[\cdot]$ denote the dimension of a physical quantity, T is the dimension of time and L is the dimension of length.

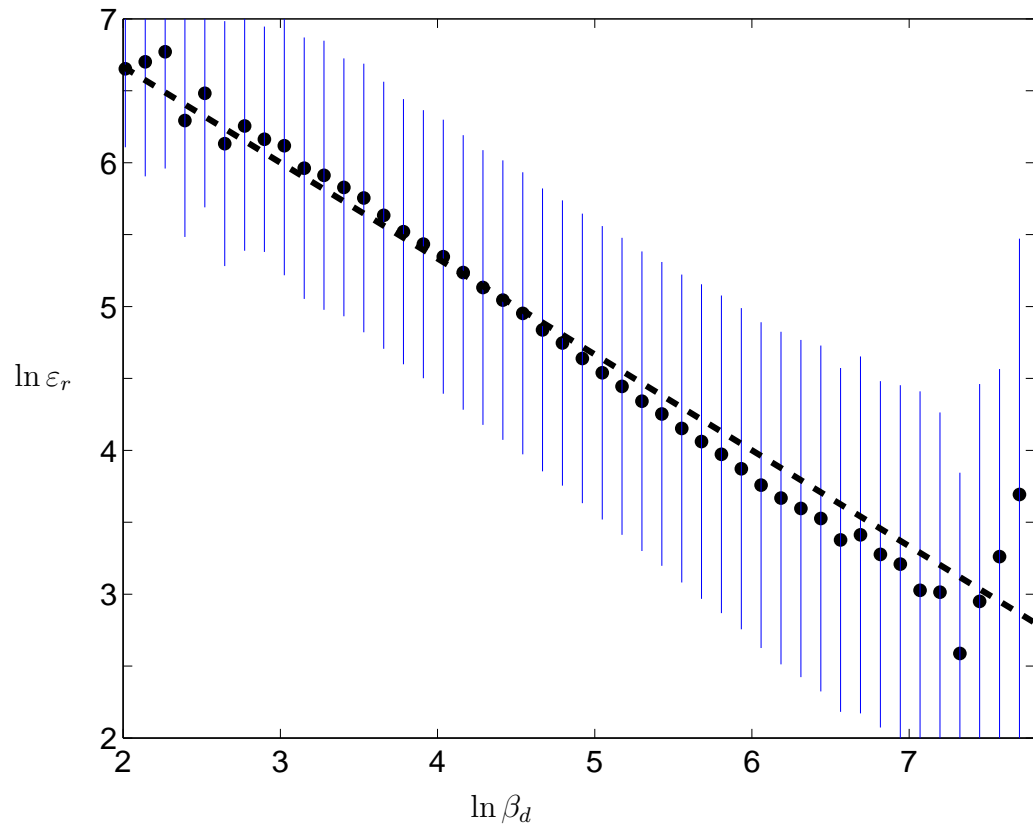


Figure 8.6: The relation between β_d and ε_r . The solid vertical lines represent standard deviations at a fixed β_d and the dots represent the mean values. The dashed line is $\beta_d \propto (\varepsilon_r)^{-2/3}$.

The probability of β_d conditioned to ε_r , $P(\beta_d|\varepsilon_r)$, is log-normally distributed, as Fig. 8.7 illustrates. Our assumption in Eq. (8.8) holds with the surrogate ε_r and β_d , where d is properly chosen (Section 8.3.2). Thus the integral of two log-normal distributions, $\int P(\beta_d|\varepsilon_r)P(\varepsilon_r)d\varepsilon_r$, is another log-normal distribution, $P(\beta_d)$. That is, if $P(\beta_d|\varepsilon_r)$ is a log-normal distribution with the mean of $\ln \varepsilon_r$, a log-normal distribution of ε_r in Castaing's method is equivalent with a log-normal distribution of β_d in Beck-Cohen's method.

8.4 Conclusions

Both Castaing and Beck-Cohen methods have been very successful in describing the non-Gaussian distribution of velocity differences in turbulence [25, 47]. Although the relation of Beck-Cohen's method and Tsallis statistics¹ to turbulence has been questioned [83, 25, 153, 216], the fit to data is quite good [98, 65, 142, 20]. We have presented a method for determining subsystem size in the Beck-Cohen method, thus eliminating the need for a fitting parameter.

We have also shown that Castaing's method can be converted to Beck-Cohen method – the log-normal distribution of ε_r in Castaing's method gives rise to a log-normal distribution of β_d in Beck-Cohen's method. In that sense, the two methods describe the non-Gaussian distribution of δv_r in the same way, $P(\delta v_r) = \int \text{Gaussian distribution} \times \text{log-normal distribution}$.

¹Beck and Cohen have shown that their method includes Tsallis statistics and other statistics [26]. A log-normal distribution is indistinguishable from Tsallis statistics except in long tails [25].

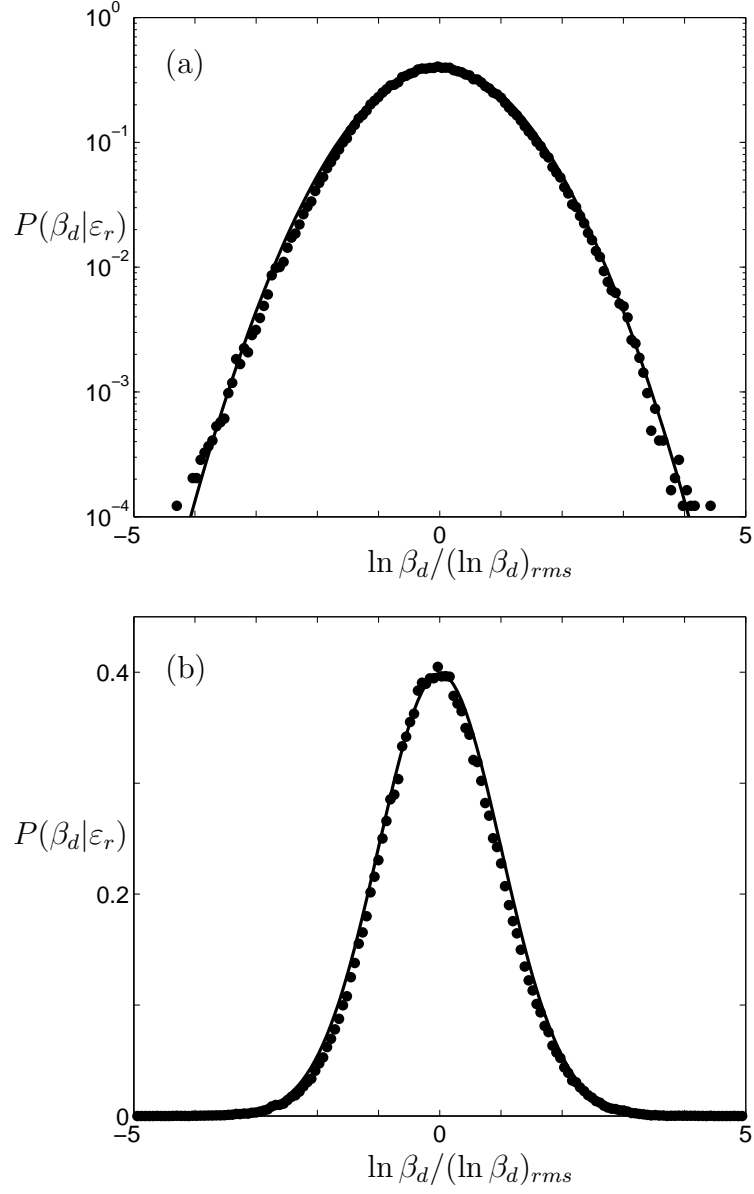


Figure 8.7: The Gaussian distribution of $\ln \beta_d$ conditioned by ε_r , plotted on (a) log and (b) linear scales. The solid lines represent a Gaussian distribution of $\ln \beta_d$, that is, the log-normal distribution of β_d . The dots represent the mean values of $\ln \beta_d$ from experiments.

Chapter 9

Energy spectrum

9.1 Introduction

Rotating turbulence on a sloped bottom (a beta-plane) is generally believed to lead to anisotropy and the formation of a jet stream [171]. Rhines noted the existence of a transition scale $(2U/\beta_{Ro})^{1/2}$, where the inverse cascade of turbulent energy ceases at a wavenumber $k_\beta = (\beta_{Ro}/2U)^{1/2}$. For scales larger than k_β^{-1} , wave-like phenomena dominate, while for scales smaller than this turbulent effects dominate. However, the characteristics of turbulence on small scales are still open to question.

Quasi-geostrophic turbulence in stably-stratified flow contains two- and three-dimensional motions. Due to unstable baroclinic (vertical) flow, energy is transferred to barotropic (horizontal) flow at wavenumbers close to that corresponding to the radius of deformation [165, 184, 183]. Consequently, energy slowly cascades to large scales and large coherent structures appear [77, 192]. This can be interpreted as a flow that conserved energy and enstrophy, each

of which is composed of 2D (barotropic) part and an effective potential (baroclinic) part. In our rotating annulus tank, the radius of deformation is infinite because of no free surface. Even though our rotating annulus tank has no stratification, the flow has 2D (barotropic-like) motion and an effective potential (baroclinic-like) motion due to the small vertical motions. In this case, the potential energy and enstrophy are introduced by the vertical variation of streamfunction, which induces vertical motion. In this chapter, we show how energy spectra on small scales change as we change the beta plane to a flat plane. By taking into account the vertical motion of the fluid, we attempt to explain the position of the energy spectrum break.

9.2 Previous Work

9.2.1 Different Scales in a Rotating Fluid

The turbulent eddy-turnover time is given by [119]

$$\tau_{Ed}(k) = \varepsilon^{-1/3} k^{-2/3}, \quad (9.1)$$

where ε is the energy transfer rate and the inverse time scale increases as $k^{2/3}$. Alternatively, the advective timescale often used is

$$\tau_{Ad}(k) = \frac{1}{U_k}, \quad (9.2)$$

and this inverse time scale grows as k . However, the Rossby wave time scale is

$$\tau_{Ro}(k) = \frac{k}{\beta_{Ro}}, \quad (9.3)$$

and this inverse time scale decreases as k^{-1} . Thus, the Rossby wave dominates large scales and the isotropic turbulent flow are dominant in smaller scales.

Equating Eqs. (9.2) and (9.3), one gets

$$k_\beta \sim \sqrt{\frac{\beta_{Ro}}{U}}. \quad (9.4)$$

This wavenumber is called the *Rhines wavenumber* and the inverse is called the *Rhines length scale* [171, 172]. This indicates a scale of balancing between the relative vorticity (ω) and the beta-effect ($\beta_{Ro}r$). On scales smaller than the Rhines length scale, the relative vorticity is larger than the beta-effect, and turbulence is not affected by Rossby waves. In the presence of small scale forcing, the energy is cascaded inversely over homogeneous and isotropic turbulence up to the Rhines scale. For scales larger than the Rhines scale, the Rossby wave forms and the beta effect dominates. Therefore, the scales smaller than the Rhines scale are independent of the existence of the beta plane.

9.2.2 Energy Spectrum in 2D Turbulence

Kraichnan [107] considers how energy and enstrophy are distributed in the 2D isotropic homogeneous turbulence. As we show in Chap. 2.2, Kraichnan's picture of 2D turbulence is that all the energy is transferred to large scales and all the enstrophy is transferred to small scales. This is often called the *dual cascade process*.

By estimating the magnitude for the triple velocity correlations, one can get the energy spectrum. In general, τ_3 , the time scale for the triple correlations responsible for inducing turbulent spectral transfer, may depend on any relevant turbulence parameters such as energy spectrum and a length scale [107]. When energy is conserved by the nonlinear interaction and a local cascade has been assumed, the energy transfer rate, which equals to the

dissipation rate ε , is independent of wavenumber k . Local cascade also implies that ε is explicitly proportional to τ_3 and depends on the wavenumber k and on the energy spectrum $E(k)$. A simple dimensional analysis leads to

$$\varepsilon = C' \tau_3(k) k^4 E^2(k) \quad (9.5)$$

where C' is a constant. When the time scale for triple correlation is simply given by the nonlinear time $\tau_3(k) = \tau_{nl} = [k^{3/2} E^{1/2}(k)]^{-1}$, Kolmogorov spectrum is obtained.

However, the difficulty encountered in understanding dynamics of geophysical flows is the influence of a rotation. This effect leads to the modification of the spectral time for energy transfer down scales [234, 43]. Zhou et al. assumed that the triple correlation time scale

$$\tau_3 \sim \Omega^{-1}. \quad (9.6)$$

By substituting the above assumed τ_3 to Eq. (9.5), one gets

$$E(k) \sim (\varepsilon \Omega)^{1/2} k^{-2}. \quad (9.7)$$

This k^{-2} energy spectrum for the inverse cascade matches with experimental observations in a rapidly rotating system [18]. There is no prediction for the higher k values. Energy spectrum in smaller scales than the forcing scales can be estimated by considering the conservations of energy and enstrophy.

Tran-Bowman-Shepherd-Constantin have pointed out the problem of Kraichnan's energy spectrum in 2D turbulence [61, 213, 211, 212]. More details are discussed in Chap. 2.2. For 2D turbulence, a direct enstrophy cascade is not possible with molecular viscosity. Energy spectra steeper than k^{-5} result from the global conservation laws of energy and enstrophy, molecular viscosity, and a spectrally localized forcing.

9.3 Model

There are various ways to approximate the horizontal divergence ($\nabla_{\perp} \cdot \mathbf{v}_{\perp}$) that is related to the variation of vertical velocity. This nonzero horizontal divergence gives correction terms in the geostrophic equation. In a classical Ekman layer, the layer is laminar and is approximated as uniformly flat with stable and viscous forces dominating the flow. Therefore, the variation of the vertical velocity along the z -direction is

$$\frac{\partial v_z}{\partial z} = -E_V^{1/2} \omega = -\frac{L_V}{2\Omega} \frac{1}{\tau_E} \omega, \quad (9.8)$$

where τ_E is the Ekman dissipation time defined as $h_0/2\sqrt{\nu\Omega}$.

For a stratified fluid, the density depends only on the vertical direction and hydrostatic equilibrium is assumed. So, the variation of v_z is given by

$$\frac{\partial v_z}{\partial z} = -\frac{2\Omega}{\mathcal{N}^2} \left\{ \frac{\partial^2 \psi}{\partial t \partial z} + \left[\psi, \frac{\partial \psi}{\partial z} \right] \right\}, \quad (9.9)$$

where $\mathcal{N} := -g/\rho_0 \, d\rho/dz$ is the stratification frequency, at which the fluid element oscillates up and down due to the density differences with the ambient fluid. Here, we present a model for an incompressible fluid that takes into account small variations of the Ekman layer which influence the height of fluid elements, and we obtain another expression for $\partial v_z/\partial z$. This nonuniform Ekman layer plays a role in breaking energy spectra into two regions.

9.3.1 Ageostrophic Model

Our new approach results in the introduction of introducing corrections to the geostrophic equation. The shallow-water equation of motion in a rotat-

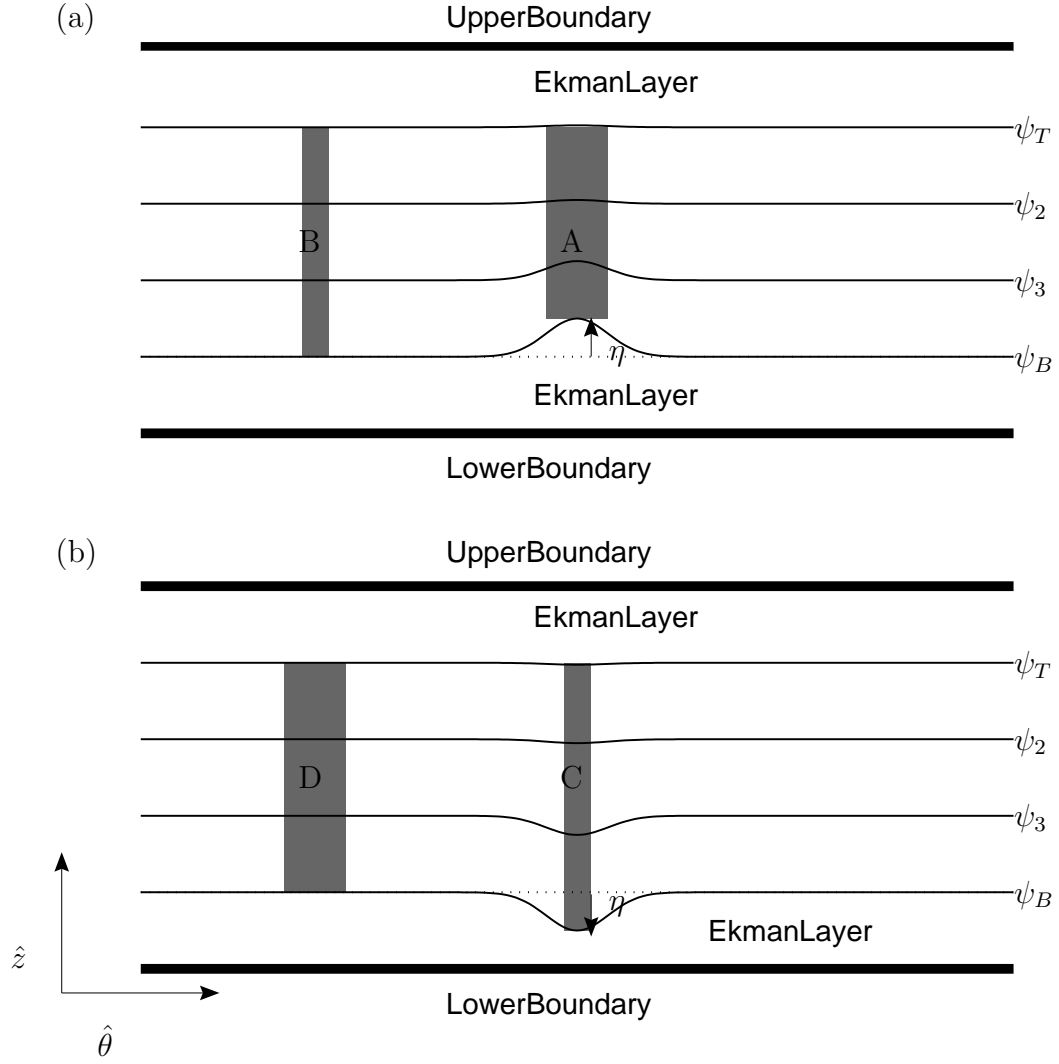


Figure 9.1: Variation of streamfunction. We consider the change of the effective height due to an unstable Ekman layer. Our correction takes into account the variation of effective height due to the fluctuation of streamfunction. Suppose a vortex columns A and B are advected by a large-scale Rossby wave. Figure (a) shows a schematic picture in a frame moving with the Rossby wave. To conserve the pseudo-potential vorticity, a vortex column A has smaller relative vorticity than a vortex column B since the height is smaller. Opposite case can be considered in Fig. (b). Similarly, a vortex column C has larger relative vorticity than a vortex column D since the height is larger.

ing frame is given by

$$\begin{aligned}\frac{\partial v_x}{\partial t} + v_x \frac{\partial v_x}{\partial x} + v_y \frac{\partial v_x}{\partial y} - 2\Omega v_y &= -\frac{1}{\rho} \frac{\partial p}{\partial x} + \nu \nabla^2 v_x \\ \frac{\partial v_y}{\partial t} + v_x \frac{\partial v_y}{\partial x} + v_y \frac{\partial v_y}{\partial y} + 2\Omega v_x &= -\frac{1}{\rho} \frac{\partial p}{\partial y} + \nu \nabla^2 v_y,\end{aligned}\quad (9.10)$$

where ∇^2 can be approximated by $\partial^2/(\partial z^2)$ because of the aspect ratio of our annulus ($L_H/L_V \gg 1$). In the annulus, x is assumed to be the azimuthal direction and y is assumed to be the radial direction the curvature of annulus neglected. With strong rotation, the flow becomes geostrophic and $v_x = -\partial\psi/\partial y$ and $v_y = \partial\psi/\partial x$.

We assume that the surface of the Ekman layers has constant pressure (p_T at the top and p_B on the bottom), constant streamfunction (ψ_T at the top and ψ_B on the bottom), and zero radial velocity. From these assumptions, the pressure can be written as $p = p_B - g\rho(z - \eta)$, where η is the displacement of Ekman layer into the bulk from its mean height of Ekman layer as in Fig. 9.1. If we have a small displacement of Ekman layer, the governing equations are

$$\frac{\partial v_x}{\partial t} + v_x \frac{\partial v_x}{\partial x} + v_y \frac{\partial v_x}{\partial y} - 2\Omega v_y = -g \frac{\partial \eta}{\partial x} + \nu \frac{\partial^2 v_x}{\partial z^2} \quad (9.11)$$

$$\frac{\partial v_y}{\partial t} + v_x \frac{\partial v_y}{\partial x} + v_y \frac{\partial v_y}{\partial y} + 2\Omega v_x = -g \frac{\partial \eta}{\partial y} + \nu \frac{\partial^2 v_y}{\partial z^2} \quad (9.12)$$

In the planetary wave, the continuity equation leads to

$$\frac{\partial v_z}{\partial z} = \frac{1}{L_V} \frac{\partial \eta}{\partial t}. \quad (9.13)$$

By assuming that the variation of v_z is moving with the Rossby wave \overline{U} , Eq. (9.13) becomes

$$\frac{\partial v_z}{\partial z} = \frac{g}{\overline{U}^2} \frac{\partial \eta}{\partial t}. \quad (9.14)$$

For the first approximation, the primary flow is assumed to be geostrophic. Streamfunction is proportional to the displacement of Ekman layer. A relation between streamfunction and the displacement of Ekman layer such as

$$\psi = \frac{g}{2\Omega}\eta, \quad (9.15)$$

leads to the geostrophic equation from a shallow-water model. By substituting the geostrophic solutions, $v_x = -\partial\psi/\partial y$ and $v_y = \partial\psi/\partial x$ into Eq. (9.12), we obtain that

$$-\frac{\partial^2\psi}{\partial t\partial y} - \left[\psi, \frac{\partial\psi}{\partial y}\right] - f_0 v_y = -f_0 \frac{\partial\psi}{\partial x} - \nu \frac{\partial^3\psi}{\partial y\partial z^2}, \quad (9.16)$$

$$\frac{\partial^2\psi}{\partial t\partial x} + \left[\psi, \frac{\partial\psi}{\partial x}\right] + f_0 v_x = -f_0 \frac{\partial\psi}{\partial y} + \nu \frac{\partial^3\psi}{\partial x\partial z^2}, \quad (9.17)$$

where 2Ω is replaced by f_0 for convenience. By using the continuity equation, Eq. (9.14) and the relation, Eq. (9.15), one gets

$$\frac{\partial q}{\partial t} + [\psi, q] = F + D, \quad (9.18)$$

where the pseudo-potential vorticity is defined as

$$q = \nabla_{\perp}^2 \psi + \frac{f_0^2}{U^2} \psi. \quad (9.19)$$

In the inviscid limit, this quantity is conserved with the trajectory of flow. This pseudo-potential vorticity is only for the flat bottom.

With the sloped bottom, the variation of the vertical velocity is

$$\frac{\partial v_z}{\partial z} = -\frac{2\Omega}{U^2} \frac{\partial\psi}{\partial t} - \frac{\beta_{Ro}}{2\Omega} \frac{\partial\psi}{\partial x}. \quad (9.20)$$

The second term represents the beta effect over the sloped bottom. The equation for pseudo-potential vorticity for the sloped bottom is

$$\frac{\partial q}{\partial t} + [\psi, q] = D + F, \quad (9.21)$$

where q is the pseudo-potential vorticity defined as

$$q := \nabla_{\perp}^2 \psi + \frac{(2\Omega)^2}{\bar{U}^2} \psi + \beta_{Ro} y. \quad (9.22)$$

For convenience, we denote $(2\Omega/\bar{U})^2$ by k_D^2 . Similarly, k_D in the stratified fluid is given as the inverse of the internal (or baroclinic) radius of deformation, $L_D := \mathcal{N}L_V/(2\Omega)$ where L_V is the vertical scale of motion.

9.3.2 Two-layers Model

We consider a simple model with two layers which are governed by Eq. (9.21). In our experiment, our two probes are measuring two layers, which are the top and bottom layers as

$$\frac{\partial q_T}{\partial t} + [\psi_T, q_T] = D_T + F_T, \quad (9.23)$$

$$\frac{\partial q_B}{\partial t} + [\psi_B, q_B] = D_B + F_B, \quad (9.24)$$

where

$$q_T = \nabla_{\perp}^2 \psi_T + \beta_{Ro} y + k_D^2 (\psi_B - \psi_T), \quad (9.25)$$

$$q_B = \nabla_{\perp}^2 \psi_B + \beta_{Ro} y + k_D^2 (\psi_T - \psi_B), \quad (9.26)$$

and subscripts T and B present the top and bottom layers, respectively. A term $k_D^2 (\psi_B - \psi_T)$ represents the relative change of the pseudo-potential vorticity due to the change of the height of fluid elements. Similarly, a two-layer model in stratified fluids is proposed by Philips [167].

We will write barotropic-like and the baroclinic-like streamfunctions in terms of streamfunctions near the top ψ_T and near the bottom ψ_B . We define the barotropic-like and the baroclinic-like streamfunctions as

$$\psi_{BT} = \frac{1}{2}(\psi_T + \psi_B), \quad \psi_{BC} = \frac{1}{2}(\psi_T - \psi_B), \quad (9.27)$$

where BT and BC represent barotropic-like and baroclinic-like parts. Using those above definitions, the equation of motions for potential vorticities are given as

$$\begin{aligned} & \frac{\partial \nabla_{\perp}^2 \psi_{BT}}{\partial t} + [\nabla_{\perp}^2 \psi_{BT}, \psi_{BT}] + [(\nabla_{\perp}^2 - k_D^2) \psi_{BC}, \psi_{BC}] \\ = & \nu \nabla_{\perp}^2 (\nabla_{\perp}^2 \psi_{BT}) + F_{BT}, \end{aligned} \quad (9.28)$$

$$\begin{aligned} & \frac{\partial (\nabla_{\perp}^2 - k_D^2) \psi_{BC}}{\partial t} + [\nabla_{\perp}^2 \psi_{BT}, \psi_{BC}] + [(\nabla_{\perp}^2 - k_D^2) \psi_{BC}, \psi_{BT}] \\ = & \nu \nabla_{\perp}^2 (\nabla_{\perp}^2 \psi_{BC} - k_D^2 \psi_{BC}) + F_{BC}. \end{aligned} \quad (9.29)$$

There are three types of triads for energy transfers; One is the interaction between two BT modes then giving energy to one BC mode. The second is the interaction between two BC modes then giving energy to one BT mode. The third is the interaction between one BT mode and one BC modes then giving energy to one BC mode. The latter two are the interaction of two BT and one BC modes. Here, we consider two types of interactions.

BT-BT-BT interaction

Interactions of three BT modes are the same as interactions in two dimensional turbulence. We will introduce three wavenumbers \mathbf{k} , \mathbf{p} and \mathbf{q} for three modes whose sum is zero. The energy and enstrophy conservations give

$$\frac{d}{dt} (E(\mathbf{k}) + E(\mathbf{p}) + E(\mathbf{q})) = 0 \quad (9.30)$$

$$\frac{d}{dt} (k^2 E(\mathbf{k}) + p^2 E(\mathbf{p}) + q^2 E(\mathbf{q})) = 0. \quad (9.31)$$

Eq. (9.31) avoids energy transfer between scales of extremely local and extremely nonlocal. For example, consider two BT modes, \mathbf{k} and \mathbf{p} , are close each other. Above energy and enstrophy equations lead to

$$2 \frac{dE(\mathbf{k})}{dt} \simeq - \frac{dE(\mathbf{q})}{dt}, \quad 2 \frac{dk^2 E(\mathbf{k})}{dt} \simeq - \frac{dq^2 E(\mathbf{q})}{dt}. \quad (9.32)$$

The only solution that we get is that $\mathbf{k} = \mathbf{q}$. It implies that no energy transfer among three wavenumbers close together. Similar results can be obtained if $\mathbf{k} \gg \mathbf{q}$. For intermediate \mathbf{k} , \mathbf{p} , and \mathbf{q} , the energy is transferred to the lower wave number, the so-called inverse energy transfer.

BT-BC-BC interaction

Let's denote \mathbf{k} for one BT mode and \mathbf{p} and \mathbf{q} for two BC mode. If $\mathbf{k}, \mathbf{p}, \mathbf{q} \gg k_D$, BT-BC-BC interactions are the same as BT-BT-BT interactions as in 2D turbulence. In the two-layer model, motions in smaller scales than $1/k_D$ consist of uncoupled BT and BC motions. However, if $\mathbf{k}, \mathbf{p}, \mathbf{q} \ll k_D$, the energy transfer between two BC modes occurs only local ($\mathbf{p} \sim \mathbf{q} \ll k_D$) or nonlocal $\mathbf{p} \ll \mathbf{q}$.

9.3.3 Energy Transfer Between BC and BT Modes

The BT kinetic energy is mostly fed at the wavenumbers close to the length scale $1/k_D$ by BC instability [192, 77]. Consequently, BT energy slowly cascades back to the large scales. Eq. (9.28) is approximated as

$$\frac{\partial \nabla_{\perp}^2 \psi_{BT}}{\partial t} + [\nabla_{\perp}^2 \psi_{BT}, \psi_{BT}] = \nu \nabla_{\perp}^2 (\nabla_{\perp}^2 \psi_{BT}) + F_{BC}, \quad (9.33)$$

where F_{BC} is the forcing from the BC mode. If we assume that the BC forcing is localized around the wavenumber k_D , this BC forcing has the eigenvalue such as

$$\nabla^2 F_{BC} = -k_D^2 F_{BC}. \quad (9.34)$$

The equation of enstrophy is given as

$$\frac{\partial (\nabla_{\perp}^2 \psi_{BT})^2}{\partial t} + [(\nabla_{\perp}^2 \psi_{BT})^2, \psi_{BT}] = \nu \nabla_{\perp}^2 (\nabla_{\perp}^2 \psi_{BT})^2 + k_D^2 F_{BC}. \quad (9.35)$$

In summary, we obtain the BT flows with two conservation laws of energy and enstrophy, a spectrally concentrated forcing and molecular viscosity. Next, we consider these conditions and a rotation and find how energy spectra change with those conditions.

The BT system with the BC forcing as in Eq. (9.33) is close to a system with a spectrally localized forcing since the energy transfers are near a single wavenumber k_D . Primitive expectation of the BT energy spectrum in this system is Kraichnan's spectrum [107]: Energy is transferred into large scales as a $k^{-5/3}$ inverse energy cascade and enstrophy cascades into smaller scales as k^{-5} . However, energy transfers caused by the nonlinearities are slowed down in the presence of a rotation [234, 43]. The time scale of triple interactions is inversely proportional to the rotation frequency Ω . Through the simple non-dimensional analysis, it leads to a k^{-2} inverse energy cascade. Another problem in Kraichnan's picture is raised by considering the conservation of energy and enstrophy with a spectrally concentrated forcing [61, 211]. Similarly, we also suggest no enstrophy cascade in our system. To get the energy spectrum, the whole process is the same as in [211].

Finally, we expect that the energy spectrum in a rapidly rotating turbulence with the flat bottom is

$$E(k) \begin{cases} \sim k^{-2} & \text{for } k < k_D \\ < k^{-5} & \text{for } k > k_D. \end{cases} \quad (9.36)$$

This energy spectrum is obtained with a strong rotation, conservation of energy and enstrophy, molecular dissipation, and spectrally localized forcing. However, a system with the sloped bottom does not satisfy Eq. (9.35) because of the term $\beta_{Ro}y$ in Eq. (9.25) and (9.26). We did not obtain any expression for the energy spectrum with the sloped bottom yet.

9.4 Experimental Observations

Using the hot film probe under the top lid and on the bottom, we measure the azimuthal and vertical velocity. If the fluctuations are small, the measured velocity is interpreted as the azimuthal velocity as in Eq. (3.5).

Measured velocities are shown in Fig. 9.2. We measured velocities on the top and bottom of the tank. Two probes are separated only in the vertical direction as shown in Fig. 3.1. Velocities on the top (V_T) and bottom (V_B) are simultaneously measured as shown in Fig. 9.2 (a). Mean velocities on the top and bottom are different by $2 - 3$ cm/s. Velocity on the bottom V_B is always smaller than velocity on the top V_T . Also, V_B has localized and periodic high-frequency signals. By using wavelet analysis, we can extract those localized high-frequency signals (Hepeng Zhang). Wavelet analysis consists of decomposing a signal or an image into a hierarchical set of approximations and details. By using Coiflet1 Wavelets, the extracted high-frequency signals are shown in inset of Fig. 9.2 (a). High-frequency signals are localized around 6, 22, and 39 seconds. Regular periodicity, 16 seconds is observed in the whole set of data (2500 seconds). By shifting V_B in order to have the same mean velocity with V_T , we can find how large-scale motions of both signals are similar and how small-scale motions are different.

Velocity time series can be converted into the spatial distribution of velocity since the fluctuation is small compared to the mean flow (Taylor frozen hypothesis [205]). Then, energy spectrum with respect to the time frequency can be converted into it with spatial wavenumber. From now on, all y axes are energy spectra in the log-scale and x -axes are either $\omega_t/2\Omega$ or k in the log-scale where ω_t is time frequency, Ω is a rotation frequency of tank, and

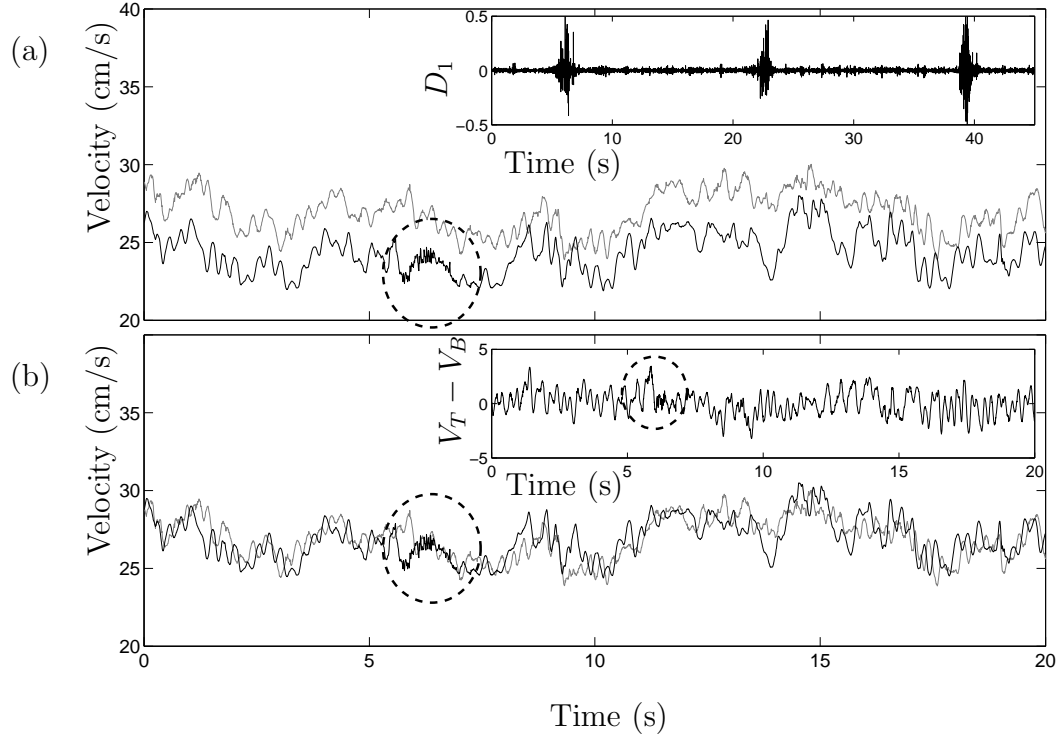


Figure 9.2: Velocity example of the top and bottom at 2 Hz and 150 cm³/s. Fig. (a) shows the velocity of the top and bottom. The black line is the velocity of the bottom (V_B) while the gray line is the velocity of the top (V_T). Ellipses indicate the high-frequency velocity variations. Those high-frequency bursts are quite periodic as shown in the inset of Fig. (a). Here, D_1 is the first-order coefficient of Coiflet1 Wavelets. Its periodicity is roughly about 17 sec. To compare more details, we shift V_B to match with V_T as in Fig. (b). Inset shows a difference between two velocities. Both velocities have similar large scale motions but different small scales motions.

k is a wavenumber. Taylor frozen hypothesis gives a relation as $k \sim \omega_t/\overline{U}$ where \overline{U} is the mean velocity of Rossby waves if vortices are assumed to be advected by Rossby waves not by the mean velocity [129]. We introduce the non-dimensional time frequency, $\omega_t/2\Omega$. With this Taylor frozen hypothesis, the wavenumber $k = k_D$ leads to a condition $\omega_t/2\Omega = 1$. Due to the strong rotational effect, this nondimensional time frequency is quite useful to investigate the structures of energy spectrum.

9.4.1 Energy Spectrum over Sloped vs. Flat Bottom

We proposed a model which assumed that there exist the crests and troughs of streamfunction or the surface of Ekman layers, which are advected by the Rossby wave. With those assumptions, BT systems are predicted to have a clear breakpoint in energy spectra over the flat bottom. This breakpoint in time frequency is predicted as $\omega_t/2\Omega = 1$, as in Chap. 9.3.3. It is the scale where BC energy is transferred into BT energy.

Fig. 9.3 shows energy spectra near the top over the flat bottom at 1 or 1.75 Hz and 150 cm³/s. One can observe break points in energy spectra near $\omega_t/2\Omega \approx 1$ as we expected. Energy spectra follow $k^{-5/3} \sim k^{-2}$ below the break points and k^{-6} above the break points. Narrow spikes in high time-frequencies are harmonics of a rotation rate. Fig. 9.4 shows energy spectra near the top over the sloped bottom at 1 or 1.75 Hz and 150 cm³/s. Similarly, break points are locate near $\omega_t/2\Omega \approx 1$. However, slopes of power-laws are different. Energy spectra over the sloped bottom are between k^{-2} and $k^{-5/3}$ below the break points and between k^{-3} and k^{-4} above the break points. In consequence, we found that energy spectra in small scales over the sloped bottom are quite

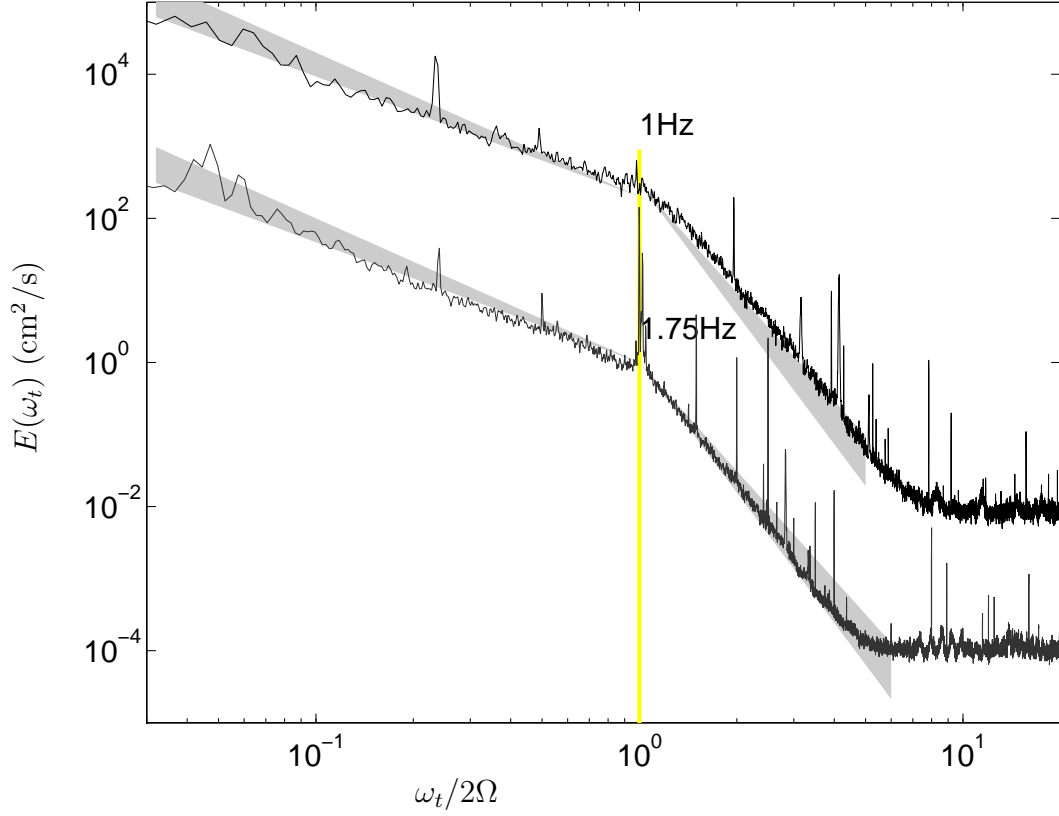


Figure 9.3: Energy spectra with two rotation rates (1 and 1.75 Hz) with a flat bottom. The pumping rate is fixed at $150 \text{ cm}^3/\text{s}$. Energy spectra are vertically shifted by arbitrary values. Shaded region on the right hand-side represents the energy spectrum between k^{-6} and k^{-5} (Lower bound is k^{-6}). Shaded region on the left guides the energy spectrum between k^{-2} and $k^{-5/3}$.

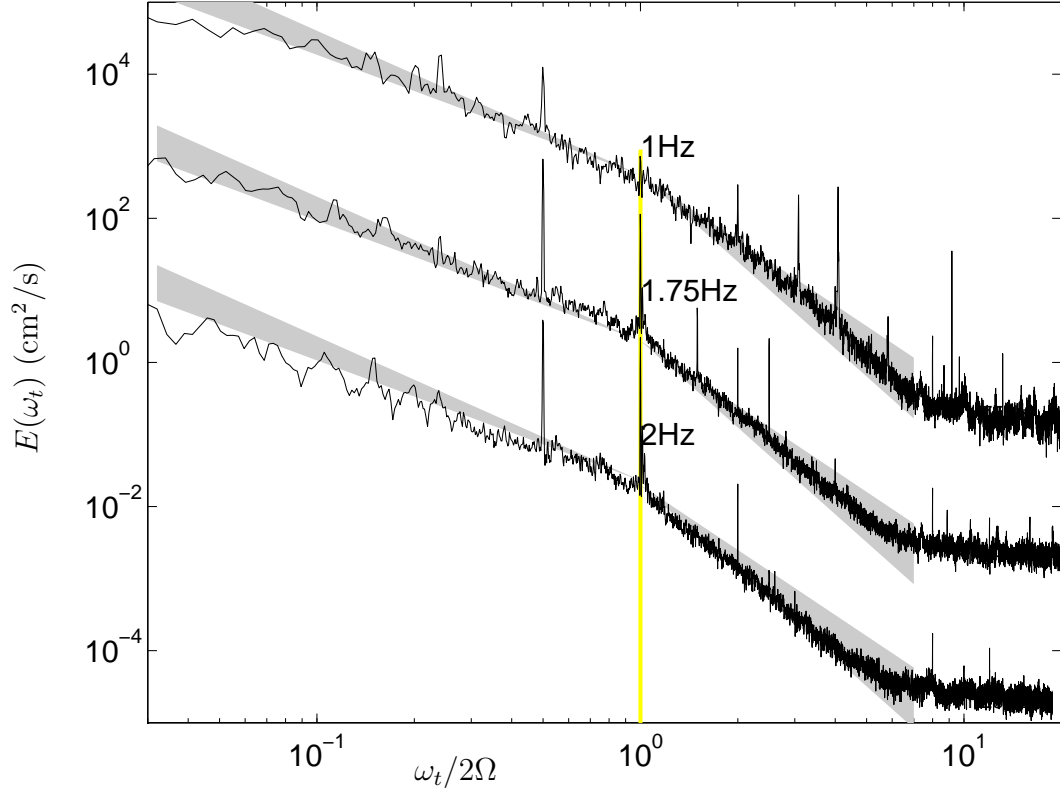


Figure 9.4: Energy spectra with various rotation rate over a sloped bottom. The rotation rates are 2 Hz, 1.75 Hz and 1 Hz. Energy spectra are vertically shifted by arbitrary values. Shaded region on the right hand-side represents the energy spectrum between k^{-4} and k^{-3} (Lower bound is k^{-4}). Shaded region on the left guides the energy spectrum between k^{-2} and $k^{-5/3}$.

different from energy spectra over the flat bottom as shown in Fig. 9.3 and 9.4. How does the beta plane affect the fluid motion in small scales?

The effect of beta plane is discussed in Chap. 3.1.2. The next question is where the beta plane plays a role. Rhines proposed that the critical scale of the beta effect is obtained by balancing the Rossby wave frequency β_{Ro}/k and an inverse advective time scale Uk . The beta plane might affect the length scales which satisfy $U(k)k^2/\beta_{Ro} < 1$ but not for $U(k)k^2/\beta_{Ro} > 1$ where $U(k)$ is velocity at the scale related with a wavenumber k .

There are various ways to define $U(k)$. Here, we choose

$$U(k) = \sqrt{E(k)k}, \quad (9.37)$$

by assuming that $U(k)$ is a function of $E(k)$ and k only. By using Eq. (9.37), a critical length scale of $U(k)k^2/\beta_{Ro} = 1$ is equivalent to

$$E(k) = (\beta_{Ro})^2 k^{-5}. \quad (9.38)$$

This expected energy spectrum ($E(k) \sim k^{-5}$) is found in very large scales [171]. In our experiment, we found that

$$\beta_{Ro} = \frac{2\Omega\eta}{h} = 2 \times 11 \text{ rad/s} \times (-0.1)/16 \text{ cm} \sim -0.12 (\text{cm s})^{-1}. \quad (9.39)$$

This critical condition implies that the beta plane affects the scales associated $E(k) < 0.01k^{-5}$ but does not affect the scales associated $E(k) > 0.01k^{-5}$.

Fig. 9.5 shows two energy spectra over the sloped and flat bottom and the dotted line indicates the critical condition of the beta effect ($E(k) = (\beta_{Ro})^2 k^{-5}$). Below the dotted line is the region where the beta effect dominates flows. Only for large scales ($k < 0.15$), the beta plane plays a role. However, we observed a significant difference of energy spectra in small scales when

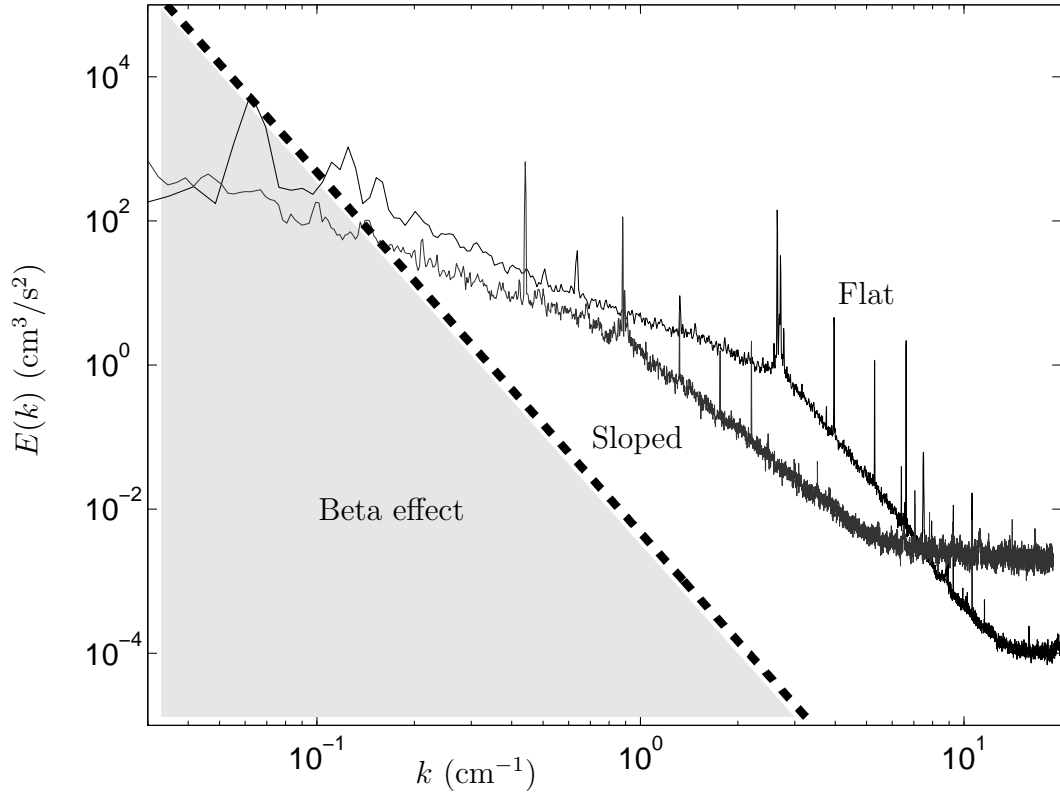


Figure 9.5: Energy spectra at 1.75 Hz and 150 cc/s over the sloped bottom and the flat bottom. The dotted line represents a condition that $[U(k)k^2]/\beta = 1$. In the shaded region, the effect of beta plane is crucial and then large scales ($k \lesssim 0.2$) are affected by beta plane. However, energy spectrum of scales $k \gtrsim 0.2$ should not be influenced by the bottom topography. The above figure shows that there might be some influences on the energy spectrum of small scales due to the bottom topography.

the sloped bottom changes to the flat bottom. It is generally believed that the beta plane manipulates the energy spectrum as k^{-5} in only large length scales. Despite of this expectation, we observed a significant difference of energy spectra in small scales. So, we conclude that Rhines' argument cannot explain our experimental observations.

9.4.2 Burstings

Velocities are measured in the bulk near the top and bottom which are located at the same position (r, θ) in a plane perpendicular to the rotation axis. For laminar flows, we expect that velocities near the top and bottom become identical if Rossby number and Ekman number approach to zero according to Taylor-Proudman theorem. Here, we present how energy spectra near the top and bottom converge as we increase the rotation frequency. The discrepancy of two energy spectra is expected due to vertical motions. We also expect that the split region of two energy spectra near the top and bottom becomes small as the rotation frequency (Ω) increases.

As shown in Fig. 9.6, the rotation affects energy spectra near top and bottom. More energetic motions in high frequencies are observed from velocities near the bottom. In contrast, the less energetic energy spectra in the small scales come from velocities near the top. This discrepancy in energy spectra near the top and bottom is quite localized and periodic in time as in Fig. 9.2. Its periodicity is about 20 sec in 1 Hz and 150 cm³/s. The source of these high-frequency burstings is unknown. We guess that these burstings are due to the turbulent Ekman layer. As we decrease the rotation rate, two energy spectra, one from top and one on bottom, separate in small scales ($\omega_t/(2\Omega) > 1$).

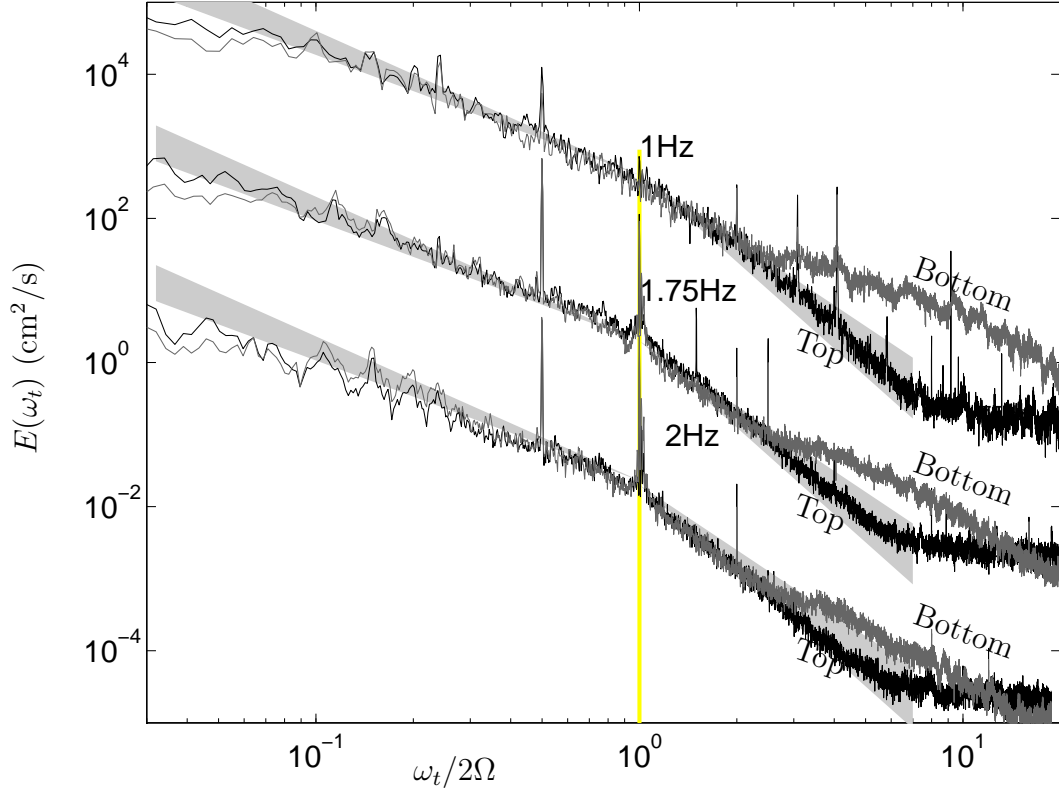


Figure 9.6: Energy spectra with various rotation rate over a sloped bottom. The rotation rate changes as 2 Hz, 1.75 Hz and 1 Hz. The curve on the top is from the probe on the bottom of tank and the curve on the bottom is from the probe beneath the top of tank. Energy spectra are vertically shifted by arbitrary values. Shaded region on the right hand-side represents the energy spectrum between k^{-4} and k^{-3} (Lower bound is k^{-4}). Shaded region on the left guides the energy spectrum between k^{-2} and $k^{-5/3}$. Separation of the energy spectra is seen in high frequency region.

It also indicates that 3D motion in the small scales are disappearing as the Rossby number goes to zero.

9.5 Conclusion and Future Work

In turbulence, the linear theory with uniform and stable Ekman layer may be not applicable. So, we proposed a simple model which takes into account the small variation of Ekman layer. Our simple model explains where the break points of energy spectra over the flat bottom are located. This prediction as 2Ω in the time-frequency domain is observed in experiments. However, the energy spectrum over the sloped bottom is still an open question.

High-frequency burstings on the bottom with the sloped bottom are observed. They are periodic and very localized. We did not study the full range of a rotation rate and a pumping rate. Those burstings are not observed with the flat bottom. More careful study on those burstings is necessary.

Chapter 10

Conclusion

Two-dimensional flow is a very interesting subject in theory, but it is hard to achieve in an experiment. Our experimental setup succeeds nicely in making quasi-two dimensional flows, and changing the rotation rate and the pumping rate over a wide range. Our experiment enables us to study the influence of rotation and pumping on fluid motion. Our experiment with a sloped bottom is a laboratory analog of the large-scale atmospheric and oceanic motion, but these naturally occurring flows are complicated and difficult to understand. Thus our experiment serves as a means for shedding light on them.

In this thesis, we have tested various theoretical approaches to describe these quasi two-dimensional flows in a rapid rotating tank. Also, we covered most of the characteristics of turbulence, including both statistical properties and the behavior of energy spectra.

10.1 Contributions

In Chap. 4, we have studied how non-axisymmetric motion mixes potential vorticity and produces a zonal circulation. As the potential vorticity mixing grows, the reservoir of potential vorticity is fully used and is organized into a final state. The zonal motion was observed to saturate at the value given by Equation (4.6).

The question of how a final state is achieved is raised in Chap. 5. By applying statistical mechanics to inhomogeneous turbulence, we have discovered experimentally that a good definition of subsystem is provided by the temporal mean of the streamfunction. With this definition, the quadratic invariants (energy and enstrophy) are statistically independent, and the resultant Gaussian probability density in a systematically chosen subsystem agrees quite well with experimental results for both the distribution of potential vorticity and the mean state of potential vorticity. We also tested statistical mechanics with nonextensive entropy in Chap. 6.

Furthermore, statistical mechanics requires a proper set of canonical coordinates (such as action-angle variables). An ensemble-averaged measure leads to a correct result only with canonical coordinates. For a long time, this measure has been performed by treating non-canonical variables. Following the novel work for the Vlasov case [149], our calculation with canonical coordinates was done with the linearized equations of 2D fluid motion.

The statistics of measures in turbulence is self-similar and non-Gaussian. Both the Kolmogorov-Castaing and Beck-Cohen methods have been very successful in describing the non-Gaussian distribution of velocity differences in turbulence [25, 47]. We have presented a method for determining the subsys-

tem size in the Beck-Cohen method, thus eliminating the need for a fitting parameter. We have also shown that Castaing’s method can be converted to the Beck-Cohen method. In this sense, the two methods describe the non-Gaussian distribution of δv_r in the same way,

$$P(\delta v_r) = \int \text{Gaussian distribution} \times (\log - \text{normal distribution}).$$

Besides the statistics of turbulence, the energy spectrum has universal features, including the exponent of its power-law behavior. Energy spectra were investigated by measuring velocities on the top and bottom of the annular tank. The energy of 2D motion is fed by the vertical motion at a scale which is related to the vertical variation of velocity. This forced energy is transformed into large scales and the forced enstrophy is dissipated at the same scale as the forcing scale. Therefore, we expect an inverse energy cascade and no enstrophy cascade for the flat bottom case. Experimental results verify our expectation.

10.2 Future Work

There are many unsolved issues that have arisen from our study of turbulence. Basic properties of turbulence are described by statistics and spectra, and details of these remain to be understood for the velocity and vorticity.

The study on the co-rotating jet remains to be done. The co-rotating jet is more stable and energetic than the counter-rotating jet and has Gaussian statistics for the velocity difference, whereas the counter-rotating jet has non-Gaussian statistics. Working with Dr. Brian Storey, we found that numerical simulations show a similar behavior. To investigate further, we need to see

structures of the velocity fields with short time intervals. Technically, a high frame rate camera is required to capture the motion for the high-velocity flow of co-rotating jets.

The mechanism for dissipation in 2D turbulence is still not very well understood. Ekman dissipation is valid in laminar and stable flows, such as the spin-down experiment. In turbulence, dissipation depends more on the dynamics rather than the uniform Ekman layer. So, we introduced a more dynamical model for the vertical velocity in Chap. 9. We need more proof for this assumption and for the experimental evidence of the advection of the 2D divergence.

We have constructed building blocks for the statistical mechanics of vorticity in a 2D fluid. However, there are a lot of issues related to statistical mechanics that need to be resolved. First, we observed the fluctuation of an intensive parameter, but due to the lack of data, we cannot see the statistics of an intensive parameter. If the statistics of an intensive parameter have a log-normal distribution, then we can proceed to show non-Gaussian statistics of the potential vorticity, as we studied in Chap. 8. Also, the enstrophy spectrum can be deduced from the fluctuation of potential vorticity.

A final goal of the fluid study might be the unification of characteristics of fluid and plasma dynamics. In the inviscid limit, both have the same structure with noncanonical brackets. The work of Chap. 7 is part of this unification. Once this unification is done, we can expand it to the solid-fluidized system and so on.

Bibliography

- [1] A.M. Crawford J. Alexander A. La Porta, G.A. Voth and E. Bodenschatz. Fluid particle accelerations in fully developed turbulence. *Nature*, 409:1017–1019, 2001.
- [2] F. Anselmet, Y. Gagne, E.J. Hopfinger, and R.A. Antonia. High-order velocity structure functions in turbulent shear flows. *J. Fluid Mech.*, 140:63–89, 1984.
- [3] R.A. Antonia, N. Phan-Yhien, and A.J. Chambers. Taylor’s hypothesis and the probability density functions of temporal velocity and temperature derivatives in a turbulent flow. *J. Fluid Mech.*, 100:193, 1980.
- [4] A. Arneodo, C. Baudet, F. Belin, R. Benzi, B. Castaing, B. Chabaud, R. Chavarria, S. Ciliberto, R. Camussi, F. Chilla, B. Dubrulle, Y. Gagne, B. Hebral, J. Herweijer, M. Marchand, J. Maurer, J.F. Muzy, A. Naert, A. Noullez, J. Peinke, F. Roux, P. Tabeling, W. vandeWater, and H. Willaime. Structure functions in turbulence, in various flow configurations, at reynolds number between 30 and 5000, using extended self-similarity. *Europhys. Lett.*, 34(6):411–416, 1996.
- [5] A. Arneodo, N. Decoster, and S.G. Roux. Intermittency, log-normal

- statistics, and multifractal cascade process in high-resolution satellite images of cloud structure. *Phys. Rev. Lett.*, 83(6):1255–1258, 1999.
- [6] A. Arneodo, S. Manneville, and J.F. Muzy. Towards log-normal statistics in high reynolds number turbulence. *Euro. Phys. J. B*, 1(1):129–140, 1998.
 - [7] A. Arneodo, J.F. Muzy, and S.G. Roux. Experimental analysis of self-similarity and random cascade processes: Application to fully developed turbulence data. *J. Phys. II*, 7(2):363–370, 1997.
 - [8] V.I. Arnolds. *Mathematical Methods of Classical Mechanics*. Springer-Verlag, 1978.
 - [9] J. Aubert, D. Brito, P. Cardin, H.C. Nataf, and J.P. Masson. A systematic experimental study of spherical shell rotating convection in water and liquid gallium. *Phys. Earth Planet. Int.*, 128:51–74, 2001.
 - [10] J. Aubert, S. Jung, and H.L. Swinney. Observational of zonal flow created by potential vorticity mixing in a rotating fluid. *Geophys. Res. Lett.*, 29(18), 2002.
 - [11] R. Badii and P. Talkner. Analysis of energy cascade models of turbulence. *Phys. Rev. E*, 59(6):6715–6723, Jun 1999.
 - [12] R. Badii and P. Talkner. Biasymptotic formula for the turbulent energy cascade. *Phys. Rev. E*, 60(4):4138–4142, Oct 1999.
 - [13] N.J. Balmforth and P.J. Morrison. A necessary and sufficient instability condition for inviscid shear flow. *preprint in 1998*.

- [14] N.J. Balmforth and P.J. Morrison. Normal modes and continuous spectra. *Ann. New York Acad. of Sci.*, 773:80–94, 1995.
- [15] N.J. Balmforth and P.J. Morrison. Singular eigenfunctions for shearing fluids. *Institute for Fusion Studies, University of Texas at Austin*, Report No. 692, 1995.
- [16] N.J. Balmforth and P.J. Morrison. Hamiltonian description of shear flow. *Large-Scale Atmosphere-Ocean Dynamics II*, 2002.
- [17] C.N. Baroud. *Transitions from three- to two-dimensional turbulence in a rotating system*. PhD thesis, University of Texas at Austin, 2001.
- [18] C.N. Baroud, B.B. Plapp, Z.S. She, and H.L. Swinney. Anomalous self-similarity in a turbulent rapidly rotating fluid. *Phys. Rev. Lett.*, 88:114501, 2002.
- [19] C.N. Baroud, B.B. Plapp, H.L. Swinney, and Z.S. She. Scaling in three-dimensional and quasi-two-dimensional rotating turbulent flows. *Phys. Fluids*, 15(8):2091–2104, 2003.
- [20] C.N. Baroud and H.L. Swinney. Nonextensivity in turbulence in rotating two-dimensional and three-dimensional flows. *Physica D*, 183:21–28, 2003.
- [21] G.K. Batchelor and A.A. Townsend. The nature of turbulent motion at large wave-numbers. *Proc. Roy. Soc. Lond. A*, 199:238–255, 1949.
- [22] C. Beck. Dynamical foundations of nonextensive statistical mechanics. *Phys. Rev. Lett.*, 87:180601, 2001.

- [23] C. Beck. On the small-scale statistics of lagrangian turbulence. *Phys. Lett.*, 287A:240–244, 2001.
- [24] C Beck. Lagrangian acceleration statistics in turbulent flows. *Europhys. Lett.*, 64(2):151–157, 2003.
- [25] C. Beck. Superstatistics in hydrodynamic turbulence. *Physica D*, 193:195–207, 2004.
- [26] C. Beck and E.G.D. Cohen. Superstatistics. *Physica A*, 322:267–275, 2003.
- [27] C. Beck, G. S. Lewis, and H. L. Swinney. Measuring nonextensivity parameters in a turbulent Couette-Taylor flow. *Phys. Rev. E*, 63(3):035303, 2001.
- [28] P. Belin, F. Tabeling and H. Willaime. Exponents of the structure functions in a low temperature helium experiment. *Physica D*, 93(1-2):52–63, 1996.
- [29] G. Boffetta, A. Celani, and M. Vergassola. Inverse energy cascade in two-dimensional turbulence: Deviations from gaussian behavior. *Phys. Rev. E*, 61(1):R29–R32, Jan 2000.
- [30] B.M. Boghosian. Thermodynamic description of the relaxation of two-dimensional turbulence using tsallis statistics. *Phys. Rev. E*, 53:4754–4763, 1996.
- [31] C. Boucher, R.S. Ellis, and B. Turkington. Derivation of maximum entropy principles in two-dimensional turbulence via large deviations. *J. Stat. Phys.*, 98(5-6):1235–1278, 2000.

- [32] F. Bouchet and J. Sommeria. Emergence of intense jets and jupiter's great red spot as maximum-entropy structures. *J. Fluid Mech.*, 464:165–207, 2002.
- [33] J.C. Bowman, B.A. Shadwick, and P.J. Morrison. Spectral reduction: A statistical description of turbulence. *Phys. Rev. Lett.*, 83:5491–5494, 1999.
- [34] M.R. Brown. Experimental evidence of rapid relaxation to large-scale structures in turbulent fluids: selective decay and maximal entropy. *J. Plasma Physics*, 57:203–229, 1997.
- [35] J.M. Burgers. On the application of statistical mechanics to the theory of turbulent fluid motion i. *Koninklijke Nederlandse Akademie van Wetenschappen*, 32:414, 1929.
- [36] J.M. Burgers. On the application of statistical mechanics to the theory of turbulent fluid motion ii. *Koninklijke Nederlandse Akademie van Wetenschappen*, 32:632, 1929.
- [37] J.M. Burgers. On the application of statistical mechanics to the theory of turbulent fluid motion iii. *Koninklijke Nederlandse Akademie van Wetenschappen*, 32:818, 1929.
- [38] J.M. Burgers. On the application of statistical mechanics to the theory of turbulent fluid motion iv. *Koninklijke Nederlandse Akademie van Wetenschappen*, 36:276, 1933.
- [39] J.M. Burgers. On the application of statistical mechanics to the the-

- ory of turbulent fluid motion v. *Koninklijke Nederlandse Akademie van Wetenschappen*, 36:390, 1933.
- [40] J.M. Burgers. On the application of statistical mechanics to the theory of turbulent fluid motion vi. *Koninklijke Nederlandse Akademie van Wetenschappen*, 36:487, 1933.
- [41] J.M. Burgers. On the application of statistical mechanics to the theory of turbulent fluid motion vii. *Koninklijke Nederlandse Akademie van Wetenschappen*, 36:620, 1933.
- [42] R. Camussi and R. Benzi. Hierarchy of transverse structure functions. *Physics of Fluids*, 9:257–259, 1997.
- [43] V.M. Canuto and M.S. Dubovikov. A dynamical model for turbulence. v. the effect of rotation. *Phys. Fluids*, 9(7):2132–2140, July 1997.
- [44] V.M. Canuto and M.S. Dubovikov. Physical regimes and dimensional structure of rotating turbulence. *Phys. Rev. Lett.*, 78(4):666, Jan 1997.
- [45] B. Castaing. Scalar intermittency in the variational theory of turbulence. *Physica D*, 73(1-2):31–37, 1994.
- [46] B. Castaing and B. Dubrulle. Fully-developed turbulence - a unifying point-of-view. *J. Phys. II*, 5(7):895–899, 1995.
- [47] B. Castaing, Y. Gagne, and E.J. Hopfinger. Velocity probability density functions of high reynolds number turbulence. *Physica D*, 46:177–200, 1990.

- [48] B. Castaing, Y. Gagne, and M. Marchand. Velocity probability density functions of high reynolds number turbulence. *Physica D*, 68:387–400, 1993.
- [49] C. Cercignani. *Mathematical methods in kinetic theory*. New York: Plenum, 1990.
- [50] B. Chabaud, A. Naert, J. Peinke, F. Chilla, B. Castaing, and B. Hebral. Transition toward developed turbulence. *Phys. Rev. Lett.*, 73(24):3227–3230, 1994.
- [51] P. Chainais, P. Abry, and J.F. Pinton. Intermittency and coherent structures in a swirling flow: A wavelet analysis of joint pressure and velocity measurements. *Phys. Fluids*, 11(11):3524–3539, 1999.
- [52] F.H. Champagne. The fine scale structure of the turbulence velocity field. *J. Fluid Mech.*, 86:67, 1978.
- [53] O. Chanal, B. Chabaud, B. Castaing, and B. Hebral. Intermittency in a turbulent low temperature gaseous helium jet. *Euro. Phys. J. B*, 17(2):309–317, 2000.
- [54] P.H. Chavanis, J. Sommeria, and R. Robert. Statistical mechanics of two-dimensional vortices and collisionless stellar systems. *Astro. J.*, 471(1):385–399, 1996.
- [55] G.R. Chavarria, C. Baudet, and S Ciliberto. Hierarchy of the energy-dissipation moments in fully-developed turbulence. *Phys. Rev. Lett.*, 74(11):1986–1989, Mar 13 1995.

- [56] E. S. C. Ching and K. L. Chau. Conditional statistics of temperature fluctuations in turbulent convection. *Phys. Rev. E*, 63(4):047303–1, Apr 2001.
- [57] U.R. Christensen. Zonal flow driven by deep convection in the major planets. *Geophys. Res. Lett.*, 13:2553–2556, 2001.
- [58] E.G.D. Cohen. Superstatistics. *Physica D*, 193:3–34, 2004.
- [59] A. Colin de Verdière. Mean flow generation by topographic rossby waves. *J. Fluid Mech.*, 94:39–64, 1979.
- [60] P. Constantin. Energy spectrum of quasigeostrophic turbulence. *Phys. Rev. Lett.*, 89:184501, 2002.
- [61] P. Constantin, C. Foias, and O. P. Manley. Effects of the forcing function spectrum on the energy spectrum in 2-d turbulence. *Phys. Fluids*, 6(1), 1994.
- [62] R. Courant and D. Hilbert. *Methods of Mathematical Physics*, volume Vol. I. Interscience Publishers, 1953.
- [63] B. Cushman-Roisin. *Introduction to Geophysical Fluid Dynamics*. Prentice-Hall, 1994.
- [64] L. Turner D. Montgomery and G. Vahala. Find it. *Phys. Fluids*, 21:757, 1978.
- [65] K. E. Daniels, C. Beck, and E. Bodenschatz. Defect turbulence and generalized statistical mechanics. *Physica D*, 193:208–217, 2004.

- [66] D. del Castillo-Negrete and P.J. Morrison. Hamiltonian chaos and transport in quasigeostrophic flows. In I. Prigogine, editor, *Research trends in physics: Chaotic dynamics and transport in fluids and plasmas*, pages 181–207. American Institute of Physics, 1992.
- [67] B. Dubrulle. Intermittency in fully-developed turbulence - log-poisson statistics and generalized scale covariance. *Phys. Rev. Lett.*, 73(7):959–962, Aug 15 1994.
- [68] P. Ehrenfest and T. Ehrenfest. *The Conceptual Foundations of the Statistical Approach in Mechanics*. Dover, 1961.
- [69] L.P. Eisenhart. *Continuous groups of transformations*. Ithaca: Cornell University Press, 1959.
- [70] J.W. Elsner and W. Elsner. On the measurement of turbulence energy dissipation. *Measurement Science and Technology*, 7(10):1334–1348, Oct 1996.
- [71] G. L. Eyink and H. Spohn. Negative temperature states and large-scale, long-lived vortices in two-dimensional turbulence. *J. Stat. Phys.*, 70:833–886, 1993.
- [72] G. L. Eyink and K. R. Sreenivasan. Onsager and the theory of hydrodynamic turbulence. Preprint, 1 2005.
- [73] M.J. Fisher and P. O. A. L. Davies. Correlation measurements in a non frozen pattern of turbulence. *J. Fluid Mech.*, 18:97, 1964.
- [74] C.A.J. Fletcher. *Computational Techniques for Fluid Dynamics*. Berlin:Springer, 1990.

- [75] U. Frisch. From global scaling, a-la kolmogorov, to local multifractal scaling in fully-developed turbulence. *Proc. R. Soc. Lond. A*, 434:89–99, 1991.
- [76] U. Frisch. *Turbulence, the Legacy of A.N. Kolmogorov*. Cambridge University Press, 1995.
- [77] L. Fu and G.R. Flierl. Nonlinear energy and enstrophy transfers in a realistically stratified ocean. *Dyn. Atmos. Oceans*, 4:219–246, 1980.
- [78] Y. Gagne, M. Marchand, and B. Castaing. Conditional velocity pdf in 3-d turbulence. *J. Phys. II*, 4(1):1–8, 1994.
- [79] C.S. Gardner. Bound on the energy available from a plasma. *Phys. Fluids*, 6(6):839–840, 1963.
- [80] M. Ghil and S. Childress. *Topics in geophysical fluid dynamics: Atmospheric dynamics, dynamo theory, and climate dynamics*, volume 60 of *Applied mathematical sciences*. Springer-Verlag, 1987.
- [81] S.T. Gille and S.G.L. Smith. Velocity probability density functions from altimetry. *Journal Of Physical Oceanography*, 30(1):125–136, 2000.
- [82] H. Goldstein. *Classical mechanics*. Addison-Wesley, 1980.
- [83] T. Gotoh and R. H. Kraichnan. Turbulence and tsallis statistics. *Physica D*, 193:231–244, 2004.
- [84] H.L. Grant, R.W. Stewart, and A. Moilliet. Turbulence spectra from a tidal channel. *J. Fluid Mech.*, 12:241–268, 1962.

- [85] H.L. Grant, R.W. Stewart, and A. Moilliet. The multifractal nature of the turbulent energy dissipation. *J. Fluid Mech.*, 224:429–484, 1991.
- [86] H.P. Greenspan. *The theory of rotating fluids*. Cambridge monographs on mechanics and applied mathematics. Cambridge U.P., London, 1968.
- [87] R.Pasmanter H.Brands, P.H. Chavnis and J.sommeria. Maximum entropy versus minimum enstrophy vortices. *Physics fluids*, 11:3465, 1999.
- [88] W. Heisenberg. Zur statistischen theories der turbulenz. *Zeit f. Phys.*, 124:628–657, 1948.
- [89] R. Hide and I. N. James. Differential rotation produced by potential vorticity mixing in a rapidly rotating fluid.,. *Geophys. J. R. astr. Soc.*, 74:301–312, 1983.
- [90] G. Holloway. Eddies, waves, circulation, and mixing: statistical mechanics. *Ann. Rev. Fluid Mech.*, 18:91, 1986.
- [91] M. Hossain. Reduction in the dimensionality of turbulence due to a strong rotation. *Phys. Fluids*, 6(3):1077–1079, March 1994.
- [92] X.P. Huang and C.F. Driscoll. Relaxation of 2D turbulence to a meta-equilibrium near the minimum enstrophy state. *Phys. Rev. Lett.*, 72:2187, 1994.
- [93] A. Ingersoll. Atmospheric dynamics of the outer planets. *Science*, 248:308–315, 1990.

- [94] L. Jacquin, O. Leuchter, C. Cambon, and J. Mathieu. Homogeneous turbulence in the presence of rotation. *J. Fluid. Mech.*, 220:1–52, November 1990.
- [95] D. Jault, C. Gire, and J. L. Le Mouel. Westward drift, core motions and exchanges of angular momentum between core and mantle. *Nature*, 333:353–356, 1988.
- [96] G. Joyce and D. Montgomery. Negative temperature states for the two-dimensional guidingcenter plasma. *J. Plasma Phys.*, 10:107–121, 1973.
- [97] S. Jung, P.J. Morrison, and H.L. Swinney. Statistical mechanics of two-dimensional turbulence. *J. Fluid Mech.*, submitted.
- [98] S. Jung, B.D. Storey, J. Aubert, and H. Swinney. Nonextensive statistical mechanics for rotating quasi-two-dimensional turbulence. *Physica D*, 193:252–264, 2004.
- [99] H. Kahalerras, Y. Malecot, Y. Gagne, and B. Castaing. Intermittency and reynolds number. *Phys. Fluids*, 10(4):910–921, 1998.
- [100] P. Kailasnath, K.R. Sreenivasan, and G. Stolovitzky. Probability density of velocity increments in turbulent flows. *Phys. Rev. Lett.*, 68(18):2766–2769, 1992.
- [101] N.G. Van Kampen and B.U. Felderhof. *Theoretical methods in plasma physics*. Amsterdam, North-Holland Pub. Co., 1967.
- [102] G. Kirchhoff. *Vorlesungen über Mathematische Physik*. Teubner, Leipzig, 1883.

- [103] Y.L. Klimontovich. *The statistical equilibrium of Non-equilibrium Process in a Plasma*. MIT Press, Cambridge, 1967.
- [104] A.N. Kolmogorov. Dissipation of energy in locally isotropic turbulence. *Dokl. Akad. Nauk SSSR*, 30:299–303, 1941.
- [105] A.N. Kolmogorov. Local structure of turbulence in an incompressible fluid at very high reynolds number. *C.R. Acad. Sci. URSS*, 30:301, 1941.
- [106] A.N. Kolmogorov. A refinement of previous hypotheses concerning the local structure of turbulence in a viscous incompressible fluid at high reynolds number. *J. Fluid Mech.*, 13:82–85, 1962.
- [107] R.H. Kraichnan. Inertial ranges in two-dimensional turbulence. *Phys. Fluids*, 10(7):1417–1423, July 1967.
- [108] R.H. Kraichnan. Statistical dynamics of two-dimensional flow. *J. Fluid Mech.*, 67:155–175, 1975.
- [109] R.H. Kraichnan. Find it. In E. Jen, editor, *Lectures in complex systems*, page 271, Addison-Wesley Publishing Co., Redwood City, 1989.
- [110] R.H. Kraichnan and S. Chen. Is there a statistical mechanics of turbulence? *Physica D*, 37:160–172, 1989.
- [111] R.H. Kraichnan and D. Montgomery. Two-dimensional turbulence. *Rep. Prog. Phys.*, 43:548–618, 1980.
- [112] M.D. Kruskal and C. Oberman. On the stability of plasma in static equilibrium. *Phys. Fluids*, 1:275, 1958.

- [113] H.L. Kuo. Dynamic instability of two-dimensional non-divergent flow in a barotropic atmosphere. *J. Meteor.*, 6:106–122, 1949.
- [114] L.D Landau and E.M. Lifshitz. *Statistical Mechanics*. Butterworth-Heinemann, second edition, 1987. Basic Statistical Mechanics in the first few chapters.
- [115] P.T. Landsberg. Is equilibrium always an entropy maximization? *Journal of Statistical Physics*, 35:159, 1984.
- [116] D.P. Lathrop, J. Fineberg, and H. L. Swinney. Transition to shear driven turbulence in couette-taylor flow. *Phy. Rev. A*, 46:6390–6405, 1992.
- [117] T.D. Lee. On some statistical properties of hydrodynamical and magneto hydrodynamical fields. *Q. Appl. Math.*, 10:69–74, 1952.
- [118] C.E. Leith. Minimum enstrophy vortices. *Phys. Fluids*, 27:1388–1395, 1984.
- [119] M. Lesieur. *Turbulence in Fluids*. Fluid mechanics and its applications. Dordrecht ; Boston : Kluwer Academic Publishers, third edition, 1997.
- [120] G. S. Lewis and H. L. Swinney. Velocity structure functions, scaling, and transitions in high-reynolds-number couette-taylor flow. *Phys. Rev. E*, 59(5):5457–5467, May 1999.
- [121] E.H. Lieb and M. Loss. *Analysis*. American Math. Soc., 2001.
- [122] E.M. Lifshitz and L.D. Landau. *Fluid Mechanics*. Butterworth-Heinemann, second edition, 1987. The remark on the variation of energy dissipation appeared in the 1st ed. of book in 1944.

- [123] J.L. Lumley. On the interpretation of time spectra measured in high intensity shear flows. *Phys. Fluids*, 8:1056, 1965.
- [124] D. Lynden-Bell. Statistical mechanics of violent relaxation in stellar systems. *Mon. Not. R. Astr. Soc.*, 181:405, 1967.
- [125] A. Mahalov and Y. Zhou. Analytical and phenomenological studies of rotating turbulence. *Phys. Fluids*, 8(8):2138, Aug 1996.
- [126] M. Majda, A.J. Holen. Dissipation, topography, and statistical theories for large-scale coherent structure. *Comm. Pure and Appl. Math.*, 50(12):1183–1234, 1997.
- [127] P.S. Marcus. Jupiter’s great red spot and other vortices. *Annu. Rev. Astron. Astrophys.*, 431:523, 1993.
- [128] P.S. Marcus and C. Lee. A model for eastward and westward jets in laboratory experiments and planetary atmospheres. *Phys. Fluids*, 10(6):1474–1489, June 1998.
- [129] P.S. Marcus and A. Youssef. The dynamics of jovian white ovals from formation to merger. *Icarus*, 162:74–94, 2003.
- [130] W.H. Matthaeus and D. Montgomery. Find it. *Ann. NY Acad. Sci.*, 357:203, 1980.
- [131] W.H. Matthaeus, W.T. Stirbling, D. Martinez, S. Oughton, and D. Montgomery. Decaying two-dimensional navier-stokes turbulence at very long times. *Physica D*, 51:531–538, 1991.

- [132] T. Maxworthy. The dynamics of a high-speed jovian jet. *Planet. Space Sci.*, 32:1053–1058, 1983.
- [133] A.D. McEwan, R.O.R.Y. Thompson, and R.A. Plumb. Mean flows driven by weak eddies in rotating systems. *J. Fluid Mech.*, 99:655–672, 1980.
- [134] J. McWilliams and G. Flierl. On the evolution of isolated lenses on a beta-plane. *J. Phys. Oceanogr.*, 9:1155 – 1182, 1979.
- [135] J.C. McWilliams. The emergence of isolated coherent vortices in turbulent flow. *J. Fluid Mech.*, 146:21–43, 1984.
- [136] S.D. Meyers. *Laboratory Studies of Coherent Structures in Quasi-Geostrophic Flows*. PhD thesis, University of Texas, Austin, 1991.
- [137] S.D. Meyers, J. Sommeria, and H.L. Swinney. Laboratory study of the dynamics of jovian-type vortices. *Physica D*, 37:515–530, 1989.
- [138] J. Miller. Statistical mechanics of euler equations in 2-d. *Phys. Rev. Lett.*, 65:2137–2140, 1990.
- [139] J. Miller, P. B. Weichman, and M. C. Cross. Statistical mechanics, euler’s equation, and jupiter’s red spot. *Phys. Rev. A*, 45:2328–2359, 1992.
- [140] F. Moisy, O. Doaré, T. Pasutto, O. Daube, and M. Rabaud. Experimental and numerical study of the shear layer instability between two counter-rotating disks. *J. Fluid Mech.*, 507:175–202, 2004.

- [141] A.S. Monin and A.M. Yaglom. *Statistical fluid mechanics*, volume II. MIT press, 1975.
- [142] N. Mordant, A. M. Crawford, and E. Bodenschatz. Experimental lagrangian acceleration probability density function measurement. *Physica D*, 193:245–251, 2004.
- [143] P.J. Morrison. The maxwell-vlasov equations as a continuous hamiltonian system. *Phys. Lett.*, 80A:383–386, 1980.
- [144] P.J. Morrison. Hamiltonian field description of two-dimensional vortex fluids an guiding center plasmas. *Princeton University Plasma Physics Laboratory Report, PPPL-1783*, 1981.
- [145] P.J. Morrison. Poisson brackets for fluids and plasmas. In M. Tabor and Y. Treve, editors, *Mathematical Methods in Hydrodynamics and Integrability in Related Dynamical Systems*, page 13. AIP, 1982.
- [146] P.J. Morrison. Hamiltonian description of the ideal fluid. *Rev. Mod. Phys.*, 70:467–521, 1998.
- [147] P.J. Morrison. Hamiltonian description of vlasov dynamics: Action-angle variables for the continuous spectrum. *Trans. Theory and Stat. Phys.*, 3:397, 2000.
- [148] P.J. Morrison. Hamiltonian and action principle formulations of plasma physics. *Phys. Plasma*, 2005.
- [149] P.J. Morrison and D. Pfirsch. Dielectric energy versus plasma energy and action-angle variables for the vlasov equation. *Phys. Fluids B*, 4:3038–3057, 1992.

- [150] P.J. Morrison and D. Pfirsch. The free energy of maxwell-vlasov equilibria. *Phys. Fluids B*, 2:1105–1113, 1992.
- [151] P.J. Morrison and B.A. Shadwick. On the fluctuation spectrum of plasma. *Phys. Fluids*, 12:to appear.
- [152] T. Nakano, D. Fukayama, A. Bershadskii, and T. Gotoh. Stretched lognormal distribution and extended self-similarity in 3d turbulence. *J. Phys. Soc. Japan*, 71(9):2148–2157, Sep 2002.
- [153] M. Nauenberg. Critique of q-entropy for thermal statistics. *Phys. Rev. E*, 67:036114, 2003.
- [154] C.L.M.H. Navier. Mémoire sur les lois du mouvement des fluides. *Mém. Acad. Roy. Sci.*, 6:389–395, 1823.
- [155] M. Nelkin. Universality and scaling in fully developed turbulence. *Advances in Physics*, 43(2):143–181, 1994.
- [156] A. Mahalov B. Nicolaenko and Y. Zhou. Energy spectra of strongly stratified and rotating turbulence. *ICASE Report No. 98-28*, 1998.
- [157] F.T.M. Nieuwstadt and J.A. Steketee. *Selected Papers of J.M. Burgers*. Kluwer, Dordrecht, 1995.
- [158] A.M. Obukhov. Some specific features of atmospheric turbulence. *J. Fluid Mech.*, 13:77–81, 1962.
- [159] P.J. Olver. A nonlinear hamiltonian structure for the euler equations. *J. Math. Anal. Appl.*, 89:233, 1982.

- [160] L. Onsager. The distribution of energy in turbulence. *Phys. Rev.*, 68:286, 1945.
- [161] L. Onsager. Statistical hydrodynamics. *Nuovo Cimento Suppl.*, 6:279–287, 1949.
- [162] N. Padhye and P.J. Morrison. Fluid element relabeling symmetry. *Phys. Lett.*, 219:287–292, 1996.
- [163] J. Paret and P. Tabeling. Experimental observation of the two-dimensional inverse energy cascade. *Phys. Rev. Lett.*, 79(21):4162–4165, 1997.
- [164] J. Paret and P. Tabeling. Intermittency in the two-dimensional inverse cascade of energy: Experimental observations. *Phys. Fluids*, 10(12):3126–3136, December 1998.
- [165] J. Pedlosky. *Geophysical fluid dynamics*. Springer Verlag, New York, 1979.
- [166] G. Pedrizzetti, E.A. Novikov, and A.A. Praskovsky. Self-similarity and probability distributions of turbulent intermittency. *Phys. Rev. E*, 53(1):475–484, Jan 1996.
- [167] N.A. Philips. Energy transformations and meridional circulations associated with simple baroclinic waves in a two-level, quasi-geostrophic model. *Tellus*, 6:273–286, 1954.
- [168] J.-F. Pinton and R. Labbé. Correction to the Taylor hypothesis in swirling flows. *J. Phys. II*, 4:1461, 1994.

- [169] J.F. Pinton, F. Plaza, L. Danaila, P. Le Gal, and F. Anselmet. On velocity and passive scalar scaling laws in a turbulent swirling flow. *Physica D*, 122(1-4):187–201, 1998.
- [170] M. Rabaud and Y. Couder. Instability of an annular shear layer. *J. Fluid Mech.*, 136:291–319, 1983.
- [171] P.B. Rhines. Waves and turbulence on a beta-plane. *J. Fluid Mech.*, 69(3):417–443, 1975.
- [172] P.B. Rhines. Geostrophic turbulence. *Annual review of fluid mechanics*, vol.11, pages 401–41, 1979.
- [173] P.B. Rhines and W.R. Young. Homogenization of potential vorticity in planetary gyres. *J. Fluid Mech.*, 122:347–367, 1982.
- [174] L.F. Richardson. Atmospheric diffusion shown on a distance-neighbor graph. *Proc. R. Soc. Lond. A*, 110:709–737, 1926.
- [175] R. Robert. A maximum-entropy principle for two-dimensional perfect fluid dynamics. *J. Stat. Phys.*, 65:531–553, 1991.
- [176] R. Robert and J. Sommeria. Statistical equilibrium states for two-dimensional flows. *J. Fluid Mech.*, 229:291–310, 1991.
- [177] R. Robert and J. Sommeria. Relaxation towards a statistical equilibrium state in two-dimensional perfect fluid dynamics. *Phys. Rev. Lett.*, 69:2776–2779, 1992.
- [178] C.G. Rossby. Relation between variations in the intensity of the zonal

- circulation of the atmosphere and the displacements of the semipermanent centers of action. *J. Marine Res.*, 2:38–55, 1939.
- [179] C.G. Rossby. On the distribution of angular velocity in gaseous envelopes under the influence of large-scale horizontal mixing process,. *Bull. Am. Met. Soc.*, 28:53–68, 1947.
 - [180] N. Rostoker. Fluctuations of a plasma .1. *Nucl. Fusion*, 1:101–120, 1961.
 - [181] N. Rostoker. Test particle method in kinetic theory of a plasma. *Phys. Fluids*, 7(4):491–498, 1964.
 - [182] S.G. Saddoughi and S.V. Verravalli. Local isotropy in turbulent boundary-layers at high reynolds-number. *J. Fluid Mech.*, 268:333, 1994.
 - [183] R. Salmon. Baroclinic instability and geostrophic turbulence. *Geophys. Astrophys. Fluid Dynamics*, 15:167–211, 1978.
 - [184] R. Salmon. Two-layer quasi-geostrophic turbulence in a simple special case. *Geophys. Astrophys. Fluid Dynamics*, 10:25–52, 1978.
 - [185] R. Salmon. Hamilton’s principle and ertel’s theorem. In M. Tabor and Y. Treve, editors, *Mathematical Methods in Hydrodynamics and Integrability in Related Dynamical Systems*. AIP, 1982.
 - [186] R. Salmon. *Lectures on Geostrophical Fluid Dynamics*. Oxford University Press, New York, 1998.
 - [187] R. Salmon, G. Holloway, and M.C. Henderschott. The equilibrium statistical mechanics of simple quasi-geostrophic models. *J. Fluid Mech.*, 75:691–703, 1976.

- [188] L.S. Schulman. *Techniques and Applications of Path Integration*. John Wiley & Sons, New York, 1981.
- [189] Z.-S. She and E. Jackson. On the universal form of energy spectra in fully developed turbulence. *Phys. Fluids A*, 5:1526 – 1528, 1993.
- [190] Z.-S. She and E. L  v  que. Universal scaling laws in fully developed turbulence. *Phys. Rev. Lett.*, 72:336–339, 1994.
- [191] Z.-S. She and E.C. Waymire. Quantized energy cascade and log-poisson statistics in fully developed turbulence. *Phys. Rev. Lett.*, 74:262–265, 1995.
- [192] K.S. Smith and G.K. Vallis. The scales and equilibration of midocean eddies: Freely evolving flow. *J. Phys. Oceano.*, 31:554–571, 2001.
- [193] L.M. Smith and F. Waleffe. Transfer of energy to two-dimensional large scales in forced, rotating three-dimensional turbulence. *Phys. Fluids*, 11(6):1608–1622, June 1999.
- [194] S.G.L. Smith and S.T. Gille. Probability density functions of large-scale turbulence in the ocean. *Phys. Rev. Lett.*, 81(23):5249–5252, 1998.
- [195] T. H. Solomon, J.W. Holloway, and H. L. Swinney. Shear flow instabilities and Rossby waves in barotropic flow in a rotating annulus. *Phys. Fluids*, 5(8):1971–1982, August 1993.
- [196] J. Sommeria, S.D. Meyers, and H.L. Swinney. Laboratory simulation of jupiter’s great red spot. *Nature*, 331(6158):689–693, February 1988.

- [197] J. Sommeria, S.D. Meyers, and H.L. Swinney. Laboratory model of a planetary eastward jet. *Nature*, 337(6202):58–61, Jan 1989.
- [198] J. Sommeria, S.D. Meyers, and H.L. Swinney. Experiments on vortices and Rossby waves in eastward and westward jets. In A. Osborne, editor, *Nonlinear Topics in Ocean Physics*, pages 227–269, 1991.
- [199] L. Sorriso-Valvo, V. Carbone, P. Veltri, G. Consolini, and R. Bruno. Intermittency in the solar wind turbulence through probability distribution functions of fluctuations. *Geophys. Res. Lett.*, 26(13):1801–1804, 1999.
- [200] R.W. Stewart, J.R. Wilson, and R.W. Burling. Some statistical properties of small scale turbulence in an atmospheric boundary layer. *J. Fluid Mech.*, 41:141–152, 1970.
- [201] G. Stolovitzky, P. Kailasnath, and K.R. Sreenivasan. Kolmogorov’s refined similarity hypotheses. *Phys. Rev. Lett.*, 69(8):1178–1179, 1992.
- [202] K. Sundermeyer. *Constrained Dynamics*. Springer-Verlag, Berlin, 1982.
- [203] P. Tabeling. Two-dimensional turbulence: a physicist approach. *Physics Reports*, 362:1–62, 2002.
- [204] P. Tabeling, G. Zocchi, F. Belin, J. Maurer, and H. Willaime. Probability density functions, skewness, and flatness in large reynolds number turbulence. *Phys. Rev. E*, 53(2):1613–1621, 1996.
- [205] G.I. Taylor. The spectrum of turbulence. *Proc. R. Soc. Lond. A*, 164:476 – 490, 1938.

- [206] R. Temam. *Infinite-Dimensional Dynamical Systems in Mechanics and Physics*. Springer, New York, second edition, 1997.
- [207] J-L. Thiffeault and P.J. Morrison. Classification of casimir invariants of lie-poisson brackets. *Physica D*, 136:205–244, 2000.
- [208] W. B. Thompson. *An Introduction to Plasma Physics*. Pergman, Oxford, 1962.
- [209] W.B. Thompson and J. Hubbard. Long-range forces and the diffusion coefficients of a plasma. *Rev. Mod. Phys.*, 32:714, 1960.
- [210] Y. Tian, E.R. Weeks, K. Ide, J.S. Urbach, C.N. Baroud, M. Ghil, and H.L. Swinney. Experimental and numerical studies of an eastward jet over topography. *J. Fluid Mech.*, 438:129–157, July 2001.
- [211] C.V. Tran and J.C. Bowman. On the dual cascade in two-dimensional turbulence. *Physica D*, 176:242–235, 2003.
- [212] C.V. Tran and J.C. Bowman. Robustness of the inverse cascade in two-dimensional turbulence. *Phys. Rev. E*, 69:036303, 2004.
- [213] C.V. Tran and T.G. Shepherd. Constraints on the spectral distribution of energy and enstrophy dissipation in forced two-dimensional turbulence. *Physica D*, 165:199–212, 2002.
- [214] C. Tsallis. <http://tsallis.cat.cbpf.br/biblio.htm>.
- [215] C. Tsallis. Possible generalization of boltzmann-gibbs statistics. *J. Stat. Phys.*, 52:479, 1988.

- [216] C. Tsallis. What should a statistical mechanics satisfy to reflect nature? *Physica D*, 193:3–34, 2004.
- [217] C. Tsallis, R.S. Mendes, and A.R. Plastino. The role of constraints within generalized nonextensive statistics. *Physica A*, 261:534 –, 1998.
- [218] TSI. *TSI Hot film manual*.
- [219] A. Turiel, G. Mato, N. Parga, and J.P. Nadal. Self-similarity properties of natural images resemble those of turbulent flows. *Phys. Rev. Lett.*, 80(5):1098–1101, 1998.
- [220] B. Turkington. Statistical equilibrium measures and coherent states in two-dimensional turbulence. *Comm. Pure and Appl. Math.*, 52(7):781–809, 1999.
- [221] G.E. Uhlenbeck. *Probability and related topics in physical sciences*. Interscience Publ., 1959.
- [222] C.W. Van Atta and W.Y. Chen. Structure functions of turbulence in the atmospheric boundary layer over the ocean. *J. Fluids Mech.*, 44:145–159, 1970.
- [223] J. Vanneste. Rossby wave interactions in a shear flow with critical levels. *J. Fluid Mech.*, 323:317–338, 1996.
- [224] A. Vincent and M. Menguzzi. The spatial structure and statistical properties of homogeneous turbulence. *J. Fluid Mech.*, 225:1–25, 1991.
- [225] L. Wang, S. Chen, J.G. Brasseur, and J.C. Wyngaard. Examination of hypotheses in the kolmogorov refined turbulence theory through high-

- resolution simulations. part 1. velocity field. *J. Fluid Mech.*, 309:113–156, 1996.
- [226] E.R. Weeks and H.L. Swinney. Anomalous diffusion resulting from strongly asymmetric random walks. *Phys. Rev. E*, 57:4915–4920, 1998.
 - [227] E.R. Weeks and H.L. Swinney. Random walks and lévy flights observed in fluid flows. *Nonlinear Science Today*, 1998.
 - [228] E.R. Weeks, Y. Tian, J.S. Urbach, K. Ide, H.L. Swinney, and M. Ghil. Transitions between blocked and zonal flows in a rotating annulus with topography. *Science*, 278:1598–1601, 1997.
 - [229] Eric R. Weeks. *Experimental Studies of Anomalous Diffusion, Blocking Phenomena, and Two Dimensional Turbulence*. PhD thesis, University of Texas, Austin, 1997.
 - [230] N. Wiener. A new type of integral expansion. *J. Math. & Phys.*, 2:167–176, 1923.
 - [231] J. Wyngaard and S.F. Clifford. Taylor’s hypothesis and high-frequency turbulence spectra. *J. Atmos. Sci.*, 34:922, 1977.
 - [232] J. C. Wyngaard and H. Tennekes. Measurements of the small-scale structure of turbulence at moderate reynolds numbers. *Phys. Fluids*, 13:1962–1969, 1970.
 - [233] Z. Yin, H.J.H. Clercx, and D.C. Montgomery. An easily implemented task-based parallel scheme for the fourier pseudospectral solver applied to 2d navier-stokes turbulence. *Computers and Fluids*, 33(4):509–520, 2004.

- [234] Y. Zhou. A phenomenological treatment of rotating turbulence. *Phys. Fluids*, 7(8):2092–2094, August 1995.

Vita

Sunghwan Jung was born in Seoul, Korea, on November 24 1974, the son of Jinsu Jung and Shinja Kim. He graduated from Daewon Foreign Language High School with Spanish major in the spring of 1993, and received a B.S. degree in Chemical engineering from Sogang University in the fall of 1999. During college years, he served as Korean Air Forces for two and half years and was stationed in the 6th Rescue Command and spent one year in Creighton University, NE. He obtained the master of Science in Physics from Pohang University of Science and Technology in the fall of 2001. He started graduate studies at University of Texas at Austin in August, 2001. He got married with Eunyoung Song on December 24th 2002 with God-blessed white snows.

Permanent Address: Sunghwan Jung

Center for Nonlinear Dynamics

University of Texas at Austin, Austin, TX

78712

This dissertation was typeset with $\text{\LaTeX} 2_{\epsilon}$ ¹ by the author.

¹ $\text{\LaTeX} 2_{\epsilon}$ is an extension of \LaTeX . \LaTeX is a collection of macros for \TeX . \TeX is a trademark of the American Mathematical Society. The macros used in formatting this dissertation were written by Dinesh Das, Department of Computer Sciences, The University of Texas at Austin.